

JOURNAL OF NUCLEAR MATERIALS

A JOURNAL ON METALLURGY, CERAMICS AND SOLID
STATE PHYSICS IN THE NUCLEAR ENERGY INDUSTRY

EDITORS:

R. W. CAHN - BIRMINGHAM, ENGLAND - J. P. HOWE - CANOGA PARK, U.S.A.
P. LACOMBE - PARIS, FRANCE - S. T. KONOBEEVSKI - MOSCOW, U.S.S.R.

CONTENTS

L. S. CASTLEMAN, Layer growth during interdiffusion in the aluminum-uranium alloy system	1
G. J. DIENES and A. C. DAMASK, An estimate of the effect of radiation on the thermal conductivity of beryllium	16
G. V. KIDSON, Some aspects of the growth of diffusion layers in binary systems	21
B. R. BUTCHER and D. BAVERSTOCK, The effect of the $\alpha \rightarrow \beta \rightarrow \alpha$ phase transformation on the preferred orientation of α uranium	30
J. DIXMIER, R. HASSON, S. MARAVAL et L. M. VINCENT, Corrosion par l'hexafluorure d'uranium. Ière partie: Méthode d'étude de la corrosion	41
Mmes BELLA BELBROCH, CLAUDIA PIEKARSKI et M. PIERRE PERIO, Influence des dimensions cristallines sur la cinétique d'oxydation de UO_2	60
LOWELL T. LLOYD, Thermal expansion of alpha-uranium single crystals	67
S. J. ROTHMAN, J. GRAY Jr., J. P. HUGHES and A. L. HARKNESS, Self-diffusion in beta uranium	72
S. J. ROTHMAN, The diffusion of gold in gamma uranium	77
R. O. TEEG and R. E. OGILVIE, Effect of orientation and temperature on the modes of deformation of uranium	81
J. C. BOKROS, Graphite-metal compatibility at elevated temperatures	89
A. P. GREEN and J. SAWKILL, Plastic anisotropy and fracture in beryllium	101
<i>Letters to the Editors -- Lettres aux Rédacteurs</i>	
J. A. HORAK and H. V. RHUDE, Irradiation growth of zirconium-plutonium alloys	111
A. MOORE, Improved mechanical properties and associated constitutional changes in commercially pure ingot beryllium as affected by heat treatment above 700° C	113
J. A. SABATO and R. W. CAHN, The recrystallization of uranium during cold or hot forging	115
H. SPINDLER, J. UHLMANN, H. E. RÖLLIG, A. MERZ und F. THÜMMER, Verhalten verschiedener Aluminium-Sinterwerkstoffe gegen Wasser hoher Temperatur und gegen Spaltstoffe	120
<i>Discussion</i>	
A. H. WILLIS, α - β thermal cycling of uranium	124
Errata	124



EDITORIAL ADVISORY BOARD — CONSEIL DES REDACTEURS

S. AAS (Kjeller, Norway)
 K. F. ALDER (Lucas Heights, Australia)
 P. ALBERT (Vitry, France)
 G. W. ARDLEY (Whetstone, U.K.)
 J. E. BURKE (Schenectady, U.S.A.)
 R. CAILLAT (Saclay, France)
 G. CHAUDRON (Vitry, France)
 H. CHISWIK (Argonne, U.S.A.)
 A. T. CHURCHMAN (Bristol, U.K.)
 A. S. COFFINBERY (Los Alamos, U.S.A.)
 A. H. COTTELL (Cambridge, U.K.)
 B. L. CUNNINGHAM (Ottawa, Canada)
 C. DECROLY (Bruxelles, Belgium)
 M. D'HONT (Mol, Belgium)
 J. D. FAST (Eindhoven, Netherlands)
 H. M. FINNISTON (Newcastle, U.K.)
 J. FRIEDEL (Paris, France)
 E. GEBHARDT (Stuttgart, Germany)

E. GRISON (Saclay, France)
 B. R. HASIGUTI (Tokyo, Japan)
 J. HERENGUEL (Antony, France)
 L. K. JETTER (Oak Ridge, U.S.A.)
 B. KIESSLING (Stockholm, Sweden)
 K. LÜCKE (Aachen, Germany)
 B. LUSTMAN (Pittsburgh, U.S.A.)
 E. MADDIN (Philadelphia, U.S.A.)
 A. MERLINI (Milan, Italy)
 P. MURRAY (Harwell, U.K.)
 R. MYERS (Sydney, Australia)
 E. C. W. PERRYMAN (Culcheth, U.K.)
 J. A. L. ROBERTSON (Chalk River, Canada)
 J. A. SABATO (Buenos Aires, Argentina)
 K. TANGHI (Bombay, India)
 P. VACHET (Paris, France)
 J. WILLIAMS (Harwell, U.K.)

Papers or letters should be sent to one of the Editors,

R. W. CAHN (Dept. of Metallurgy, University of Birmingham, Birmingham 15, England).
 J. P. HOWE (Atomics International, P.O. Box 309, Canoga Park, California, U.S.A.).
 P. LACOMBE (Centre de Recherches Métallurgiques de l'Ecole des Mines, Blvd. St. Michel 60, Paris VI, France)
 S. T. KONOBEVSKI (U.S.S.R. Academy of Sciences) Leninsky Prospekt 14, Moscow V-71, U.S.S.R.

either directly or through a member of the Editorial Advisory Board.

Papers or letters should be written in English, French or German; papers should have a summary in the appropriate language. Translations of the summary into the two other languages and in Russian will be added by the Editors.

Instructions to contributors will be found in Vol. 1, No. 1 (pp. 111-112).

Books for review should be sent to one of the Editors.

The Journal of Nuclear Materials will be published monthly.

The subscription price of a volume of 360 pages is \$ 18.00, 130s., Gld. 68.50 per volume, post-free.

Subscriptions should be sent to the publishers, North-Holland Publishing Company, P.O. Box 103, Amsterdam or to any subscription-agent.

No part of this issue may be reproduced in any form, by print, photoprint, microfilm or any other means without written permission from the publisher. Reprints, photoprints or microfilms are obtainable at cost from the publisher.

Les articles ou les lettres devront être envoyés à un des Rédacteurs-en-chef,

R. W. CAHN (Dept. of Metallurgy, University of Birmingham, Birmingham 15, England).
 J. P. HOWE (Atomics International, P.O. Box 309, Canoga Park, California, U.S.A.).
 P. LACOMBE (Centre de Recherches Métallurgiques de l'Ecole des Mines, 60 Bd. St. Michel, Paris VI, France)
 S. T. KONOBEVSKI (Académie des Sciences de l'U.S.S.R.) Leninsky Prospekt 14, Moscow V-71, U.S.S.R.

ou directement ou par un membre du Conseil des Rédacteurs.

Les articles ou les lettres devront être rédigés en anglais, français ou allemand, les articles avec un résumé dans la langue correspondante. Les traductions du résumé dans les deux autres langues et en russe seront ajoutées par les Rédacteurs-en-chef.

Les instructions aux auteurs se trouvent dans le Vol. 1, No. 2 (pp. 211-212).

Les livres (exemplaires de presse) devront être envoyés à un des Rédacteurs-en-chef.

Le Journal des Matériaux Nucléaires paraîtra tous les mois.

Prix de souscription par volume d'environ 360 pages: \$ 18.00, 130s., Gld. 68.50, franco.

Les abonnements devront être envoyés aux éditeurs, North-Holland Publishing Company, P.O. Box 103, Amsterdam, ou à votre librairie.

JOURNAL OF NUCLEAR MATERIALS
JOURNAL DES MATERIAUX NUCLEAIRES

EDITORIAL ADVISORY BOARD — CONSEIL DES REDACTEURS

- | | |
|----------------------------------------|------------------------------------------|
| S. AAS (Kjeller, Norway) | E. GRISON (Saclay, France) |
| K. F. ALDER (Lucas Heights, Australia) | R. R. HASIGUTI (Tokyo, Japan) |
| P. ALBERT (Vitry, France) | J. HERENGUEL (Antony, France) |
| G. W. ARDLEY (Whetstone, U.K.) | L. K. JETTER (Oak Ridge, U.S.A.) |
| J. E. BURKE (Schenectady, U.S.A.) | G. ÖSTBERG (Stockholm, Sweden) |
| R. CAILLAT (Saclay, France) | K. LÜCKE (Aachen, Germany) |
| G. CHAUDRON (Vitry, France) | B. LUSTMAN (Pittsburgh, U.S.A.) |
| H. CHISWIK (Argonne, U.S.A.) | R. MADDIN (Philadelphia, U.S.A.) |
| A. T. CHURCHMAN (Bristol, U.K.) | A. MERLINI (Milan, Italy) |
| A. S. COFFINBERRY (Los Alamos, U.S.A.) | P. MURRAY (Harwell, U.K.) |
| A. H. COTTRELL (Cambridge, U.K.) | R. MYERS (Sydney, Australia) |
| R. L. CUNNINGHAM (Ottawa, Canada) | E. C. W. PERRYMAN (Culcheth, U.K.) |
| C. DECROLY (Bruxelles, Belgium) | J. A. L. ROBERTSON (Chalk River, Canada) |
| M. D'HONT (Mol, Belgium) | J. A. SABATO (Buenos Aires, Argentina) |
| J. D. FAST (Eindhoven, Netherlands) | K. TANGRI (Bombay, India) |
| H. M. FINNISTON (Newcastle, U.K.) | J. TERRAZA (Madrid, Spain) |
| J. FRIEDEL (Paris, France) | P. VACHET (Paris, France) |
| E. GEBHARDT (Stuttgart, Germany) | J. WILLIAMS (Harwell, U.K.) |

JOURNAL OF NUCLEAR MATERIALS

A JOURNAL ON METALLURGY, CERAMICS AND SOLID
STATE PHYSICS IN THE NUCLEAR ENERGY INDUSTRY

Editors :

R. W. CAHN — BIRMINGHAM, ENGLAND

J. P. HOWE — CANOGA PARK, U.S.A.

P. LACOMBE — PARIS, FRANCE

S. T. KONOBEEVSKI — MOSCOW, U.S.S.R.

VOLUME 3

JANUARY 1961 — APRIL 1961



NORTH-HOLLAND PUBLISHING COMPANY — AMSTERDAM

DES MATERIAUX NUCLEAIRES

PRINTED IN THE NETHERLANDS
DRUKKERIJ HOLLAND N.V., AMSTERDAM

LAYER GROWTH DURING INTERDIFFUSION IN THE ALUMINUM-URANIUM ALLOY SYSTEM †

L. S. CASTLEMAN

General Telephone & Electronics Laboratories, Inc., Bayside Laboratories, Bayside 60, New York, USA

Received 29 March 1960

Interdiffusion in the aluminum-uranium system has been investigated over the temperature range 400°–600° C, and over the pressure range 1½–10 tsi for diffusion times of 24 hours and less. The pressure-induced increase in UAl_3 layer thickness has been confirmed. Interesting correlations have been shown to exist between annealing time, annealing temperature, and applied pressure on the one hand, and the nature and distribution of structural defects in the UAl_3 diffusion zone on the other. It has been demonstrated that the solubility range within the UAl_3 phase must be at least 2.6 at % uranium. It has been shown that the growth of the UAl_4 and UAl_2 phases in incremental couples is much slower than the growth of UAl_3 in aluminum-uranium couples. Finally, it is proposed that the effect of pressure on UAl_3 layer growth is primarily mechanical in that higher pressures repress the tendency for the formation of macroscopic voids and thus effectively increase the cross-sectional area available for interdiffusion.

L'interdiffusion dans le système aluminium-uranium a été étudiée dans l'intervalle de température 400°–600° C et dans le domaine de pression, de 1,25 à 10 tsi (200 à 1575 kg/cm²) pour des durées de diffusion de 24 heures ou moins. L'accroissement de l'épaisseur de la couche de UAl_3 en fonction de la pression a été confirmé. On a montré qu'il existe des corrélations intéressantes entre le temps de recuit, la température de recuit et la pression appliquée d'une part, et la nature et la répartition des défauts de structure de la zone de diffusion de UAl_3 d'autre part. On a démontré que la solubilité de l'uranium dans la phase UAl_3 doit

atteindre au moins 2,6 atomes %. On a montré que la croissance des phases UAl_4 et UAl_2 dans des couples différentiels est beaucoup plus lente que la croissance de UAl_3 dans les couples aluminium-uranium.

Finalement, on suggère que l'effet de la pression sur la croissance de la couche de UAl_3 est principalement d'ordre mécanique car l'augmentation de pression entrave la tendance à la formation de cavités macroscopiques et accroît ainsi effectivement la section efficace disponible pour l'interdiffusion.

Im System Aluminium-Uran wurde die gegenseitige Diffusion im Temperaturbereich von 400 bis 600° C und im Druckbereich von 2 bis 15,7 kg/mm² über Diffusionszeiten bis zu 24 Stunden untersucht. Es bestätigte sich, dass die Dickenzunahme der UAl_3 -Schicht druckabhängig ist. Zwischen Glühdauer, Glühtemperatur und angewendetem Druck einerseits und der Natur und Verteilung von Strukturfehlern in der UAl_3 -Diffusionszone andererseits ergaben sich interessante Zusammenhänge. Die Löslichkeit von Uran in UAl_3 beträgt nach den Versuchsergebnissen wenigstens 2,6 At %. Es wurde gezeigt, dass das Wachstum von UAl_4 und UAl_2 in speziell zusammengesetzten Diffusionsproben viel langsamer als das Wachstum von UAl_3 in gewöhnlichen Uran-Aluminium-Proben ist. Schliesslich wird der Einfluss des Drucks auf das Wachstum von UAl_3 -Schichten primär auf eine rein mechanische Wirkung zurückgeführt, indem durch höhere Drücke die Bildung makroskopischer Poren vermindert und damit der für die Diffusion massgebende Querschnitt erhöht wird.

1. Introduction

The joining of dissimilar metals by diffusion bonding techniques has assumed an important place in reactor fuel element technology. As a

consequence, considerable interest is developing in the study of intermetallic layer growth during diffusion bonding and more generally in the mechanisms and kinetics of interdiffusion in

† This work was performed as part of AEC Contract No. AT(30-1) 2102.

multi-phase multi-component metallic systems. The widespread use of aluminum-clad uranium fuel elements has focussed particular attention on the aluminum-uranium system, and in recent years a number of investigations of interdiffusion in this system have been reported. The earliest study relating to these two metals was apparently made by Bareis¹⁾, who discovered that clean surfaces of aluminum and uranium underwent an alloying reaction when brought into mutual contact within the temperature range 250° C to 450° C; anodization of the aluminum surface prevented the alloying reaction. He found that the intermetallic compound UAl_3 was formed during the reaction, and he advanced the following tentative conclusions: (a) UAl_3 is formed by the diffusion of the uranium through the UAl_3 layer; and (b) an increase in applied pressure is accompanied by an increase in the thickness of the UAl_3 layer. Storchheim and Zambrow²⁾ confirmed the pressure effect on the UAl_3 layer thickness in the temperature range 400° C to 550° C and concluded from marker motion studies that aluminum diffused faster into uranium than vice versa. Independently LeClaire and Bear³⁾ also observed the pressure effect in the temperature range 480° C to 620° C. They found that the UAl_3 layer increased in thickness parabolically with time, as would be expected if volume diffusion were rate controlling. In addition, they indicated that in a critical temperature range, 525° C to 570° C, the layer thickness increased with decreasing temperature if pressures of 790 kg/cm² and 1575 kg/cm² (5 tsi and 10 tsi) were used, (a minimum occurring in the vicinity of 570° C), whereas the more conventional behavior was realized if the pressure employed was 200 kg/cm² (1½ tsi). The authors suggested that the effects of pressure cannot be attributed to changes in the diffusion coefficients, but possibly either to changes in the interface concentrations or to allotropic changes in existing phases or to the nucleation of new phases which become stable under the pressure conditions employed. Most recently, Bierlein and Green⁴⁾ investigated the

maximum penetration of uranium into aluminum in the temperature range 200° C to 390° C. They observed that surface preparation affected the course of interdiffusion markedly; cathodically vacuum etched surfaces permitted the maximum growth of the UAl_3 layer at 390° C, whereas layer growth inhibition occurred in identical samples whose surfaces had only been chemically cleaned.

The results of the previous investigations into aluminum-uranium interdiffusion appeared to be anomalous in several respects. In the first place, the effect of applied pressure in increasing layer growth was surprising, since a contrary effect had been observed in the aluminum-nickel system^{5,6)}. A pressure-induced decrease in layer growth appeared to be much more plausible, since it could readily be explained on the basis of pressure-induced decreases in the diffusion coefficients⁶⁾. Second, the existence of a "negative activation energy" temperature region as reported by LeClaire and Bear was quite curious. Since the data reported by the previous investigators had been obtained from relatively short-time diffusion runs lasting at most a few hours, a question arose as to whether the reported results reflected transient conditions associated with bond formation and early stages of interdiffusion, or whether the findings were valid over much longer diffusion times. Accordingly, it was decided to re-examine interdiffusion in the aluminum-uranium system in order to clarify the nature of the interdiffusional processes; the results are reported in this paper.

2. Experimental Procedure

The aluminum-uranium diffusion couples were prepared from high-purity (99.99 %) aluminum and reactor-grade uranium rods; the chemical analysis of the uranium indicated the major impurities to be 0.05 wt % carbon, 0.01 wt % iron, and 0.005 wt % nickel. Half-inch-diameter discs one quarter inch thick were machined and given grain coarsening anneals; the aluminum was heated to 600° C for 24 hours in air and the uranium to 550° C for 24 hours in evacuated Vycor capsules. The faces

of the discs were electropolished in a Disa electropolishing unit (A-2 solution), and the samples were rinsed in water and acetone, and dried; the thicknesses of the discs were then measured with a traveling microscope. Subsequently, diffusion couples were assembled consisting of one aluminum disc and one uranium disc with 0.0013 cm (0.0005 inch) diameter tungsten wires and 0.0025 cm (0.001 inch) thick molybdenum strips inserted between the mating surfaces as markers.

All of the diffusion bonding runs were made in an evacuated hot-pressing apparatus under dead weight loading conditions; the apparatus has been described in a previous paper⁶). At the start of a diffusion run the specimen was placed on the bottom punch inside the die, and the furnace assembled with the upper ram out of contact with the specimen. The system was evacuated to 0.5 μ or less, and the specimen heated to the desired temperature; as soon as the temperature was stabilized to within $\pm 2^\circ\text{C}$, pressure was applied to the specimen and maintained throughout the run. It generally took about two hours for the specimen to be heated up to temperatures in the range of 500–600° C and stabilized. Experiments showed, however, that a negligible error in interdiffusion measurements was introduced by the heating time, since diffusion effectively started only after the pressure was applied. At the end of the run, the load was removed at the same time as the furnace power was cut off, and the specimen was allowed to cool in the die. For runs lasting less than eight hours, the die containing the specimen was cooled by the introduction of flowing helium into the furnace. It was found that the specimen temperature dropped 100° C in 10 minutes or less under these circumstances; without helium cooling, it took twice as long. The error in interdiffusion measurement resulting from the cooling-down time was found to be less than one percent for runs of three hours or more.

After the completion of the diffusion anneals, the specimens were sectioned, electrolytically polished (and in some cases etched with 5 per-

cent ammonium persulfate solution containing a little hydrogen peroxide), and the intermediate phase and remaining uranium and aluminum layer thicknesses were then determined. Six to twelve measurements were made of each layer thickness with a traveling microscope, and an average thickness and standard deviation calculated.

In general, there appeared to be no difficulty with layer growth inhibition due to the formation of an oxide layer (except in those instances specifically noted in the discussion of UAl_3 vs. uranium diffusion couples). In order to check the procedure, an aluminum-uranium diffusion couple was annealed for 110 hours at 390° C under a pressure of 5 tsi; subsequently, the uranium penetration into the aluminum was measured and compared with similar results obtained by Bierlein and Green using cathodic vacuum etching procedures⁴). The value determined (0.31 cm; 0.124 inch) compares favorably with the Bierlein and Green value (0.07 cm; 0.027 inch), even if allowance is made for the enhancement in growth rate of the UAl_3 to be expected at 5 tsi.

For several of the experiments it was necessary to prepare UAl_3 discs. This was accomplished by the use of an interdiffusion technique similar to that used in previous work for the preparation of bulk Ni_2Al_3 ⁶). A diffusion couple consisting of a 0.19 cm (0.075 inch) thick uranium disc and a 0.44 cm (0.177 inch) thick aluminum disc was interdiffused at 600° C for 48 hours under an applied pressure of 10 tsi. The UAl_3 intermetallic phase formed was then homogenized at 720° C for 24 hours and at 900° C for 168 hours within an evacuated quartz capsule.

A few determinations were made of the uranium concentration in the UAl_3 layer of a diffusion couple by means of a nuclear track emulsion technique. An Eastman Kodak type NTA nuclear tracking emulsion film was placed in contact with longitudinal sections of diffusion couples for several hours and then developed. The tracks left in selected areas of the emulsion by alpha particles produced in the decay of

the U^{238} and U^{235} isotopes were then counted with a microscope, and the counts were converted to uranium concentration with the aid of suitable standards.

3. Experimental Results and Discussion

3.1. LAYERS APPEARING DURING INTER-DIFFUSION

The aluminum-uranium phase diagram is reproduced in fig. 1⁷⁾. There are three inter-metallic phases with highly restricted solubility ranges, and their compositions and volumes per gram atom are included in the table below:

Phase	Volume (cc per gram atom)
Al	10.0 ⁸⁾
UAl ₄	12.1 ⁹⁾
UAl ₃	11.7 ¹⁰⁾
UAl ₂	12.0 ¹¹⁾
U	12.6 ⁸⁾

In the present investigation, it was found that only the UAl₃ phase grows as a layer of substantial thickness in the aluminum-uranium diffusion couples; a typical microstructure is shown in fig. 3c. The UAl₂ phase appears only infrequently in the form of a reasonably continuous thin layer, as is evidenced in fig. 2; however, it is detected in the form of a precipitate within the UAl₃ layer contiguous to the uranium. The existence of a multi-phase region

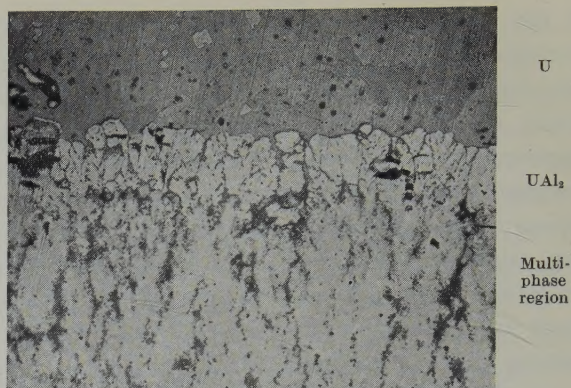


Fig. 2. Phases appearing in Al-U diffusion couple annealed at 520° C for 24 hours under an applied pressure of 5 tsi; etched with 5 % ammonium persulfate solution containing a little hydrogen peroxide.

in a two-component system is peculiar, and will be discussed in the next section. No signs were found of a UAl₄ phase layer in any of the couples during the metallographic examination.

The above results agree generally with those reported by other investigators^{1-4, 12)}, but there are specific points of difference. LeClaire and Bear³⁾ found by X-ray diffraction that traces of the UAl₂ phase existed in their samples at all temperatures and pressures; however, they noticed metallographically observable layers only at 540° C and above. In the present study, the UAl₂ phase layer was observed to occur only sporadically in specimens as a rule, but nevertheless in specimens annealed below 540° C. Also, LeClaire and Bear reported the existence of a two-phase structure principally at the lower temperatures (480° C and vicinity), whereas in the present study a multi-phase region adjacent to the UAl₃-uranium interface appeared in all couples.

3.2. PHYSICAL APPEARANCE OF DIFFUSION LAYERS

It was observed by previous investigators^{1-4, 12)} that the diffusion zone in aluminum-uranium couples is brittle, porous, and easily cracked. In the present study it was found that interesting correlations exist between the applied pressure, the diffusion temperature, the diffusion time, and the nature of the macroscopic

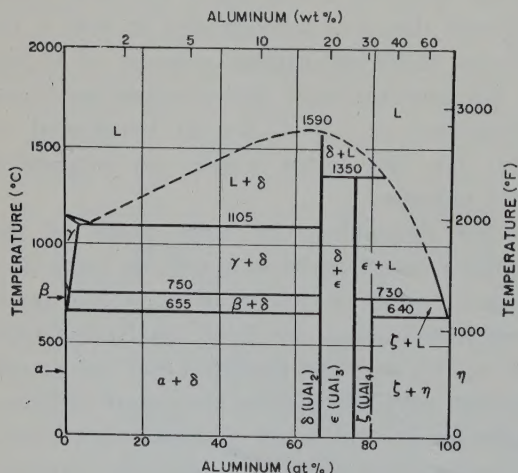
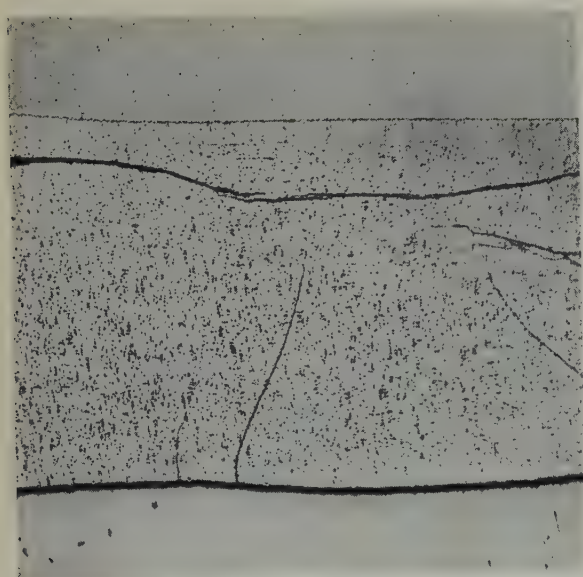


Fig. 1. The system aluminum-uranium.



(a) 110 hours at 390° C. 12 ×



(b) 24 hours at 520° C. 12 ×

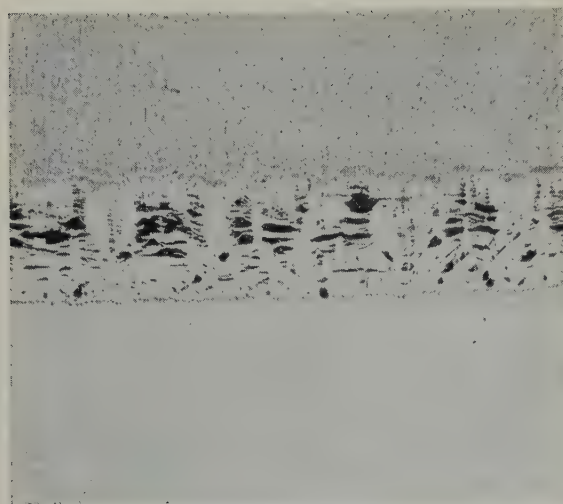


(c) 24 hours at 560° C. 12 ×

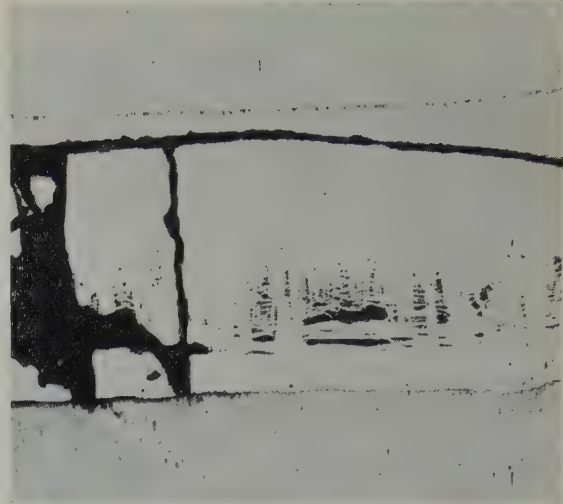
Fig. 3. Al-U diffusion couples annealed under an applied pressure of 5 tsi for varying diffusion temperatures and times; samples unetched; aluminum at the bottom in each photomicrograph.

defects occurring within the diffusion zone. In figs. 3a, 3b and 3c the effect of diffusion temperature is shown on diffusion couples annealed under an applied pressure of 5 tsi for times sufficient to produce diffusion zones 4–5 mm thick. In the 390° C specimen, the diffusion zone has a porous appearance, the porosity being

distributed uniformly throughout the UAl_3 layer. (The large cracks seen in this and other specimens occurred either when the couples were removed from the die or during the rough grinding step of the metallographic preparation.) The 520° C specimen contains short, prominent cracks or voids which lie in planes perpendicular



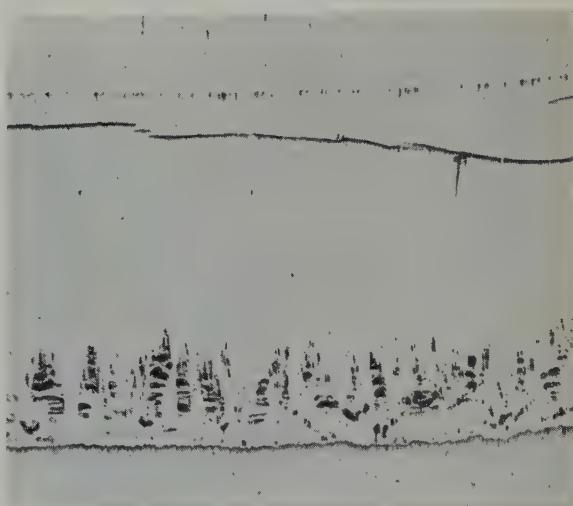
(a) 3 hours. 12 ×



(c) 16 hours. 12 ×



(b) 8 hours. 12 ×



(d) 24 hours. 12 ×

Fig. 4. Al-U diffusion couples annealed at 520° C under an applied pressure of 5 tsi for varying times; samples unetched; aluminum at the bottom in each photomicrograph.

to the diffusion direction and which occupy about one-quarter of the UAl_3 layer width near the UAl_3 -aluminum interface. The sample diffused at 560° C has a much sounder appearance; the voids or cracks are much fewer in number and lie in a narrow band near the UAl_3 -aluminum interface. The effect of increasing diffusion time in specimens diffused at a given temperature (520° C) and under a given applied pressure (5 tsi) is shown in figs. 4a, 4b, 4c and 4d. It appears as though a porous or cracked band

of constant thickness (1.4 mm thick in the present case) forms and persists in the vicinity of the UAl_3 -aluminum interface at all diffusion times; the remainder of the sample is quite brittle, as evidenced by the formation of the large cracks, but is free of porosity. In figs. 5a, 5b and 5c, a series of photomicrographs is shown of samples annealed at different pressures, but at the same temperature (570° C) and for the same time (8 hours). It is evident that the diffusion zone becomes relatively more sound as

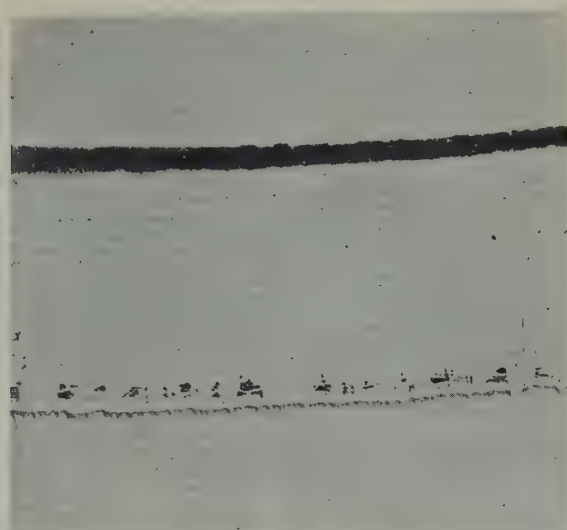
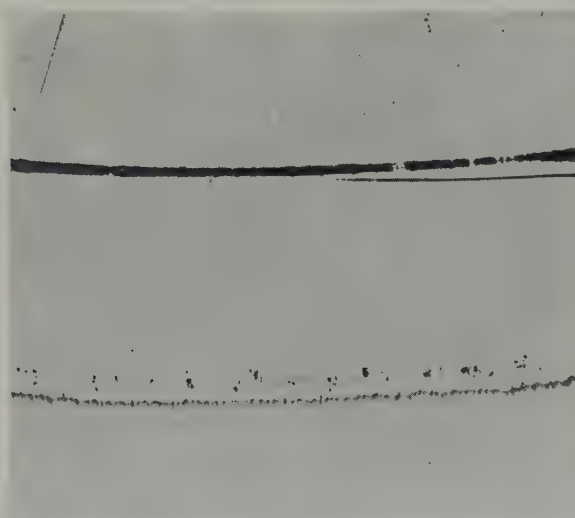
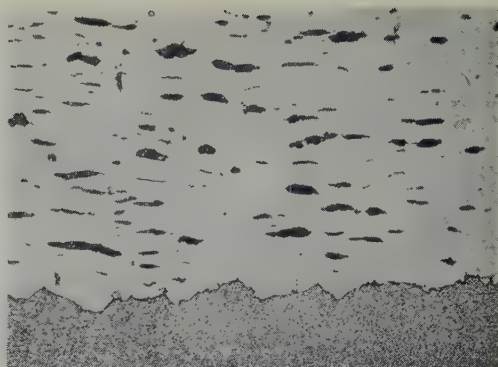
(a) $1\frac{1}{4}$ tsi. $12\times$ (b) 5 tsi. $12\times$ (c) 10 tsi. $12\times$

Fig. 5. Al-U diffusion couples annealed at 570°C for 8 hours under varying applied pressures; samples unetched.

the pressure is increased. The extent of void or crack formation is much less in the sample annealed under an applied pressure of 10 tsi than in the $1\frac{1}{4}$ tsi sample.

A rather unusual situation is found to exist in the UAl_3 layer contiguous to the uranium (fig. 6). At the UAl_3 -uranium interface, stringers of uranium are visible penetrating into the UAl_3 phase in a direction roughly parallel to the diffusion direction; traces of a third phase, identified by X-ray diffraction as UAl_2 , occur as a fine precipitate along the boundaries

between the stringers and the UAl_3 matrix. Apparently, the rapid and irregular growth of the UAl_3 phase entraps regions of uranium, which diminish in size and number as interdiffusion continues by reaction with the surrounding UAl_3 phase to form the UAl_2 phase. In time, the UAl_2 phase particles within the UAl_3 layer are also converted to the UAl_3 phase, since they are thermodynamically unstable in contact with a UAl_3 phase presumably unsaturated in uranium. It is also evident from an examination of fig. 6 that cracks appear in the

(a) Near the UAl_3 -uranium interface. $250\times$ (b) Near the aluminum- UAl_3 interface. $250\times$ Fig. 6. Al-U diffusion couple annealed for 8 hours at 400°C under a pressure of 5 tsi; samples unetched.

UAl_3 phase which begin and terminate at the uranium fingers or islands; the cracks run perpendicular to the diffusion direction and seem to increase in length as their distance from the UAl_3 -uranium interface increases. In regions removed from the multi-phase band, the cracks take on a more oval shape and give the UAl_3 phase a porous appearance at low magnification. The precise mechanism causing crack initiation is not known, but it is suspected that it is associated with volume changes accompanying the conversion of the uranium stringers to UAl_2 and eventually to UAl_3 . The tabulated crystal structure data show that a gram atom in the UAl_2 or UAl_3 phase configuration occupies about 4–7 % less volume than does a gram atom in elemental uranium. It is probable, therefore, that transformation stresses are generated which are sufficiently high to crack the UAl_3 matrix. As was mentioned previously, it is easily demonstrable that the UAl_3 phase is quite brittle at room temperature. Moreover, hot hardness readings taken at elevated temperatures indicate that the UAl_3 phase maintains considerable hardness at the lower diffusion temperatures used in this investigation, as the following table shows:

Temperature ($^\circ\text{C}$)	Hardness (DPH)
25	605
450	340

Thus, at a diffusion temperature of 390°C , the UAl_3 phase probably has a hardness in excess of 400 DPH and is sufficiently brittle to crack as transformation stresses build up. At higher temperatures, however, the ductility of the UAl_3 may be sufficiently high to prevent cracking.

The origin of the voids appearing at the higher diffusion temperatures near the UAl_3 -aluminum interface is not clear. One possible explanation is as follows: it is supposed that cracks are formed during the early stages of interdiffusion at all temperatures by the mechanism discussed above; however, as interdiffusion proceeds at the higher temperatures, conditions change in some as yet undetermined way, and cracks no longer form. Marker motion studies made during the present investigation show that diffusion in the UAl_3 phase occurs predominantly by the motion of aluminum ions. The explanation advanced herein predicts that one should see a band of defects near the UAl_3 -aluminum interface and nowhere else, since the defects would behave as internal markers. They would move relative to the uranium- UAl_3 interface, where the UAl_3 was being formed by the reaction between aluminum and uranium, and exhibit no displacement relative to the UAl_3 -aluminum interface.

3.3. KINETICS OF LAYER GROWTH OF UAl_3

Layer growth data for the aluminum-uranium system are listed in table 1, and are plotted in

TABLE 1
Growth of UAl_3 layer in the aluminum-uranium system

Diffusion		Layer growth vs. applied pressure					
		200 kg/cm ² (1 $\frac{1}{4}$ tsi)		790 kg/cm ² (5 tsi)		1575 kg/cm ² (10 tsi)	
Temp. (° C)	Time (h)	Thickness (mm)	Std. dev. (mm)	Thickness (mm)	Std. dev. (mm)	Thickness (mm)	Std. dev. (mm)
390	110	—	—	4.30	0.06	—	—
400	3	—	—	0.27 (0.20)	0.08	0.84	0.01
	8	—	—	0.78 (0.24)	0.05	1.41	0.04
	16	—	—	1.76 (0.26)	0.02	1.93	0.06
	24.5	—	—	2.59 (0.41)	0.06	2.34	0.03
	72	—	—	3.59 (0.49)	0.11	—	—
480	3	—	—	—	—	1.62 (0.97)	0.03
	8	—	—	—	—	2.56	0.02
	24	—	—	—	—	4.39	0.07
520	0.5	—	—	—	—	0.85	0.01
	3	1.08 (0.24)	0.03	1.45 (0.26)	0.02	1.75	0.07
	8	—	—	2.33 (0.61)	0.05	1.81	0.10
	16	2.61 (1.88)	0.03	3.30	0.04	2.55 (0.44)	0.04
	24	3.05	0.28	4.09	0.04	—	—
				4.21	0.03	4.39 (0.87)	0.07
540	3	—	—	—	—	1.59	0.04
560	3	—	—	1.64 (0.90)	0.03	1.68 (0.42)	0.01
	8	—	—	2.78	0.03	—	—
	16	—	—	4.09	0.04	—	—
	24	—	—	4.99 (0.89)	0.10	—	—
	29	—	—	5.44	0.09	—	—
565	24	—	—	5.02	0.28	—	—
570	0.5	—	—	—	—	0.84	0.02
	3	1.75	0.03	1.70	0.02	1.77 (0.35)	0.02
	8	2.79 (0.63)	0.05	2.96	0.03	2.96	0.02
	16	3.98 (0.80)	0.08	4.23	0.08	2.95	0.05
	24	4.42 (0.94)	0.13	5.16	0.05	5.27	0.14
600	3	1.91	0.05	1.99	0.01	2.04 (0.62)	0.07
	4.5	—	—	2.42	0.10	—	—
	6.25	2.80	0.05	—	—	3.01	0.07
	8	—	—	3.25	0.11	3.42	0.02
	16	—	—	4.59	0.06	—	—
	24	5.07	0.21	—	—	6.04	0.10
600	3	2380 kg/cm ² (15 tsi)		2.03 \pm	0.03		
600	3	3150 kg/cm ² (20 tsi)		2.07 \pm	0.03		

figs. 7 through 11. The thickness measurements include the contributions of the UAl_3 phase and of the multi-phase region near the UAl_3 -uranium interface (fig. 2), which is predominantly UAl_3 , except for stringers or islands of partially reacted uranium. It was difficult to estimate the thickness of the multi-phase region without introducing large subjective errors, since there was obviously no sharp line of demarcation between the single-phase and multi-phase regions. Nevertheless, some estimates were made of the width of the two-phase region in various diffusion couples, and the values obtained are listed parenthetically in table 1.

The time dependence of UAl_3 layer growth is most readily ascertained from figs. 7, 8 and 9, where the thickness vs. time data are plotted logarithmically. The rapidity with which the UAl_3 phase grows is striking, since, for example, the layer attains thicknesses of more than 5 mm after 24 hours at 560°C . For the most part, the growth kinetics appear to be conventional in the time range investigated; a parabolic growth law is obeyed, and it seems proper to draw the conclusion that volume diffusion is the rate controlling factor^{3, 6)}. However, there are two anomalies—the 400°C , 5 tsi data (fig. 8), and the 520°C , 10 tsi data (fig. 9). The low temperature data are reminiscent of similar results obtained in the aluminum-nickel system; since the 400°C , 10 tsi data appear to be conventional, it is suspected that the low values obtained for the 5 tsi data reflect less favorable initial bonding conditions. The 520°C , 10 tsi data are peculiar, and are probably associated with the structural changes in the UAl_3 layer previously discussed.

The pressure dependence of the data is shown in fig. 10. It is clear that applied pressure (with few exceptions) increases UAl_3 layer growth. The greatest effect seems to occur as the pressure is increased from $1\frac{1}{4}$ to 5 tsi in the 24 hours runs at the higher temperatures. The data indicate that the UAl_3 layer thickness approaches an asymptotic value as the pressure is increased to a value of 10 tsi or thereabouts. There is essentially no increase in layer thickness

as the pressure is increased from 10 tsi to 20 tsi during 3 hour runs at 600°C .

The temperature dependence of layer growth

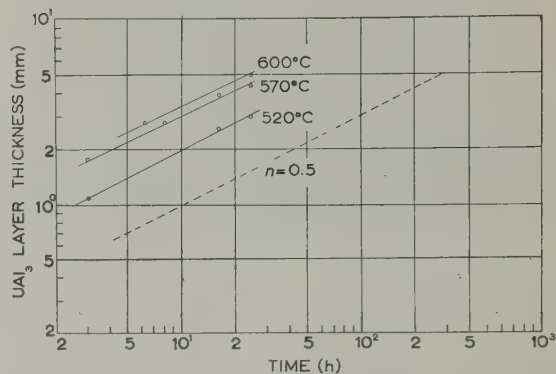


Fig. 7. UAl_3 layer thickness vs. diffusion time for Al-U couples diffused under an applied pressure of $1\frac{1}{4}$ tsi.

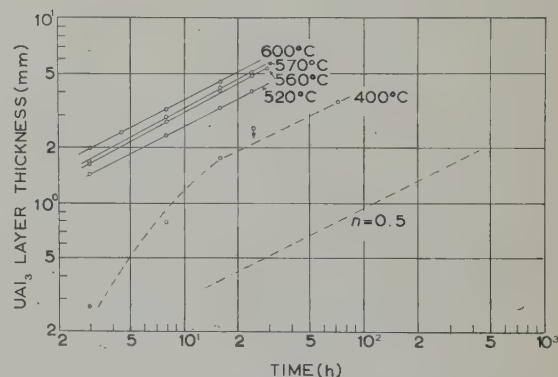


Fig. 8. UAl_3 layer thickness vs. diffusion time for Al-U couples diffused under an applied pressure of 5 tsi.

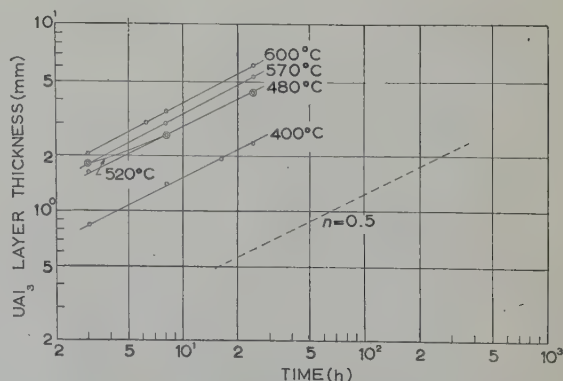


Fig. 9. UAl_3 layer thickness vs. diffusion time for Al-U couples diffused under an applied pressure of 10 tsi.

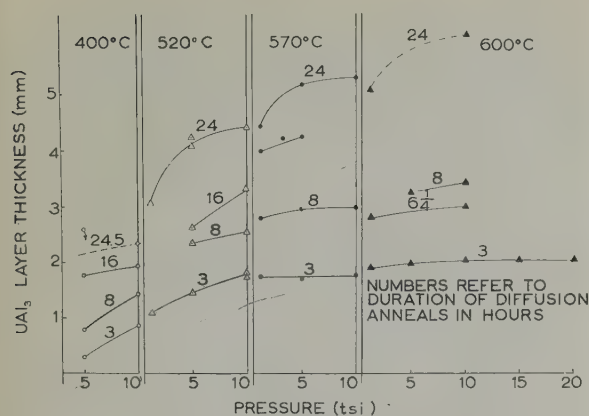


Fig. 10. UAl_3 layer thickness vs. pressure in Al-U couples diffused at various temperatures and times.

data is customarily expressed in terms of an activation energy obtained graphically as follows: a plot is made of the logarithm of the time required for the intermetallic phase to grow to a selected constant thickness vs. the reciprocal of the absolute temperature. If the plot is linear, the slope of the straight line is interpreted as being proportional to the activation energy for interdiffusion through the intermetallic phase. Certain conditions must be satisfied to make the procedure a valid one and they have been discussed in a previous paper⁶). In brief, the predominant rate-controlling factor throughout the temperature range considered must be volume diffusion, and diffusion should effectively be occurring only in the phase which comprises the bulk of the diffusion zone. In the

case of interdiffusion in the aluminum-uranium system, the second condition is obviously fulfilled, and at any one of the higher temperatures, the data indicate that volume diffusion is rate controlling. Several complicating factors arise, however, in establishing the temperature dependence of layer growth: (1) the effective cross-sectional area for diffusion varies with temperature (for a given pressure) since the distribution and kinds of macroscopic defects change with temperature; and (2) changes may occur in the thickness of the multi-phase region which are temperature dependent. Thus, the interpretation of the slope of the $\ln(1/t)$ vs. $(1/T)$ plot (where t is the interdiffusion time to reach constant thickness and T the absolute temperature) becomes difficult. In general, one would not expect to obtain a constant slope under these circumstances. Surprisingly, if the data of figs. 7, 8 and 9 are replotted in this manner, a good straight line is obtained for the 5 tsi data, and a fair straight line for the $1\frac{1}{4}$ tsi data (a constant thickness of 4 mm was selected); a definite break exists in the 10 tsi plot which results from the coincidence of the 520°C and 480°C curves in fig. 9. The activation energy values obtained for the $1\frac{1}{4}$ and 5 tsi data are 16 400 and 11 400 cal/mol, which compare to values ranging from 14 000 to 16 000 cal/mol reported by LeClaire and Bear. The interpretation of these values in terms of ion migration is questionable for the reasons cited

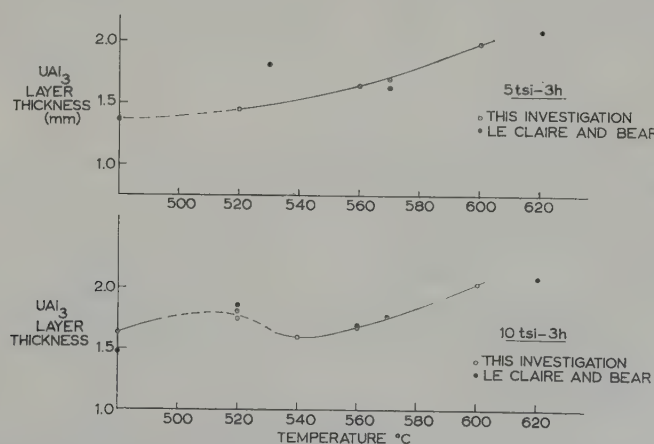


Fig. 11. UAl_3 layer thickness vs. temperature in Al-U couples diffused under applied pressures of 5 and 10 tsi.

above. To the extent that they are meaningful, they indicate that the energy barrier retarding migration of aluminum ions in the UAl_3 phase (since it is the aluminum ions which are diffusing predominantly) is rather low.

According to the available data obtained during the present investigation, it appears that the "negative activation energy phenomenon" reported by LeClaire and Bear for 5 tsi and 10 tsi diffusion runs does indeed exist—at least for the 10 tsi runs. Layer thickness vs. temperature data for 3 hour diffusion runs under applied pressures of 5 and 10 tsi are plotted in fig. 11, including points taken from the work of LeClaire and Bear. The agreement between the two sets of data is reasonably good (except for the 5 tsi data in the vicinity of 530°C), and a definite minimum does seem to occur near 540°C in the 10 tsi data. However, the significance to be attached to the results is open to question. Relatively small variations in the thicknesses of the multi-phase region or in the distribution and kind of macroscopic defects would be sufficient to account for the phenomenon.

3.4. LAYER GROWTH OF UAl_2 AND UAl_4

Several exploratory runs with incremental diffusion couples have been completed so that some idea could be obtained of the kinetics of growth of the UAl_4 phase and the UAl_2 phase; the results are listed in table 2. No special difficulty arose in obtaining satisfactory layer growth in aluminum vs. UAl_3 couples. Two runs were completed in which aluminum vs. UAl_3

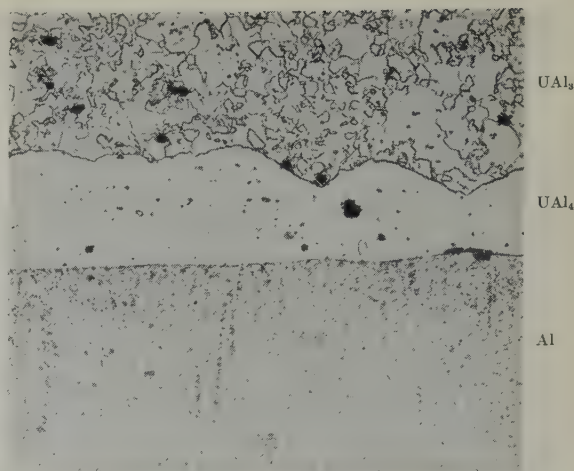


Fig. 12. Aluminum vs. UAl_3 diffusion couple annealed at 600°C for 4 hours under a pressure of $2\frac{1}{2}$ tsi; sample etched with hydrofluoric plus nitric acid.

couples were annealed at 600°C for 4 and 24 hours under an applied pressure of $2\frac{1}{2}$ tsi. The thickness of the UAl_4 phase in the sample annealed for 4 hours (fig. 12) was 0.087 mm—less than $\frac{1}{25}$ th the thickness of the UAl_3 phase obtained in an aluminum vs. uranium couple annealed under similar conditions. The diffusion coefficient calculated from this one run for the UAl_4 phase, using the method outlined in ref. ⁶), is about three orders of magnitude less than that of the UAl_3 phase. The situation turned out to be different in obtaining kinetics data for UAl_2 phase layer growth by the use of UAl_3 vs. uranium diffusion couples; the attempts made were unsuccessful. Two UAl_3 vs. uranium couples were first run at 600°C —one for 72 hours under a pressure of 2 tsi, and the second

TABLE 2
Growth of UAl_4 and UAl_2 layers in the aluminum-uranium system

Diffusion		Diffusion couple Reactants	Applied pressure (tsi)	Layer growth	
Temp. ($^\circ\text{C}$)	Time (h)			Thickness (mm)	Std. d.v. (mm)
600	4	$\text{Al} + \text{UAl}_3 \rightarrow \text{UAl}_4$	2.5	0.087	0.006
	24			0.146	0.026
600	72	$2\text{UAl}_3 + \text{U} \rightarrow 3\text{UAl}_2$	2.0	0.0007	—
	144		5.0	0.0019	0.0002

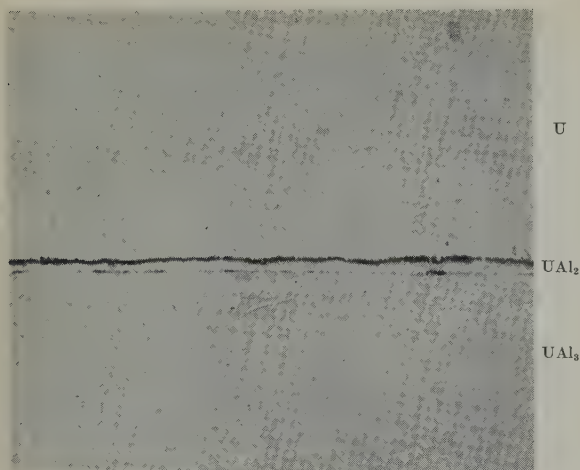


Fig. 13. UAl_3 vs. uranium diffusion couple annealed at 600°C for 144 hours under a pressure of 5 tsi; sample unetched.

for 144 hours under a pressure of 5 tsi. In the first case, examination of the interface after diffusion revealed a very thin layer of a dark phase, presumably uranium oxide, less than one micron thick, and practically no sign of the UAl_2 phase. In the second case, the presence of the UAl_2 phase was observed in addition to the dark layer, its thickness being about two microns (fig. 13). Since the UAl_2 phase had occasionally been observed to grow to thicknesses of 40 microns in aluminum vs. uranium couples diffused under circumstances theoretically less favorable for its growth than in UAl_3 vs. uranium couples, it was felt that the oxide layer was acting as a diffusion barrier. Consequently, a different scheme was tried in which a restricted thickness of aluminum was used in an aluminum

vs. uranium couple. It was expected that the aluminum would be quickly depleted, forming the UAl_3 -uranium phase, and that subsequently the UAl_2 phase would grow at the UAl_3 -uranium interface without hindrance. Two couples were diffusion annealed under a pressure of 10 tsi for 144 hours—one at 560°C , and the other at 600°C . Surprisingly, even though the UAl_3 -uranium interface was found to be free of the dark oxide layer, no layers of UAl_2 were observed to be present in appreciable thickness. The conclusion appears inescapable that the formation or growth of the UAl_2 phase is a very slow process under the conditions existing in a diffusion couple.

3.5. SOLUBILITY RANGE OF THE UAl_3 PHASE

The strikingly rapid growth of the UAl_3 phase would be difficult to explain unless an appreciable concentration gradient existed in the UAl_3 phase. In the published aluminum-uranium phase diagram¹⁰ (fig. 1), no appreciable solubility range is attributed to UAl_3 . However, the work done to determine the phase diagram was admittedly in the nature of a survey, and no attempt was made to determine exactly such features as solid solubility limits. Consequently, an attempt was made in the present investigation to demonstrate the existence of a solubility range by means of a nuclear track emulsion technique. Several determinations were made of the uranium concentration at two locations in the UAl_3 phase layer of an aluminum vs. uranium diffusion couple, and the results are listed in the following table:

Sample	Location	Tracks/unit area		Uranium composition	
		Mean	Std. dev.	(wt %)	(at %)
U-Al couple	In U	163.2	± 3.8	100	100
	*In UAl_3 near UAl_3 -U boundary	98.4	± 1.0	**76.0	**26.3
	In UAl_3 near Al- UAl_3 boundary	85.0	± 3.0	**73.3	**23.7
Bulk UAl_3 standards					
25.5 at % U	—	95.0	± 3.7	75.2	25.5
23.3 at % U	—	83.5	± 2.7	72.8	23.3

* In single-phase region of UAl_3 phase.

** Obtained by interpolation or extrapolation.

The solubility range of the UAl_3 phase appears to be greater than 2.6 at % or 2.7 wt % uranium. The limits of solubility occur at uranium concentrations somewhat less than 23.7 at % and somewhat greater than 26.3 at %. As a matter of incidental interest, one may use the Bragg-Kleeman relationship¹³⁾ to calculate the range of alpha particles in uranium and in the UAl_3 phase, and the alpha counts obtained from the aluminum-uranium couple to determine more approximate values of the uranium concentrations. The values so obtained are 22.4 at % and 25.9 at % uranium, as compared to the more accurate values of 23.7 and 26.3 at % uranium determined by means of bulk UAl_3 standards of known composition.

More recent measurements made elsewhere with the electron beam microprobe indicate a wider solubility in the UAl_3 phase than those reported above¹⁴⁾.

3.6. MECHANISM OF PRESSURE EFFECT

It is well known that pressure decreases self-diffusion coefficients of metals, particularly those having high compressibilities. In multi-phase two-component systems undergoing interdiffusion, however, the situation is much more complicated. Not only must one consider the effects of pressure on diffusion coefficients, but also the effects of pressure on phase equilibria. Appreciable changes in phase equilibria would change interface concentrations, which in turn would influence the course of interdiffusion. Where pressure decreases layer growth, as in the case of Ni_2Al_3 in the aluminum-nickel system⁶⁾, it is possible to explain the results on the basis of pressure-induced decreases in diffusion coefficients. However, in the aluminum-uranium system, where pressure increases the growth of UAl_3 layers, it is not possible to rationalize the results on the basis of diffusion coefficients alone. It has been suggested by LeClaire and Bear that the effect of pressure may be to shift the equilibrium interface concentrations in such a manner that the concentration gradients in UAl_3 are increased and interdiffusion is enhanced. An estimate has therefore been made in a

separate paper¹⁵⁾ of the magnitude of the pressure-induced shifts in equilibrium concentrations to be expected in the aluminum-uranium system. It is concluded that it is unlikely that the observed UAl_3 layer growth increase with pressure can be accounted for in this manner. An alternative hypothesis is therefore advanced herein which, it is felt, may be adequate to explain many of the observed phenomena. It is proposed that the predominant effect of pressure is mechanical; an increase in pressure represses the tendency for the formation of macroscopic voids and thus increases the effective cross-sectional area available for interdiffusion. If this explanation is correct, one would expect the pressure-induced increase in layer growth to disappear once the applied pressure is sufficiently great to eliminate the macroscopic defects; this appears to be the case, as is evidenced by the 600° C data in table 1 and in fig. 10.

4. Summary

Interdiffusion in the aluminum-uranium system has been investigated over the temperature range 400°–600° C, and over the pressure range $1\frac{1}{4}$ –10 tsi for diffusion times of 24 hours and less. The pressure-induced increase in UAl_3 layer thickness has been confirmed. Interesting correlations have been shown to exist between annealing time, annealing temperature, and applied pressure on the one hand, and the nature and distribution of structural defects in the UAl_3 diffusion zone on the other. It has been demonstrated that the solubility range within the UAl_3 phase must be at least 2.6 at % uranium. It has been shown that the growth of the UAl_4 and UAl_2 phases in incremental couples is much slower than the growth of UAl_3 in aluminum-uranium couples. Finally, it is proposed that the effect of pressure on UAl_3 layer growth is primarily mechanical in that higher pressures repress the tendency for the formation of macroscopic voids and thus effectively increase the cross-sectional area available for interdiffusion.

Acknowledgements

The author is pleased to acknowledge the helpful discussions that he held with Dr. L. L. Seigle during the course of this work. He also wishes to express his appreciation to Mr. J. J. Gitto for his painstaking efforts in performing the experimental work and in making the layer thickness measurements.

References

- 1) D. W. Bareis, US Atomic Energy Commission Publication, AECD-3795 (1949)
- 2) S. Storchheim and J. L. Zambrow, Report SEP-102 (1952) (Confidential)
- 3) A. D. LeClaire and I. J. Bear, *J. Nuc. Energy* 2 (1955-56) 229
- 4) T. K. Bierlein and D. R. Green, *Nuc. Sci. & Eng.* 2 (1957) 778
- 5) S. Storchheim, J. L. Zambrow and H. H. Hausner, *AIME Trans.* 200 (1954) 269
- 6) L. S. Castleman and L. L. Seigle, *AIME Trans.* 212 (1958) 589
- 7) H. A. Saller and F. A. Rough, Geneva Conf. Paper P/558 (1955)
- 8) *Metals Handbook* (American Society for Metals, Cleveland, Ohio) (1948) 20
- 9) B. S. Borie, Jr., *AIME Trans.* 191 (1951) 800
- 10) P. Gordon and A. R. Kaufmann, *AIME Trans.* 188 (1950) 182
- 11) R. E. Rundle and A. S. Wilson, *Acta Cryst.* 2 (1949) 148
- 12) L. S. DeLuca and H. T. Sumsion, USAEC Report KAPL-1747 (1957)
- 13) H. Yagoda, *Radioactive Measurements with Nuclear Emulsions* (John Wiley & Sons, New York) (1949) 83
- 14) Y. Adda (Centre d'Etudes Nucléaires de Saclay, France) (private communication)
- 15) L. S. Castleman, *Acta Met.* 8 (1960) 137

AN ESTIMATE OF THE EFFECT OF RADIATION ON THE THERMAL CONDUCTIVITY OF BERYLLIUM †

G. J. DIENES †† and A. C. DAMASK †††

University of California, Los Alamos Scientific Laboratory, Los Alamos, New Mexico, USA

Received 28 April 1960

The thermal conductivity and electrical resistivity of beryllium at low temperatures are analysed. From existing data on the effect of reactor irradiation on the electrical resistivity of beryllium, the effect of reactor irradiation at low temperatures on the thermal conductivity is predicted. The arguments show that a reactor exposure of 10^{19} nvt (fast) should decrease the thermal conductivity of beryllium by approximately $0.04 \text{ watt/cm}^\circ \text{K}$ at temperatures of 20°K to 30°K . This is measurable, but probably unimportant in practice. High and low purity beryllium should be affected similarly. Warming to 250°K should cause rapid and complete annealing of the radiation-induced change of thermal conductivity.

Les données de conductibilité thermique et de résistivité électrique du béryllium sont analysées dans le cas des basses températures. En partant des données existantes sur l'effet d'une irradiation dans un réacteur sur la résistivité électrique du béryllium, on déduit l'effet de l'irradiation dans un réacteur aux basses températures sur la conductibilité thermique. D'après les données, une exposition de 10^{19} nvt (rapides) doit diminuer la conductibilité thermique du béryllium aux températures de 20°K à 30°K

d'environ $0,04 \text{ watt/cm}^\circ \text{K}$. Cette diminution est mesurable mais probablement elle est sans importance dans la pratique. Le béryllium de haute ou de faible pureté serait affecté de la même manière. Un chauffage à 250°K provoquerait un recuit rapide et complet des variations de conductibilité thermiques induites par l'irradiation.

Es wird die thermische Leitfähigkeit und der elektrische Widerstand von Beryllium bei niedrigen Temperaturen untersucht. Aus den vorliegenden Daten über den Einfluss einer Reaktorbestrahlung auf den elektrischen Widerstand von Beryllium wird die Wirkung einer Reaktorbestrahlung bei niedrigen Temperaturen auf die Wärmeleitfähigkeit vorhergesagt. Die Überlegungen zeigen, dass eine Bestrahlungsdosis von 10^{19} nvt (schnelle Neutronen) die Wärmeleitfähigkeit von Beryllium um etwa $0,04 \text{ Watt/cm}^\circ \text{K}$ bei 20 bis 30°K herabsetzen dürfte. Dies ist zwar messbar, aber wahrscheinlich in der Praxis unwichtig. Beryllium unterschiedlicher Reinheit sollte gleich beeinflusst werden. Erwärmen des Berylliums auf 250°K sollte die Änderung der Wärmeleitfähigkeit, welche durch die Bestrahlung hervorgerufen wurde, rasch und vollständig rückgängig machen.

1. Introduction

In many reactor applications it is of importance to know the effect of nuclear radiation on the thermal conductivity of various materials. The measurement of thermal conductivity is a time-consuming and expensive experiment, particularly if data at low temperatures are desired. If one wants to determine the influence

of nuclear radiation on the thermal conductivity at low temperatures then both low temperature irradiations and measurements are required since annealing of the radiation damage occurs as the temperature is raised. A study of the electron transport properties is far easier to carry out in terms of electrical resistivity. For a metal there is a close connection between

† Performed under the auspices of the US Atomic Energy Commission.

†† Permanent address: Brookhaven National Laboratory, Upton, New York.

††† Supported by a Secretary of the Army Fellowship. Permanent address: Pitman-Dunn Laboratories, Frankford Arsenal, Philadelphia, Pennsylvania.

electrical and thermal properties and one should be able to estimate the effect of radiation on thermal conductivity from a measurement of the change in electrical resistivity. The purpose of this note is to describe such an estimate for beryllium in the 10° to 100° K temperature range.

2. The Relation between Electrical and Thermal Conductivity for Beryllium at Low Temperatures

The thermal conductivity of a metal is dominated at very low temperature by boundary scattering, and in this region the thermal conductivity is proportional to the specific heat and increases as the third power of the temperature. At higher temperatures electronic conduction dominates, i.e. the thermal current is carried essentially by the electrons and the thermal conductivity is limited by electron scattering. In this regime the conductivity decreases with increasing temperature. The thermal conductivity, therefore, goes through a maximum at some low temperature (about 20° K for copper, for example)¹).

Single crystals of beryllium of high purity exhibit metallic behavior as illustrated by the data of Grüneisen and Erfling²) shown in fig. 1. The electrical resistivity is seen to be low at low temperature and increases with increasing temperature. The thermal conductivity is high at low temperature and falls with increasing temperature with a maximum somewhere below 20° K. The high temperature data of Powell³) on a commercial cast beryllium, also shown in fig. 1, agree reasonably well with an extrapolation of the low temperature single crystal data.

Recently, Powell, Harden and Gibson⁴) obtained extensive low temperature data on beryllium at the National Bureau of Standards (Boulder, Colorado). Their thermal conductivity and electrical resistivity data are shown by the dashed lines in fig. 2. The thermal conductivity is seen to be low and increases rapidly with increasing temperature, a behavior very different from that shown in fig. 1. The electrical

resistivity is independent of the temperature up to about 60° K, and over the whole range the Wiedemann-Franz law is obeyed very well. This is somewhat surprising since the Wiedemann-Franz ratio is not expected to be obeyed below the Debye temperature (about 1000° K for Be) and, as expected, the Grüneisen-Erfling data deviate from this law. A simple interpretation of the unusual behavior shown by the Bureau of Standards data is given below.

The Wiedemann-Franz law states that

$$K\rho = LT \quad (1)$$

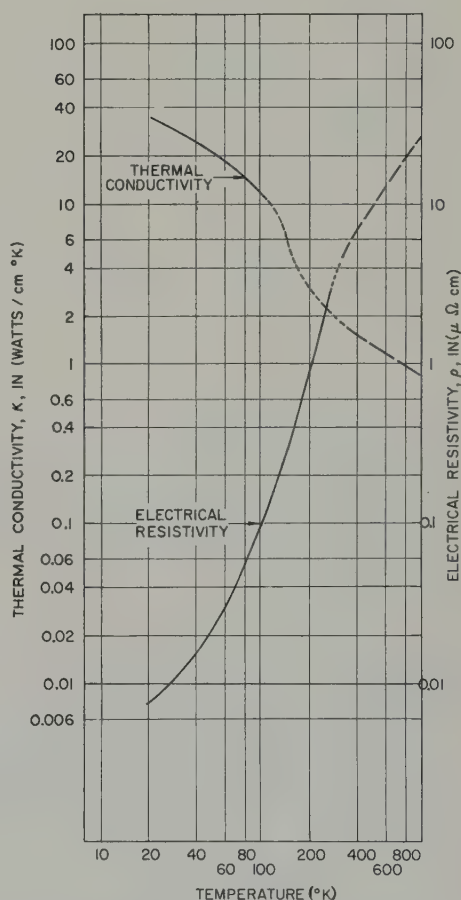


Fig. 1. Thermal conductivity and electrical resistivity of beryllium as a function of temperature. — Single crystal data of Grüneisen and Erfling²) perpendicular to the hexagonal axis (samples Be 3 and Be 8 in their paper). — High temperature data of Powell³) (sample V in his paper). ---- Interpolated connecting lines.

where

K =thermal conductivity in watt/cm $^{\circ}$ K

ϱ =electrical resistivity in ohm cm

T =absolute temperature in $^{\circ}$ K

L =Lorenz number, a constant whose theoretical value for free electron metals is 2.45×10^{-8} (volts/deg) 2 .

The physical reason for the validity of this law is that the same electron scattering processes alter both the electrical and the thermal conductivities. As far as scattering by thermal vibrations is concerned, the law is valid near and above the Debye temperature. At lower temperatures the situation is complex since a detailed theory of inharmonic vibrations is needed for a full description. For impurity or defect scattering the law is valid at any temperature. The scattering of electrons by impurities and defects may dominate at low temperature to such an extent that the normal thermal conductivity maximum is swamped by this effect. The total thermal resistivity may be written as 1)

$$\frac{1}{K} = R = R_0 + R_T \quad (2)$$

where R_0 is thermal resistivity due to scattering by impurities and defects and R_T is thermal resistivity due to scattering by thermal vibrations. R_0 obeys the Wiedemann-Franz law and, therefore,

$$\frac{1}{K_0} = R_0 = \frac{\varrho_0}{LT} \quad (3)$$

where

ϱ_0 =residual electrical resistivity.

R_T is proportional to T^2 at temperatures 5) below $\theta/10$ (i.e., below 100° K for Be), and therefore,

$$R = \frac{\varrho_0}{LT} + \alpha T^2. \quad (4)$$

If sufficient impurities or defects are present the first term dominates, the thermal conductivity obeys the Wiedemann-Franz law and increases linearly with increasing temperature; i.e.,

$$R = \frac{\varrho_0}{LT} \quad (5)$$

The data shown in fig. 2 obey eq. (5) with an L value that fluctuates between 2.2×10^{-8} and 2.5×10^{-8} (volts/deg) 2 (i.e. very close to the theoretical value for L). The temperature independent resistivity and the high value of this residual resistivity is characteristic of impurity scattering. It is concluded that the electron transport properties of these beryllium samples are impurity controlled.

These conclusions are supported by analysis of the polycrystalline specimens used by Powell, Harden and Gibson. A combination of chemical and spectroscopic methods showed that these samples contained metallic impurities in the 0.04 % to 0.2 % concentration range. Non-metallic impurities, such as oxygen, were not determined.

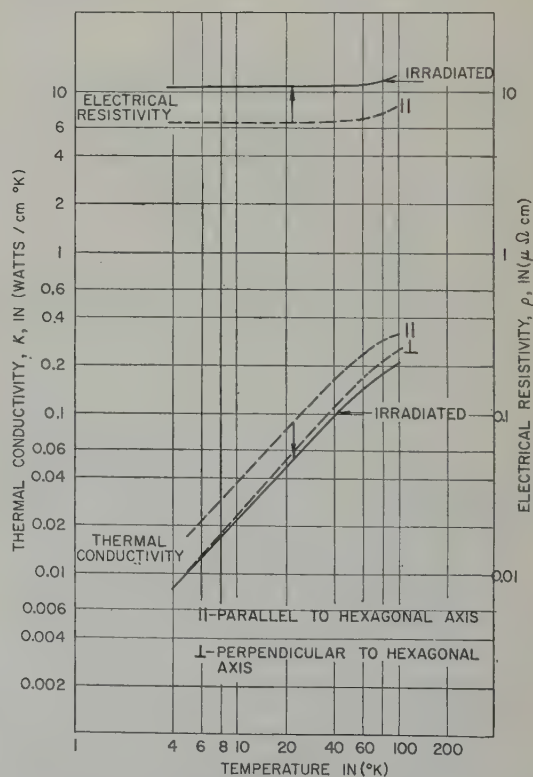


Fig. 2. The effect of reactor irradiation on the electrical and thermal conductivity of impure beryllium. ---- Data of Powell, Harden and Gibson 4). — Calculated change in electrical resistivity and thermal conductivity for an exposure of 10^{19} nvt. The arrows indicate the magnitude and direction of the radiation induced change.

3. The Effect of Reactor Irradiation on the Electron Transport Properties of Beryllium

It is easy to estimate the effect of fast neutron bombardment on the electrical and thermal conductivities of the impure samples since defects behave analogously to impurities as far as the Wiedemann-Franz law is concerned. Blewitt ⁶⁾ has measured the change in resistivity of a sample of Be irradiated at 20° K to 4×10^{17} nvt. He found a resistivity increase of 0.173 $\mu\Omega$ cm for a sample of initial resistivity of 1.181 $\mu\Omega$ cm. Recovery started at about 30° K and amounted to about 40 % at 50° K. Since there is very little or no recovery at 20–30° K it is expected that the damage rate is constant and that linear extrapolation is valid with respect to exposure. The curves in the present note are given for an exposure of 10^{19} nvt, which gives a resistivity increment of 4.33 $\mu\Omega$ cm. Thus, even for impure samples the radiation effect is significant. From $\Delta\rho$ one can immediately calculate the change in conductivity via eq. (5). The results are shown by the arrows and the solid lines in fig. 2. There is a significant decrease in conductivity, of the same order of magnitude as the difference between samples oriented parallel and perpendicular to the hexagonal axis. This estimate of the change in K should be good to about 20 % (from the variation in the Lorenz number) or better at 20–30° K. At higher temperatures appreciable annealing takes place ⁶⁾ and the actual damage will be less than the calculated curves of fig. 2 where no annealing was assumed (i.e. a maximum effect was calculated). If commercial material of much higher purity becomes available its thermal conductivity may be 2–3 orders of magnitude higher than that of the NBS samples. In this case, however, radiation damage at low temperature will pull the conductivity back down again to the present NBS range.

4. Conclusions

1. Pure single crystalline beryllium behaves as a typical metal and exhibits high thermal and electrical conductivity with the expected temperature dependence for a pure metal.

2. Thermal and electrical conductivities are controlled by impurity scattering in beryllium having a few tenths of a percent of impurities. For such cases, the Wiedemann-Franz law is obeyed and the temperature dependence is typical of impurity dominated transport properties; i.e., at very low temperatures the electrical resistivity is independent of temperature while the thermal conductivity increases nearly linearly with increasing temperature.

3. Since the Wiedemann-Franz ratio applies, the change in thermal conductivity resulting from radiation damage is calculable from the known damage to the electrical resistivity. For 10^{19} nvt (fast) one obtains a $\Delta K = 0.031$ watt/cm° K at 20° K and $\Delta K = 0.047$ at 30° K. These are measurable but in practice probably unimportant decreases in conductivity. At higher temperatures the damage is less because of annealing. These estimates are considered accurate to at least 20 %. From a practical standpoint, therefore, low temperature experimentation with irradiated samples is not required.

4. Irradiation to 10^{19} nvt has an equivalent effect on the electrical and thermal properties of beryllium to a few tenths of a percent impurities. Therefore, not much improvement in these properties is to be gained by using high purity beryllium in a radiation field at low temperature.

5. If beryllium is warmed to 250° K there is rapid and complete annealing of the neutron induced change of electrical resistivity ⁵⁾ and therefore of the associated changes of thermal conductivity.

Acknowledgements

We are indebted to R. L. Powell, J. L. Harden and E. F. Gibson for the use of their beryllium data prior to publication, and to O. R. Simi and C. F. Metz of Los Alamos Scientific Laboratory for the chemical analysis of these samples.

References

- 1) See, for example, C. Kittel, Introduction to Solid State Physics, Second Ed. (John Wiley and Sons, 1956) pp. 147-151
- 2) E. Grüneisen and H. D. Erfing, Ann. J. Phys. **38** (1940) 399
- 3) R. W. Powell, Phil. Mag. **44** (1953) 645
- 4) R. L. Powell, J. L. Harden and E. F. Gibson, Submitted to J. Appl. Phys.
- 5) Sommerfeld and Bethe, Handbuch d. Phys. **24/2** (1933) 535
- 6) T. Blewitt, US Atomic Energy Comm. Document ORNL-2614 (1958) p. 66

SOME ASPECTS OF THE GROWTH OF DIFFUSION LAYERS IN BINARY SYSTEMS

G. V. KIDSON†

Research Metallurgy Branch, Atomic Energy of Canada, Ltd., Chalk River, Ont., Canada

Received 1 June 1960

It is shown that the application of Fick's First law to polyphase diffusion in binary systems leads to simple but rigorous expressions for the interface positions as functions of time and temperature. Systems of two and three phases are treated and the results generalized to an n -phase system. Some aspects of the temperature behaviour of the rate constants are considered. In particular the conditions are defined under which the phases may or may not grow to observable widths in the diffusion zone.

On montre que l'application de la première loi de Fick à la diffusion en phases multiples dans les systèmes binaires conduit à des expressions simples mais rigoureuses en fonction du temps et de la température pour les positions de l'interface. Des systèmes à deux ou trois phases ont été étudiés et les résultats généralisés à un système à n phases. Quelques aspects de

l'influence de la température sur les constantes de vitesse ont été considérés. En particulier on définit les conditions suivant lesquelles les phases peuvent ou ne peuvent pas atteindre une largeur observable dans la zone de diffusion.

Es wird gezeigt, dass die Anwendung des 1. Fickschen Gesetzes auf mehrphasige Diffusionszonen binärer Systeme zu einfachen aber genauen Ausdrücken führt, welche die Lage der Grenzflächen in Funktion der Zeit und der Temperatur beschreiben. Es werden Systeme mit 2 und 3 Phasen behandelt. Die Ergebnisse werden für n -phasige Systeme verallgemeinert. Einige Züge des Temperaturverlaufs der Geschwindigkeitskonstanten werden in die Betrachtung einbezogen. Insbesondere werden auch die Bedingungen herausgestellt, unter denen die Schichtdicke der einzelnen Phasen auf eine beobachtbare Grösse anwächst.

1. Introduction

It has frequently been asserted that if two metals which do not form a continuous series of solid solution interdiffuse, each single phase present in the equilibrium diagram of the system at the diffusion temperature will be formed in the diffusion zone. Polyphase zones of this type occur frequently in the solution of metallurgical engineering problems, a particular case arising in the use of sheath materials for reactor fuel elements when a metallurgical bond exists between the sheath and the fuel.

An understanding of the factors controlling the occurrence and growth rates of the various phases is desirable both from a practical design point of view and because of its intrinsic interest. Numerous experimental observations of the isothermal growth of the intermediate phase layers in binary systems have been reported, and it has generally been found that both the position of the phase interfaces and the width of the diffusion layers formed follow a simple parabolic time law. However, while some observers have found that all the phases predicted by the equilibrium diagram appear in the diffusion zone (Bückle)¹⁾, it has been found quite frequently, as for example in the case of Al-Ni (Castleman and Seigle)²⁾ that some phases are not detectable.

One approach to an understanding of the problem has been to seek an analytical expression for the concentration $C(x, t)$ of one of the components throughout the polyphase region. Such procedures necessarily require that the diffusion coefficient D in Fick's second law of diffusion

$$\frac{\partial c}{\partial t} = \frac{\partial}{\partial x} \left[D \frac{\partial c}{\partial x} \right] \quad (1)$$

† Present Address: Metallurgy Department, McMaster University, Hamilton, Ontario, Canada.

be assumed independent of concentration within a given phase so that (1) may be rewritten as

$$\frac{\partial c}{\partial t} = D \frac{\partial^2 c}{\partial x^2}. \quad (2)$$

Kirkaldy³⁾ has given a general solution for an n -component system which can be conveniently used for two components.

Castleman⁴⁾ has reviewed the use of such solutions in the interpretation of polyphase diffusion, with particular reference to the movement of the interfaces between layers, and the growth rates of intermediate phases.

The results of such analyses, however, for all but the simplest cases, become rather cumbersome, making it difficult to draw generalized conclusions about the behaviour of more complicated systems.

It is the purpose of the present note to point out that a considerable insight into the problem of interface movement and layer width growth can be obtained without explicitly solving for $C(x, t)$.

Expressions for the interface positions and layer widths are derived in a simple and straightforward manner for systems of two, three, or in general n -phases by a direct application of Fick's first law, or alternatively by an application of the Matano-Boltzmann solution to Fick's second law. The relationships so obtained take into account the concentration dependence of the diffusion coefficients involved, with the parabolic time dependence following in a natural way.

The factors in the rate constant are clearly defined and an interpretation of the various possible cases arising is relatively simple. In particular, the occurrence or non-occurrence of phases of detectable widths is considered and some aspects of the behaviour of the layers as a function of annealing temperature are discussed.

2. The Matano-Boltzmann Method

Although no methods exist for obtaining analytical solutions for eq. (1), Boltzmann⁵⁾ was able to show that any solution $C(x, t)$ for (1) subject to rather general boundary conditions will always be of such a form that we may write $C(x, t) = C(\lambda)$, where $\lambda = x/\sqrt{t}$. If the transformation of variables in equation (1) is then made, using

$$\begin{aligned} \frac{\partial}{\partial x} &= \frac{1}{\sqrt{t}} \frac{d}{d\lambda} \\ \frac{\partial^2}{\partial x^2} &= \frac{1}{t} \frac{d^2}{d\lambda^2} \\ \frac{\partial}{\partial t} &= -\frac{x}{2t^{3/2}} \frac{d}{d\lambda} \end{aligned}$$

an ordinary differential equation is obtained which is used in the well-known Matano-Boltzmann analysis of diffusion experiments when the diffusion coefficient D is concentration dependent.

It has been shown by Jost⁶⁾ that the application of this analysis to eq. (1) is valid for systems in which a finite number of discontinuities occur in the diffusion coefficient D and the concentration c . His observation was developed by Heumann⁷⁾, who applied it to a determination of the diffusion coefficients in the β , γ and ϵ phases of the Ag-Zn system. Heumann assumed a linear concentration curve within a given phase and obtained a diffusion coefficient for the average concentration within each phase. By a simple extension of Heumann's analysis, generalized expressions for the layer width and interface positions as functions of time may easily be derived. Since, however, the same expressions can be obtained from a direct application of Fick's first law (eq. (3)), which provides a simple physical picture of the phenomena occurring, the Matano-Boltzmann analysis method will not be considered here.

3. The Application of Fick's First Law to a Two Phase System

Fick's first law of diffusion

$$J = -D \frac{\partial c}{\partial x} \quad (3)$$

simply states that the flow of material J across unit area in unit time is proportional to the concentration gradient. The proportionality factor D is the diffusion coefficient (or, more strictly, the interdiffusion coefficient, if we refer our distance measurements to the Matano-Interface). Let us consider the application of (3) to a diffusion couple made up of two pure metals which have limited solubility in the primary phases, and no intermediate phases. Fig. 1 shows the

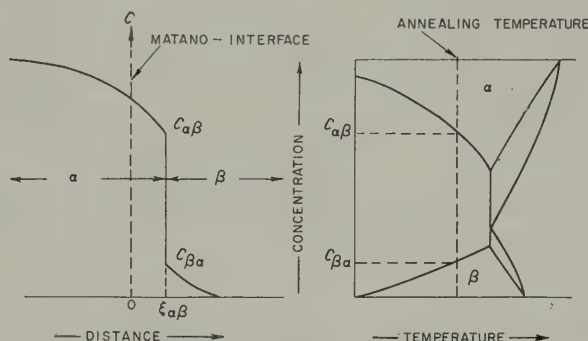


Fig. 1. The relationship between the equilibrium diagram, the diffusion annealing temperature and the diffusion zone interface concentrations for a two phase system.

c - x curve and corresponding equilibrium diagram. It is assumed that the concentrations at the interface are constant and equal to the equilibrium values (Kirkaldy)³. If we consider the flux of material from left to right, the rate of advance of the interface at $\xi_{a\beta}$ is given by

$$[C_{\alpha\beta} - C_{\beta\alpha}] \frac{d\xi_{a\beta}}{dt} = J_{\alpha\beta} - J_{\beta\alpha}. \quad (4)$$

That is to say, $J_{\alpha\beta}$, the flux from the α phase at the interface, must supply the surplus quantity $(C_{\alpha\beta} - C_{\beta\alpha})d\xi$ per unit time in order to advance the α phase into the β -phase region. Substituting for J 's from (3), we have:

$$\frac{d\xi_{a\beta}}{dt} = \frac{1}{C_{\alpha\beta} - C_{\beta\alpha}} \left[\left(-D \frac{\partial c}{\partial x} \right)_{\alpha\beta} - \left(-D \frac{\partial c}{\partial x} \right)_{\beta\alpha} \right]^\dagger. \quad (5)$$

Now the system considered fulfils the conditions required for the application of the Boltzmann theorem; thus the concentration $C(x, t)$ may be expressed as a function of a single parameter $\lambda = x/\sqrt{t}$, and we may write

$$\frac{\partial c}{\partial x} = \frac{1}{\sqrt{t}} \frac{dc}{d\lambda}. \quad (6)$$

If, as has been assumed, the concentrations remain constant at the interface, then the value of the parameter λ , in terms of which c is expressed, must be constant. But $dc/d\lambda$ is again a function of λ alone, and hence it also is constant at the interface. Thus (5) may be rewritten as

$$\frac{d\xi_{a\beta}}{dt} = \left[\frac{(DK)_{\beta\alpha} - (DK)_{\alpha\beta}}{C_{\alpha\beta} - C_{\beta\alpha}} \right] \frac{1}{\sqrt{t}} \quad (7)$$

† This expression was first stated by Wagner, as described by Jost⁸, (1952) p. 72, eq. 1. 308). A typographical error occurs in the book. It is also implicitly contained in eq. 7, p. 920 of Kirkaldy's paper (1958)³.

where

$$K_{ij} = \left(\frac{dc}{d\lambda} \right)_{ij} = \sqrt{t} \left(\frac{\partial c}{\partial x} \right)_{ij}.$$

Integrating (7):

$$\begin{aligned} \xi_{\alpha\beta} &= 2 \left[\frac{(DK)_{\beta\alpha} - (DK)_{\alpha\beta}}{C_{\alpha\beta} - C_{\beta\alpha}} \right] \sqrt{t} \Bigg\} \\ &= A_{\alpha\beta} \sqrt{t}. \end{aligned} \quad (8)$$

Equation (8) exhibits the experimentally observed parabolic time dependence of the interface movement. It also indicates that the rate constant $A_{\alpha\beta}$ depends on the temperature through the D 's. It should be noted, however, that it will not have a simple Arrhenius temperature dependence, of the form $A = A_0 \exp - (Q/RT)$ because it depends on the difference between two interdiffusion coefficients which themselves are weighted averages of the more fundamental partial diffusion coefficients of the two interdiffusing species (see LeClaire⁹). $A_{\alpha\beta}$ will be positive, zero or negative, depending on the relative magnitudes of the terms $(DK)_{\alpha\beta}$ and $(DK)_{\beta\alpha}$. The interface $\xi_{\alpha\beta}$ will move into one side, remain stationary or move into the other side in accordance with the sign of the rate constant. The physical significance of the various cases is clear from the point of view of the relative magnitudes of the fluxes at $\xi_{\alpha\beta}$.

4. A Three-Phase System

Fig. 2 shows c - x curve and corresponding equilibrium diagram for a system in which a single intermediate phase occurs in addition to the two primary phases. Applying Fick's law to the $\xi_{\alpha\beta}$ interface as before, we get

$$\xi_{\alpha\beta} = 2 \left[\frac{(DK)_{\beta\alpha} - (DK)_{\alpha\beta}}{C_{\alpha\beta} - C_{\beta\alpha}} \right] \sqrt{t} \quad (9)$$

and similarly for the $\xi_{\beta\gamma}$ interface

$$\xi_{\beta\gamma} = 2 \left[\frac{(DK)_{\gamma\beta} - (DK)_{\beta\gamma}}{C_{\beta\gamma} - C_{\gamma\beta}} \right] \sqrt{t}. \quad (10)$$

But the width of the β phase layer as a function of time is simply

$$\begin{aligned} W_{\beta} &= \xi_{\beta\gamma} - \xi_{\alpha\beta} \\ &= 2 \left\{ \left[\frac{(DK)_{\gamma\beta} - (DK)_{\beta\gamma}}{C_{\beta\gamma} - C_{\gamma\beta}} \right] - \left[\frac{(DK)_{\beta\alpha} - (DK)_{\alpha\beta}}{C_{\alpha\beta} - C_{\beta\alpha}} \right] \right\} \sqrt{t} \Bigg\} \\ &= B_{\beta} \sqrt{t} \end{aligned} \quad (11)$$

again giving a parabolic time law with a temperature-dependent rate constant, which now involves the diffusion coefficients in its two bordering primary phases as well as those in the β phase itself.

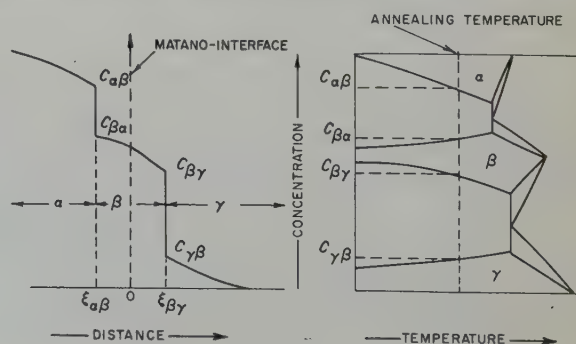


Fig. 2. The relationship between the equilibrium diagram, the diffusion annealing temperature and the diffusion zone interface concentrations for a three phase system.

The remarks above concerning the temperature dependence of $A_{\alpha\beta}$, apply of course to B_β , which has an even more complex sum of fundamental diffusion coefficients. Thus, the assignment of an energy of activation to the growths of a diffusion layer can at most be only a rather crude average of a total of eight fundamental activation energies. If a reasonably linear plot of $\log W$ vs $1/T$ occurs, it is useful empirically. However, it indicates only that either one of the terms predominates over the others, or that the activation energies are not too different from one another.

5. The General Case of n -Phases

Consider the j^{th} layer in a system of n phases separated by $(n-1)$ interfaces. In the same way as above, we get at the $(j-1, j)$ interface

$$\xi_{j-1,j} = 2 \left[\frac{(DK)_{j,j-1} - (DK)_{j-1,j}}{C_{j-1,j} - C_{j,j-1}} \right] \sqrt{t} \quad (12)$$

and at the $(j, j+1)$ interface:

$$\xi_{j,j+1} = 2 \left[\frac{(DK)_{j+1,j} - (DK)_{j,j+1}}{C_{j,j+1} - C_{j+1,j}} \right] \sqrt{t} \quad (13)$$

from which

$$\begin{aligned} W_j &= 2 \left\{ \left[\frac{(DK)_{j+1,j} - (DK)_{j,j+1}}{C_{j,j+1} - C_{j+1,j}} \right] - \left[\frac{(DK)_{j,j-1} - (DK)_{j-1,j}}{C_{j-1,j} - C_{j,j-1}} \right] \right\} \sqrt{t} \\ &= B_j \sqrt{t}. \end{aligned} \quad (14)$$

Although K implicitly depends on all of the diffusion coefficients in the system (see appendix) it can be evaluated graphically at the phase boundaries in the same way that D must be evaluated from the Matano-Boltzmann analysis. In this sense the width of any phase, as a function of time, depends only upon the measurable parameters D and K within that phase and its two immediately adjacent phases.

6. Discussion

Equation (14) indicates that from a purely algebraic point of view, the rate constant B_j may be positive, zero or negative, depending upon the relative values of the miscibility gaps in the equilibrium diagram, and the (DK) terms involved. The physical significance of these three cases are discussed below.

CASE 1. $B_j > 0$

We begin by recalling that:

$$\frac{\partial}{\partial t} (W_j) = \frac{B_j}{\sqrt{t}} \quad (15)$$

or:

$$\begin{aligned} \frac{\partial}{\partial t} (W_j) &= \frac{\partial \xi_{j,j+1}}{\partial t} - \frac{\partial \xi_{j-1,j}}{\partial t} \\ &= \left[\frac{J_{j,j+1} - J_{j+1,j}}{C_{j,j+1} - C_{j+1,j}} \right] - \left[\frac{J_{j-1,j} - J_{j,j-1}}{C_{j-1,j} - C_{j,j-1}} \right]. \end{aligned} \quad (16)$$

Thus $B_j > 0$ simply means that the rate of formation of new j phase from the $(j+1)$ phase is greater than the transition of the j to the $(j-1)$ phase and consequently, the width of the j phase increases with time. The two interfaces can both move to the left or to the right with different rates, or in opposite directions, relative to the Matano interface.

CASES 2 AND 3. $B_j \leq 0$

From eq. (16) $B_j = 0$ requires that

$$\left[\frac{J_{j,j+1} - J_{j+1,j}}{C_{j,j+1} - C_{j+1,j}} \right] = \left[\frac{J_{j-1,j} - J_{j,j-1}}{C_{j-1,j} - C_{j,j-1}} \right]. \quad (17)$$

Physically, this condition would imply that the formation of new j phase at the $(j, j+1)$ interface is exactly counterbalanced by the concurrent transition of the j to the $(j-1)$ phase at the $(j-1, j)$ interface. Such a dynamic balance would result in the absence of the j phase in the diffusion zone, at least in the sense of ordinary microscopic observability.

Similarly, the case of $B_j < 0$ would imply that the rate of supply of excess material from the $(j-1)$ to the j phase was so fast compared to the flow rate in the j phase, that there would be no time for new j to form from the $(j+1)$ phase. In effect, a "pile-up" of excess material would occur, sufficient to result in the direct transition from the $(j-1)$ to the $(j+1)$ phase. Again, no j phase would appear in the diffusion zone.

We must, however, reject these two cases on thermodynamic grounds, since the situation discussed above would imply an infinite chemical potential gradient at the $(j-1, j+1)$ interface. This is in contradiction to the thermodynamic requirement that the chemical potential be continuous and monotonic throughout the sample. In his analysis of a three phase system, assuming constant diffusion coefficients in a given phase, Castleman⁴⁾ has shown that $B_\beta \leq 0$ implies $D_\beta \leq 0$. We conclude, therefore, that while the rate constants can vary over a wide range, they must be positive finite, however small. The apparent absence of certain phases as reported in the literature, implies that the rate constants are too small to permit detection of the phase layers by ordinary microscopic techniques. It would be interesting to examine such a diffusion zone under the electron microscope.

Some observations may be made here concerning the relative widths of the phases appearing in the diffusion zone. It can be seen from the expression for the rate constant that B_j will be large or small according to the difference in the rate of advance of the two bordering interfaces of the j phase. The concentration terms appearing in B_j are those across the miscibility gaps between adjacent phases. Thus the rate of advance of any particular interface will increase as the miscibility gap decreases, for the simple reason that the amount of "excess material" required to nucleate the advancing phase is smaller for a smaller miscibility gap.

The role played by the solubility range of the j phase is not explicit in the expression for B_j , but is contained in the parameter K . (In the appendix, an explicit expression is obtained and discussed.) It does not follow, that wide solubility limits in the equilibrium diagram imply a correspondingly wide diffusion layer, or that very narrow limits imply a narrow layer. The widths of the phases are determined by the balance of flow rates and miscibility gaps at the two interfaces concerned. For example, in the U-Al system (LeClaire and Bear¹⁰⁾), three intermediate phases occur, UAl_4 , UAl_3 and UAl_2 . All of them have essentially zero solubility ranges. Nevertheless, the growth of the UAl_2 and UAl_3 layers is very rapid. Conversely, in the Al-Ni system (Castleman and Seigle²⁾), four phases occur in the equilibrium diagram. The β phase has zero solubility range, the γ and ϵ phases moderate ranges and the δ phase a relatively wide range. In the diffusion zone, for annealing temperatures below the eutectic, only the β and γ phases appear at all, the δ and ϵ phases being too small to detect.

The influence of the diffusion coefficients can be described as follows: If D_j is small, compared to those of its neighboring phases, the rate of supply of material at the $(j, j+1)$ interface required to advance the j phase, will be small. Likewise the accumulation of the excess at the $(j, j-1)$

interface will be rapid. Both of these effects will tend to make the width of the j phase small. On the other hand, if D_j is relatively large, the phase will tend to grow rapidly.

7. The Temperature Dependence of the Rate Constant

The discussion up to this point has been confined to a single annealing temperature. If we now consider the temperature dependence of the rate constant some interesting possibilities emerge. We assume B_j depends on temperature through the (DK) terms only, since these change exponentially whereas the miscibility gaps will change relatively slowly.

The interdiffusion coefficients D are made up of the partial diffusion coefficients of the two species by

$$D = \left[\frac{N_2}{N} D_1 + \frac{N_1}{N} D_2 \right] \quad (18)$$

$$\text{where } D_i = D_{0i} \exp - \frac{Q_i}{RT}$$

and N_i/N = partial molar fraction of component i .

(See, for example, LeClaire⁹.)

The K 's depend implicitly on all of the diffusion coefficients in the system since

$$K = \sqrt{t} \frac{\partial}{\partial x} c[x, t, D_1, D_2 \dots D_n].$$

If we differentiate B_j with respect to temperature, making the simplifying assumption that

$$Q_1 = Q_2 = \bar{Q} \text{ say,}$$

we get an expression of the form

$$\frac{\partial B_j}{\partial T} = \frac{2}{RT^2} \left\{ \left[\frac{(DKM)_{j+1,j} - (DKM)_{j,j+1}}{C_{j,j+1} - C_{j+1,j}} \right] - \left[\frac{(DKM)_{j,j-1} - (DKM)_{j-1,j}}{C_{j-1,j} - C_{j,j-1}} \right] \right\} \quad (19)$$

where

$$M_{i,m} = \left[\bar{Q} + \frac{1}{K} \sum_{i=1}^n D_i Q_i \frac{\partial K}{\partial D_i} \right]_{i,m}. \quad (20)$$

We see that eq. (19) for $\partial B_j / \partial T$ is of similar form to eq. (14) for B_j but each term in (19) is multiplied by the appropriate M factor. It is apparent that the balance of the terms upon which the magnitude of B_j depends will be altered in the expression for $\partial B_j / \partial T$, and here there is no reason for excluding the possibility of a negative sign. That is to say, one may expect systems to exist in which the rate constant decreases with increasing temperature, giving rise to an apparent "negative" activation energy. While such cases may be rare in practice, it is interesting to note that just this type of behavior has been reported by LeClaire and Bear¹⁰) in their study of the interdiffusion of Al and U. In the diffusion zone consisting of layers of UAl_2 and UAl_3 it was observed that for constant annealing times the width of the UAl_2 layer increased with increasing temperature up to 560° C (i.e. $\partial B / \partial T > 0$ for $T \leq 560^\circ$ C), but that it decreased in width with further increases in temperature, i.e. $\partial B / \partial T < 0$ for $T > 560^\circ$ C. Unfortunately the interpretation here is not completely unambiguous, since a pressure was applied to the specimens during the annealing in the above experiments. However, the described behavior did take place for a single pressure. A temperature dependence of this type illustrates very clearly the fallacy of attributing an "activation energy" to such a complex system.

It is well known that some intermetallic compounds found in a diffusion zone have undesirable mechanical properties, for example they are frequently brittle and subject to cracking under

stress. It has been found practicable in the case of Al-Ni for example, to form a very strong bond between the two metals by hot extruding the aluminium onto the nickel, under conditions such that essentially no observable diffusion layer widths are found (Kidson¹¹). If the diffusion parameters involved were favorable an alternative technique could be the judicious choice of annealing temperature which would preclude the growth of an undesirable phase.

8. Conclusions

The application of Fick's first law to polyphase diffusion in binary systems leads to a simple physical interpretation of various possible types of behavior in the growth of diffusion layers. It has been shown that there is no justification for assuming that each phase in the equilibrium diagram of a system will grow to an observable width in a diffusion couple.

The occurrence or non-occurrence of a phase is governed by conditions peculiar to a particular annealing temperature, rather than depending solely upon sufficiently high annealing temperatures or long annealing times. Throughout this analysis, no simplifying assumptions were made other than the constancy of the interface concentrations and, in the discussion of $\partial B_j / \partial T$, the equivalence of Q_{j1} and Q_{j2} . It has been implicitly assumed that the growth rates are determined entirely by volume diffusion. No account was taken of possible rate controlling effects due to the nucleation of new phases etc. It is felt, nevertheless, that a better understanding of the problem has been attained, without the restriction of assuming concentration independent diffusion coefficients in the phases. Of course, one can use the structure of the expression for B_j , and substitute analytical expressions for the K 's obtained from a solution of eq. (3) (see the appendix).

The results are so complicated, however, that little new information can be obtained about the general behavior, other than a better indication of the role played by the solubility ranges of the phases.

Acknowledgements

Much of the work on this problem was done while the author was attached to AERE, Harwell, England. He would like to express his appreciation to Mr. A. D. LeClaire for the many stimulating discussions regarding the present work and related topics.

Appendix

For unidirectional diffusion, and constant D , Fick's second law may be written as:

$$\frac{\partial c}{\partial t} = D \frac{\partial^2 c}{\partial x^2}. \quad (\text{i})$$

Kirkaldy³) has given a general solution for an n -component system, which, for two components, reduces to

$$c(x, t) = a + b \operatorname{erf} \left[\frac{x}{2\sqrt{Dt}} \right]. \quad (\text{ii})$$

The coefficients a and b may be determined in the polyphase diffusion couple by applying the condition that the concentrations at the interfaces are constant and equal to the equilibrium values. Thus

$$C_{j,j-1} = a_j + b_j \operatorname{erf} \left[\frac{\xi_{j,j-1}}{2\sqrt{D_j t}} \right] \quad (\text{iii})$$

and

$$C_{j,j+1} = a_j + b_j \operatorname{erf} \left[\frac{\xi_{j,j+1}}{2\sqrt{D_j t}} \right] \quad (\text{iv})$$

from which

$$a_j = \frac{C_{j,j-1} \operatorname{erf} \left[\frac{\xi_{j,j+1}}{2\sqrt{D_j t}} \right] - C_{j,j+1} \operatorname{erf} \left[\frac{\xi_{j,j-1}}{2\sqrt{D_j t}} \right]}{\operatorname{erf} \left[\frac{\xi_{j,j+1}}{2\sqrt{D_j t}} \right] - \operatorname{erf} \left[\frac{\xi_{j,j-1}}{2\sqrt{D_j t}} \right]} \quad (\text{v})$$

and

$$b_j = \frac{C_{j,j-1} - C_{j,j+1}}{\operatorname{erf} \left[\frac{\xi_{j,j-1}}{2\sqrt{D_j t}} \right] - \operatorname{erf} \left[\frac{\xi_{j,j+1}}{2\sqrt{D_j t}} \right]}. \quad (\text{vi})$$

The coefficient K , which was defined as

$$K_{ij} = \sqrt{t} \frac{(\partial c)}{(\partial x)_{ij}}$$

may be explicitly expressed as

$$K_{ij} = \sqrt{t} \left[\frac{b}{\sqrt{\pi D t}} \exp - \left[\frac{x}{2\sqrt{D t}} \right]^2 \right]_{ij}. \quad (\text{vii})$$

If the above is inserted in the expression for $W_j(t)$, using the appropriate values for b_j , we get

$$W_j(t) = \frac{2}{\sqrt{\pi}} \left\{ \left[\frac{\Delta C_{j+1} \sqrt{D_{j+1}} \Phi_{j+1,j} - \Delta C_j \sqrt{D_j} \Phi_{j,j+1}}{\delta C_{j,j+1}} \right] - \left[\frac{\Delta C_j \sqrt{D_j} \Phi_{j,j-1} - \Delta C_{j-1} \sqrt{D_{j-1}} \Phi_{j-1,j}}{\delta C_{j,j-1}} \right] \right\} \sqrt{t} \quad (\text{viii})$$

where $\Delta C_j = C_{j,j-1} - C_{j,j+1}$ = solubility range of the j phase in the equilibrium diagram,

$\delta C_{j,j+1} = C_{j,j+1} - C_{j+1,j}$ = miscibility gaps between the j and $j+1$ phases and

$$\Phi_{j,j+1} = \frac{\exp - \left[\frac{\xi_{j,j+1}}{2\sqrt{D_j t}} \right]^2}{\operatorname{erf} \left[\frac{\xi_{j,j+1}}{2\sqrt{D_j t}} \right] - \operatorname{erf} \left[\frac{\xi_{j,j-1}}{2\sqrt{D_j t}} \right]}.$$

The roles of the solubility ranges of the phases as well as the miscibility gaps between them are shown explicitly in eq. (viii). The full complexity of the expression for W_j in terms of the diffusion coefficient and concentrations can be appreciated by noting that all of the D 's and c 's involved in the whole system enter into W_j through the Φ 's. Consequently no simple generalizations can be made about a correlation between the phase diagrams and the relative phase widths in a diffusion zone, other than to note again the dependence upon a balance of terms occurring at the bordering interfaces.

It is felt, therefore, that a graphical evaluation of the K 's and \tilde{D} 's from an experimental $c-x$ curve serves to provide useful and well-defined parameters for a quantitative discussion of the behavior of the phase layer growth rates.

References

- 1) H. Buckle, Metallforsch. **1** (1946) 47; (1947) 175
- 2) L. S. Castleman and L. L. Seigle, Jour. Met. **9** (1957) 1173
- 3) J. S. Kirkaldy, Can. Jour. Phys. **36** (1958) 917
- 4) L. S. Castleman, Nucl. Sci. and Eng. **4** (2) (1958) 209
- 5) L. Boltzmann, Weid. Ann. **53** (1894) 959
- 6) W. Jost, Zeit. Physik **127** (1952) 163
- 7) T. Heumann, Zeit. Electrochem. **60** (1952) 1160
- 8) W. Jost, (Academic Press, 1952) 72
- 9) A. D. LeClaire, Progress in Metal Physics **1** (1949) 364
- 10) A. D. LeClaire and I. J. Bear, Jour. Nucl. Energy **2** (1956) 229
- 11) G. V. Kidson, Atomic Energy of Canada Report, AECL CRMet-683 (1957)

THE EFFECT OF THE $\alpha \rightarrow \beta \rightarrow \alpha$ PHASE TRANSFORMATION ON THE PREFERRED ORIENTATION OF α URANIUM

B. R. BUTCHER and D. BAVERSTOCK

UKAEA Research Group, Metallurgy Division, Atomic Energy Research Establishment, Harwell, Didcot, Berks., UK

Received 7 June 1960

Dilatometric, metallographic, and X-ray observations have been made on specimens of rolled uranium rod which have been subjected to varying amounts of transformation into the β phase in a temperature gradient. The results show that the phase change is accomplished by a transformation band of mixed α and β phases passing through each specimen, and that the amount of the loss of preferred orientation is a function of the degree of transformation. A mechanism to account for this is discussed.

Des échantillons de barreaux d'uranium laminé qui ont été soumis à différents taux de transformation en phase β dans un gradient de température ont été étudiés par dilatométrie, métallographie et rayons X. Les résultats montrent que le changement de phase est accompagné d'une bande de transformation de

phases α et β mélangées se propageant à travers chaque échantillon et que le taux de diminution de l'orientation préférentielle est une fonction du degré de transformation. Un mécanisme rendant compte de ces faits est proposé.

An Proben aus gewalzten Uranstäben wurden dilatometrische, metallographische und röntgenographische Untersuchungen durchgeführt. Die Proben wurden zuvor in verschieden starkem Masse in einem Temperaturgradient in die β -Phase überführt. Die Ergebnisse zeigen, dass die Phasenumwandlung durch ein Umwandlungsband aus α - und β -Kristallen bewirkt wird, welches durch jede Probe hindurchwandert. Dabei ist die auftretende Orientierungsabnahme eine Funktion des Umwandlungsgrades. Ein hierfür passender Mechanismus wird besprochen.

1. Introduction

There is no doubt that there are two mechanisms whereby the β phase may transform to the α in dilute uranium alloys, and that these mechanisms apply even to the very dilute alloys such as commercially pure uranium¹). The mechanism at high α phase temperatures seems to be of the normal nucleation and growth type, but at lower temperatures a martensitic type of transformation takes place. If the $\alpha \rightarrow \beta$ phase change were also martensitic, then rapid cooling from the β phase should give retention of any preferred orientation of the α phase on the $\alpha \rightarrow \beta \rightarrow \alpha$ cycle, since most martensitic transformations are reversible. If not, the preferred orientation should disappear. At the time that this work was started there was some evidence that the $\alpha \rightarrow \beta$ transformation was martensitic²). There was also evidence, how-

ever, that β treatment destroyed preferred orientation, while if the $\alpha \rightarrow \beta$ transformation were not fully completed, the retention of the α preferred orientation was almost complete³). This work was started to investigate the disappearance of preferred orientation after the $\alpha \rightarrow \beta \rightarrow \alpha$ cycle.

2. Previous Work

Work on the $\alpha \rightarrow \beta \rightarrow \alpha$ transformation up to 1956 has already been reviewed by the author²), but since then several relevant papers have been published.

Klepfer and Chiotti⁴) studied the $\alpha \rightarrow \beta$, $\beta \rightarrow \gamma$, $\gamma \rightarrow \beta$, $\beta \rightarrow \alpha$ transformations of pure uranium by electrical resistance measurements and a sonic technique. They found anomalous resistance changes after the $\beta \rightarrow \alpha$ transformation in short samples which were being

$\alpha \rightarrow \beta \rightarrow \gamma \rightarrow \beta \rightarrow \alpha$ cycled at $\frac{1}{4}$ cycle per minute, if the cycling was interrupted to allow the bar to dwell in the γ and β regions, or in the β region alone. They attributed these anomalies to rapid β grain growth, combined with the orientation dependence of all four transformations and the partial reversibility of the transformations. They discovered that increasing the cycling rate up to 1 cycle a minute had three effects: the temperature of the onset of thermal twinning in the α phase was increased, the resistance of the newly formed α phase was increased, and the temperatures at which the $\gamma \rightarrow \beta$ and $\beta \rightarrow \alpha$ phase changes took place decreased with each successive cycle. These effects they ascribed to progressive lattice hardening due to a martensitic transformation.

The most surprising result they found, however, was that all four transformations were partly athermal in nature, and that although transformation could proceed isothermally up to a certain point, the phase change was never completed until a temperature well above or below the supposed equilibrium transformation temperature was reached, (depending on whether the phase changes took place on heating or cooling respectively).

McDonell⁵⁾ investigated the $\alpha \rightarrow \beta \rightarrow \alpha$ transformation by finding the loss of preferred orientation and increase in grain size of fine grained rolled uranium plate as functions of the heating time and temperature in the β phase range, and the cooling conditions. At temperatures from 670° C to 685° C the $\alpha \rightarrow \beta$ transformation took a progressively decreasing time to occur, as suggested from the grain coarsening results, while at 690° C the transformation was almost instantaneous. However, the times for the complete disappearance of the preferred orientation were approximately four times as long as the times for maximum α phase grain coarsening to occur. Quenching the specimen, as opposed to air-cooling it, at stages intermediate between these times decreased both the the grain size and the remanent preferred orientation.

Donze and Faivre⁶⁾ made dilatometric studies

of α phase single crystals of uranium which were heated into the β phase temperature range. They found that it was possible to regenerate the single crystals, after the $\alpha \rightarrow \beta$ transformation had taken place, by cooling them through the $\beta \rightarrow \alpha$ transformation, providing a certain temperature in the β temperature range was not exceeded. This temperature was markedly affected by the purity of the material, being 2° above the transformation temperature for the purest material available, (37 ppm carbon), and 14° above for material deliberately contaminated with 150 ppm carbon. An analogous phenomenon took place with iron single crystals, and regeneration was possible at slow heating and cooling rates where the $\alpha \rightarrow \gamma \rightarrow \alpha$ transformation was not orientation dependent. Since regeneration in uranium was also possible with slow heating and cooling rates, Donze¹⁴⁾ claimed that, with this material also, regeneration was not due to the martensitic nature of the transformation, but to remanent α nuclei which he associated with the carbon content of the material.

Bement and Wallace⁷⁾ have postulated a martensitic mechanism for the $\beta \rightarrow \alpha$ transformation of uranium, on the basis of their interpretation of hardness measurements. These were taken at room temperature, on specimens which had been quenched after isothermal treatment for varying times and temperatures in the α range, after two minutes soaking at a temperature in the β range. The graphs of hardness versus isothermal holding time showed a sharp drop in hardness after a short incubation period, and then a gradual decline. The sharp drop was thought to be due to the start of a diffusion-controlled transformation, and the gradual decline to the progress of this transformation, but since the sharp drop was approximately half the total fall, it seems just as likely that this initial drop was due to total transformation, and that the gradual softening could be accounted for by the annealing of the transformation strains.

Konobeevsky *et al.*⁸⁾ have reported measurements on the preferred orientation of the β

phase resulting from rapidly heating rolled sheet of uranium-molybdenum alloy, of known α preferred orientation, into the β temperature range and then quenching it to stabilise the β phase. They found a definite orientation relationship for the $\alpha \rightarrow \beta$ transformation, in which $(100)\alpha$ was parallel to $(001)\beta$, and $[012]\alpha$ was parallel to $[110]\beta$, but this relationship was different from any previously reported for the $\beta \rightarrow \alpha$ transformation of dilute alloys.

Finally, Slattery¹⁵) has reported that bars of uranium of commercial purity that have been heated rapidly into the high β range and then quenched have a slight texture. Three types of bars have undergone this treatment, namely, cast, α -rolled, and α -extruded, and the texture has been different in each case. In some way the effect of working has persisted throughout the $\alpha \rightarrow \beta \rightarrow \alpha$ transformation, although it is not known whether the slight texture is remanent from the working operation.

3. Material

The uranium used in these experiments was calcium-reduced material which had been remelted in a graphite crucible and cast into 3.2 cm diameter bars. The analysis is given below. This "dirty" material was used in the hope that the α grain size resulting from the $\alpha \rightarrow \beta \rightarrow \alpha$ cycle would be small enough to enable reliable preferred orientation measurements to be made.

Element	Fe	Al	Si	C	O ₂	H ₂	N ₂	Other metallic elements (total)
Content (ppm)	83	100	15	810	100	4	<10	approx. 50

The bars were rolled to 2.5 cm diameter, using small passes at a temperature of 300° C, reheating being carried out between each pass. They were then annealed at 640° C for 24 hours, and rolled down to 1.3 cm diameter, using a similar procedure. After this they were parted to make specimens 5 ± 0.005 cm in length. Some of these specimens were subsequently annealed at 645° C for 24 hours.

4. Apparatus and Methods

Three experimental methods were used. The specimens were heated in a gradient furnace, while the extent of the transformation, and the linear coefficient of thermal expansion along the rod axis before and after transformation, were determined dilatometrically. They were then cut into eight pieces approximately 0.6 cm thick, and examined metallographically. Finally a direct measure of the preferred orientation of these pieces was made by means of a Schulz diffractometer.

4.1. THE DILATOMETER

A simple type of dilatometer was used. The specimen was placed in a vertical silica tube sealed at the lower end, which was attached rigidly to a base plate. A silica rod was placed on top of the specimen, and registered on a dial gauge reading to 0.0001" (2.5 μ) which was also attached firmly to the base plate. A thermocouple rested on top of the specimen, and the signal from this was fed to a Honeywell Brown Electronik recorder. The dilatometer was evacuated to a pressure of less than 5×10^{-4} mm of mercury. Dial gauge and temperature readings were taken at fixed time intervals.

The furnace was suspended round the dilatometer tube so that it could be lowered away from the tube at any chosen instant. Cooling started instantaneously, there being no "overshoot" of temperature. In this way the $\alpha \rightarrow \beta$ transformation could be stopped when only partially

completed. There was a temperature gradient in the furnace so that transformation started from the bottom of the specimen. With no specimen and measured in air, this gradient was 8° C/cm. Judging from the dilatation-temperature curves, the actual gradient in the specimen was approximately 2° C/cm, assuming that most of the transformation in any small volume of the specimen occurred at the same

temperature. The heating rate was controlled by a motor-driven Variac transformer, and varied from 7.5 to 8.3° C/min up to the start of the $\alpha \rightarrow \beta$ transformation. The cooling rate through the $\beta \rightarrow \alpha$ transformation was 40 to 60° C/min.

The dilatometer was tested with a copper specimen. The expansion curves on heating and cooling were not coincident except at the maximum and minimum temperatures, but this was ascribed to the position of the thermocouple and the thermal gradient in the specimen. The average dilatation coefficient for copper, as measured from the average slope of temperature-dilatation curve, was within 5 % of the accepted value.

With the uranium specimens the average slope on cooling was taken as a measure of preferred orientation. The average coefficients of thermal expansion from 0 to 600° C are $34.5 \times 10^{-6}/^\circ\text{C}$ in the a direction, $-7.5 \times 10^{-6}/^\circ\text{C}$ in the b direction, and $30.1 \times 10^{-6}/^\circ\text{C}$ in the c direction, with a value for randomly oriented polycrystalline material of $19.3 \times 10^{-6}/^\circ\text{C}$, according to figures given by Holden¹⁰).

Specimens were numbered in the order in which they were used. Those prefixed by A were annealed before use.

4.2. METALLOGRAPHY

Each specimen was cut into eight 0.6 cm slices, and the upper surface of each slice, i.e. the last part to transform, was polished by normal means; emery paper, diamond dust paste, followed by attack polishing in a chromic-acetic acid mixture with γ alumina. Each piece was numbered from the top, which was the last part of the specimen to transform; e.g. sample A4.3 represents a section 1.3 cm from the top of the fourth annealed specimen. The samples were examined under polarised light.

4.3. PREFERRED ORIENTATION MEASUREMENTS

The Schulz diffractometer has already been described¹¹). The specimens were electropolished just before examination, and the variation of the intensity of the (020) reflection

was found at tilt angles up to 60° from the rod axis. Scanning was effected by reciprocating and rotating the specimens during examination. It was hoped that the electropolishing would produce a standard surface for examination. After examination, the intensities from one or two specimens at a few tilt angles were re-measured. The values were the same as those for the first examination, proving that virtually no oxidation of the specimen surface had occurred during the time of measurements.

The defocussing correction was estimated using a random sample made from spherical uranium powder mixed with "Durofix". Unfortunately on this sample the (020) reflection intensity could hardly be distinguished from the background, but as it has been shown that the defocussing depends on the type of material more than the angle of the reflection¹¹), the correction was made using the average defocussing from the (111), (131), and (112) α uranium lines, which are well separated from adjoining reflections.

The results are presented corrected for defocussing and background. It was not necessary to correct for dead time with the type of counter used and the intensities found.

5. Results

5.1. DILATOMETRY

The results are summarised in table 1, and typical curves are shown in figure 1. Above 550° C, the unannealed specimens started to shrink, (fig. 1a), and on cooling the specimens lengthened. This was attributed to a sharpening of the [010] texture by recrystallisation, since the annealed specimens showed a negative coefficient of dilatation averaged over the α range (fig. 1b). The average coefficient was approximately $-4 \times 10^{-6}/^\circ\text{C}$.

When the specimens had transformed to some extent, the coefficient of dilatation was always greater than $-4 \times 10^{-6}/^\circ\text{C}$. By assuming that the texture after transformation had two components (the original texture, and a random one whose coefficient of dilatation was $19.3 \times$

TABLE 1

Specimen number	Temperature attained ($^{\circ}\text{C}$)	% transformation	Average coefficient of thermal expansion ($\text{cm}/\text{cm}/^{\circ}\text{C} \times 10^{-6}$)
As received			
4	640	0	-2.4
6	666	60	-3.5
15	669	60	-3.4
16	668	60	-3.1
10	668	85	-2.2
9	667	95	5.0
11	670	95	5.2
7	676	100	15.8
8	675	100	12.8
14	678	100	14.0
1	696	100 plus superheat	17.8
12	703	100 plus superheat	20.5
13	697	100 plus superheat	19.5
Annealed			
A 1	640	0	-3.9
A 2 (micro + P.O.)	645	0	-4.2
A 3	666	60	-2.3
A 9 (micro + P.O.)	668	60	-1.2
A 4	672	95	3.1
A 8 (micro + P.O.)	668	95	7.2
A 7 (micro + P.O.)	671	100	12.7
A 5	706	100 plus superheat	16.5
A 6 (micro + P.O.)	704	100 plus superheat	18.7
A10	696	100 plus superheat	20.8

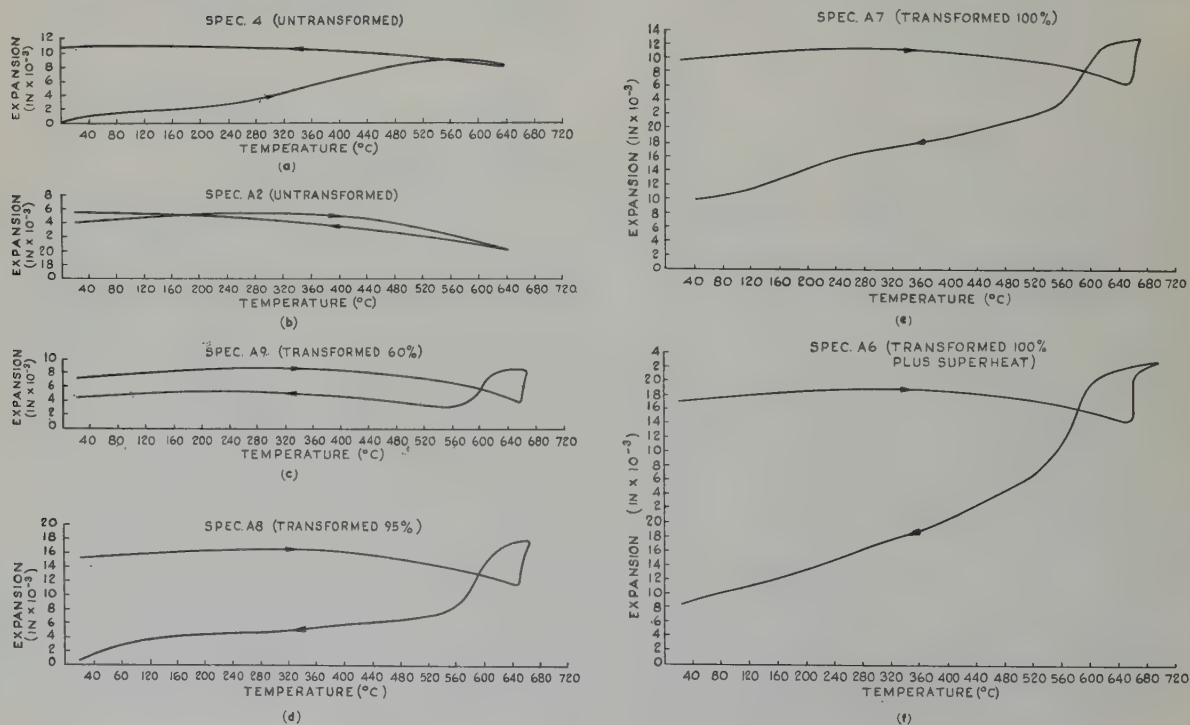


Fig. 1. Dilatation curves for selected specimens.

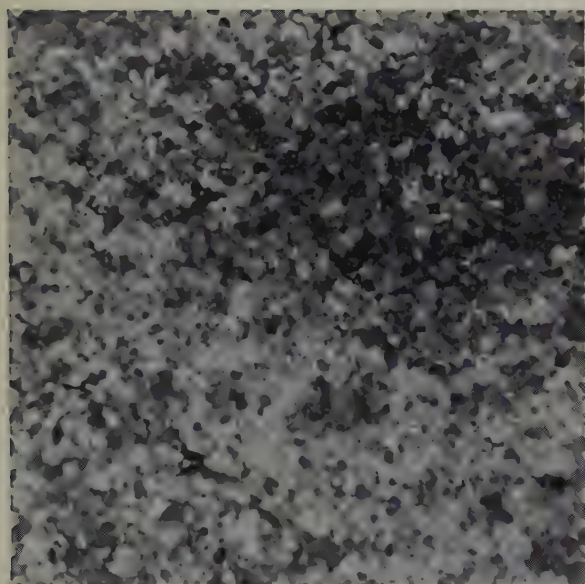


Fig. 2. Structure of specimen A2. Polarised light.
× 40.

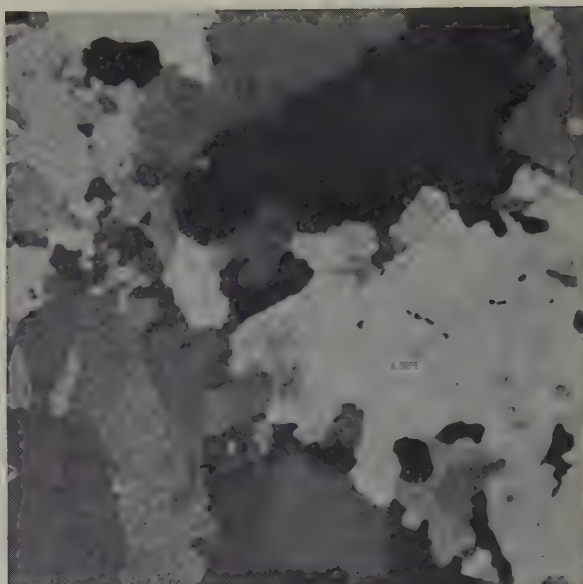


Fig. 4. Structure of specimen A9.6. Polarised light
× 40.

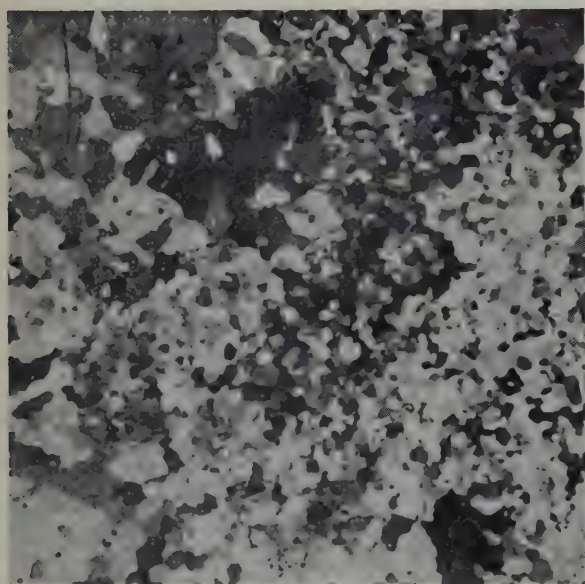


Fig. 3. Structure of specimen A9.2. Polarised light.
× 40.

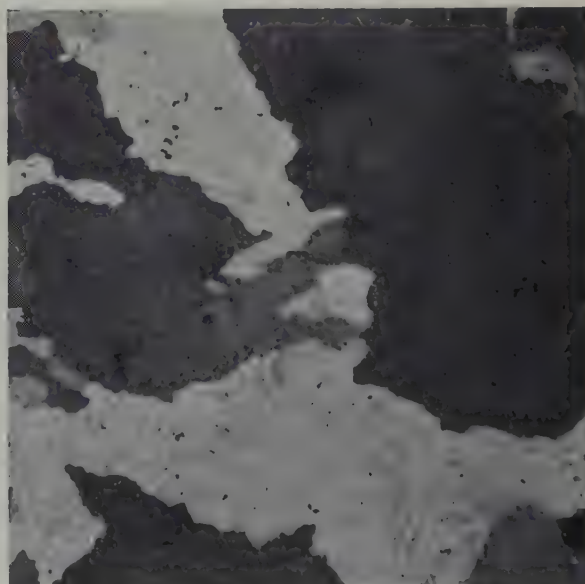


Fig. 5. Structure of specimen A9.8. Polarised light.
× 40.

$10^{-6}/^{\circ}\text{C}$), it was possible to define the amount of texture lost, by equating the observed coefficient of dilatation after transformation to $10^{-6}\{19.3x - 4(1-x)\}$, where x was the fractional loss of texture. However, " x " could not be related with any certitude to the fraction of α which had transformed to β , since it was impossible to determine the latter with an accuracy greater than 5 %. For example, the fraction transformed could be defined as the length change due to the partial $\alpha \rightarrow \beta$ transformation divided by the length change due to the full $\alpha \rightarrow \beta$ transformation, but the latter, when measured on specimens which had been fully transformed and then heated into the β range, was not constant. This lack of accuracy was particularly annoying since most of the texture loss was evident only in specimens which had passed through the later stages of the $\alpha \rightarrow \beta$ transformation.

Nevertheless it is clear that, under these experimental conditions, the specimens transformed up to 85 % retained most of the preferred orientation, specimens near the end of transformation (95 %) retained about half the preferred orientation, while those which have almost completely transformed kept about a quarter of the texture.

5.2. METALLOGRAPHY

The structure of the untransformed α annealed specimen A2 is shown in fig. 2.

Specimen A9 had been transformed 60 %, and thus the top of this specimen (sample A9.1, the coolest part of specimen A9) must have been almost at the transformation temperature. Nevertheless the structure of A9.1 was indistinguishable from that shown in figure 2, and there could have been no grain growth in the α temperature range. Thus any grain coarsening must have taken place as the result of the $\alpha \rightarrow \beta \rightarrow \alpha$ transformation. Sample A9.2 (fig. 3) showed large amounts of the original structure mixed with some coarser grains, and sections A9.3, A9.4 and A9.5 showed decreasing amounts of the original structure, and a progressive coarsening of the grains that had been trans-

formed to β . The original structure was barely detectable in sample A9.6 (fig. 4) and not at all in samples A9.7 and A9.8; the latter showed a very coarse α grain size (fig. 5). In specimens A8 and A7, which had transformed 95 % and 100 % respectively, sample A8.1 showed a structure similar to that of A9.6 (fig. 4) and sample A7.1 a structure similar to that of A9.7. The coarsest structures seen, even in the specimen which had been heated well into the β range, were similar to that of sample A9.8 (fig. 5).

Evidently transformation in a temperature gradient was accomplished by the passage through the material of a transformation band of mixed α and β phases. Such a band has been postulated by Kehoe¹²).

5.3. PREFERRED ORIENTATION

The results of the preferred orientation measurements are plotted graphically in fig. 6, where the intensity of reflection is shown as a function of the angle from the rod axis, ϕ . The results should be considered in the light of fig. 6e, which shows what could be expected from a specimen with little or no preferred orientation. Unfortunately the grain size of the transformed specimens were too large to give statistically valid results from any one slice. The wavy solid line in fig. 6e is the average value of the intensity from all slices for each ϕ value, and the arithmetic mean of these values was approximately 700 counts/min.

Comparing figs. 6a and 6e, the α annealed specimen (A2) had appreciable [010] texture in the rolling direction, but the maximum [010] texture was at 25° to the rolling direction. At 60° to the rolling direction, no intensity due to [010] reflection was detectable from A2. The curves in fig. 6a are more regular in form than those in fig. 6e, due to the much finer grain size. It is not known why the curves differ slightly for each slice. It can only be attributed to variation in surface condition in spite of the standard surface preparation.

An estimate of the accuracy of measurement was carried out by assuming that there was no

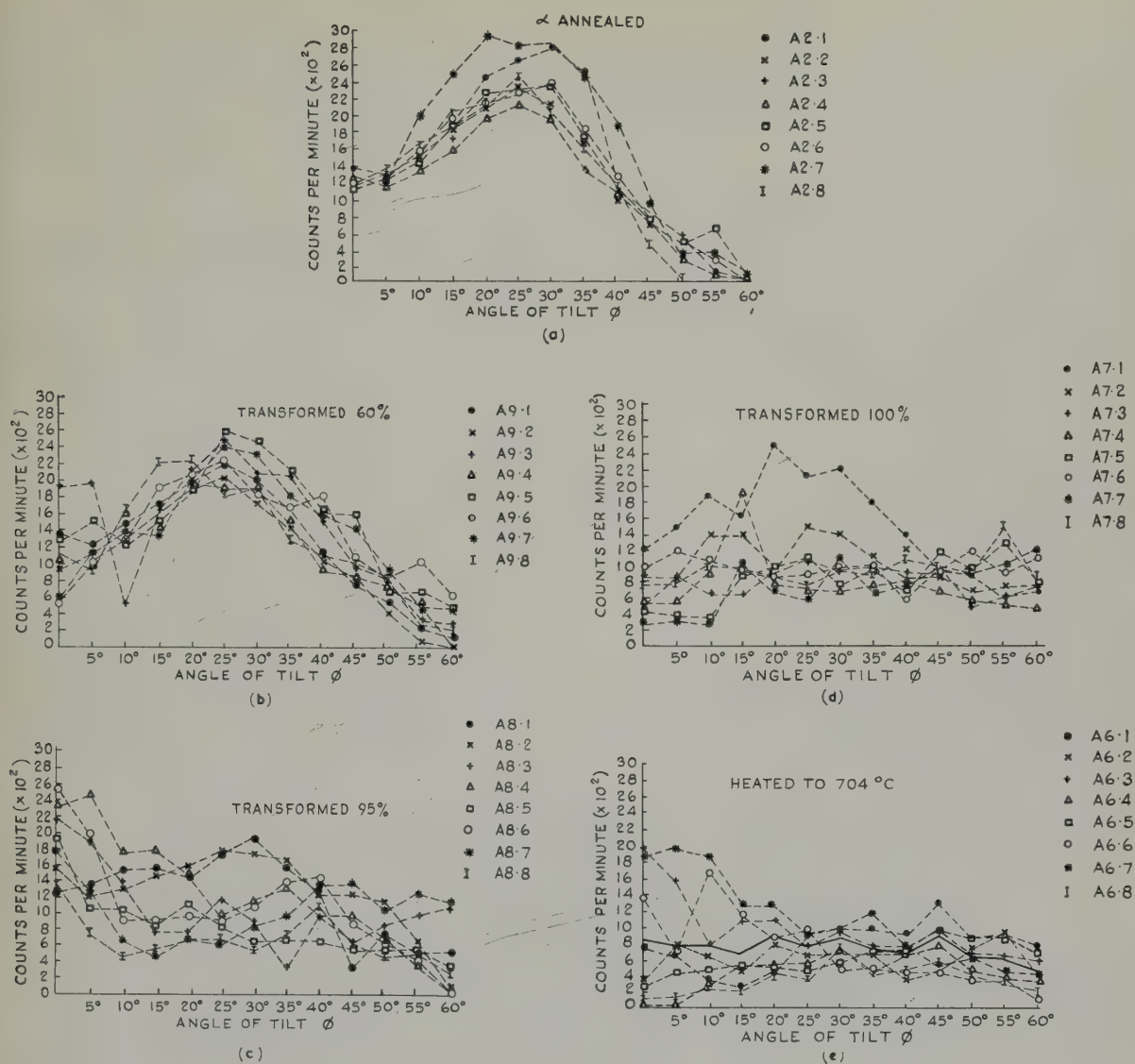


Fig. 6. Intensity of the (020) X-ray reflection for selected specimens.

preferred orientation in specimen A6, i.e. that the intensity of the [010] reflection would remain at 700 counts/min from $\phi = 60^\circ$ to $\phi = 90^\circ$, and that there was no [010] intensity from $\phi = 60^\circ$ to $\phi = 90^\circ$ in specimen A2. A measure of the total number of reflecting planes for any reflection is given by

$$\int_{\phi=0}^{\phi=\frac{1}{2}\pi} I \sin \phi \, d\phi,$$

where I is the intensity of reflection¹³). These integrals should be the same for all specimens

for a chosen reflection. For specimens A6 and A2, taking average intensities for each ϕ value, they differed by 20 % which is reasonably satisfactory considering the assumptions, the low intensities, and the uncertainty of the contribution to the integrals at low values of ϕ .

The results from specimen A9 (fig. 6b) showed, as might be expected from the dilatation coefficient, that most of the preferred orientation has been retained, but that some intensity had been transferred from the peak to higher ϕ values, especially in the case of

slices A9.6 and A9.7. In particular, the results showed that A9.7 and A9.8, which appeared from metallographic examination to have transformed fully to β , retained most of their preferred orientation.

Specimen A8 is puzzling, in that, although it retained approximately 50 % of its preferred orientation according to the dilatometric measurements, only slices 8.1 and 8.2 showed any X-ray evidence of this retention. There is, however, a consistently high intensity at low ϕ values, which is not repeated by any of the other specimens and so must be put down to chance.

Specimen A7 shows that A7.1 and to a lesser extent A7.2 retained some preferred orientation, which again is to be expected from the dilatometric measurements.

6. Discussion

The presence of untransformed α phase in a partly transformed specimen does not lead to a full retention of preferred orientation, since

specimen A8, which definitely contained some untransformed α , lost a great deal of preferred orientation. On the other hand, specimen A7, which metallographically appeared to have fully transformed to β , retained about $\frac{1}{4}$ of its preferred orientation.

Considering the sequence of events in the transformation, the increase in α grain size after the transformation could not have been due to grain growth in the α phase. It seems probable that, at the cooling rates used, the $\beta \rightarrow \alpha$ transformation was martensitic, in which case the α grain size resulting from $\beta \rightarrow \alpha$ transformation would be less than or equal to the β grain size. Thus the increase in α grain size must have been due to the $\alpha \rightarrow \beta$ transformation. Large β grains could be formed in two ways; either the β grains nucleate, normally or martensitically, and then grow at the expense of the surrounding α , or all the α turns martensitically to β and the β grains grow. The relative amounts of fine and coarse-grained α in specimen A9 were roughly in the same proportion as the

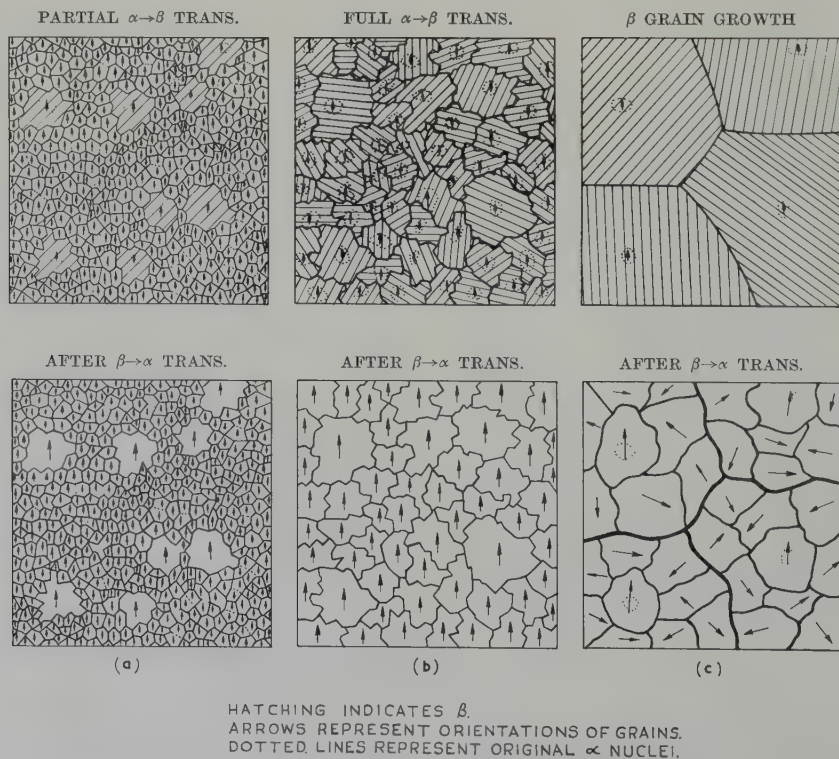


Fig. 7. Schematic representation of the loss of preferred orientation on transformation.

untransformed and transformed fractions of this specimen, suggesting that very little, if any, of the fine grained α could have been in the β phase. Thus the first mechanism probably applied, and the growth on to the β nuclei must have been very rapid.

This is a mechanism for increasing the α grain size, but the retention of preferred orientation still has to be explained. It could be due to the carbon content, at postulated by Donze by analogy with iron. Such an analogy may be false, however. The maximum solubility of carbon in α iron is over 200 ppm¹⁶). The solubility of carbon in α uranium is not known, but in γ uranium at 800° C it is 65 ppm¹⁷). Since it is impossible to modify the form of the carbide precipitate by heat treatment in the β and α temperature ranges¹⁸) and since the $\beta \rightleftharpoons \alpha + \text{UC}$ reaction is of the eutectoid type¹⁹), the solubility of carbon in α uranium is probably considerably less. Thus the carbon in the α uranium single crystals would be in the form of a uranium carbide precipitate. The association of remanent α nuclei with carbon in the high temperature phase may therefore involve different mechanisms for iron and uranium.

However, if nucleation in the $\alpha \rightarrow \beta$ phase change is martensitic, the retention of preferred orientation could be easily explained when the rate of cooling is sufficiently high to ensure that the $\beta \rightarrow \alpha$ transformation is also martensitic. The problem then is to explain the disappearance of preferred orientation and this can be done by postulating rapid β grain growth. The various stages are shown schematically in fig. 7. On partial $\alpha \rightarrow \beta$ transformation, the martensitic nucleation ensures that a memory of the α grain is carried into the β phase, so that when the β grain transforms, it reverts to an α grain of the same orientation as that of the original nucleus, and a structure of mixed grain size results (fig. 7a). When the metal is cooled as soon as the $\alpha \rightarrow \beta$ transformation has been completed, the α grain size is enlarged, and the orientation retained (fig. 7b). However, β grain growth can sweep from the material the memory of many α grains, and if the α grain

size after transformation is less than that of the β , a large part of the preferred orientation will be lost (fig. 7c). It is necessary to assume that the memory of the orientation of an α grain is restricted to the site originally occupied by the α grain.

This mechanism could explain the results presented here and also those of McDonell⁵). It might even be used to explain Donze and Faivre's results on uranium, if it could be said that the function of the carbide particles in uranium is to restrain β grain growth. Especially it could explain Slattery's results (see previous work), whereas Donze's hypothesis would have difficulty in so doing; it would be difficult to imagine any mechanism whereby a memory of α phase grain orientations can be maintained at temperatures high in the beta range, unless martensitic nucleation is involved.

In reality, it is quite possible that both mechanisms apply, that proposed by Donze being applicable at low heating and cooling rates, and the one proposed herein being applicable at high heating and cooling rates. It is clear, however, that much work remains to be done on the $\alpha \rightarrow \beta \rightarrow \alpha$ transformation before it is fully understood.

Acknowledgements

The authors would like to thank Dr. H. M. Finniston for suggesting this work and encouraging its progress, and Mr. D. C. Minty for his help with some of the experimental work and the discussion.

References

- 1) G. V. Jeminson, UKAEA Industrial Group Report, IGR-TN/C 856 (1958)
- 2) B. R. Butcher, J. Nucl. Energy 1 (1957) 273
- 3) G. Cabane and J. Petit, Rev. Met. 51 (1954) 603
- 4) H. H. Klepfer and P. Chiotti, Iowa State College (USA) Report, ISC-893 (1957)
- 5) W. R. McDonell, Nuclear Engineering and Science Congress (USA) (1958), preprint 172
- 6) G. Donze and R. Faivre, Comptes Rendus 246 (1958) 3619
- 7) A. L. Bement and W. P. Wallace, Hanford (USA) Report, HW-51084 REV (1957)

- ⁸⁾ S. T. Konobeevsky *et al.*, Second Geneva Conference (1958) 15/P/2230
- ⁹⁾ L. G. Schulz, J. Appl. Phys. **20** (1949) 1030
- ¹⁰⁾ A. N. Holden, Physical Metallurgy of Uranium (Addison-Wesley, USA, 1958) p. 39
- ¹¹⁾ B. R. Butcher, UKAEA Research Group Report, AERE R-3005 (1959)
- ¹²⁾ R. B. Kehoe, UKAEA Industrial Group Report, IGR TN/C 1073 (1959)
- ¹³⁾ W. P. Chernock, J. Singer, M. H. Mueller and P. Beck, J. Appl. Phys. **27** (1956) 1170
- ¹⁴⁾ G. Donze, Saclay (France) Report, CEA 1107 (1959)
- ¹⁵⁾ G. Slattery, private communication
- ¹⁶⁾ M. Hansen and K. Anderko, Constitution of Binary Alloys (New York, McGraw Hill, 1958) p. 359
- ¹⁷⁾ B. Blumenthal, given in Battelle Memorial Institute (USA) Report, BMI-1300 (1958) p. 19
- ¹⁸⁾ K. E. G. Meredith, private communication
- ¹⁹⁾ B. Blumenthal, given in Argonne National Laboratory (USA) Report ANL-5797 (1958) p. 47

CORROSION PAR L'HEXAFLUORURE D'URANIUM

Ière PARTIE

METHODE D'ETUDE DE LA CORROSION

J. DIXMIER, R. HASSON, S. MARAVAL et L. M. VINCENT

*Centre d'Etudes Nucléaires de Saclay, Gif-sur-Yvette (S & O), France,**Département de Physico-Chimie, Service des Etudes de Séparation des Isotopes de l'Uranium*

Reçu le 15 juin 1960

Les propriétés chimiques de l'hexafluorure d'uranium ont conduit à mettre au point des méthodes nouvelles pour étudier la corrosion des métaux par ce gaz. Les processus de corrosion sont caractérisés par les réactions entre une phase gazeuse anhydre et une phase solide, ce qui est comparable aux phénomènes d'oxydation sèche des métaux. Après une revue critique des principales méthodes de mesure utilisées dans ce domaine, les auteurs se sont arrêtés au principe de la méthode gravimétrique discontinue: Les éprouvettes sont pesées avant et après corrosion sous hexafluorure. Parallèlement des éprouvettes polies subissent des examens micrographiques.

La dimension des éprouvettes a été choisie de manière à se mettre dans les conditions optima pour les pesées à la micro-balance. Les modes de préparation et les états de surfaces sont soigneusement définis. La corrosion s'effectue dans des tubes en forme de H, entièrement métalliques, y compris les joints, raccords, sièges et clapets de vanne. L'étanchéité de l'appareillage permet d'effectuer de façon courante un dégazage préalable sous un vide de 10^{-6} mm de Hg, à des températures pouvant atteindre 400°C . Après dégazage, l'hexafluorure est introduit dans l'appareillage de corrosion, où il subit une triple distillation. Les tubes sont ensuite conservés en étuve. Chaque tube comporte à l'extrémité de l'une de ses branches un appendice de condensation, qui permet, grâce à un point froid, d'avoir une réserve d'hexafluorure solide et une pression gazeuse fixe.

Lorsqu'un tube est prélevé pour examen, il est à nouveau soumis à un pompage pour éliminer l'hexafluorure résiduel. Il est ensuite ouvert en boîte à gants, sous atmosphère inerte, puis les éprouvettes sont manipulées à l'abri de l'air, afin d'éviter l'altération des produits de corrosion. Les micro-pesées et les examens micrographiques sont effectués. Ces derniers portent sur la morphologie des dépôts; ils ont permis, entre autre, de mettre en évidence les divers sous-

fluorures d'uranium. Par élimination progressive des dépôts, les examens métallographiques révèlent des figures de corrosion. Celles-ci affectent fréquemment la forme de sillons aux joints de grains ou de micro-piqûres. L'évolution de leur profondeur est étudiée. Elle suit, en fonction du temps des lois d'allures paraboliques similaires aux courbes d'oxydation sèche. Les précautions prises pour la préparation des éprouvettes et la distillation de l'hexafluorure permettent une excellente reproductibilité des résultats. La sensibilité des micro-pesées permet d'évaluer la formation d'une monocouche de fluorure.

En conclusion, l'ensemble: méthode de corrosion + méthodes de mesures, a été choisi comme l'un des plus aisément adaptables à la technologie de l'hexafluorure d'uranium, tout en donnant une grande sensibilité, et en permettant d'effectuer des essais en série sur une vaste échelle. Cet ensemble s'adapte avec souplesse à l'étude de nombreuses variables, telles que temps, température, pression, etc.

The chemical properties of uranium hexafluoride have prompted the development of new methods for studying the corrosion of metals by this gas. The corrosion process is characterised by the reactions between an anhydrous gaseous phase and a solid phase, which is comparable to the dry oxidation of metals. After a critical review of the principal methods used in this field, the authors decided on the principle of discontinuous gravimetry: Samples are weighed before and after attack by hexafluoride. Polished samples, run simultaneously, are examined micrographically.

Specimen dimensions were chosen to achieve optimum conditions for microbalance weighing. Methods of preparation and surface condition of the specimens were carefully defined. Corrosion was effected in H-shaped tubes; the tubes, including joints,

unions, seats and butterfly valves, were entirely made of metal. The apparatus was sufficiently vacuum-tight to permit routine degassing under a vacuum of 10^{-6} mm of mercury, at temperatures up to 400°C . After degassing, hexafluoride is introduced into the apparatus and triple-distilled, and the tube is then kept warm. Each tube incorporates at the end of one of its legs a condensing attachment which, with the help of local cooling, permits a reservoir of solid hexafluoride to be maintained, with consequent constancy of gas pressure.

When a tube is removed for examination, it is again pumped out to remove residual hexafluoride. It is opened in an inert atmosphere in a glove-box and the specimens manipulated out of contact with air, to avoid alteration of the corrosion products. Micro-weighing and micrographic examination are carried out; the latter have a bearing on the morphology of the deposits, and have made possible, inter alia, demonstrations of the presence of the various uranium subfluorides. Progressive elimination of the deposits revealed etch pits, which often affected the shape of grain boundary grooves or micro-pits. Their growth in depth was found to follow parabolic time-laws similar to those characteristic of dry oxydation curves. The precautions taken in preparing specimens and distilling the hexafluoride resulted in excellent reproducibility of the results. The sensitivity of the microbalance was sufficient to follow the formation of a fluoride monolayer.

The ensemble of corrosion apparatus and methods of measurement was selected as being one of the most easily adaptable to the technology of uranium hexafluoride, in that it gave great sensitivity and allowed serial experimentation on a vast scale. The ensemble is readily adapted to the study of numerous variables, such as time, temperature, pressure, etc.

Die chemischen Eigenschaften von UF_6 haben dazu geführt, zum Studium der Korrosion von Metallen durch dieses Gas neue Methoden anzuwenden. Die Korrosionsvorgänge sind durch Reaktionen zwischen einer wasserfreien Gasphase und einer festen Phase gekennzeichnet. Sie gleichen somit den Erscheinungen bei der trockenen Oxydation. Nach einer kritischen Durchsicht der hauptsächlich in diesem Bereich gebräuchlichen Messverfahren haben sich die Verfasser im Prinzip auf die gravimetrische, diskontinuierliche Methode geeinigt. Dabei werden die Proben vor und nach der Korrosion unter UF_6 gewogen. In Parallelversuchen werden polierte Proben einer mikroskopischen Untersuchung unterzogen.

Die Probenabmessungen wurden so gewählt, dass beim Wägen auf der Mikrowaage optimale Bedingungen herrschten. Die Art der Vorbereitung und der Zustand der Oberflächen wurde sorgfältig festgelegt. Die Korrosion läuft in einem H-förmigen Reaktionsrohr ab, welches, einschliesslich Verbindungen, Übergangsstücken, Ventilsitzen und Ventilkappen, ganz aus Metall hergestellt ist. Die Dichtheit der Apparatur ermöglicht es, eine vorherige Entgasung unter einem Vakuum von 10^{-6} mm Hg bei Temperaturen bis 400°C vorzunehmen. Nach der Entgasung wird Hexafluorid in die Korrosionsapparatur eingelassen und dort einer dreifachen Destillation unterzogen. Die Rohre werden sodann in einem Heizbehälter aufbewahrt. Jedes Reaktionsrohr trägt am Ende eines seiner Schenkel einen Ansatz zur Kondensation. Dadurch ist es mit Hilfe einer gekühlten Stelle möglich, einen Vorrat an festem UF_6 aufrecht zu erhalten und einen konstanten Gasdruck einzustellen.

Zur Untersuchung wird jedes Reaktionsrohr herausgenommen und nochmals ausgepumpt, um restliches Hexafluorid zu entfernen. Dann wird es in einer Glove-Box unter inerter Atmosphäre geöffnet. Die Handhabung der Proben geschieht unter Luftabschluss, damit jegliche Veränderung der Korrosionsprodukte vermieden wird. Es werden Mikrowägungen und mikroskopische Untersuchungen vorgenommen. Diese tragen bei zur Kenntnis der Morphologie der Ablagerungen. Unter anderem erlaubten sie, die verschiedenen Uransubfluoride sichtbar zu machen. Durch schrittweises Abtragen der Ablagerungen werden bei der mikroskopischen Untersuchung die Korrosionserscheinungen aufgedeckt.

Diese betreffen häufig die Form der Vertiefung an Korngrenzen und Mikroanfressungen. Das Anwachsen ihrer Tiefe wurde untersucht. Es gehorcht einem parabolischen Zeitgesetz entsprechend den Kurven bei trockener Oxydation. Die getroffenen Vorsichtsmassnahmen bei der Probenvorbereitung und Destillation von UF_6 ermöglichen eine ausgezeichnete Reproduzierbarkeit der Ergebnisse. Die Empfindlichkeit der Mikrowägungen ermöglicht sogar die Bestimmung einmolekularer Fluoridschichten.

Zusammenfassend lässt sich sagen, dass eine der am einfachsten der Technologie von Uranhexafluorid anzupassenden Korrosions- und Messmethoden ausgewählt wurde. Diese ergibt eine grosse Genauigkeit und erlaubt, weitreichende Serienversuche durchzuführen. Dabei lässt sich ohne Schwierigkeiten der Einfluss zahlreicher Variablen, wie Zeit, Temperatur, Druck u.a. untersuchen.

Cette publication a pour objet de passer en revue l'ensemble des méthodes que nous avons été amenés à sélectionner et à développer depuis plusieurs années pour l'étude des problèmes de corrosion posés par l'hexafluorure d'uranium. Des études critiques sur certaines de ces méthodes seront publiées ultérieurement et elles seront alors mieux précisées.

1. Introduction

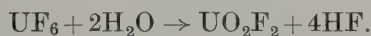
Il est bien connu que l'hexafluorure est le seul composé de l'uranium pratiquement utilisé pour la séparation isotopique par diffusion gazeuse, en raison de ses propriétés physiques. Quant à ses propriétés chimiques, elles sont particulières et dominent toute la technologie de construction d'une usine de diffusion.

Rappelons brièvement quelques propriétés de l'hexafluorure d'uranium, l'"Hex" pour ses familiers.

1) Il livre facilement une partie de ses atomes de fluor pour se décomposer en une famille de sous-fluorures: α et β UF_5 , U_2F_9 , U_4F_{17} , UF_4 ... (figs. 1 et 2) qui eux, restent à l'état solide jusqu'à leur point de décomposition.

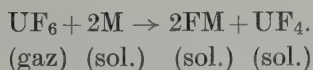
2) Il réagit énergiquement avec la presque totalité des corps organiques, solvants, graisses, vernis, élastomères et plastiques.

3) Il se décompose immédiatement en présence d'eau pour donner de l'acide fluorhydrique et du fluorure d'uranyle solide suivant la réaction:



4) Il réagit enfin avec tous les métaux dès la température ambiante pour donner les fluorures métalliques correspondants.

Différents schémas de réactions sont possibles. Par exemple:



Sauf quelques cas exceptionnels les fluorures métalliques formés sont solides dans ces conditions. Les sous-fluorures d'uranium l'étant

également, il s'ensuit que tout phénomène de corrosion se traduit:

- a) par une disparition de phase gazeuse;
- b) par une attaque du métal qui se couvre de dépôts solides formés des produits de corrosion proprement dits et des sous-fluorures d'uranium.

Signalons en outre que tous ces sous-fluorures sont extrêmement peu solubles dans l'eau ou



Fig. 1. Aiguilles vertes d' UF_4 . $\times 49$.

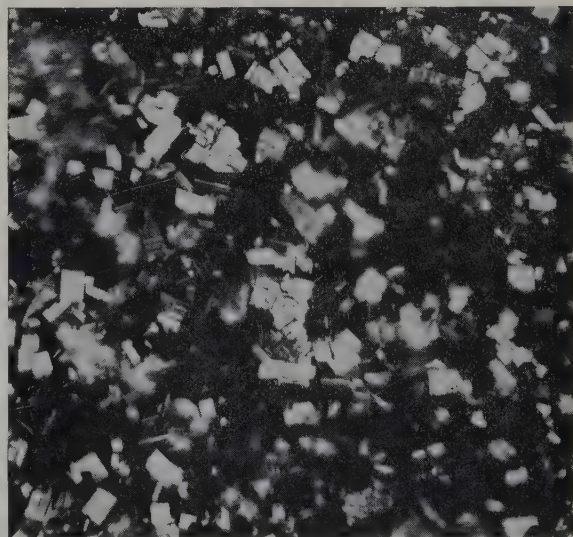


Fig. 2. Croûte de corrosion composée de cristaux d' α UF_5 noyés dans une matrice d' U_2F_9 . $\times 384$.

bien réagissent plus ou moins rapidement avec elle en se décomposant. Par exemple :



Quant au fluorure d'uranyle, il est soluble dans l'eau et le méthanol. Ces différentes propriétés ont pour conséquence de rendre impraticable la plupart des solutions utilisées classiquement en génie chimique ou en construction mécanique. La totalité des circuits de l'usine doit être débarrassée de toutes traces de vapeur d'eau, et maintenue à un haut degré d'étanchéité. Tout ce qui est graisse ou huile doit généralement être proscrit, ce qui pose des problèmes ardues pour toutes les pièces tournantes ou traversées étanches sous UF_6 . Les matériaux usuellement utilisés pour les joints de bride, raccords, sièges ou clapets, isolants thermiques ou électriques sont inutilisables sous UF_6 .

Enfin, aucune peinture ou vernis connu n'est susceptible de protéger utilement les pièces métalliques ou les parois en contact avec l'"Hex". Bien au contraire, l'attaque rapide des produits organiques se traduit le plus fréquemment par une décomposition active de UF_6 et formation de HF.

Dans une usine de diffusion, les surfaces de parois, (tuyauterie, échangeurs, etc.) se chiffrent par dizaines d'hectares, auxquels doivent être ajoutées les très grandes surfaces des diaphragmes poreux où s'effectue la diffusion proprement dite.

On conçoit l'importance dans ces conditions des phénomènes de corrosion et l'obligation de fixer celle-ci à un taux extrêmement bas, de l'ordre de 10 à 1000 fois plus faible que ceux rencontrés habituellement dans l'industrie. Faute de quoi, outre la perte de rendement occasionnée par la disparition d'une fraction importante de la phase gazeuse, le fonctionnement des cascades de diffusion serait gravement perturbé tant par l'obstruction des diaphragmes causée par les produits de corrosion que par les accidents mécaniques que peuvent causer ces dépôts et éventuellement la corrosion du métal lui-même.

2. Choix des méthodes d'étude de la corrosion

Cette microcorrosion est donc une réaction entre phases solide-gaz avec interposition à l'interface des produits formés. Le gaz corrosif doit être anhydre, puisque toute trace de vapeur d'eau réagit avec lui. On peut également considérer que l'eau fixée sur les parois est rapidement éliminée dans ces conditions. Actuellement, aucun fait expérimental ne s'inscrit en faux contre cette hypothèse, qui reste la plus vraisemblable. Nous envisageons de présenter ultérieurement une étude plus détaillée de cette question.

Cela exclut les corrosions de type électrochimique classique, du moins en ce qui concerne l' UF_6 , car bien entendu une réalisation aussi complexe qu'une usine de diffusion gazeuse pose également des problèmes de corrosion de différente nature. Ces problèmes, qui sont d'ailleurs d'importance secondaire vis à vis de UF_6 , sont en dehors du cadre de cette étude et nous ne les aborderons pas ici.

La corrosion par UF_6 est donc une corrosion chimique dont le déroulement a une proche parenté avec l'oxydation sèche des métaux ^{1,12,13}). Tout naturellement nous avons été guidés dans le choix de nos méthodes par les travaux effectués dans ce domaine.

Ce choix a été déterminé bien entendu en tenant compte des propriétés de UF_6 , mais aussi pour répondre à la nécessité d'effectuer un très grand nombre d'essais et d'explorer commodément différentes variables. Nous allons effectuer une rapide revue critique des différentes méthodes qui s'offraient à nous.

2.1. PARTICULARITÉS DUES À L'HEXAFLUORURE D'URANIUM

Il y a lieu de distinguer les mesures de la corrosion des méthodes de mise en corrosion proprement dite. Si les premières peuvent s'apparenter à des techniques classiques, les autres ont dû être entièrement élaborées pour tenir compte des propriétés que nous avons rappelées plus haut. Elles exigent notamment l'utilisation d'appareils rigoureusement étanches aux vides poussés permettant un dégazage

TABLEAU I
Pénétration de la corrosion

	Vitesse en mm/heure	10 ⁻³	10 ⁻⁴	10 ⁻⁵	10 ⁻⁶	10 ⁻⁷	10 ⁻⁸
Corrosions industrielles	Acier Inox. (d'après Colombier ²⁰))	Mauvais	Bon	Très bon			
	Acier Inox. (d'après Uhlig ²¹))	Mauvais		Bon	Très bon		
	Alliages de Ni (d'après Arbellot ²³))	Mauvais	Médiocre	Bon			
UF ₆		Mauvais			Médiocre		Bon

efficace des matériaux utilisés avant l'introduction de gaz corrosif. Il faut tenir compte également du fait que l'UF₆ réagit non seulement sur les éprouvettes expérimentées, mais aussi sur la totalité de l'appareillage utilisé pour les essais de corrosion.

2.2. MESURES DE CORROSION

Les méthodes de mesure choisies devaient être compatibles avec les conditions de mise en

corrosion. D'autre part elles devaient offrir une sensibilité suffisante pour permettre une étude du taux de corrosion extrêmement faible défini par les impératifs des procédés. Afin de situer le problème, le tableau ci-dessus permet de comparer les ordres de grandeur de corrosions usuellement rencontrées dans l'industrie ^{20,21}) et ceux que nous avons été amenés à définir.

Rappelons cependant que la comparaison des vitesses de corrosion n'est valable que pour des

Mesures concernant:	Méthodes
I. La méthode seule	<ol style="list-style-type: none"> Méthode gravimétrique <ul style="list-style-type: none"> Pesée discontinue { éprouvette débarassée des dépôts de corrosion (perte de poids) Observation des figures de corrosion (forme, densité, répartition, profondeur) Perte des propriétés mécaniques Variations des propriétés électriques
II. Le métal + le dépôt	<ol style="list-style-type: none"> Méthodes gravimétriques (gains de poids) <ul style="list-style-type: none"> a) pesée discontinue { avant } corrosion { après } b) pesée continue { thermobalance microbalance Gulbransen balance à ressort Mesure d'épaisseur du dépôt Mesures réflectométriques
III. Le dépôt	<ol style="list-style-type: none"> Dosages chimiques Mesure des rayonnements (comptage) Dissolution électrolytique
IV. La phase gazeuse	<ol style="list-style-type: none"> Mesures manométriques Analyse quantitative { discontinue continue

lois linéaires et que la comparaison des courbes est seule correcte dans les autres cas.

Le tableau ci-dessus rappelle les principales méthodes de mesures utilisables *a priori* ³⁾.

Il convient d'ajouter à ce tableau les méthodes d'examen qui ne constituent pas des mesures quantitatives de la corrosion (ou qui constituent des mesures indirectes, telles que l'examen micrographique des dépôts de corrosion, la diffraction des rayons X, la diffraction électronique, ces différentes méthodes étant surtout destinées à déterminer les mécanismes de corrosion et les structures des dépôts).

2.3. MÉTHODES DE MESURES CONTINUES

a) *Thermobalances*

Malgré l'intérêt de suivre en continu l'évolution de la corrosion, les méthodes de mesures en continu présentent de sérieux inconvénients. En effet, les méthodes gravimétriques continues ainsi que les mesures manométriques conduisent à effectuer les mesures dans l'appareillage de corrosion. Aussi ne permettent-elles de traiter qu'un petit nombre d'échantillons à moins de disposer d'un nombre important d'appareils. Elles se prêtent donc plus difficilement à l'exploration de variables autres que le temps.

La nécessité d'obtenir un vide poussé amène des difficultés dans l'emploi des thermobalances, celles-ci devant être placées dans l'enceinte expérimentale. Mais alors elles sont ensuite soumises au fluide corrosif. Ceci conduit à des difficultés de réalisation très importantes. La balance à ressort spirale en quartz utilisée par Leontis et Rhines ³⁾ est plus utilisable. Toutefois, elle manque de sensibilité et l'on est conduit à réduire la charge en utilisant des matériaux de grande surface telle que des feuilles métalliques finement laminées. Ceci limite les conditions de nature et d'états des métaux à expérimenter et restreint, malgré leur intérêt, l'emploi de ces balances à quelques cas spéciaux.

La microbalance du type Gulbransen ¹⁾ est mieux adaptable et plus sensible mais elle garde l'inconvénient du dispositif de mesure en contact avec UF_6 et celui de ne pouvoir traiter qu'un seul échantillon à la fois.

b) *Mesures manométriques*

Les mêmes inconvénients pratiques se rencontrent pour les méthodes de mesures manométriques: difficultés de traiter simultanément un nombre important d'échantillons, réaction de UF_6 avec les appareils du même ordre de grandeur qu'avec les éprouvettes, etc. A cela s'ajoute les difficultés d'interprétation des mesures manométriques du fait de la complexité des réactions et des phénomènes d'absorption sur les parois.

c) *Résistance électrique*

Une dernière méthode continue consiste à mesurer la variation de résistance électrique d'un fil du métal étudié ²⁾. Elle présente, mais à un moindre degré car l'appareillage est plus simple, les inconvénients précédents par manque de souplesse et limitation à des échantillons pouvant être étudiés sous forme de fil ou de ruban. Nous avons cependant utilisé les deux dernières méthodes, à titre complémentaire: la méthode manométrique pour effectuer certains recoupements: la méthode électrique pour étudier les corrosions à température élevée (400 à 1000°).

2.4. MÉTHODES DE MESURES DISCONTINUES

Dans ces méthodes les éprouvettes sont soumises à la corrosion, puis retirées du fluide corrosif pour être examinées.

a) *Mesures des caractéristiques mécaniques*

Nous avons abandonné celles qui évaluent les pertes de propriétés mécaniques (traction, flexion, etc.). Nous verrons plus loin que les attaques sont beaucoup trop faibles pour la sensibilité de ces méthodes ⁴⁾.

b) *Comptage*

La radioactivité de l'uranium semblait une propriété de choix pour la mesure des dépôts de décomposition. En fait, nous avons abandonné cette méthode en raison des délais de plusieurs mois nécessités par la mise en équilibre de la radioactivité existant après corrosion.

c) *Mesure des figures de corrosion*

Pour la même raison que plus haut, les mesures de perte d'épaisseur, de profondeur des piqures ("pitting") au moyen de sphéromètres, comparateurs ou aiguilles^{2,4)} ne sont pas utilisables. Les mesures par différences de profondeur de champs, coupes droites ou biaisées sont utilisables seulement dans des cas extrêmes de corrosion très importante (à cette échelle). Diverses considérations d'ordre pratiques (trop faible sensibilité, manque de généralité, effets perturbateurs divers) nous ont conduits à éliminer les mesures au moyen d'un rugosimètre ou les mesures interférentielles.

d) *Centres de corrosion*

Le comptage des centres de corrosion, densité des piqures, des taches, etc., n'est pas applicable d'une manière générale; en effet une forme d'attaque rencontrée fréquemment est la formation de sillons aux joints de grains. D'autre part, de tels procédés peuvent permettre la comparaison entre des matériaux différents, mais se prêtent mal à l'étude cinétique des phénomènes

e) *Dissolution électrochimique des dépôts*

Ces méthodes qui visent à mesurer l'épaisseur des couches de corrosion ont fait l'objet de nombreux travaux^{10,11,14-17)}. Elles se ramènent principalement à deux types principaux:

Réduction cathodique

La mesure est basée sur le nombre de coulombs nécessaires pour réduire la couche des produits de corrosion, la fin de la dissolution étant indiquée par une diminution de l'intensité. Il est indispensable dans ce cas, que les autres processus de réduction correspondent à des potentiels plus négatifs.

Dissolution électrochimique

On mesure le temps de dissolution de la couche de corrosion en suivant la variation du potentiel de dissolution sans appliquer un courant à l'électrode. Cette méthode n'est valable que si le potentiel du métal sous-jacent est plus noble. Une variante consiste à déter-

miner le nombre de coulombs nécessaire à la dissolution de la couche de corrosion sous courant appliqué. La fin de l'opération est appréciée par la variation du potentiel de dissolution.

Dans le cas d'électrolyse, étant donné la minceur des couches de corrosion, il est indispensable d'avoir des intensités de courant très faibles pour que les temps mesurés demeurent suffisamment longs. Ces méthodes sont susceptibles, en choisissant judicieusement les conditions de mesures d'être non seulement quantitatives, mais aussi spécifiques de la nature des dépôts. Nous en avons entrepris l'application, mais elles nécessitent pour chaque nouvelle étude de corrosion des mises au point susceptibles d'être longues et délicates. Leur étude est en cours.

f) *Dosages chimiques*

La méthode chimique présente un grand intérêt théorique. Cependant elle est d'une application très délicate. En effet, un simple dosage d'uranium et de fluor est insuffisant et demande cependant un nombre d'heures de travail important. A cette échelle, et à cause du milieu défavorable, tout travail de série est exclu. Si de plus, on demande de distinguer les différentes valences de l'uranium et les fluorures métalliques formés sans attaque du métal sous-jacent, et ceci pour un grand nombre de métaux ou alliages, on est très vite conduit à un nombre d'échantillons considérable et à des délais déraisonnables. Cependant il est nécessaire d'insister sur l'intérêt de telles méthodes non pas pour l'exploration des variables qui dirigent l'évolution de la corrosion mais pour la compréhension des phénomènes dans des cas bien définis.

2.5. MÉTHODES PHYSIQUES

Les diagrammes de rayons X et la diffraction électronique sont aussi utilisés comme méthode d'appoint pour l'étude de la structure et de la nature des couches.

La mesure du pouvoir réfléchissant est d'une grande commodité d'emploi, mais elle n'est

utilisable que pour certains cas limités de ternissement des surfaces. Elle n'est plus applicable lorsque les éprouvettes sont entièrement recouvertes de dépôts de fluorures. C'est donc aussi une méthode d'appoint. Elle est cependant intéressante pour l'étude des débuts de corrosion.

En citant les méthodes de corrosion que nous avons été conduits à éliminer ou à conserver comme méthodes auxiliaires, nous ne prétendons pas avoir fait un travail bien exhaustif. Bien entendu, d'autres méthodes sont possibles, et certaines des méthodes éliminées sont applicables dans des cas particuliers. Mais il est indispensable de se souvenir que la ou les méthodes retenues devaient permettre d'explorer avec précision de nombreux paramètres et d'effectuer un très grand nombre d'essais dans des conditions d'économie et de délais raisonnables. De plus un examen, même superficiel de ces problèmes montre que pour obtenir une grande quantité de résultats dans des conditions strictement définies et avec la haute sensibilité nécessaire il faut un appareillage dont les caractéristiques deviennent vite contradictoires. Cela n'a pas été la moindre des limites imposées à notre choix. *C'est pourquoi en définitive nous avons retenu comme méthode de base :*

La corrosion en appareillage séparé.

La pesée avant et après corrosion, d'abord en gain de poids, puis en perte de poids avec élimination des dépôts de corrosion.

Les examens micrographiques des dépôts de corrosion.

Les examens métallographiques avant et après corrosion, les dépôts étant éliminés progressivement.

3. Description des méthodes

3.1. PRÉPARATION DES ÉPROUVETTES

a) *Forme et dimension*

En l'absence de phénomène électrolytique, les effets de pointe se montrent sans influence. Nous avons choisi pour les éprouvettes la forme de plaquettes carrées (fig. 3) qui se prête bien à un usinage précis dans des matériaux très

divers. L'épaisseur de 2 mm est l'épaisseur minimum pratique pour le polissage des éprouvettes métallographiques. La dimension de 20×20 mm donne une surface de contact totale de $9,66 \text{ cm}^2$ et même dans le cas de métaux aussi denses que le platine, le poids des éprouvettes n'excède pas la charge d'une microbalance.

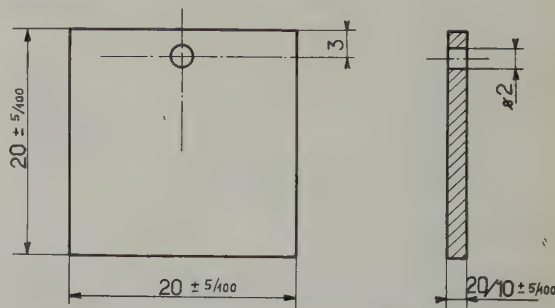


Fig. 3. Eprouvette de corrosion.

b) *Usinage et tolérances*

Bien entendu, les précautions classiques sont prises pour le découpage des éprouvettes, en vue d'éviter les modifications de structure ou de propriétés des métaux.

Les tolérances d'usinage ont été fixées pour les cas usuels à $\pm 5/100$.

Cette valeur permet la préparation en série d'un nombre élevé d'échantillons, tout en admettant une erreur possible maximum de 2,38 % sur la surface (tableau 2). Bien entendu, pour certains essais, la précision peut être poussée beaucoup plus loin.

TABLEAU 2

Variation tridimensionnelle $\Delta L(\text{cm})$	Tolérance d'usinage correspondante (mm)	Variation de surface totale
0,01	$\pm 0,05$	2,38
0,02	$\pm 0,1$	4,80
0,05	$\pm 0,25$	11,97
0,1	$\pm 0,5$	—

Dans tous les cas particuliers où il n'est pas possible d'utiliser des éprouvettes rigoureusement normalisées, celles-ci sont mesurées au comparateur. Des abaques permettent le calcul

des surfaces réelles et des limites d'erreur. Les éprouvettes normalisées sont vérifiées par les méthodes de métrologies usuelles en construction mécanique (calibre, comparateurs, glace interférentielle, etc.).

c) *Etat de surface*

Les éprouvettes préparées pour la pesée sont uniformément abrasées au papier émeri (grain 320). Ceci permet d'obtenir un état de surface standard reproductible en éliminant la surface originelle plus ou moins contrôlée, les écailles de calamine, etc. La microgéométrie correspond aux rayures d'un usinage fin: les sillons ont environ 2 à 3 μ de profondeur et 8,5 μ de large.

Les éprouvettes destinées aux examens métallographiques sont polies jusqu'à l'alumine 24 heures, à la pâte diamantée ou à la magnésie selon la dureté du métal⁵⁾.

En raison de la très grande variété de métaux que nous avons été amenés à étudier et du fait que les échantillons doivent être rigoureusement exempts de micropiqûres et de toute autre trace d'attaque, nous n'avons pas utilisé, malgré ses avantages, le polissage électrolytique.

Il s'agit là bien entendu de la préparation d'états de surfaces standard, le polissage électrolytique étant employé éventuellement pour certains essais où la présence d'un léger derme écroui risque de perturber les essais.

d) *Marquage*

La méthode idéale consiste à éviter tout marquage et à repérer uniquement les éprouvettes par leur emplacement. En raison du nombre important de plaquettes manipulées quotidiennement au laboratoire, les risques de confusion seraient cependant importants et nous avons préféré supporter l'inconvénient d'un marquage.

Celui-ci est effectué au stencylographe; la hauteur des chiffres n'excède pas un m/m et le tracé est très léger. Ceci limite la perturbation de la surface à une fraction très petite de la totalité de l'éprouvette (0,3 % environ). Le système d'immatriculation permet le repérage individuel des éprouvettes et l'identification de

l'échantillon dans lequel elles ont été découpées. Cette précaution s'est révélée importante en cas de résultats divergents.

e) *Dégraissage et manipulation*

Les éprouvettes sont ensuite dégraissées au soxhlet par le benzène pur, puis rincées avec de l'acétone, qualité pour analyses. Les solvants chlorés ont été éliminés en raison des risques de micropiqûres.

Toutes les éprouvettes sont manipulées avec des gants de nylon et des pinces brucelles. Sitôt après dégraissage, elles sont placées dans un dessiccateur, sous atmosphère inerte pour conserver leur surface fraîchement abrasée et diminuer les risques d'oxydation ultérieure.

f) *Pesées*

Les micropesées sont effectuées en salle à atmosphère conditionnée, sur des éprouvettes en équilibre de température. Les éprouvettes sont pesées sous atmosphère inerte. Les pesées préparatoires sont effectuées sur une balance automatique au 1/10 de mg.

Les dimensions choisies pour les éprouvettes permettent l'étude des couches de corrosion avec une sensibilité optimum. Les pesées sont effectuées avec une sensibilité de 4 microgrammes. Pour une éprouvette recouverte de façon uniforme de tétrafluorure d'uranium, de densité 6,73, un poids de 4 microgrammes correspond à une couche de:

$$4 \times 10^{-6} / 6.73 \times 9,66 \text{ cm} = 6.8 \text{ \AA}.$$

On voit que la limite théorique de sensibilité de cette détermination est de l'ordre d'une couche monomoléculaire, puisque les paramètres cristallographiques de UF_4 sont: $a = 10,4$, $b = 10,8$, $c = 8,39 \text{ \AA}$.

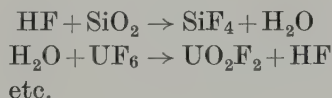
3.2. APPAREIL DE CORROSION

La corrosion sous UF_6 s'effectue par tubes laboratoire connectés à une "rampe". Les rampes que nous utilisons peuvent recevoir dix tubes à corrosion. L'une des extrémités de la rampe est reliée à un groupe de pompage comprenant pompe à palettes à double étage.

et pompe à diffusion d'huile, jauges, piège à azote liquide, vannes, sécurités diverses. L'autre extrémité est connectée à un générateur d' UF_6 .

Lors de nos tout premiers essais, nous nous étions adressés à un appareillage en verre. L'étanchéité des rodages était assurée par des cires chlorofluorées sélectionnées après divers essais malheureux sur des graisses à vide classiques. Ces cires nécessitaient l'emploi de nombreux sèche-cheveux au laboratoire pour la manœuvre des robinets. Cette cire chlorofluorée même après avoir fait l'objet de plusieurs fractionnements réagissait encore trop avec l' UF_6 ; il a été montré qu'il s'agissait d'une réaction photo-chimique. Les cires et leurs produits de réaction doués d'une tension de vapeur notable allaient former sur les éprouvettes un "voile blanc" qui perturbait les essais et rendait toute micro-pesée impossible.

La présence de ces cires, fusibles entre 60 et 80°C, s'opposait en outre à un dégazage préalable à température suffisamment élevée. En dernier lieu, on pouvait craindre une réaction cyclique avec la silice, du type:



Ces raisons nous ont conduit, après divers essais, à la réalisation d'un appareillage de corrosion, d'où toute matière organique telles que caoutchouc synthétique, téflon, kel-F, etc.; et évidemment les graisses sont exclues⁶⁾. L'appareillage est entièrement métallique y compris les joints, raccords, sièges et clapets de vanne, etc. Ceci a pu être réalisé en collaboration avec les services techniques du département de physico-chimie. Le succès d'un tel appareillage tient en grande partie à la mise au point par le service d'une vanne étanche, à grande voie de pompage, entièrement métallique, parfaitement dégazable et cependant très maniable en laboratoire^{7,8)}. Toutes les canalisations sont de large section. L'ensemble possède une conductance élevée⁹⁾.

Le principe de l'appareillage reste essentiellement le même que dans le modèle primitif.

I. La rampe (figs. 4, 5, 6) est connectée au groupe de pompage par l'intermédiaire d'un piège à azote liquide, empêchant le "back streaming". L'autre extrémité de la rampe est connectée au générateur à travers un réservoir intermédiaire.

Les tubes à corrosion (fig. 7) affectent la forme d'un H dont l'une des branches est prolongée par un appendice de condensation.

L'ensemble, excepté le générateur d'hex est placé dans l'enceinte d'un four à circulation d'air chaud, pouvant atteindre 400°C. La température est réglée par pyromètres à couples.

Le générateur d' UF_6 est enfermé dans une étuve thermostatée thermiquement indépendante.

Les tubes à corrosion sont garnis de leurs éprouvettes, suspendues à un support par de

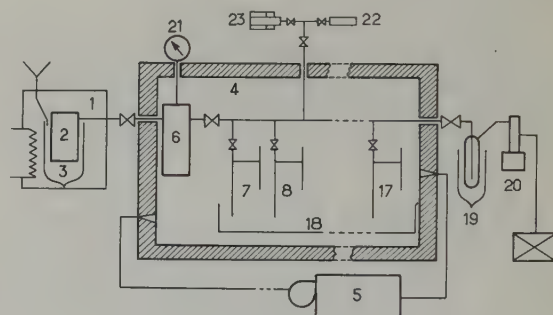


Fig. 4

- 1. Etuve
- 2. Réservoir d'hexafluorure
- 3. Vase Dewar
- 4. Four
- 5. Batterie chauffante
- 6. Réservoir intermédiaire

- 7-17. Tubes à corrosion
- 18. Bac à circulation de saumure
- 19. Piège froid
- 20. Pompe à diffusion
- 21. Manomètre
- 22-23. Jauges

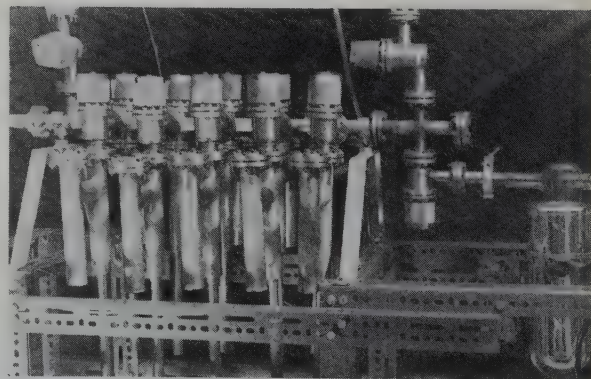


Fig. 5. Rampe à corrosion (élément principal).

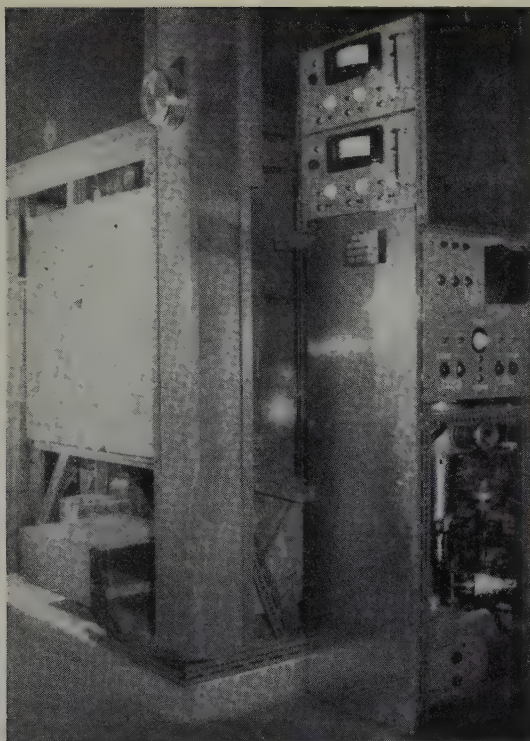
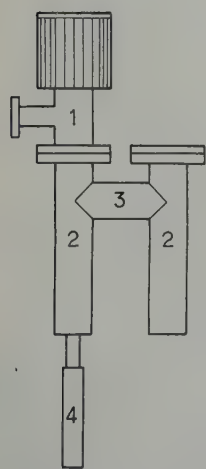


Fig. 6. Rampe à corrosion. Ensemble complet avec four, régulation et groupe de pompage.



- 1. Vanne entièrement métallique
- 2. Tubes laboratoires
- 3. Branche de raccordement
- 4. Appendice de piègeage

Fig. 7

petits crochets en nickel (fig. 9). La surface de contact entre arêtes et génératrices peut être négligée. En l'absence de corrosions électrolytiques, la suspension par un crochet métallique ne présente pas d'inconvénients évidents *a priori*. L'expérience n'a pas infirmé ce point de

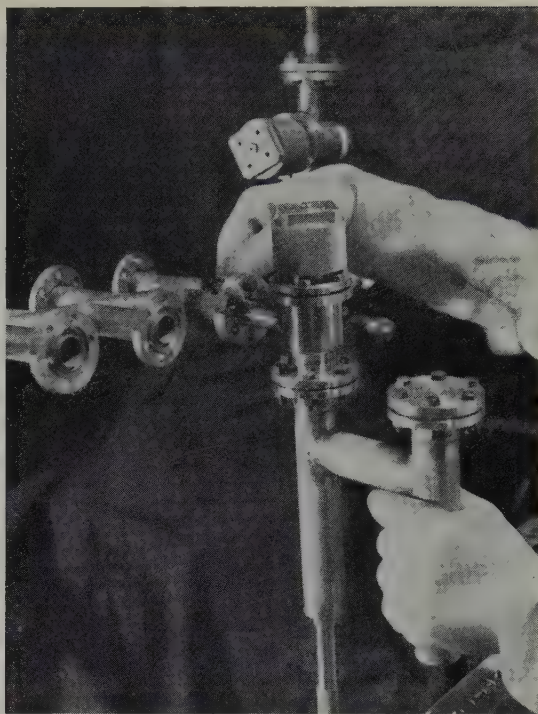


Fig. 8. Tube à corrosion.

vue. Nous n'avons jamais rencontré d'attaque préférentielle au voisinage des contacts des supports, non plus que d'effet de pointe au bord des éprouvettes. L'emploi d'isolants tels que le téflon aurait par contre présenté des inconvénients certains dus au dégazage de ces matériaux et de la limitation de température.

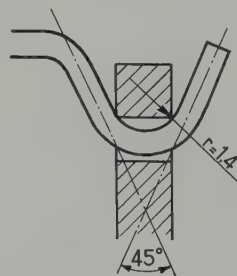


Fig. 9

3.3. MISE EN ROUTE DES ESSAIS DE CORROSION SOUS UF_6

Le choix des éprouvettes à placer dans le tube n'est pas indifférent. Il est important de ne mettre dans un tube que des matériaux d'un comportement à la corrosion voisin ou de

propriétés chimiques ou physiques voisines. Sinon, on risquerait, comme le signale Akimov, d'avoir de l'interaction au lieu d'obtenir l'identité de conditions d'essai recherchée.

Les éprouvettes doivent être réparties dans les tubes de manière à assurer l'homogénéité des conditions. L'opération s'effectue de la façon suivante: après montage des tubes à corrosion sur la rampe, l'étanchéité de l'ensemble est contrôlée au spectrographe de masse à hélium et les assemblages réglés jusqu'à obtenir un taux de fuite inférieur à 10^{-5} lusec.

Le dégazage est effectué par obtention préalable d'un vide "dynamique" stable compris entre 10^{-5} et 10^{-6} torr en fin d'appareil, puis chauffage progressif de l'ensemble jusqu'à la température choisie afin d'éviter l'oxydation des échantillons.

La température de dégazage est la température maximum compatible avec la nature des métaux essayés et leur histoire mécanique et thermique. Le vide est contrôlé par jauges Pirani et Penning. On considère que le dégazage est pratiquement terminé lorsque l'on obtient à l'extrémité de l'appareil opposée aux pompes, un vide stable pendant plusieurs dizaines d'heures à la plus haute température possible.

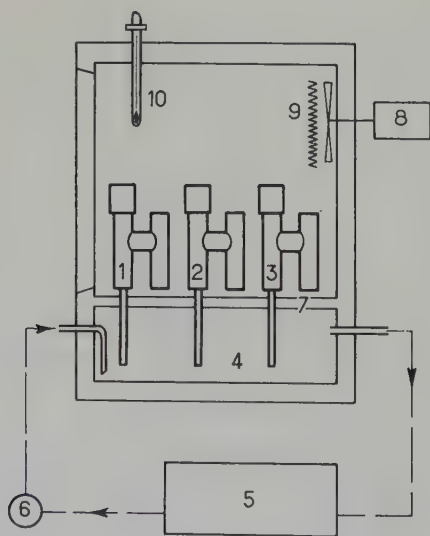


Fig. 10

Etuves Bithermes

1-2-3. Tubes à corrosion

4 Bac à circulation froide

5. Groupe réfrigérant

6. Pompe à circulation

7. Diaphragme

8-9. Circulation d'air chaud

10. Régulateur

La pression doit alors être inférieure à 10^{-4} torr, l'étanchéité préalable ayant été contrôlée à nouveau par remontées de pression.

L'appareillage est alors refroidi et l'hexafluorure introduit. L'opération continue en éliminant par pompage et piégeage annexe, l'hexafluorure gazeux du générateur, les vannes de communication entre rampe et tubes restant fermées.

En effet, malgré l'utilisation d'un UF_6 particulièrement purifié, cette partie risque d'être souillée par la réaction de UF_6 sur son réservoir. La quantité d' UF_6 nécessaire à l'essai est ensuite sublimée dans le réservoir intermédiaire où il se recondense. Le générateur est alors isolé et la totalité du contenu du réservoir intermédiaire est remise en phase gazeuse.

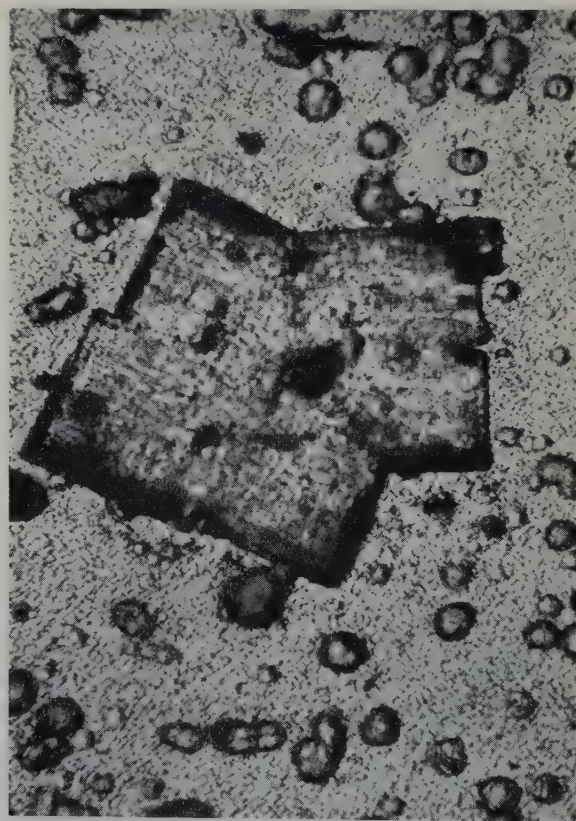


Fig. 11. Cristaux en cours de pseudomorphose. Cristal d'aspect cubique centré sur une inclusion. La transformation commence à partir du centre. U_2F_9 noir donne UF_4 vert. (Cristal déposé sur une matrice microglobulaire d' UO_2F_2 . $\times 384$.)

Entre temps, les appendices de condensation des tubes à corrosion ont été refroidis dans un bain à circulation de saumure jusqu'à être tous parfaitement à la même température. Les vannes des tubes sont alors ouvertes et UF_6 gazeux vient se condenser de façon homogène dans tous les tubes de la rampe. Chaque tube reçoit ainsi un fluide corrosif rigoureusement égal en qualité et en quantité (cela est contrôlé ultérieurement). L'opération (contrôlée par un capteur de pression) une fois terminée, les tubes sont fermés, l'hex résiduel est évacué dans le piège. Les tubes sont démontés et prêts pour la conservation.

3.4. MISE EN CORROSION

La mise en corrosion s'effectue en installant les tubes dans des étuves spéciales bithermes (fig. 10). Les corps des tubes restent dans l'étuve à circulation d'air chaud proprement dit, cependant que les appendices de condensation plongent dans la partie inférieure formant point froid thermostaté. Ce dispositif possède des avantages importants qui sont les suivants:

L'appendice peut contenir une réserve d' UF_6 amplement suffisante même pour des essais de très longue durée, sans qu'il y ait risque d'appauvrissement de la phase gazeuse. Ceci élimine ainsi l'influence des parois sur la consommation du gaz corrosif. D'autre part, les conditions de pression sont rendues indépendantes de la température de corrosion. Il est ainsi possible, lors d'essais systématiques, de ne faire varier qu'un seul facteur à la fois.

Cette pression, facilement réglable par la température du bain reste constante tant qu'il existe de l' UF_6 solide. L'absence de phase liquide élimine les risques de ruissellement et de condensation sur les échantillons. La forme H permet de doubler si nécessaire la capacité en éprouvettes des tubes et se prête à de nombreuses adaptations. Un dispositif d'échantillonnage permet d'effectuer l'analyse de l' UF_6 à chaque manipulation.

On peut constater qu'un tel dispositif est extrêmement souple et peut se prêter à l'exploration de beaucoup de variables telles que le

temps, la température, la pression et la nature des matériaux sont les plus usuelles.

Si un tube doit recevoir un assortiment de métaux, ceux-ci sont choisis de sorte que leur comportement soit présumé assez voisin pour que les plus mauvais ne risquent pas de souiller les autres.

3.5. DÉSORPTION

Lorsqu'un tube est prélevé pour examen, il suit le chemin inverse. Il est d'abord remonté sur une rampe à corrosion réservée à cet effet en vue d'éviter la souillure éventuelle de l'appareillage et de permettre de récupérer séparément l' UF_6 ayant servi à la corrosion. Le tube est ouvert et UF_6 évacué dans un piège par pompage. UF_6 récupéré est ensuite redistillé avant réemploi.

Le tube est alors refermé sous vide et démonté. Puis il est transféré dans une boîte à gants sous atmosphère inerte, où il est ouvert et les éprouvettes en sont retirées. Ceci a pour but d'éviter l'altération des produits de corrosion au contact de l'air humide (fig. 11). Cette altération fausserait l'examen des produits de

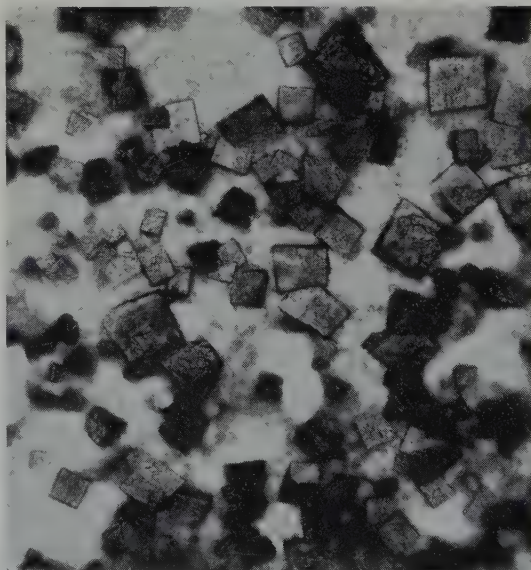


Fig. 12. Cristaux de $\text{UF}_5\beta$ cubiques déposés sur matrice d' UF_4 d'aspect amorphe au microscope photonique. $\times 1400$.

corrosion eux-mêmes, et en outre de l'acide fluorhydrique étant souvent dégagé, produirait une attaque postérieure de l'éprouvette, dont l'ordre de grandeur risquerait d'être bien supérieur à celui de la corrosion proprement dite. Les éprouvettes sont alors enfermées individuellement dans des flacons tarés, ceux-ci placés dans un dessiccateur sous azote.

4. Mesures et examen des éprouvettes

Les éprouvettes sont alors pesées, sauf celles qui sont destinées aux examens métallographiques. Elles sont entreposées 24 h à l'avance pour être en état d'équilibre physique avec l'atmosphère de la salle des balances.

Les produits de corrosion sont ensuite séparés des éprouvettes aux fins d'analyse, dosages d'U, rayons X, etc.

Les valeurs obtenues sont les gains bruts de

poids, représentant la totalité des dépôts formés. Ceux-ci comprennent, en général:

- les sous-fluorures du métal ou de l'alliage dont est constituée l'éprouvette;
- les sous-fluorures d'uranium UF_4 — U_2F_9 — U_4F_{17} — UF_5 etc. (fig. 12), dont la présence est, en général, en accord avec le diagramme d'Agron¹⁾.

Il est important de noter que, lorsque les conditions de corrosion sont telles que des dépôts épais sont susceptibles de se former, le phénomène d'écaillage ("descaling") est observé fréquemment durant la corrosion (fig. 13). Il faut alors utiliser un dispositif de nacelles susceptibles de recueillir les fragments de dépôts détachés de l'éprouvette.

De même, nous avons observé que si certaines éprouvettes sont mises brutalement à l'air libre, les dépôts de corrosion éclatent littéralement. Cela a été principalement observé sur les aciers à fort pourcentage en carbone (0,3–0,8 % C) et on obtient de petites écailles composées d'une faible quantité de fluorures métalliques, principalement du β - UF_5 .

4.1. PERTES DE POIDS

Pour éviter les inconvénients dûs à l'écaillage, et pour atteindre de façon directe les pertes de métal par corrosion, nous avons cherché à évaluer les pertes de poids. Dans la presque totalité des essais que nous avons effectués, lorsque le joint de grain était attaqué, cette attaque affectait la forme d'un sillon relativement peu profond, où les produits de corrosion pouvaient être aisément atteints.

Ces méthodes de pertes de poids ne sont évidemment plus applicables lorsqu'il y a attaque intergranulaire profonde, ou bien lorsque les études de corrosion portent sur des matériaux frittés^{2,11,12)}.

La mise en solution des produits de corrosion sans attaque de métal sous-jacent est, dans les essais de corrosion, très fréquemment délicate à mettre en œuvre. Dans le cas de l' UF_6 , cela présente des difficultés particulières. En effet, l'expérience nous a montré que les valeurs de

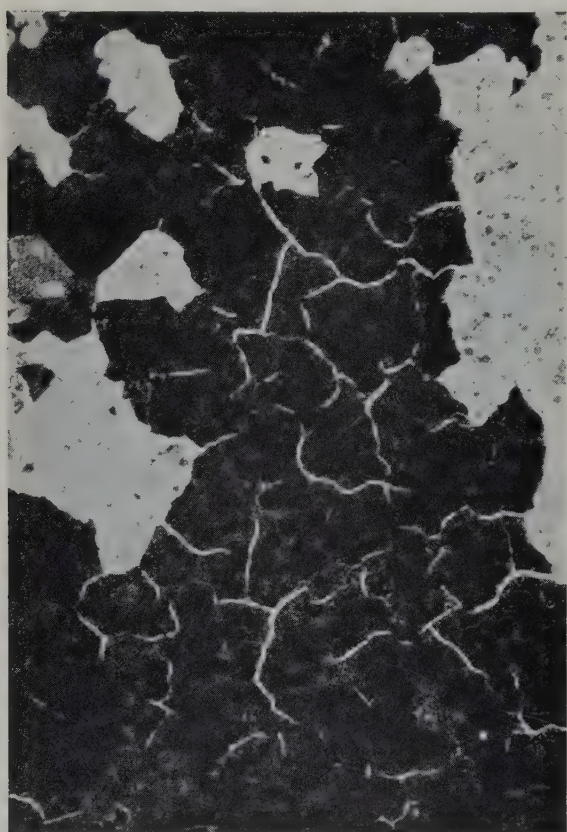


Fig. 13. *Figures d'écaillage ("descaling")*: couche d' UF_4 en foncé sur le cliché. $\times 77$.

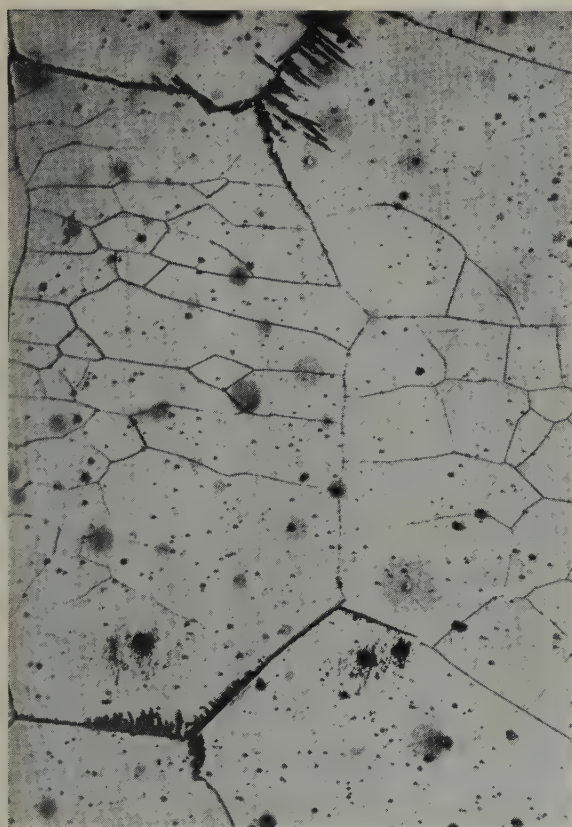


Fig. 14. *Corrosion intergranulaire* mise en évidence par UF_6 des joints de grains et sous-grains de polycristallisation (alliage Ticonal pour aimant permanent).
× 210.



Fig. 15. *Micropiqûres*: Figure de corrosion délimitée par l'empreinte d'un dépôt de surface avec une inclusion au centre (essai de corrosion sur acier doux).
× 816.

corrosion sont extrêmement faibles, de l'ordre de $0,05 \text{ mg/cm}^2$ en 1000 h par exemple, mais nous avons eu fréquemment des valeurs encore moindres à mesurer. Il est couramment admis qu'une méthode de perte de poids est utilisable à condition que le métal enlevé par dissolution représente moins de 10 % de la perte par corrosion⁴). Dans l'exemple cité, ceci implique une valeur inférieure à $6 \mu/\text{cm}^2$. La solubilité du tétrafluorure d'uranium est faible: 10^{-4} mole par litre. La simple élimination par voie aqueuse (dissolution, brossage sous courant d'eau etc.) peut conduire à des erreurs grossières.

Nous avons constaté que la formation d'acide fluorhydrique peut fortement attaquer les échantillons pendant la période du nettoyage. Par exemple, sur un acier au carbone (C = 0,45 %), l'addition d'une goutte d'eau sur un

dépôt de surface fait passer la profondeur de corrosion de $150 \text{ m}\mu$ à 1μ environ.

Dans quelques cas particuliers, on peut utiliser une méthode de dissolution qui a été mise au point par divers auteurs^{18,19}). L'attaque du métal est évitée par l'emploi d'un inhibiteur de corrosion. La mise au point d'une méthode particulière serait nécessaire pour chaque métal ou alliage étudié. Aussi, pour pouvoir effectuer l'étude de matériaux variés, avons-nous utilisé le procédé suivant:

Il consiste à essuyer à la main avec précautions, le dépôt de corrosion au moyen d'une suspension d'alumine 24 h très concentrée sur feutre très doux ou simplement à la peau de chamois lorsque le dépôt est peu adhérent, ce qui est assez fréquent.

Ce contrôle microscopique et le contrôle



Fig. 16. Agglomérat de cristaux d' UF_6 . Figures de croissance en marche d'escalier (dislocation). $\times 480$.

TABLEAU 3

Perte de poids en fonction du temps d'essuyage à l'alumine			
Durée (sec)	Perte de poids (mg)	Epaisseurs correspondantes (en μ)	Perte de poids (mg/sec)
180	1,104	353	0,0061
360	2,274	718	0,0063
540	2,976	950	0,0055
720	4,662	1490	0,0066

Valeur pour une éprouvette de dureté superficielle 195 VPN. (Vickers pyramidal number.)

analytique permettent de s'assurer qu'il ne reste plus de cristaux adhérents dans les cavités de corrosion.

Les quantités de métal enlevées par ce procédé sont généralement de deuxième ordre devant les corrosions étudiées. Les essais

effectués ont permis d'évaluer ces quantités pour différents métaux (tableau 3).

Nous n'avons jusqu'alors appliqué cette méthode qu'aux éprouvettes présentant un poli spéculaire, afin de pouvoir mesurer la profondeur des micropiqûres qui sont les figures de corrosion les plus fréquemment rencontrées. D'autre part, l'enlèvement correct des produits de corrosion dans le trou de suspension reste très délicat.

En bref, ce procédé possède l'avantage de permettre d'effectuer des pertes de poids sur des matériaux extrêmement variés, sans nécessiter une longue mise au point préalable. Par contre, il possède l'inconvénient de donner des résultats relativement moins précis. Des améliorations importantes sont encore possibles. Cependant, il reste précieux, à titre de recouplement, et dans tous les cas où il n'est pas possible d'effectuer des mesures par gain de poids.

4.2. PROFONDEURS DE CORROSION

La méthode des pertes de poids, et ceci est vrai quel que soit l'agent corrosif, possède un grand défaut. Elle n'indique qu'une valeur globale qui ne tient pas compte de la répartition de l'attaque du métal. Les profondeurs de corrosion calculées à partir des pertes de poids sont des profondeurs théoriques, admettant que la corrosion est uniformément répartie. Ces valeurs peuvent être gravement entachées d'erreurs, en particulier si l'on a affaire à des corrosions par piqûres. Or, le cas se présente fréquemment avec l' UF_6 .

Aussi, l'étude de la corrosion serait-elle incomplète sans une mesure des profondeurs d'attaque. Là encore, nous nous sommes fréquemment trouvés en présence d'un ordre de grandeur échappant aux méthodes de mesures habituellement pratiquées.

Les mesures par aiguilles solidaires d'un comparateur ou d'un micromètre décrites par différents auteurs^{3,5}), les coupes optiques, les coupes obliques, l'emploi de rugosimètres de différents modèles n'étaient pas assez sensibles. Dans certains cas, nous avons pu effectuer des mesures par différence du pouvoir de résolution

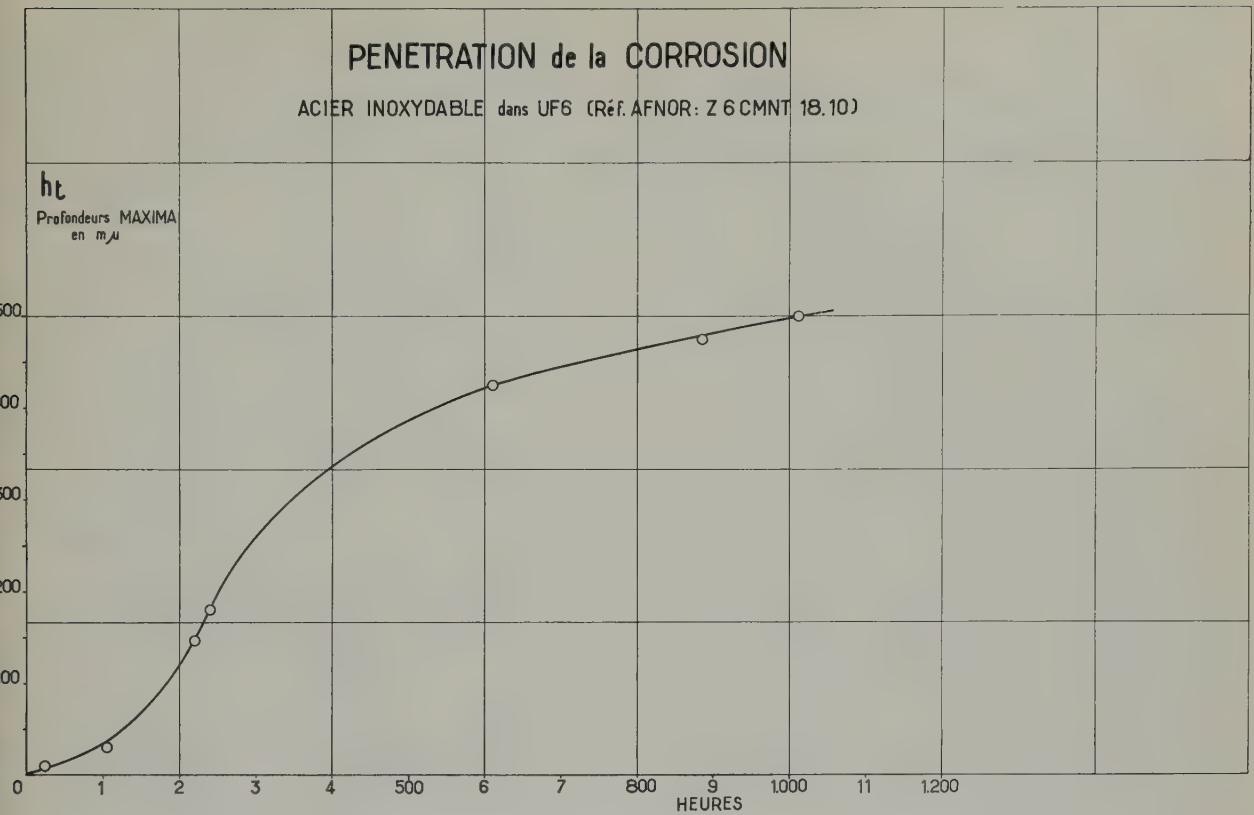


Fig. 17

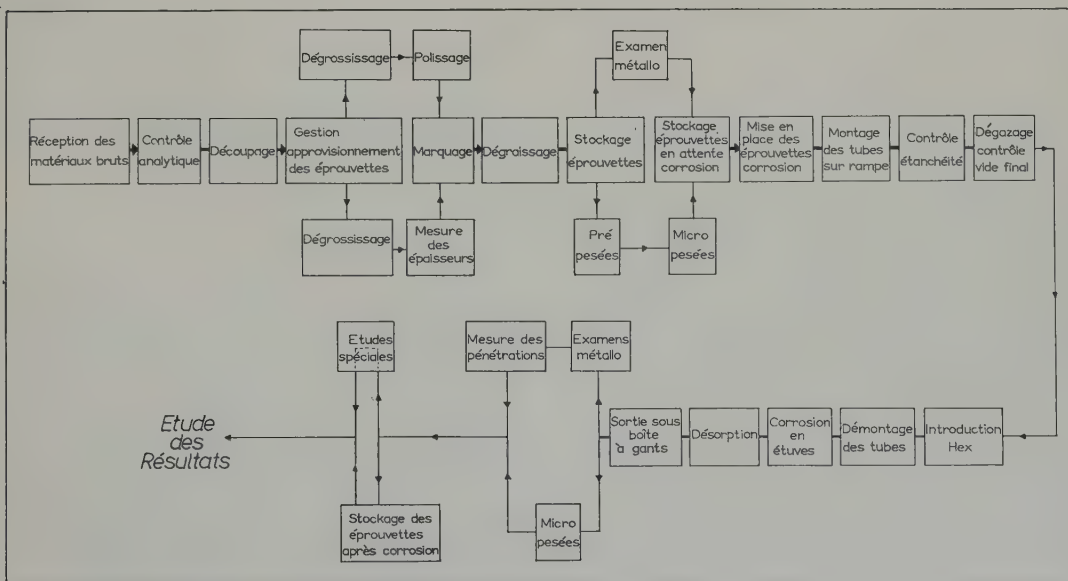


Fig. 18

verticale au microscope photonique (valeurs limites: $0,5 \mu$).

Pour les mesures d'attaques plus faibles, nous avons mis au point une autre méthode. Nous résumerons seulement ici son principe, ses justifications et son détail opératoire devant être publiés par ailleurs²²). La méthode consiste à enlever les produits de corrosion par essuyage à l'alumine comme indiqué plus haut, puis ceux-ci étant enlevés, à poursuivre le polissage d'un métal jusqu'à la disparition complète de la figure de corrosion, dont on peut mesurer la profondeur. L'éprouvette qui avait été pesée avant corrosion est alors pesée à nouveau. La différence de poids permet de mesurer l'épaisseur enlevée et partant, la profondeur des figures.

La notion de profondeur maximum de piqure, comme critère de corrosion a été justement critiquée. La méthode ci-dessus permet, toutes les fois où cela est nécessaire d'obtenir la courbe de dispersion des différentes profondeurs d'attaques, en effectuant des pesées successives. On peut établir alors la courbe en cloche correspondante qui donne la valeur statistique moyenne et permet de calculer le "facteur de perforation", défini par:

$$P = M + 2\delta$$

où M = profondeur moyenne,
 δ = déviation standard.

Cette méthode permet de mesurer aisément des valeurs de $10 m\mu$.

La comparaison des différentes valeurs concomitantes: gains de poids, pertes de poids calculées par analyses et mesures en profondeur des figures de corrosion permet, outre les recoupement nécessaires, de se former une idée précise de la façon dont progresse l'attaque du métal.

A titre d'exemple, la figure 17 montre l'évolution de l'attaque d'un acier inoxydable austéno-ferritique en fonction du temps. La composition de l'acier stabilisé au Ti était

$$\begin{aligned} \text{C} &= 0,06 \% & \text{Cr} &= 18 \% & \text{Mn} &= 10 \% \\ \text{Ni} &= 1,75 \%, & & & & \text{en poids.} \end{aligned}$$

4.3. EXAMENS MICROGRAPHIQUES

Tous les échantillons essayés font l'objet d'une étude métallographique minutieuse avant corrosion. Ceci est particulièrement nécessaire pour éviter des confusions entre certaines inclusions, micro-phases hors solution, et les micropiqures dues à l' UF_6 .

Après corrosion, les dépôts sont examinés par les méthodes micrographiques usuelles, en fond clair ou noir, lumière rasante, en lumière normale ou polarisées, etc. Si nécessaire, ces observations peuvent être faites en boîtes à gants, sous atmosphère inerte. En opérant avec ménagements, la méthode d'essuyage à l'alumine nous a permis d'observer la structure des dépôts de corrosion, qui se présentent fréquemment sous forme de films superposés.

Les méthodes physiques indiquées précédemment complètent les données sur la nature des couches et leur structure.

Les figures de corrosion revêtent le plus fréquemment la forme de micropiqures mettant en évidence les joints de grains (fig. 14) ou bien d'empreintes des dépôts de corrosion, délimitées par des piqures et micropiqures (fig. 15).

Le schéma no. 18 résume la chaîne des opérations effectuées pour les essais. En raison de la multiplicité de ces opérations successives, leur mise en œuvre et l'exploitation des résultats ont rendu nécessaire l'utilisation de tableaux de charge ("plannings") et de dispositifs mécanographiques, analogues à ceux qu'utilise la production industrielle.

5. Conclusions

L'ensemble des méthodes de corrosion et de mesure que nous venons de décrire, a été choisi comme l'un des plus aisément adaptables à la technologie de l'hexafluorure d'uranium.

Il nous a permis, tout en fournissant une grande sensibilité de mesures, d'effectuer des essais en série, sur une vaste échelle, dans de bonnes conditions de délais et de prix de revient.

Cet ensemble s'est montré capable de s'adapter avec souplesse à l'étude des différentes variables (temps, température, etc.) ainsi qu'à celle de nombreux cas particuliers.

L'examen critique de ces méthodes, l'étude des précisions obtenues, la reproductibilité des essais et les causes d'erreurs rencontrées feront l'objet d'un exposé ultérieur.

Bibliographie

- ¹⁾ O. Kubaschewski et B. Hopkins, *Oxydation of Metals and Alloys* (Butterworth, London 1953)
- ²⁾ F. A. Champion, *Corrosion Testing Procedure* (Chapman, London, 1952)
- ³⁾ T. E. Leontis, et F. M. Rhines, *Trans. Amer. Inst. Min. (Metall.) Engrs.* **166** (1948) 265
- ⁴⁾ G. V. Akimov, *Théorie et méthodes d'essais de la corrosion* (Dunod, Paris, 1957)
- ⁵⁾ A. Roos, *Techniques métallographiques* (Dunod, Paris, 1960)
- ⁶⁾ D. Heymann et F. E. T. Kelling, *Corrosion Technology* **5** (1958) 148
- ⁷⁾ C.E.A. Brevet français, no. 783-893 du 13.1.59
- ⁸⁾ P. Noe, M. Carteret et D. Delafosse, *Vanne de laboratoire étanche au vide poussé requise pour l'hexafluorure d'uranium*, Note ESU-202 (1958) C.E.A. (France)
- ⁹⁾ P. Noe, M. Carteret et M. Aubry, *Appareillage de laboratoire pour hexafluorure d'uranium et vide poussé*, Note ESU-203 (1958) C.E.A. (France)
- ¹⁰⁾ U. R. Evans et L. C. Bannister, *Proc. Roy. Soc. A* **72** (1950) 2084
- ¹¹⁾ U. R. Evans, *Précis de Corrosion* (Dunod, Paris, 1952)
- ¹²⁾ U. R. Evans, *The Corrosion and Oxydation of Metals* (Edw. Arnold, London, 1960)
- ¹³⁾ M. Ballay, J. Benard, G. Chaudron, J. Duflot, P. Lacombe et A. Portevin, *Introduction à l'Etude de la Corrosion Métallique* (Paris, 1952)
- ¹⁴⁾ H. A. Miley, *J. Amer. Chem. Soc.* **59** (1937) 2626
- ¹⁵⁾ H. A. Miley, *Carnegie Schol. Mem. of Iron and Steel Inst.* **25** (1936) 200
- ¹⁶⁾ L. E. Price et G. J. Thomas, *J. Inst. Met.* **63** (1938) 21
- ¹⁷⁾ L. E. Price et G. J. Thomas, *Trans. Electrochem. Soc.* **76** (1939) 308
- ¹⁸⁾ J. Aubert, *Nettoyage aqueux de l'acier inoxydable attaqué par UF₆*, Rapport ESU, 377 (1959) C.E.A. (France)
- ¹⁹⁾ C. Makram et J. Aubert, *Nettoyage aqueux de l'aluminium attaqué par l'hexafluorure d'uranium*, Rapport ESU, 443 (1959) C.E.A. (France)
- ²⁰⁾ L. Colombier et J. Hochmann, *Aciers inoxydables, aciers réfractaires* (Dunod, Paris, 1955)
- ²¹⁾ H. H. Uhlig, *Corrosion Handbook* (John Wiley, New York, 1948)
- ²²⁾ J. Dixmier, R. Hasson, S. Maraval, L. M. Vincent, *J. Mat. Nucl.*, à paraître
- ²³⁾ L. Arbellot, *Corrosion, Anticorr.* **5** (1957) 112

INFLUENCE DES DIMENSIONS CRISTALLINES SUR LA CINETIQUE D'OXYDATION DE UO_2

Mmes BELLA BELBEOCH, CLAUDIA PIEKARSKI et M. PIERRE PERIO

Centre d'Etudes Nucléaires de Saclay, Gif-sur-Yvette, (S. & O.) France

Reçu le 5 juillet 1960

Nous avons essayé, en tenant compte de la surface spécifique, de préciser le mécanisme d'oxydation à basse température de UO_2 , la nature et les propriétés des phases quadratiques dans le domaine O/U compris entre 2,3 et 2,4. Les résultats confirment raisonnablement le mécanisme de diffusion discontinue proposé antérieurement ⁴⁾.

We have sought to determine the exact mechanism of oxydation of uranium dioxide at low temperatures, taking into account the specific surface area of the powder; the nature and properties of the tetragonal phases with O/U ratios between 2.3 and 2.4 were

studied. The results are in reasonable agreement with the discontinuous diffusion mechanism previously proposed ⁴⁾.

Es wurde versucht, den Mechanismus der Tieftemperatur oxydation von Urandioxyd exakt zu ermitteln. Hierbei wurde die spezifische Oberfläche des Pulvers berücksichtigt. Der Zustand und die Eigenschaften der tetragonalen Phasen mit O/U-Verhältnissen zwischen 2,3 und 2,4 wurden untersucht. Die Ergebnisse stimmen in vernünftiger Weise überein mit dem früher vorgeschlagenen Mechanismus ⁴⁾ der diskontinuierlichen Diffusion.

1. Introduction

Il est généralement reconnu que l'oxydation de UO_2 est contrôlée par la diffusion de l'oxygène. Néanmoins deux mécanismes ont été proposés:

1) oxydation en phase homogène (Anderson¹⁾, Aronson²⁾, Lustman³⁾).

2) schéma diphasique d'oxydation avec formation d'une phase quadratique à l'extérieur de chaque grain (Perio⁴⁾ (modèle de diffusion discontinue), Blackburn⁵⁾).

Ces deux mécanismes justifient également la cinétique d'oxydation; toutefois le second processus étant sensible à la dimension des grains élémentaires, nous avons cherché à mettre en évidence l'influence de ce paramètre, lié directement à la surface spécifique, sur l'évolution de UO_2 au cours de l'oxydation.

2. Oxydation de UO_2

Pour tous les oxydes donnant un spectre de rayons X bien défini, l'oxydation à une température inférieure à 200° C s'accompagne de la formation immédiate d'une phase quadratique de $c/a \approx 1,01$, le retard à la détection de cette couche réoxydée pouvant se justifier par des considérations d'extension. Pendant longtemps on a cru que les oxydes de grande surface ($s > 6 \text{ m}^2/\text{g}$) s'oxydaient en phase cubique homogène. Un examen plus précis montre nettement une déformation quadratique. L'évolution ultérieure des poudres dépend essentiellement de leur surface spécifique. Nous les classerons en:

petites surfaces: $s < 1 \text{ m}^2/\text{g}$

moyennes surfaces: $1 \leq s \leq 5 \text{ m}^2/\text{g}$

grandes surfaces: $s > 5 \text{ m}^2/\text{g}$ (Tableau 1)

TABLEAU 1

	Produits de départ			Résultats de l'oxydation
	Surface m^2/g	Titre chimique	Aspect du diagramme	
Grandes Surfaces	6 18	2,14 2,28	$a = 5,465 \text{ \AA}$ $\pm 0,001$ $a = 5,438 \text{ \AA}$ $\pm 0,001$	Oxydation monophasique pseudo-homogène jusqu'à $\text{O/U} \approx 2,4$ puis diphasique $\text{UO}_{2,4} + \text{UO}_3$
Moyennes Surfaces	1 2	 2,05	Spectre normal à cubique faces centrées $a = 5,4685 \pm 0,0007 \text{ \AA}$	Oxydation diphasique état initial $\text{UO}_2 + \gamma (c/a \approx 1,01)$ état final $\text{O/U} = \gamma_1 (\text{O/U} = 2,38, c/a = 1,033)$
Petites Surfaces	$\leq 0,5$	2,00	Très bien cristallisé $a = 5,4685 \pm 0,0007 \text{ \AA}$	Oxydation diphasique pour $\text{O/U} < 2,25$ puis apparition de la zone de déformation

Les oxydations ont été effectuées à 150 et 180° C.

2.1. UO_2 DE MOYENNE SURFACE (entre 1 et 5 m^2/g)

Les produits de départ ont un titre voisin de $\text{UO}_{2,05}$. L'oxydation est diphasique. La phase quadratique est décelable dès que $\Delta(\text{O/U}) \approx 0,05$. La phase quadratique initialement formée a un c/a voisin de 1,01. On pourrait croire en début d'oxydation à l'existence d'un oxyde quadratique de $c/a < 1$. En fait, ceci est dû à la superposition des raies de UO_2 cubique à l'une des composantes du doublet quadratique (fig. 1). On note une faible variation du c/a autour de 1,01. En début d'oxydation $c/a = 1,009$ ($c = 5,466 \text{ \AA}$), puis pour $\Delta(\text{O/U}) = 0,30$, $c/a = 1,011$ ($c = 5,479 \text{ \AA}$).

A ce stade il subsiste très peu d'oxyde cubique dont la composition évolue progressivement avant disparition totale. On observe ensuite une déformation des raies correspondant à une transition entre différentes espèces quadratiques, sans variation de poids appréciable (ce qui n'exclut pas une reprise d'oxygène avec élimination d'eau par exemple). On ne peut pas définir de paramètres précis pour ces phases intermédiaires correspondant à $\text{O/U} \approx 2,35$. Une faible oxydation ultérieure ($\Delta(\text{O/U}) = 0,33$) transforme totalement le produit en une phase homogène quadratique bien définie. C'est l'oxyde

γ_1 de Perio⁴) de titre $\text{O/U} = 2,38$.

$$\frac{c}{a} = 1,032_5$$

$$c = 5,556 \pm 0,005 \text{ \AA}$$

$$a = 5,381 \pm 0,006 \text{ \AA}$$

2.2 UO_2 DE TRES PETITE SURFACE

Jusqu'à $\text{O/U} = 2,25$ l'oxydation est diphasique comme pour les produits de moyenne

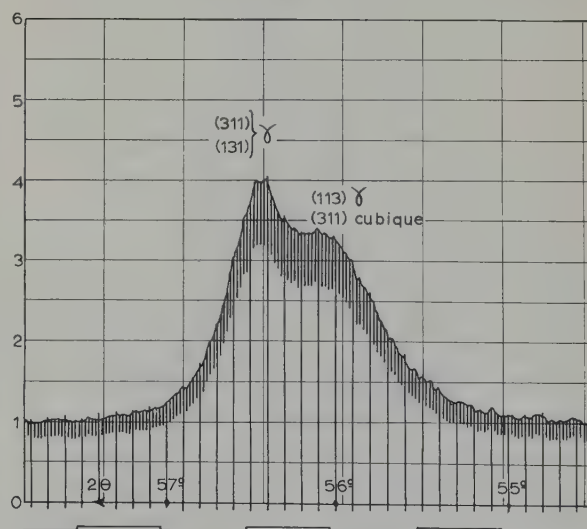


Fig. 1. $\text{UO}_2(s = 2 \text{ m}^2/\text{g})$ oxydé 34 heures à 180° C : oxyde quadratique ($c/a = 1,01$) + UO_2 .

surface avec apparition du même oxyde quadratique $c/a=1,01$. L'oxydation est naturellement beaucoup plus lente que précédemment. Au-dessus de $O/U=2,25$ le phénomène se complique; la réflexion (111) se dissocie progressivement en un triplet (fig. 2). L'évolution paraît terminée pour $\Delta(O/U)=0,33$. Les raies d'indices plus élevés n'ont pu être résolues en leurs différentes composantes. Un traitement de 2000 heures à 180°C n'a amené aucun changement de diagramme. Par contre, si on recuit le produit oxydé en enceinte scellée sous vide à 350°C , on aboutit au quadratique γ_1 . Ceci met en évidence la parenté de comportement avec les oxydes de moyennes surfaces. Si l'on suppose que l'oxydation progresse à l'intérieur du grain par formation de couches successives d'oxyde quadratique (modèle de diffusion discontinue de Perio⁴), on

est amené à penser que le triplet traduit l'existence d'une déformation dans des zones de transition au raccordement de deux zones successives de diffusion. Le phénomène est beaucoup moins visible pour les grains plus petits pour lesquels l'extension des zones de raccordement est moins grande. On n'observe plus alors au-delà de $O/U=2,30$ que la superposition de quadratiques mal définis avec $1,01 < c/a < 1,03$.

La décomposition de la raie (111) en un triplet serait un des rares exemples où la déformation cohérente du réseau entre deux domaines de diffusion est visible par rayons X.

2.3. UO_2 DE GRANDE SURFACE

Ces oxydes sont mal cristallisés et l'étude par diffraction des rayons X est rendue délicate par l'élargissement des raies lié au facteur de taille. Pour des produits dont la surface est de $6\text{ m}^2/\text{g}$, on peut au départ déterminer un paramètre moyen en supposant la maille cubique. Ainsi on trouve $a=5,465 \pm 0,001\text{ \AA}$ correspondant à un titre $\text{UO}_{2,0}$, alors que l'analyse chimique donne $\text{UO}_{2,14}$. Néanmoins une analyse de Rachinger du profil d'une raie comme la (620) montre une traînée diffuse du côté des grands angles indiquant l'existence à l'ambiance d'une partie déjà fortement réoxydée. Cette traînée s'accroît au cours de l'oxydation et à partir de $\Delta(O/U)=0,28$ on ne peut même plus déterminer de paramètre moyen; en effet les raies ne sont pas dédoublées, mais sont fortement dissymétriques. Elles peuvent toutes être résolues en leur différentes composantes en admettant une déformation quadratique à $c/a \geq 1$. Ainsi la dégénérescence du cubique donne trois raies pour la raie (620). Pour $c/a=1,01$ et $c=5,466\text{ \AA}$:

TABLEAU 2

	(620) (260)	(062) (602)	(206) (026)
2θ	$128,46^\circ$	$128,24^\circ$	$126,52^\circ$

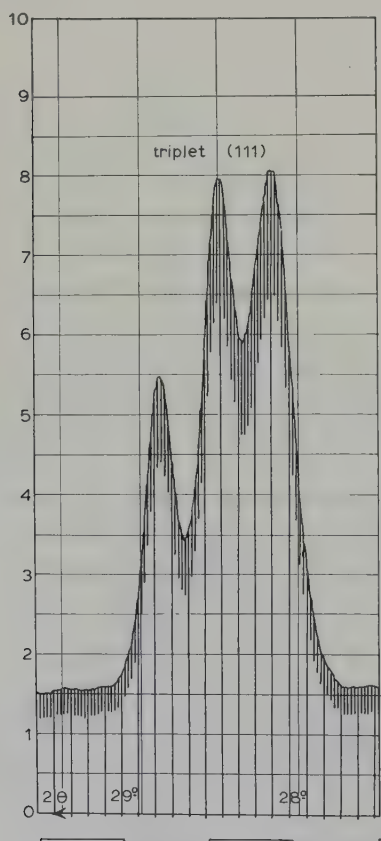


Fig. 2. UO_2 ($s < 0,5\text{ m}^2/\text{g}$) oxydé deux mois à 150°C ; (111): triplet dû à la déformation du réseau.

Le facteur de taille étant très important, deux des composantes sont pratiquement con-

fondues; on observe une seule raie large non résolue dont le maximum passe effectivement vers $128,35^\circ$, la troisième composante se traduisant par une déformation nette aux petits angles (fig. 3).

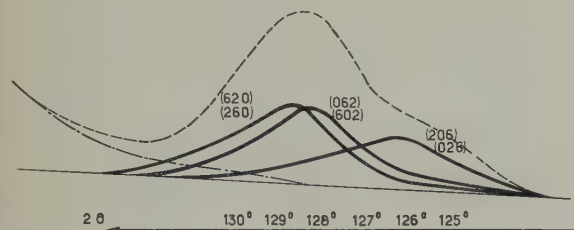


Fig. 3. UO_2 ($s = 15 \text{ m}^2/\text{g}$) oxydé 400 heures à 180°C déformation quadratique de la raie (620).

---- profil expérimental
— analyse en 3 composantes.

La quadratisation est plus rapide pour les produits de $15\text{--}18 \text{ m}^2/\text{g}$ que nous avons oxydés à 180°C . Elle se traduit au bout de 17 heures à 180°C par l'élargissement de la raie (311) comparée à la (222). Le titre déduit pondéralement, en tenant compte de la forte hygroscopicité du produit, est d'environ 2,4. On doit remarquer:

1) que la position angulaire de la raie (620): $2\theta = 128,35^\circ$ reste fixe lorsque l'oxydation se poursuit; l'oxyde quadratique formé est donc défini par un c/a constant,

2) lorsqu'on oxyde ces produits de grande surface à des températures légèrement plus élevées (250°C), il ne se forme pas d' U_3O_8 . Par contre on aboutit à UO_3 amorphe. Ces deux phénomènes nous conduisent à proposer le mécanisme d'oxydation suivant:

oxydation en phase unique pseudo-homogène jusqu'à $\Delta(\text{O}/\text{U}) = 2,3\text{--}2,4$ par déformation progressive du cubique en phase quadratique avec un c/a final de 1,01.

L'oxydation est ensuite diphasique. Il se forme en surface une couche de UO_3 amorphe qui progresse vers l'intérieur jusqu'à transformation complète en UO_3 si la température est suffisamment élevée.

Les résultats globaux concernant l'oxydation sont consignés dans le tableau 1.

3. Stabilité des oxydes quadratiques

Par recuit les oxydes de grande surface n'ont jamais recristallisé, ils ne permettent pas la préparation de la forme quadratique γ bien cristallisé. Le recuit amène la décomposition en $\text{U}_4\text{O}_9 + \text{UO}_{2,60}$ mal définis.

Obtenue à partir des petites et moyennes surfaces la phase γ_1 de titre $\approx 2,38$ est stable jusqu'aux températures de $430\text{--}460^\circ \text{C}$. Au-dessus de ce domaine de température, il y a dismutation en $\gamma_2 + \text{UO}_{2,60}$. La phase γ_2 est remarquablement bien cristallisée. Nous l'avons obtenue pure en recuisant à 350°C un produit de titre 2,35 contenant essentiellement un oxyde quadratique de $c/a = 1,01$ (fig. 1). En phase homogène et après traitement à 350°C nous notons $c/a = 1,017_1$ (fig. 4); $a = 5,4033 \pm 0,0015 \text{ \AA}$. La phase γ_2 ainsi obtenue est stable jusqu'à $600\text{--}640^\circ \text{C}$. Au-dessus de 640°C , elle se décompose en U_4O_9 et $\text{UO}_{2,60}$ orthorhombique. Le rapport c/a varie avec la température et partant la composition (fig. 5). Le plus petit c/a observé étant 1,012, l'espèce $c/a = 1,01$ rencontrée au stade initial de l'oxydation est extérieure au domaine γ_2 . Nous ne pouvons pas préciser ses relations avec la phase désignée par Perio comme γ_3 et qui n'a pas été retrouvée dans cette étude. (Remarquons toutefois que nous n'avons pas effectué de recuits dans le domaine de composition 2,25–2,30 où elle avait été signalée.)

La figure 6 schématise le domaine d'extension du quadratique γ_2 . Il est possible qu'un domaine de très faible largeur existe pour γ_1 .

Expérimentalement les transitions $\gamma_1 \rightarrow \gamma_2$ et $\gamma_2 \rightarrow \text{U}_4\text{O}_9 + \text{UO}_{2,6}$ sont observées dans une bande de température plutôt qu'à une température fixe. En particulier à la limite supérieure du domaine vers $600\text{--}640^\circ \text{C}$, on observe fréquemment la coexistence des trois phases U_4O_9 , $\text{UO}_{2,3}$ et $\text{UO}_{2,6}$. La réversibilité n'a jamais encore été obtenue. Mais le traitement thermique entre 400 et 600°C amène une recristallisation prononcée de γ_2 permettant la résolution des doublets $\alpha_1\alpha_2$. Nous estimons que ces phases doivent présenter un domaine de stabilité thermodynamique vraie. La structure des oxydes quadratiques est apparentée à celle de

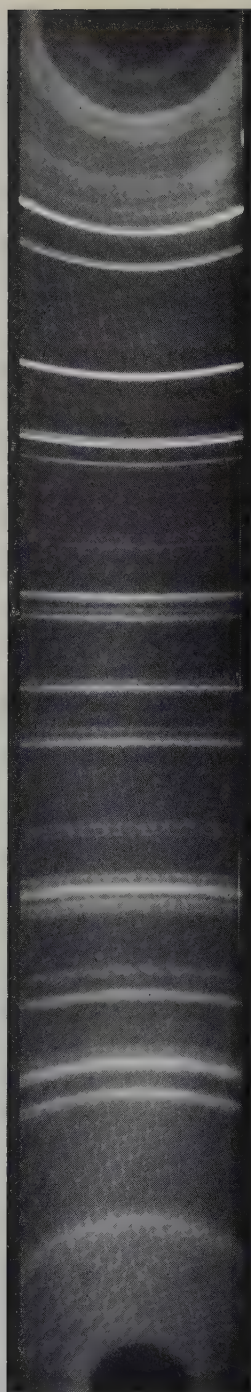


Fig. 4. Cliché Debye-Scherrer de l'oxyde quadratique γ_2 ($\text{UO}_{2,35}$ recuit 18 jours à 350°C)
 $c/a = 1,017_1$.

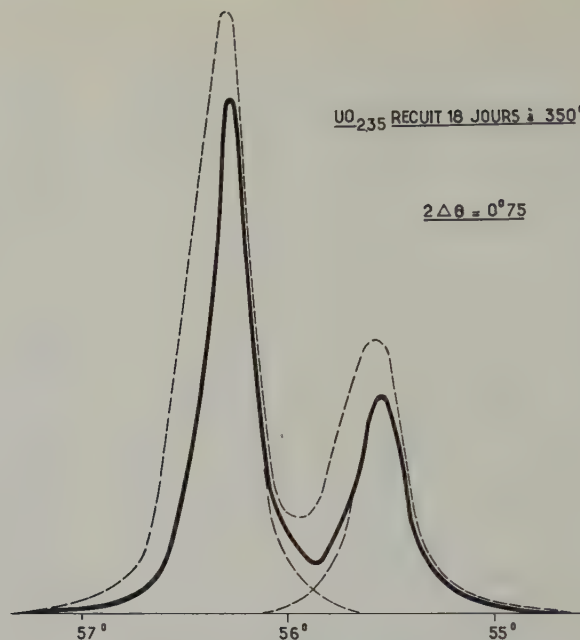


Fig. 5a. 18 jours à 350°C .

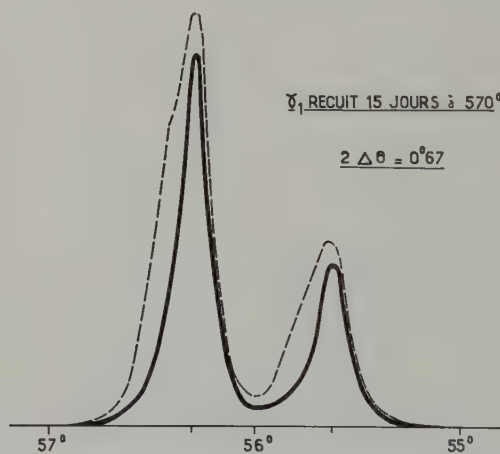


Fig. 5b. 15 jours à 570°C .

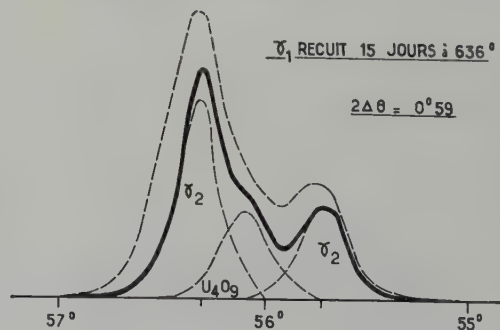


Fig. 5c. 15 jours à 636°C .

Fig. 5. Variation du rapport c/a de la phase γ_2 avec la température de recuit (a, b, c).
 ---- profil expérimental ——— après élimination de α_2 .

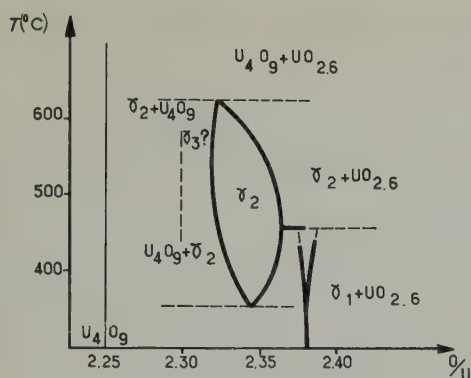


Fig. 6. Représentation schématique des relations de phases entre oxydes quadratiques.

U_4O_9 , avec probablement une maille élémentaire encore plus grande. La stabilité d'une telle structure doit dépendre considérablement de son extension surtout quand celle-ci est de l'ordre de quelques périodes élémentaires ($\approx 100 \text{ \AA}$). Il est concevable que les énergies élastiques (contraintes internes et tension superficielle) représentent une part importante de l'énergie libre de transformation. Dans des systèmes polydispersés on peut donc s'attendre à une dispersion des températures d'équilibre correspondant à la dispersion des dimensions cristallines.[†]

4. Discussion des Résultats

Dans cette étude, nous avons mis en évidence l'influence des dimensions cristallines sur l'évolution des phases métastables au cours de la cinétique d'oxydation à des températures inférieures à 200°C .

Pour les oxydes de surface inférieure à $6 \text{ m}^2/\text{g}$ l'oxydation est diphasique dès le début, l'état final étant la phase quadratique γ_1 . Dans le cas des oxydes à grande surface, la taille des grains est de l'ordre d'une couche de quadratique; l'insertion d'oxygène dans le réseau primitivement cubique entraîne une déformation quadratique progressive qui aboutit à un oxyde γ mal cristallisé de $c/a = 1,01$; l'oxydation est ensuite diphasique, $\gamma + \text{UO}_3$. [Il est

[†] Les surfaces spécifiques mesurées par B.E.T. ne donnent en réalité qu'une valeur moyenne sans aucun renseignement sur la répartition des dimensions.

probable qu'il se forme de UO_3 en surface même pour des oxydes de petite surface. En effet sur des oxydes quadratiques γ_1 conservés à l'ambiante en atmosphère confinée nous avons observé après plusieurs mois l'apparition d'hydrates de UO_3 bien caractérisés par leurs diagrammes de Rayons X. Ceci est peut-être à rapprocher de la loi particulière d'oxydation observée par Anderson⁷⁾ à des températures inférieures à 50°C . Note dans les épreuves].

Nous avons montré l'existence de zones de déformations cohérentes conciliables avec le modèle de diffusion discontinue proposé par Perio.

Nous confirmons l'existence d'au moins deux phases quadratiques:

$$\gamma_1 \left(\frac{c}{a} = 1,033 \right)$$

$$\gamma_2 \left(\frac{c}{a} \text{ variant de } 1,017 \text{ à } 1,012 \right),$$

contrairement aux résultats publiés récemment par Blackburn⁵⁾. Celui-ci considère l'oxydation comme diphasique dès les premiers stades de l'oxydation avec formation d'un oxyde quadratique $\gamma\text{U}_3\text{O}_7$ et variation continue de c/a au cours de l'oxydation. Cette évolution est attribuée à une action épitaxiale de UO_2 sous-jacent. Un tel effet nous paraît incompatible avec ce que l'on sait des propriétés élastiques des solides de ce type. L'observation expérimentale des différents γ à l'état pratiquement pur permet de le rejeter définitivement. L'ensemble de ces résultats est en accord avec les données que nous a communiquées Siegel⁶⁾ à la seule réserve du rapport c/a de la phase quadratique formée initialement.

5. Nota

L'essentiel des désaccords entre les différents chercheurs provient de la façon dont ils exploitent leurs données expérimentales. D'après notre expérience, les méthodes de rayons X photographiques classiques sont insuffisantes pour la détection des phases mal organisées présentes dans des mélanges complexes et pour l'étude précise de l'évolution des quadratiques en présence de phases étrangères (UO_2 ou U_4O_9 .)

Nous utilisons conjointement la méthode photographique et le diffractomètre à compteur. Ce dernier donne un relevé direct des profils dont l'analyse permet l'identification des différents constituants. Le rapport c/a est déterminé à partir de l'écart angulaire $2\Delta\theta$ du doublet (311)–(113).

$$\frac{c}{a} = \sqrt{\frac{4 + \Delta\theta \cotg \theta_{311}}{4 - 10 \Delta\theta \cotg \theta_{311}}}$$

pour $\delta(\Delta\theta) = 0,01^\circ$, $\Delta(c/a) = 5 \cdot 10^{-4}$

La séparation du doublet est très sensible aux variations de c/a comme le montre le tableau 3.

TABLEAU 3

c/a	$2 \Delta\theta$
1,013	$0,58^\circ$
1,017	$0,75^\circ$
1,033	$1,40^\circ$

Pour calculer c , on utilise le couple des raies (311) et (133) qui rend minimum l'erreur due au

pointé des raies et à l'excentrement de l'échantillon. On a :

$$\frac{\lambda^2}{4c^2} = \frac{\cos 2\theta_{311} - \cos 2\theta_{133}}{16}$$

La précision est cependant médiocre ($\Delta c/c = 10^{-3}$).

Lorsque l'échantillon est bien cristallisé (par exemple γ_2), nous déterminons photographiquement a à partir des réflexions aux grands angles (622) et (444), ce qui donne $\Delta(a/a) = 3 \times 10^{-4}$; c est ensuite déterminé à partir de a et de c/a mesuré par diffractométrie.

Bibliographie

- 1) J. S. Anderson et K. B. Alberman, J. Chem. Soc. UK, S 2 (1949) 303
- 2) S. Aronson, R. B. Roof et J. Belle, J. Chem. Phys. 27 (1957) 137
- 3) B. Lustman et J. Belle, Westinghouse Atomic Power Division (USA) Report WAPD 184 (1957)
- 4) P. Perio, Thèse de doctorat, Paris (1955)
- 5) P. E. Blackburn, J. Weissbart et E. A. Gulbransen, J. Phys. Chem. USA 62 (1958) 902
- 6) S. Siegel, Communication personnelle
- 7) J. S. Anderson, L. E. J. Roberts, E. A. Harper, J. Chem. Soc. (1955) 3946

THERMAL EXPANSION OF ALPHA-URANIUM SINGLE CRYSTALS

LOWELL T. LLOYD

Argonne National Laboratory, Argonne, Ill., USA

Received 14 July 1960

Dilatometry has been used to measure the thermal expansions of alpha-uranium single crystals between 25° C and 650° C. Equations for length (L) in the three principal crystallographic directions and volume (V) as functions of temperature (t° C) are as follows:

$$L_{[100]t} = L_{[100]0} (1 + 23.53 \times 10^{-6}t + 13.74 \times 10^{-9}t^2 + 9.94 \times 10^{-12}t^3)$$

$$L_{[010]t} = L_{[010]0} (1 + 1.16 \times 10^{-6}t - 9.43 \times 10^{-9}t^2 - 11.79 \times 10^{-12}t^3)$$

$$L_{[001]t} = L_{[001]0} (1 + 19.38 \times 10^{-6}t + 21.58 \times 10^{-9}t^2 + 3.32 \times 10^{-12}t^3)$$

$$V_t = V_0 (1 + 43.98 \times 10^{-6}t + 26.88 \times 10^{-9}t^2 + 1.00 \times 10^{-12}t^3).$$

The differences in the [010] and [001] expansions obtained by dilatometry when compared with values calculated from lattice parameter data are ascribed to elastic strains in the polycrystalline X-ray samples.

On a mesuré la dilatation thermique des monocristaux d'uranium α entre 25 et 650° C par dilatométrie. Les équations donnant la longueur (L) dans les trois directions cristallographiques principales et le volume (V) en fonction de la température (t° C) sont les suivantes:

$$L_{[100]t} = L_{[100]0} (1 + 23,53 \times 10^{-6}t + 13,74 \times 10^{-9}t^2 + 9,94 \times 10^{-12}t^3)$$

$$L_{[010]t} = L_{[010]0} (1 + 1,16 \times 10^{-6}t - 9,43 \times 10^{-9}t^2 - 11,79 \times 10^{-12}t^3)$$

$$L_{[001]t} = L_{[001]0} (1 + 19,38 \times 10^{-6}t + 21,58 \times 10^{-9}t^2 + 3,32 \times 10^{-12}t^3)$$

$$V_t = V_0 (1 + 43,98 \times 10^{-6}t + 26,88 \times 10^{-9}t^2 + 1,00 \times 10^{-12}t^3).$$

1. Introduction

A knowledge of thermal expansion behavior is important in the interpretation of various phenomena observed in alpha-uranium and requisite to measurements of other physical

La différence des résultats entre les valeurs obtenues par dilatométrie et les valeurs calculées à partir des paramètres de la maille pour les variations dimensionnelles dans les directions [010] et [001] est attribuée aux contraintes élastiques dans les échantillons polycristallins utilisés pour déterminer les paramètres.

Die thermische Ausdehnung von Einkristallen aus α -Uran im Bereich von 25 bis 650° C wurde in Dilatometermessungen ermittelt. Folgende Gleichungen für die Längenausdehnung (L) in den drei Kristallhauptrichtungen und für die Volumenausdehnung (V) in Abhängigkeit von der Temperatur (t° C) wurden gefunden:

$$L_{[100]t} = L_{[100]0} (1 + 23.53 \times 10^{-6}t + 13.74 \times 10^{-9}t^2 + 9.94 \times 10^{-12}t^3)$$

$$L_{[010]t} = L_{[010]0} (1 + 1.16 \times 10^{-6}t - 9.43 \times 10^{-9}t^2 - 11.79 \times 10^{-12}t^3)$$

$$L_{[001]t} = L_{[001]0} (1 + 19.38 \times 10^{-6}t + 21.58 \times 10^{-9}t^2 + 3.32 \times 10^{-12}t^3)$$

$$V_t = V_0 (1 + 43.98 \times 10^{-6}t + 26.88 \times 10^{-9}t^2 + 1.00 \times 10^{-12}t^3).$$

Für die Ausdehnung in [010] und in [001]-Richtungen ergeben sich bei Dilatometermessungen Ergebnisse, die mit den aus Gitterparameterwerten berechneten Werten nicht übereinstimmen. Diese Unterschiede werden elastischen Spannungen zugeschrieben, welche in den polykristallinen Proben der Röntgenversuche vorgelegen haben.

properties as functions of temperature. Since the lattice structure is orthorhombic, the temperature dependence of the lengths in the three principal crystallographic directions cannot be measured directly from polycrystalline samples;

however, lattice parameter data¹⁻³) as functions of temperature have been used to calculate these thermal expansions. Thermal cycling tests have shown that multi-grained samples are subject to residual elastic strains as well as to plastic deformations⁴). Therefore, the polycrystalline specimens of the lattice parameter studies may have contained elastic strains which influenced the calculated thermal expansions.

Single crystals are not subject to restraints imposed by neighboring grains. Mean thermal expansion coefficients have been reported by Lehr and Langeron^{5,6}) for "single crystals" grown by cooling in a temperature gradient through the beta to alpha transformation. Since the samples contained lineage structure, the orientations of the testing directions and, consequently, the expansion data are subject to question. Crystals, free from lineage structure, can be prepared by grain coarsening techniques⁷), and their length changes with temperature can be measured by dilatometry. This paper describes dilatometric studies of alpha-uranium single crystals prepared in this way and compares the results to previously reported information.

2. Experimental Procedures

The crystals used in this work ranged up to 5 mm in diameter and approximately 12 mm in length. They were isolated from other grains and prepared with two parallel faces perpendicular to the desired testing direction by usual metallographic procedures, and the residual distorted surface layers were removed by a final electrolytic polish. Prior to testing, the crystals were observed metallographically for structural irregularities, and the crystallographic identities of the polished surfaces were determined by Laue back-reflection X-ray photograms.

Thermal expansion measurements were made with a recording quartz differential dilatometer⁸). Several dilatation tests were run for each crystal between room temperature and 650° C at heating and cooling rates of approximately 4° C per minute. After testing, the thin corrosion films were removed by electropolishing,

and the surfaces were re-examined metallographically.

3. Results

Metallographic observations indicated that only minor structural changes resulted from heating and cooling the single crystals. For the most part, twins present prior to testing were absorbed during the first runs, and subsequent expansion curves were reproducible.

Seven dilatation measurements in directions within 0.5° of the principal crystallographic axes were obtained from five pseudo-unit cell single crystals; two crystals were measured in two different principal directions. Two determinations were made of expansion in the [100] direction, three in the [010] and two in the [001]. Indicated expansions were read from the dilatation curves at intervals of 25° C over the range from 25° to 650° C. These values were corrected for expansion of the quartz components of the dilatometer and normalized to represent fraction expansion (f_t), according to the equation:

$$f_t = \frac{L_t - L_{25}}{L_{25}}$$

where L_t equals the corrected crystal length at t° C and L_{25} equals its initial length at 25° C. The fraction expansion values for a given principal direction were averaged for each temperature and fitted by least mean square analyses to equations of the type:

$$f_t = k_0' + k_1't + k_2't^2 + k_3't^3$$

where, k_0' , k_1' , k_2' and k_3' are constants.

These equations were converted to ones of the type:

$$X_t = X_0(1 + k_1t + k_2t^2 + k_3t^3)$$

where, X_t and X_0 represent the dimensions at t° C and 0° C, respectively. Table 1 gives the constants which relate the lengths in the principal directions and volume to temperature and the respective values at 0° C. The volume equation constants were derived by curve fitting values obtained upon multiplying the

TABLE 1

Constants for equations relating expansion of alpha-uranium principal directions and volume to temperature †

Dimension (X)	Constants		
	$k_1 \times 10^6$	$k_2 \times 10^9$	$k_3 \times 10^{12}$
Based on single crystal dilatation data			
[100]	23.53	13.74	9.94
[010]	1.16	-9.43	-11.79
[001]	19.38	21.58	3.32
V	43.98	26.88	1.00

Based on lattice parameter data of Bridge, Schwartz and Vaughan ¹⁾

[100]	22.50	11.83	14.98
[010]	0.61	-2.32	-18.15
[001]	19.36	5.50	23.60
V	42.95	18.82	14.59

Based on lattice parameter data of Chiotti, Klepfer and White ²⁾

[100]	18.51	25.62	—
[010]	-0.66	7.69	-30.07
[001]	15.11	23.70	—
V	32.63	58.85	-31.52

† Constants are for equations of the type:

$$X_t = X_0(1 + k_1 t + k_2 t^2 + k_3 t^3)$$

where X_t equals the dimension at temperature $t^\circ\text{C}$ and X_0 equals the dimension at 0°C .

normalized and averaged lengths of the three principal directions for each temperature and converting them to represent fraction volume expansion. Table 1 also gives the constants for comparable equations obtained by curve fitting the lattice parameter data of Bridge *et al.* and Chiotti *et al.* Figs. 1, 2, 3 and 4 graphically compare the three sets of equations. The single crystal results agreed well with the curves from lattice parameter data for the [100] direction and volume expansions, whereas the single crystal [010] curve fell below the lattice parameter curves and the [001] fell above.

Experimentally measured fraction expansion data of six randomly oriented crystals were compared to expansions calculated from the

principal direction data and the orientation of the crystals' testing direction. The relationship used was:

$$f_t = f_{t(a)} \cos^2 \alpha + f_{t(b)} \cos^2 \beta + f_{t(c)} \cos^2 \gamma$$

where, α , β and γ are the inclinations of the testing direction from the principal directions [100], [010] and [001], and f_t , $f_{t(a)}$, $f_{t(b)}$ and $f_{t(c)}$ are the fraction expansions at temperature $t^\circ\text{C}$ for the random, [100], [010] and [001] directions, respectively. Fig. 5 plots the corrected experimental and calculated curves for a crystal tested in a direction 86° from the [100],

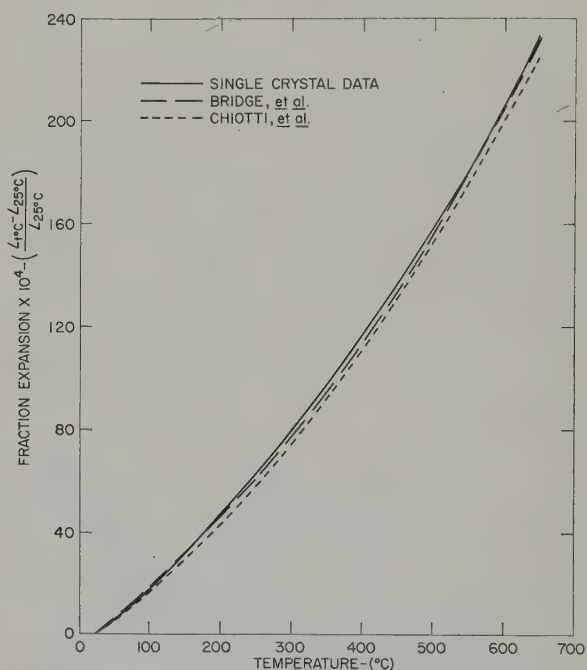


Fig. 1. Fraction expansion of alpha-uranium in the [100] direction.

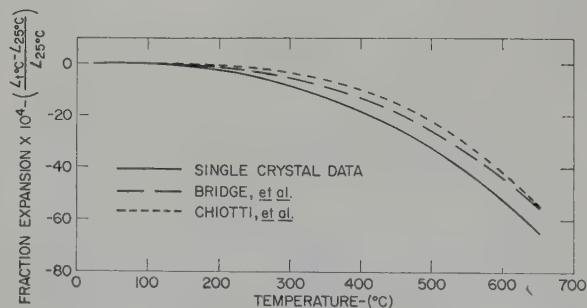


Fig. 2. Fraction expansion of alpha-uranium in the [010] direction.

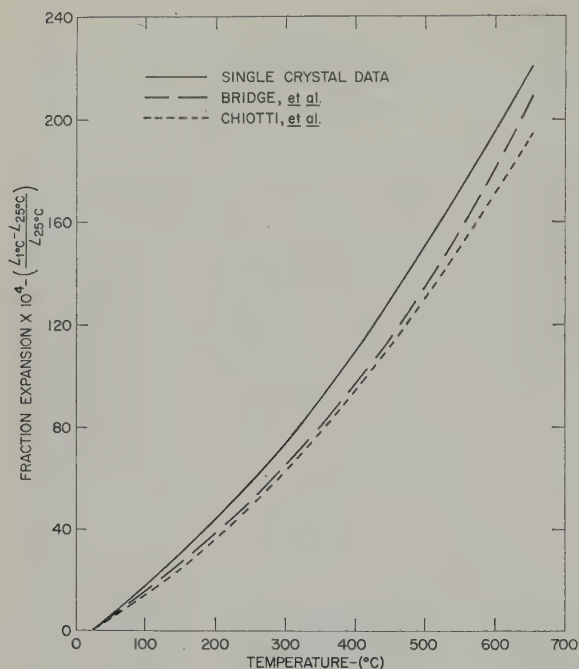


Fig. 3. Fraction expansion of alpha-uranium in the [001] direction.

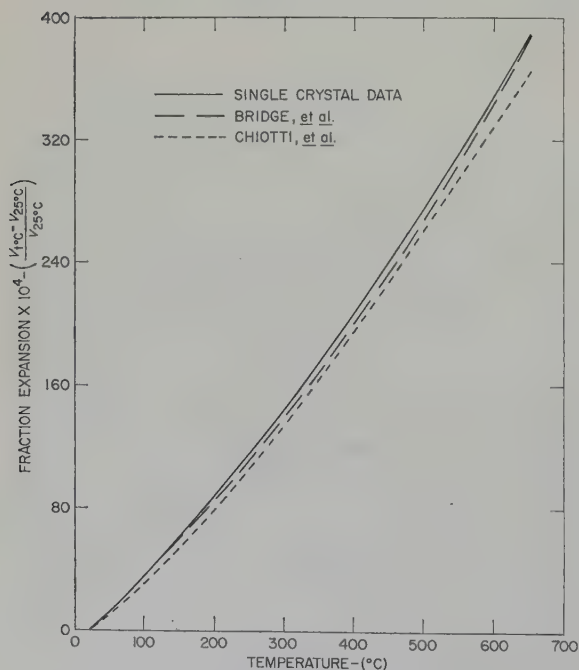


Fig. 4. Volumetric fraction expansion of alpha-uranium.

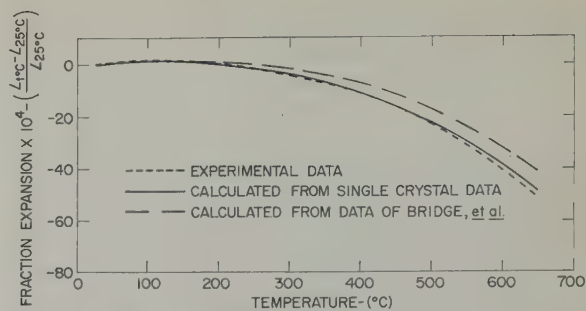


Fig. 5. Fraction expansion of a randomly oriented alpha-uranium single crystal.

13.5° from the [010] and 77° from the [001]. The calculated curve based upon the single crystal principal direction data agreed well with the experimental curve, whereas the curve based upon the lattice parameter data of Bridge *et al.* fell above it. The curve based upon the data of Chiotti *et al.* was not included; it fell further above the experimental curve.

The curves of the other five randomly oriented crystals, also tested in directions near the [010], were similar to the ones shown in fig. 5. One of the crystals showed good agreement with the curve calculated from single crystal principal direction data, and the experimental curves of two others fell between the single crystal and Bridge *et al.* calculated curves, but closer to the former. The experimental curve of a fourth crystal also was between the two calculated curves, but closer to the one from the data of Bridge *et al.* Finally, the experimental curve of the fifth crystal was above the Bridge *et al.* calculated curve. The two crystals which gave the poorest agreement with the single crystal calculated curves and another which also gave poor agreement were from the same source metal. All three crystals contained appreciable quantities of twins prior to testing, whereas the other three of six randomly oriented crystals did not. After testing, some of the twins persisted in the former three crystals, and their presence could well explain the poor agreement with the curves calculated from single crystal expansions. In any event, it was significant that five of the six experimental curves fell below those calculated from the data of Bridge *et al.*

4. Discussion

The thermal expansions obtained from dilatometric measurements of single crystals were somewhat different from those based upon lattice parameter data, namely with regard to the expansions found for the [010] and [001] directions (figs. 2 and 3). It is believed that these differences were caused by elastic strains in the polycrystalline samples employed for the lattice parameter measurements. In effect, the strains prevent the [010] direction from contracting as much as it could, and, in opposition, they prevent the [001] direction from expanding.

Three aspects of the data presented herein supported this viewpoint. The first was the fair agreement found for the volumetric expansions as derived from the three groups of data (fig. 4). If the inconsistencies associated with the lattice parameter data were not elastic in nature, there would be significant differences between the lattice parameter and the single crystal volumetric expansions. This agreement appeared to substantiate the internal validity of each group of data. Secondly, the association of elastic restraints with grain interactions was supported by a comparison of the single crystal expansions with those derived from the two sets of lattice parameter data. In both instances the restraints associated with the data of Chiotti *et al.* were greater than those indicated from the data of Bridge *et al.* (figs. 2 and 3). This was what might be expected since the former used massive samples for their measurements and the latter used more finely divided filings; intuitively, the elastic restraints in a massive polycrystalline sample would be greater than those in filings. Finally, the overall better agreement between observed and calculated expansion of randomly oriented crystals, as derived from the single crystal expansions, indicated that these data are more applicable than the lattice parameter data.

5. Conclusions

Dilatometric measurements performed on alpha-uranium single crystals of known orienta-

tion indicated that previously reported lattice parameter data were subject to inconsistencies because of elastic interactions between grains of the polycrystalline samples used for the measurements. Contraction in the [010] direction was restrained by the interactions as was expansion in the [001] direction. Single crystal and lattice parameter derived expansions for volume and the [100] direction agree well. The constants for equations representing expansion in the three principal crystallographic directions and volumetric expansion with temperature are given.

Acknowledgements

The author would like to thank J. L. Walker for assistance in performing some of the dilatometric measurements. In addition, he is extremely grateful to M. D. Odie who so carefully prepared the small single crystal specimens. This work was performed at Argonne National Laboratory under the auspices of the U.S. Atomic Energy Commission.

References

- 1) J. R. Bridge, C. M. Schwartz and D. A. Vaughan, Trans. AIME 206 (1956) 1282
- 2) P. Chiotti, H. H. Klepfer and R. W. White, Trans. ASM 51 (1959) 772
- 3) S. T. Konobeevsky, A. S. Zaimovsky, B. M. Levitsky, Y. N. Sohursky, N. T. Chebolarev, Y. V. Bobkov, P. P. Egorov, G. N. Nikolaev and A. A. Ivanov, Second Geneva Conference (1958) 15/P/2230
- 4) See for example the group of papers in Trans. ASM 50 (1958):
S. T. Zegler, R. M. Mayfield and M. H. Mueller, 905;
R. M. Mayfield, 926;
J. E. Burke and A. E. Turkalo, 943;
L. T. Lloyd and R. M. Mayfield, 954
- 5) P. Lehr and J. P. Langeron, Rev. de Met. 54 (1957) 257
- 6) P. Lehr and J. P. Langeron, Comp. Rend. 241 (1955) 1130
- 7) E. S. Fisher, Trans. AIME 209 (1957) 882
- 8) L. T. Lloyd, Argonne (USA) Report ANL 5372 (1959)

SELF-DIFFUSION IN BETA URANIUM

S. J. ROTHMAN, J. GRAY Jr., J. P. HUGHES and A. L. HARKNESS

Argonne National Laboratory, Argonne, Illinois, USA

Received 11 August 1960

The self-diffusion coefficient of uranium decreases by a factor of one hundred and fifty when the crystal structure changes from the b.c.c. gamma phase to the complex tetragonal of the beta phase. Even at temperatures high in the beta phase, the plots of $\log C$ vs. X^2 are curved, indicating that self-diffusion in beta uranium does not take place by isotropic volume diffusion alone.

Le coefficient d'autodiffusion de l'uranium décroît d'un facteur de 150 quand la structure cristalline de l'uranium passe de la phase γ cubique centrée à la phase β tétragonale complexe. Même aux températures élevées, les représentations graphiques de $\log C$ en

fonction de X^2 sont courbes pour la phase β , ce qui indique que l'autodiffusion n'est pas seulement due à une diffusion isotrope en volume.

Der Selbstdiffusionskoeffizient nimmt bei Umwandlung des Urans aus der kubisch raumzentrierten γ -Phase in die komplexe tetragonale Phase um den Faktor 150 ab. Selbst im oberen Temperaturbereich der β -Phase führen die Messergebnisse bei Auftragung von $\log C$ gegen X^2 zu gekrümmten Kurven. Dies stellt ein Anzeichen dafür dar, dass die Selbstdiffusion in β -Uran nicht nur als eine isotrope Volumendiffusion abläuft.

1. Introduction

The study of self-diffusion in uranium, initiated by the work on γ uranium^{1,2,3}, has been extended to the β phase. Self-diffusion in β uranium is of interest per se and because of its bearing on self-diffusion in the γ phase; the argument that the latter takes place by volume diffusion would be open to grave doubts if the plot of $\log D$ vs. $1/T$ were to continue as a straight line across the gamma-beta transformation temperature.

2. Experimental Techniques

Except when noted, the materials and techniques used in this work were the same as before¹).

Cylindrical diffusion samples, 1 cm diameter and about $\frac{1}{2}$ cm long, were prepared from high purity uranium containing 0.0343 % U^{235} (table 1). The preliminary heat-treatment and preparation of the samples were described previously. U^{235} was the tracer isotope.

TABLE 1

Chemical composition of highly depleted uranium †

Element	Content (ppm)
C	20
O ₂	10
N ₂	L10
Al	7
Cr	10
Cu	5
Fe	20
Mg	1
Mn	3
Ni	10
Si	10

L = less than

All other elements are below limit of spectrographic detection.

† C, N₂ and O₂ analysis courtesy of Ralph Bane, others of Joe Goleb.

The diffusion sample geometry used was that of the thin layer on a "semi-infinite" rod. Samples β -22, β -23, β -27 and β -28 (see table 2)

TABLE 2
Diffusion results

Run number	Annealing temperature, (° C)	Annealing time	Method of calculating D	D (cm ² /sec)	Estimated † maximum error in D (%)
β -22	700.0	340 h 16 min	Least squares fit of all eleven points	1.1×10^{-11}	13
β -23	760.0	264 h	Line drawn by eye through points 2, 4, 5, 6	2.1×10^{-11}	50
β -25	728.7	167 h 39 min	Line drawn by eye through points 1, 3, 4, 5, 6	6.0×10^{-12}	50
β -26	678.0	240 h	From relation $X = 2\sqrt{Dt}$ using first four points	2.7×10^{-12}	50
β -27	728.7	502 h 30 min	Line drawn by eye through points 2, 3, 5, 6	1.3×10^{-11}	50
β -28	688.0	185 h	Used for autoradiography		

† These were calculated by drawing different lines through the points. The error due to experimental factors is estimated to be 12 %.

were prepared by the cathodic sputtering technique⁴). Samples β -25 and β -26 were prepared in a similar manner, except that the preliminary gettering step was omitted, and, after the sample had been cleaned by cathodic sputtering, the U²³⁵ layer was deposited by vacuum evaporation instead of cathodic sputtering. The penetration curves showed that the evaporated isotope layers were one tenth as thick as the ones deposited by cathodic sputtering.

The samples were annealed in electric resistance furnaces. The specimens were placed directly into furnaces running at temperature to start the anneal, and were water-quenched to end it. The temperature fluctuations were $\pm 1^\circ\text{C}$. The given temperatures are accurate to $\pm 1^\circ\text{C}$.

After annealing, the samples were sectioned on a lathe⁵). Since a low diffusion coefficient was expected, thin sections (ca. 0.001 cm) were cut. The chips were weighed to ± 0.2 mg.

Sample β -27 and sections 11 and 12 from sample β -23 were analyzed for U²³⁵ mass

spectrometrically. The U²³⁵ contents of the other sections were determined using a fission counting apparatus developed by one of the authors⁶); the total uranium in these sections was determined either from chip weights or by chemical analysis.

Accurate fission counting requires so-called weightless deposits to avoid slowing of recoil atoms. These were prepared as follows: The chips from a section were transferred to a 25 ml volumetric flask and dissolved in 2-3 ml warm concentrated HNO₃. After cooling, the solution was made up to volume with 10 % HNO₃, and 25 microliters were pipetted onto a 2.3 cm (15/16") diameter, 0.013 cm (0.005") thick platinum foil. A 0.3 cm (1/8") wide ring at the outer circumference of the foil had first been coated with Zapon to keep the solution from flowing off the foil. Several drops of distilled water were added to fill the area inside the Zapon ring, and the solution was mixed with a slow air jet. The foil was placed under a canopy in a slow flow of NH₃, and the solution was evaporated slowly with a heat lamp. When

all the liquid was gone, the canopy was removed and the NH_4NO_3 film was sublimed with the heat lamp. Finally, the foil was flashed to a red heat in the flame of a Bunsen burner.

The determination of quantities of U^{235} by fission counting is based on the equation ⁷⁾:

$$N = \sigma \phi A$$

where N is the number of fissions in unit time, σ the fission cross-section of U^{235} , ϕ the neutron flux, and A the number of fissionable atoms present. This means that if one of the above described foils is irradiated in a known flux and the number of fissions is counted, the number of U^{235} atoms on the foil, and therefore the U^{235} concentration in the section, can be calculated.

The fission counter in which these determinations were carried out consists of two ionization chambers back to back. The sample foil and a standard foil were placed with their active faces away from each other in the center. A voltage of 135 volts was put across each chamber, and P-10 gas, a mixture of argon and methane, was flowed through the chambers. The whole assembly was inserted into a thermal column of reactor CP-5 at the Argonne Laboratory. Each ionization chamber had a separate counting circuit consisting of an amplifier, a single-channel analyzer, and a scaler. For this experiment, the analyzers were set to count all events above a certain energy level, which was taken as the center of the broad, flat plateau of the curve relating counts per minute to pulse height. Thus only fission events, which are much more energetic than other radiation encountered in the pile, were counted. It can be shown that under these conditions each fission is counted once, providing that the deposits are "weightless".

The flux was calculated from the number of fissions in the standard. The number of fissionable (U^{235}) atoms on the standard was accurately known from alpha counting. The scalers for sample and standard were turned on and off simultaneously to eliminate errors due to flux changes caused by pile oscillations. Since the thermal flux gradient in CP-5 is high, and the

foils were a finite distance from each other, a flux correction factor, f , which is a function of position in the pile, had to be determined. This was done using two standards.

2.1. AUTORADIOGRAPHY

To check the possibility of grain-boundary diffusion, autoradiographic studies were made on sample β -28. After the anneal, a taper section was cut inclined 3° to the initial interface and intersecting it. The autoradiograph shown was taken in a lead box in the West thermal column of CP-5 using an Ilford K-2 plate, which is supposedly sensitive only to fission tracks. The exposure was 2×10^{12} nvt.

3. Results

The solution of the diffusion equation that applies to the geometry used here is ⁸⁾:

$$C = \frac{q}{\sqrt{(\pi Dt)}} \exp(-X^2/4Dt)$$

where C is the concentration of U^{235} diffused into a section, X the distance of the center of the section from the original interface, q the amount of isotope deposited, t the time of anneal, and D the diffusion coefficient. The U^{235} concentrations were calculated from the fission counting data, and values of X were calculated from the chip weights. The corrections for the micrometer measurements of amounts of material removed ¹⁾ were not made because these measurements were too small to be accurate. Also, the first sections from many samples were not analyzed because these sections often contain oxidized U^{235} that did not partake in the diffusion.

The above equation predicts that plots of log C vs. X^2 (fig. 1) should be linear. The plot for sample β -25 is linear, the curve for sample β -22 is too scattered to tell, and the others are curved. For the last, straight lines were drawn through the first few points and D values were calculated from their slopes. The D values are given in table 2, and are plotted vs. $1/T$ in fig. 2 together with the data and least squares line of Adda *et al.*⁹⁾ and the data for self-

diffusion in gamma uranium^{1,2,3}). Because of the curved penetration plots, the scatter of D values, and the very narrow temperature

range, the activation energy and D_0 were not calculated.

4. Discussion

Since curved plots of $\log C$ vs. X^2 indicate possible grain boundary diffusion, plots of $\log C$ vs. X were made for several samples (fig. 3). These are in part straight lines. Such plots can be produced by either grain boundary diffusion¹⁰, or anisotropic diffusion. β -uranium, being tetragonal, has two diffusion coefficients, one parallel and one perpendicular to the 4-fold axis¹¹). If the grain size is larger than the mean penetration distance, and several large grains of different orientations make up the sample, penetration plots similar to these would be obtained. The autoradiographic studies indicate, within the resolution of the picture, that both grain boundary diffusion and anisotropic diffusion are present (fig. 4).

In view of the approximate method of determining D , the scatter in the D values[†] and the disagreement with some of the D values of Adda *et al.*⁹) is not serious. It is not clear whether these authors measured only volume

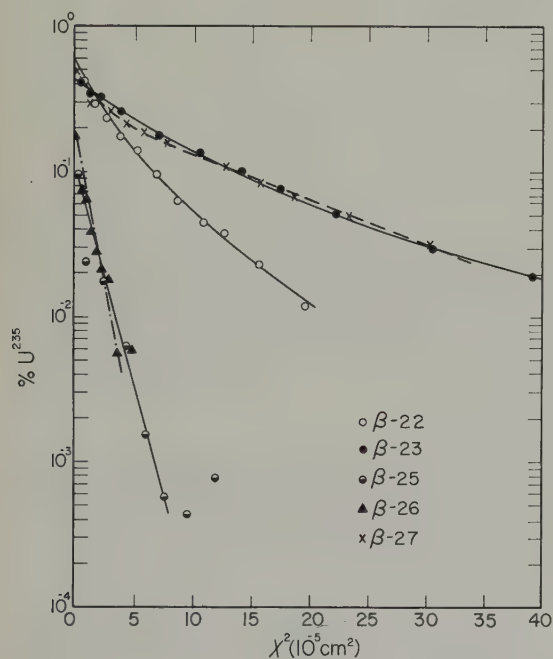


Fig. 1. Plots of $\log C$ vs. X^2 for self-diffusion in beta uranium.

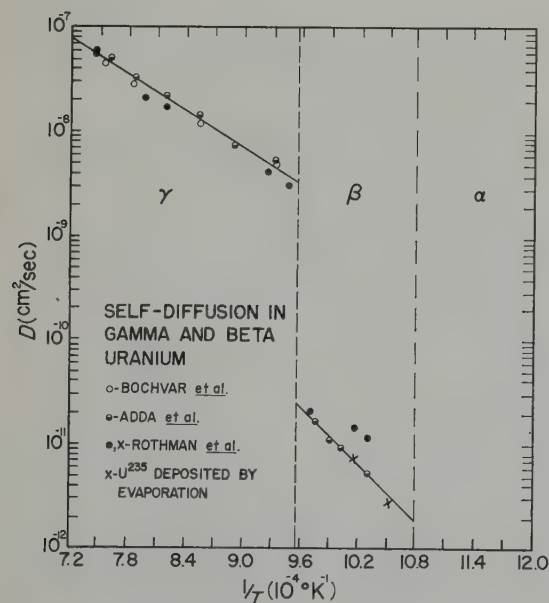


Fig. 2. Arrhenius plot for self-diffusion in gamma and beta uranium.

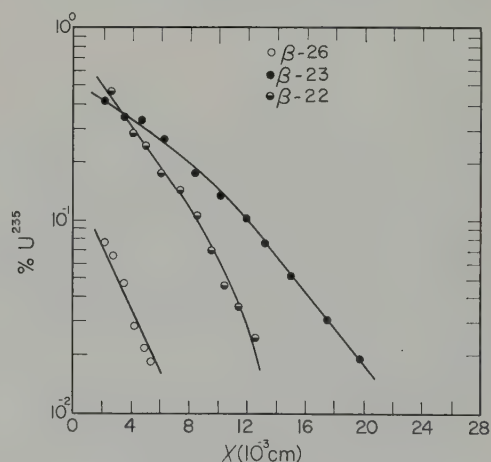


Fig. 3. Plots of $\log C$ vs. X for self-diffusion in beta uranium.

[†] For instance, the two D values obtained from samples on which the isotope layer was deposited by evaporation are lower than those from samples on which the isotope layer was deposited by cathodic sputtering. We believe that there are not enough data to say whether this is a real effect.



Fig. 4. Autoradiograph of sample β -28. A. Indication of grain boundary diffusion. B. Trace of grain in which diffusion took place faster than in its surroundings. $\times 64$.

diffusion or not. A possible explanation might be differences in grain size and orientation from sample to sample. In any case, the drastic decrease of D on crossing from the gamma phase into the beta phase is self evident. It is undoubtedly due to a change to covalent and strongly directional bonding in beta uranium, as suggested by Adda *et al.*

Acknowledgements

The authors are pleased to acknowledge the assistance of Stanley Swierk, R. E. Sowl, Matt Laug, Maurice Odie, J. R. Huizenga, M. Petheram, L. J. Nowicki, W. Sturm and Stanley Moore. The wet chemical analyses were done through the courtesy of L. E. Ross, Jean Vincenzi and R. P. Larsen. The authors are indebted to L. T. Lloyd, H. H. Chiswick and Y. Adda, CEN, Saclay, for discussions, and to Y. Adda for communicating his results prior to publication. The problem was first suggested by H. H. Chiswick. This work was performed at Argonne National Laboratory under the auspices of the U.S. Atomic Energy Commission.

References

- ¹⁾ S. J. Rothman, L. T. Lloyd and A. L. Harkness, Trans. AIME, 218 (1960) 605, or Argonne (USA) report ANL-5971 (1959)
- ²⁾ Y. Adda and A. Kirianenko, Comptes Rendus 247 (1958) 744
- ³⁾ A. A. Bochvar, V. Kuznetsova and V. S. Sergeev, Second Geneva Conference (1958) 15/P/2306
- ⁴⁾ R. Weil, S. J. Rothman and L. T. Lloyd, Rev. Sci. Instr. 30 (1959) 541
- ⁵⁾ S. J. Rothman and L. J. Sobocki, Rev. Sci. Instr. 30 (1959) 201
- ⁶⁾ J. Gray, Jr. and F. T. Hagemann, Unpublished work
- ⁷⁾ S. Gladstone and M. C. Edlund, The Elements of Nuclear Reactor Theory (New York, Van Nostrand, 1952) p. 44
- ⁸⁾ W. Jost, Diffusion in Solids, Liquids and Gases (New York, Academic Press, 1952) p. 17
- ⁹⁾ Y. Adda, A. Kirianenko and C. Mairy, J. Nucl. Mat. 1 (1959) 300
- ¹⁰⁾ J. C. Fisher, J. Appl. Phys. 22 (1951) 74
- ¹¹⁾ J. F. Nye, Physical Properties of Crystals (Oxford, 1957) p. 23

THE DIFFUSION OF GOLD IN GAMMA URANIUM

S. J. ROTHMAN

Argonne National Laboratory, Lemont, Ill., USA

Received 4 April 1960, and in revised form 11 August 1960

The diffusion of gold in gamma uranium has been measured using a radioactive tracer and the sectioning technique. The values of D_0 and the activation energy are 4.86×10^{-3} cm²/sec and 30 400 cal/mol respectively, fairly close to the values for self-diffusion in gamma uranium.

La diffusion de l'or dans l'uranium γ a été mesurée avec un traceur radioactif en utilisant la technique de sectionnement. Les valeurs de D_0 et l'énergie d'activation sont respectivement $4,86 \times 10^{-3}$ cm²/sec

et 30 400 cal/mol; elles sont assez proches des valeurs de l'autodiffusion dans l'uranium γ .

Die Diffusion von Gold in γ -Uran wurde unter Anwendung radioaktiver Spuren und durch Zerschneiden der Proben verfolgt. Für D_0 und die Aktivierungsenergie ergaben sich Werte von 4.86×10^{-3} cm²/sec und 30 400 cal/mol. Diese Werte kommen denen für die Selbstdiffusion in γ -Uran ziemlich nahe.

1. Introduction

This study is an attempt to throw some light on the anomalously low values of D_0 and the activation energy for self-diffusion in gamma uranium ^{1,2,3}).

The activation energy for self-diffusion in the case of the vacancy mechanism is the sum of the energies for vacancy formation and vacancy motion. Most of the latter is expended in pushing apart the atoms that surround the path between the diffusing atom and the vacancy, or in compressing the diffusing atom ⁴). By studying the diffusion of a tracer with a compressibility different from that of the base metal, it should be possible to see whether the compressibility of the uranium atom, or an internal electronic transition that makes the uranium atom smaller, is responsible for the anomalously low activation energy for self-diffusion. This idea is also applicable if self-diffusion in gamma uranium takes place by the ring mechanism ^{3,5}), since then a large part of the activation energy would be expended in expanding the lattice or in compressing the diffusing atom.

The tracer chosen in this study was gold. It

has a smaller compressibility than uranium (0.6×10^{-12} cm²/dyne for Au, 0.897×10^{-12} cm²/dyne for U at room temperature), as well as other desirable properties (finite solid solubility in gamma uranium, convenient radio-isotope etc.).

2. Experimental

Specimens of high purity uranium (table 1), 1 cm in diameter and $\frac{1}{2}$ to 1 cm thick, were cut from swaged rod. The specimens were water quenched from 690° C, annealed at 450° C, given a metallographic polish on one face,

TABLE 1

Chemical composition of uranium used in this study † (parts per million by weight)

Element ††	Content
C	11-13
N ₂	13
O ₂	27
Si	20
Mn	2

† All others below limit of spectrographic detection.

†† C, N₂ and O₂ analyses courtesy of Ralph Bane, others of Joe Goleb.

electropolished in a phosphoric acid bath, and given a final cleaning by cathodic sputtering⁶⁾. The radioactive gold tracer was deposited on the samples by vacuum evaporation. Two diffusion couples were prepared at one time. They were placed with their prepared faces against each other in a tantalum cup, which was sealed off in vacuo in a quartz capsule.

The diffusion anneals were carried out in electrical resistance furnaces controlled by millivoltmeter controllers with high current-low current circuits. The specimen temperatures were measured with calibrated Pt-10 % Rh Pt thermocouples. To start the anneal, the samples were placed directly into a furnace running at temperature. At the end of the anneal they were water quenched.

The samples were sectioned on a lathe after machining 0.1 to 0.13 cm off the radius; ten to sixteen sections, 0.005 to 0.01 cm thick, were cut from each sample. The total thickness of material removed from each specimen was measured with a micrometer. The chips were weighed to an accuracy of 1 % and dissolved in aqua regia, and the solutions were made up to 2 ml volume. Aliquots from these solutions were made up to standard height in a gamma counting tube and counted in a well-type scintillation counter. At least 10 000 counts were taken from each section. Corrections were made for decay and for the activity of the uranium when these exceeded 1 %.

3. Results

The solution to the diffusion equation for these experimental conditions is⁷⁾:

$$I = K \exp(-X^2/4Dt)$$

where I is the specific activity of a section in CPM/MG, X the distance of the section from the original interface, t the annealing time, D the diffusion coefficient, and K a constant for one sample. The values of X were determined from chip weights and corrected for chip losses and thermal expansion. The time required to heat the sample up to the beta-gamma transformation temperature was subtracted from the

annealing time, and the remaining time was adjusted to an average temperature using formulas similar to Armstrong's⁸⁾ and graphical integration. The D values were adjusted so that the total thickness removed equaled the difference between the micrometer measurements before and after sectioning. In the case of sample 5B, the difference between the measurements by micrometer and by weight of the amount of material removed was so great that the D value from this specimen was discarded.

Fig. 1 shows typical plots of $\log I$ vs. X^2 . Straight lines could be drawn through at least the first eight points (out of ten) on all curves; on some, the last point or two lay above the straight line. Such points were not used in calculating D .

Values of D , calculated by the method of least squares, are given in table 2 and plotted as a function of $1/T$ in fig. 2. A least-squares analysis of these data yields:

$$D = (4.86 \pm 1.3) \times 10^{-3} \cdot \exp(-30400 \pm 520/RT) \text{ cm}^2/\text{sec.}$$

The errors in the individual diffusion coefficients are estimated to be 5 %. The reported temperatures are accurate to better than $\pm 1^\circ \text{C}$, due to the averaging process mentioned above.

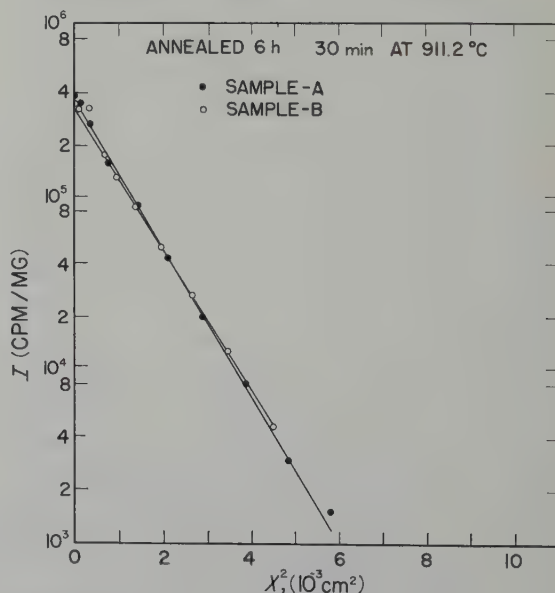


Fig. 1. Penetration plots for samples 3A and 3B.

TABLE 2
Diffusion data

Sample	Diffusion Temp. (°C)	Time	D (10^{-9} cm ² /sec)
1A	784.6	46 h 30 min	2.70
1B	784.6	46 h 30 min	2.63
2A	843.5	16 h 50 min	5.33
2B	843.5	16 h 50 min	5.47
3A	911.2	6 h 30 min	11.8
3B	911.2	6 h 30 min	10.9
4A	949.7	3 h 7 min	19.8
4B	949.7	3 h 7 min	18.9
5A	1006.8	2 h 0 min	31.8
5B †	1006.8	2 h 0 min	42.8

† Value discarded. See text.

4. Discussion

Although the activation energy for the diffusion of gold in uranium is significantly greater than that for self-diffusion (fig. 2), it does not approach the value expected from the usual correlation⁹⁾ with melting points, i.e. 56 kcal/mol. In terms of the ideas considered in the introduction, it can be said that the great difference between the measured activation energy for self-diffusion and the expected value is not due to ease of compression of the moving uranium atom. If it were, one would expect that the activation energy for the diffusion of gold would be in the neighborhood of 56 kcal/mol. If self-diffusion takes place by the vacancy mechanism, the low activation energy may be due to easy deformation of the crystal lattice (weak bonding) in gamma uranium, as suggested by its very low mechanical strength, or to a very low energy of vacancy formation. A quantitative discussion of this point is not possible because the elastic constants of gamma uranium are not known. For the same reason, quantitative comparison with other theories of diffusion is also difficult. The direction of the change in the activation energy is in agreement with the theory proposed by Lazarus¹⁰⁾; the activation energy for solute diffusion is greater than that for self-diffusion because the valence of the solute is less than the valence of the solvent.

These data are not evidence for or against ring diffusion in gamma uranium. The closeness of the activation energy and D_0 to those for self-diffusion indicate that the diffusion of gold takes place by the same mechanism as self-diffusion.

Comparison of the present data with the recent work of Adda and co-workers on the diffusion of impurities in gamma uranium^{11,12)} shows that:

1. the present D values are at least an order of magnitude lower,
2. the present activation energy is about 2 kcal/mol lower than their lowest,
3. the present D_0 is two orders of magnitude lower than the lowest reported by Adda *et al.*

Neither the activation energy nor the D_0 values found by the Saclay group correlate with the valence or the atomic size of the solutes. The present data do not fit the only correlation they did observe, a monotonic decrease of D with increasing Goldschmidt radius of the solute. The data on self-diffusion do not fit their plot either.

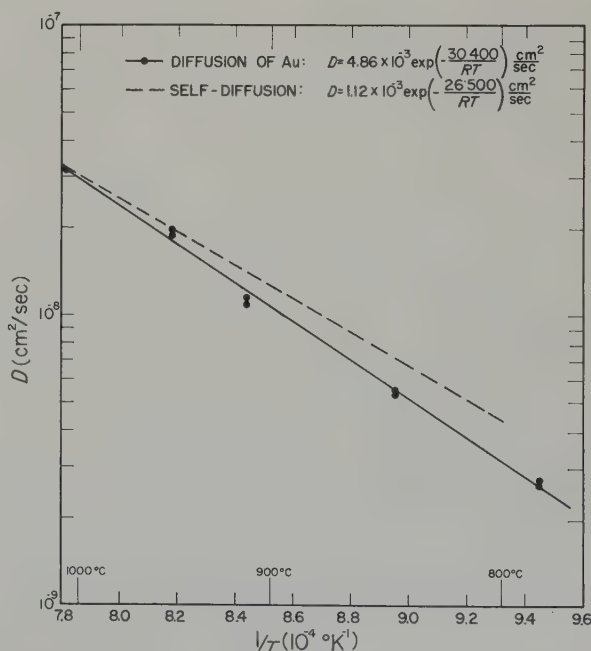


Fig. 2. Arrhenius plot for diffusion in uranium (data on self-diffusion area composite of 1,2,3.)

Acknowledgements

The author is obliged to Peter Moskal of Central Shops for help with the sectioning, Mrs. Ruth Hanna and L. E. Ross of R. P. Larsen's group, Chemical Engineering Division, for the counting, S. A. Moore of this Division for help with the experimental work and calculations, H. J. Wheeler and H. J. Thatcher of Reactor Engineering Division and B. S. Garbow and W. G. Greenhow of Applied Mathematics Division for doing the least-squares analyses, and to L. T. Lloyd and H. H. Chiswik of this Division and Y. Adda of CEN, Saclay, for helpful discussions. This work was performed at Argonne National Laboratory under the auspices of the U.S. Atomic Energy Commission.

References

- 1) A. Bochvar, V. Kuznetsova and V. Sergeev, Second Geneva Conference (1958) P/2306
- 2) Y. Adda and A. Kirianenko, *Comptes Rendus* **247** (1958) 744
- 3) S. J. Rothman, L. T. Lloyd and A. L. Harkness, *Trans. AIME* **218** (1960) 605
- 4) R. A. Swalin, *Acta Met.* **5** (1957) 443
- 5) G. M. Pound, W. R. Bitler and H. W. Paxton, Private communication
- 6) R. Weil, S. J. Rothman and L. T. Lloyd, *Rev. Sci. Instr.* **30** (1959) 772
- 7) W. Jost, *Diffusion in Solids, Liquids and Gases* (New York, 1952) p. 17
- 8) H. Armstrong, *Trans. AIME* **212** (1958) 450
- 9) W. Jost, *Diffusion in Solids, Liquids and Gases* (New York, 1952) p. 239
- 10) D. Lazarus, *Phys. Rev.* **93** (1954) 973
- 11) Y. Adda, Mlle. V. Levy, Z. Hadari and J. Tournier, *Mem. Sci. Rev. Met.* **57** (1960) 278
- 12) M. Mosse, Mlle. V. Levy and Y. Adda, *Comptes Rendus* **250** (1960) 3171

EFFECT OF ORIENTATION AND TEMPERATURE ON THE MODES OF DEFORMATION OF URANIUM†

R. O. TEEG

Central Research Laboratories of Texas Instruments, Dallas, Texas, USA

and

R. E. OGILVIE

Massachusetts Institute of Technology, Cambridge, Mass., USA

Received 1 September 1960

Slip in alpha uranium on the $\{110\}$ at -196°C was established by two-surface analysis and the slip direction was determined to be the $\langle 001 \rangle$. Some evidence is presented which permits the postulation that the mechanism involves a movement in two $\langle 112 \rangle$ directions to produce an overall slip direction of $\langle 001 \rangle$. The critical shear stress for $\{010\} \langle 100 \rangle$ slip and cross-slip was found to increase substantially relative to other mechanisms at low temperature. A direct confirmation of the $\langle 100 \rangle$ slip direction was obtained by the disappearing trace method. Kinking on the (100) plane was observed to take a number of forms. Kink bands as narrow as 5 microns and as thick as 100 microns were observed, as well as a new microkinking mechanism. The axis of rotation for kinking was confirmed to be the $\langle 001 \rangle$ direction. Twinning on the $\{130\}$, $\{176\}$ and $\{172\}$ planes was observed, with the $\{130\}$ plane by far the most active at both -196°C and 350°C . Areas of operability were consistent with theoretical predictions. No new twin planes were observed.

La déformation par glissement à -196°C sur le plan $\{110\}$ dans l'uranium α fut établi par l'analyse des traces sur deux surfaces, ce qui conduisit à la direction de glissement $\langle 001 \rangle$. On présente quelques faits expérimentaux qui permettent de penser que le mécanisme de déformation implique un mouvement dans deux directions $\langle 112 \rangle$ ce qui conduit à une direction de glissement finale $\langle 001 \rangle$. Le taux de cisaillement critique pour le glissement $\{010\} \langle 100 \rangle$ et le glissement transverse (cross-slip) augmentent beaucoup à basse température comparativement à d'autres mécanismes. Une confirmation directe de la direction de glissement $\langle 100 \rangle$ fut donnée par la méthode de la "trace évanescence":

On observa que le pliage sur le plan (100) prenait

un certain nombre de formes. Des bandes de pliage aussi étroites que 5 microns et aussi épaisses que 100 microns furent observées ainsi qu'un nouveau mécanisme de "micropliage". L'axe de rotation pour le pliage fut confirmé comme étant la direction $\langle 001 \rangle$. Le maclage sur les plans $\{130\}$, $\{176\}$ et $\{172\}$ fut observé, le maclage sur le plan $\{130\}$ étant de loin le plus actif à la fois à -196° et 350°C . Sur le diagramme stéréographique, les orientations des cristaux donnant lieu à tel ou tel mécanisme de déformation concordait avec celles prévues théoriquement. Aucun nouveau plan de maclage ne fut observé.

Das Gleiten in α -Uran, das bei -196°C auf $\{110\}$ stattfindet, wurde durch Analyse von zwei Oberflächen festgestellt. Als Gleitrichtung wurde $\langle 001 \rangle$ gefunden. Es waren einige Anzeichen vorhanden, die zu der Annahme berechtigen, dass die Gesamtgleitung in $\langle 001 \rangle$ -Richtung sich aus Bewegungen in zwei $\langle 112 \rangle$ -Richtungen zusammensetzt. Die kritische Schubspannung für $\{010\} \langle 100 \rangle$ -Gleiten und Quergleiten wächst im Vergleich zu anderen Mechanismen bei niedrigerer Temperatur beträchtlich an. Ein direkter Nachweis der $\langle 100 \rangle$ Gleitrichtung gelang mit Hilfe der Methode verschwindender Gleitspuren. Es wurde beobachtet, dass Knicken auf der (100) Ebene auf verschiedene Art stattfindet. Knickbänder von $5\ \mu$ und von $100\ \mu$ Dicke wurden ebenso gefunden wie ein neuer Mechanismus für Mikroknicken. Es bestätigte sich, dass die Rotationsachse beim Knicken in $\langle 001 \rangle$ -Richtung weist. Weiterhin wurden Zwillingsbildungen auf den $\{130\}$ -, $\{176\}$ - und $\{172\}$ -Ebenen beobachtet. Dabei wurde die $\{130\}$ -Ebene sowohl bei -196°C als auch bei 350°C weitaus am meisten betätigt. Die wirksamen Verformungsflächen waren im Einklang mit theoretischen Voraussagen. Neue Zwillingsebenen wurden nicht beobachtet.

† This paper is based on a thesis submitted by R. O. Teeg in partial fulfillment of the requirements for the Sc.D. degree. The work was sponsored by AEC contract AT(30-1)-981.

1. Introduction

The modes of deformation in alpha uranium that have been reported by Cahn, Lloyd and Chiswick are summarized in table 1. Cahn¹⁾ working with large-grained polycrystalline material deformed by thermal cycling, abrasion and compression, reported numerous mechanisms of deformation. As a consequence of the polycrystalline nature of the material and the method of deformation, the operative modes were not reported as a function of orientation or temperature.

In room temperature studies of single crystals Lloyd and Chiswick²⁾ observed additional slip and twinning mechanisms. They also confirmed many of Cahn's results, but, in spite of compressing apparently ideally oriented specimens, did not observe $\{110\}$ slip. As a consequence of using single crystals, Lloyd and Chiswick were able to report their data as a function of orientation. There are indications from both publications that all slip and cross-slip planes whose poles lie in the (100) zone may have the $\langle 100 \rangle$ slip direction.

In this work, high purity uranium was

obtained in the form of 1" diameter bar through the courtesy of Argonne National Laboratory. The processing of the uranium was based on the work of Fisher³⁾: the material was first quenched from the gamma phase in order to obtain an optimum dispersion of impurity particles. A fine equi-axed grain structure with a strong $\langle 010 \rangle$ rod texture was produced by a series of swaging and recrystallization operations, and then large crystals were obtained by gradient annealing the final 0.5 cm ($\frac{3}{16}$ ") rods at 655° C. The specimens were mounted in plastic in order to prevent deformation during the grinding operations required to isolate single crystals.

Laue back reflection photographs were taken on two adjacent metallographic faces 90° apart and the orientations thus determined were generally found to be consistent with each other to within 1 degree. As indicated by the size and shape of the reflections, the crystals showed good perfection and were free of substructure. The orientations of occasional $\{130\}$ twins observed in as-prepared crystals permitted an additional independent check on the orientation of the crystals.

TABLE 1
Summary of data on modes in alpha uranium

	Cahn's ¹⁾ evidence		Lloyd and Chiswick's ²⁾ evidence	
	No. of pole loci	2 surface proof	No. of pole loci	2 surface proof
(130) twin	numerous	×	38	×
"(172)" twin	numerous		62	×
"(176)" twin			20	×
(112) twin	7		6 (short)	
(121) twin	3		6 (short)	
(110) twin			1	
(110) slip	4		1	
(010) slip	6		12	×
(011) slip			9	
(011) cross-slip	observed			
(013) cross-slip	observed			
(001) cross-slip	considered "probable"		5 crystals	
(023) cross-slip	considered "probable"			
(100) kinking	5		1	×

A total of 12 crystals were oriented and their direction of compression with respect to their principal crystallographic axes is shown in fig. 1.

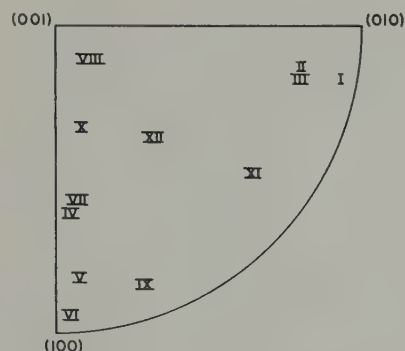


Fig. 1. Orientation of single crystals prepared for this study.

A total of 17 compressions were made on crystals at -196°C . The compression device consisted of a vice arrangement with the compression platens closely aligned parallel to each other, with the direction of movement exactly normal to the plane of the platens. Temperature control was achieved by immersing the entire apparatus in a bath of liquid nitrogen. In order to ascertain that thermal stresses resulting from the rapid cooling did not, in themselves, cause deformation traces, a number of specimens were thermally cycled between -196°C and ambient temperature. Except for an infrequent $\{130\}$ twin this cycling did not appear to affect the crystal.

Seven crystals, five of which were prepared by regrinding and polishing undeformed sections of samples previously compressed at low temperature, were deformed at 350°C in a resistance-heated evacuated compression device evacuated to 10^{-5} millimeters. The temperature was controlled by a chromel-alumel thermocouple immediately adjacent to the specimen. All deformed specimens were observed metallographically and angular measurements of the traces were made with a precision optical protractor. The data were plotted stereographically by the usual methods.

2. Results and Discussion

2.1. $\{010\}$ SLIP

Slip on the $\{010\}$ plane at room temperature was observed by both Cahn¹⁾ and Lloyd and Chiswik²⁾ and was considered to be a major mode of deformation by both investigators. Slip may be expected to be less active at -196°C because the critical shear stress for slip increases with decreasing temperature, while the stress required to initiate twinning is considered to be relatively insensitive to temperature.

This is certainly the case. Deformation of ten crystals (I, II, IV, V, VII, VIII, IX, X, XI, XII) at liquid nitrogen temperatures did not produce a single trace of slip on the $\{010\}$, while twinning on the $\{130\}$ and $\{176\}$ planes was much in evidence. In particular, crystal XI was oriented so that the direction of applied stress made an angle of $\theta = 38^{\circ}$ with the pole of the (010) and $\chi = 55^{\circ}$ with the $[100]$ slip direction, producing a relative applied shear stress ($\cos \theta \cos \chi = 0.45$) which was 90 percent of the maximum for an ideally oriented specimen. The fact that no slip occurred in crystal XI emphasized the strong effect of temperature on the critical stress for $\{010\}$ slip.

The results on crystals I and II provide further information. These crystals deformed exclusively by $\{130\}$ twinning at -196°C , but evidenced $\{010\}$ slip along with $\{130\}$ twinning at 350°C , even though neither crystal was desirably oriented for $\{010\}$ slip. Furthermore, crystal XII evidenced no slip mechanisms at low temperature, but contained substantial $\{010\}$ slip with cross-slip at 350°C . It was not possible to identify the cross-slip planes with accuracy because of the shortness of the traces.

With regard to slip direction, both previous investigators concurred on the $\langle 100 \rangle$. Cahn¹⁾ defined the direction by noting that cross-slip was not observable when the $\langle 100 \rangle$ direction (common to all participating planes) was roughly parallel to the surface of the specimen. Lloyd and Chiswik²⁾ indicated the $\langle 100 \rangle$ from Laue rotations about the (001) reflection, this pole being mutually perpendicular to the

slip direction and the pole of the slip plane.

Crystal II permitted a direct confirmation of the slip direction. This crystal was prepared so that the $\langle 100 \rangle$ was nearly parallel to face B and the absence of slip traces in this face confirmed the slip direction by direct observation.

2.2. (100) KINKING

Kinking may be described crystallographically as a rotation of the lattice about an axis which is normal to major slip direction and to the pole of the major slip plane. For kinking associated with the $\{010\} \langle 100 \rangle$ slip system in alpha uranium, this axis is the $\langle 001 \rangle$.

Kinking was observed in crystals V, VI, IX, and XI. Although the plane of the kink band was approximately the same for all traces the appearance of the bands varied substantially. The broad (about 100 microns thick) bands observed in crystal IV at -196°C , were reported previously by Lloyd and Chiswick²).

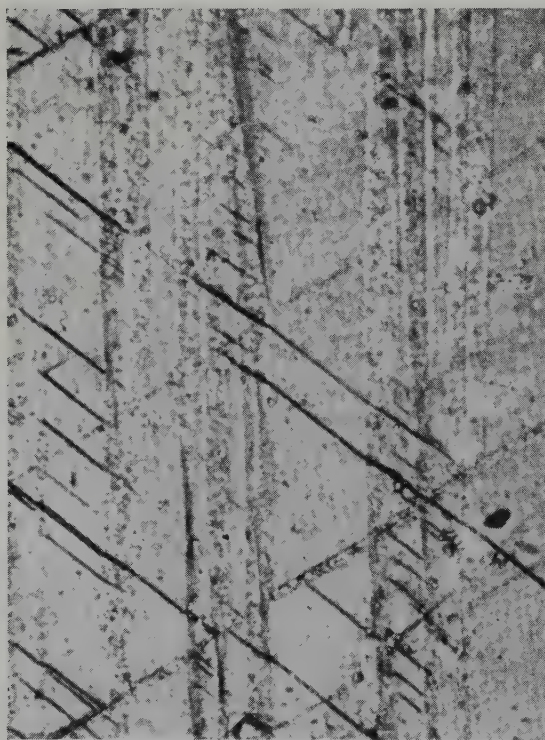


Fig. 2. Thin kink bands shown with $\{130\}$ twins after -196°C compression. Crystal V. $450\times$ Pol. Lt.



Fig. 3. Wavy traces observed after 350°C compression. Crystal VI. $140\times$ Bright Ill.

In crystal V at -196°C , however, the kinks formed had a thickness of only about 5 microns, as shown in fig. 2. The plane of these thin kink bands could be determined quite accurately, and it was found to be near the (310) while the thicker bands had been found to fall nearer the (110). This is consistent with the crystallographic description of kinking as a rotation about the (001), such rotation causing the apparent pole of the kink plane to move on the (001) zone away from the (100) pole.

In addition to the above-mentioned bands, a "microkinking" mechanism was observed in crystals V and VI at 350°C . This mechanism is shown in fig. 3 and is quite similar in superficial appearance to the "non-crystallographic" slip occasionally reported in the literature. The true identity of these markings in crystal VI was established by three experimental arguments. First, a stereographic solution of an extension of the short traces on two faces of the crystal indicated the pole of the plane to lie in the (001) zone, between the (310) and (110) poles, consistent with kinking. Second, a metallographic

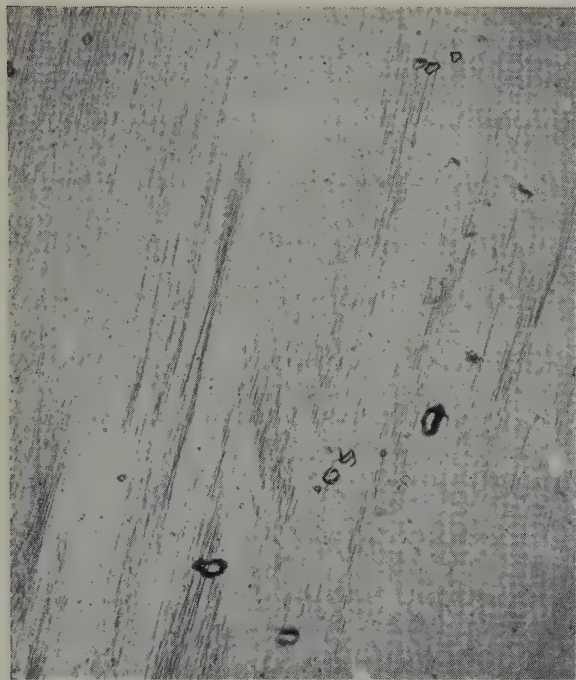


Fig. 4. Same face as shown in fig. 3 after grinding and electro-polishing showing rotated lattice under polarized light. Crystal VI. $75\times$

electrolytic polish of the surface showed small regions of rotated lattice when viewed under polarized light (fig. 4). And finally, the orientation of the specimen was such that the $[001]$ was normal to one of the faces, permitting a macroscopic observation of the rotation accompanying kinking.

The fourth form of kinking was recorded in crystal XI at -196°C . This crystal was well oriented for $(010) [100]$ slip and the presence of kinking is evidence of the high critical shear stress for such slip at low temperatures. It is the appearance of the kink which is of interest here. Fig. 5 shows an almost "classical" appearance, with the kink delineated by $\{130\}$ twins which pass through it. Of particular interest is the gradual transition of the lattice from unknicked to knicked structure, in sharp contrast to the narrow kink boundaries in crystal V.

2.3. $\{110\}$ SLIP

Previous investigators have noted about five pole loci which were consistent with the $\{110\}$

plane. Cahn¹⁾ predicted that the slip direction for such a plane would likely be the $\langle 110 \rangle$ or the $\langle 112 \rangle$. He noted that an experimental determination of the slip direction would be of theoretical interest since the $\langle 112 \rangle$ is the closer packed direction, but the atoms are not packed in a strictly straight line. Attempts by Lloyd and Chiswick to confirm the existence of $\{110\}$ slip proved unsuccessful in spite of their careful attempts to orient a specimen ideally for $\{110\}$ $\langle 110 \rangle$ slip.

Two-surface analyses of crystals IV and VII both yielded unequivocal proof of the existence of $\{110\}$ slip. A total of 16 traces were paired on faces A and B of crystal IV after the first compression, and numerous traces were paired in crystal VII. Both crystals contained both (110) and $(1\bar{1}0)$ traces after deformation at -196°C .

Identification of the traces as slip traces was



Fig. 5. "Classical" kink band delineated by $\{130\}$ twins in crystal XI.

accomplished by lightly electropolishing the slipped faces and noting that all evidence of the traces disappeared when viewed under bright or polarized illumination. This procedure was followed after numerous deformations of both crystals and always resulted in the disappearance of all evidence of all $\{110\}$ traces. The slip lines are more properly termed bands, since they had substantial thickness.

The slip directions were determined by an application of the disappearing trace method to crystal IV, then double checked with crystal VII. In the first compression of crystal IV, face A contained the $[114]$, midway between the $[001]$ and $[112]$ directions in the $(1\bar{1}0)$ slip plane. Slip was observable in both faces. A repolish of the specimen to an included angle of 110° then placed the $[001]$ parallel to face A. A second compression of this specimen gave $(1\bar{1}0)$ and (110) traces in face B, but no visible traces in face A, indicating the slip direction to be $[001]$! Another repolish of the specimen to an included angle of 71° to place the $[112]$

in face A and another compression at -196°C resulted in clear $(1\bar{1}0)$ traces in face A, confirming that the $[112]$ was indeed not the slip direction.

In order to check the slip direction, crystal VII was prepared with the $[001]$ parallel to face A. Heavy compression at -196°C produced very sharply defined $(1\bar{1}0)$ and (110) traces (see fig. 6) in face B with no slip traces visible in face A, confirming the $[001]$ slip direction.

The wide, feathered twin bands shown in fig. 6 are $\{176\}$ twins and the thin, vertical trace is a twin of the $\{130\}$ type. After approximately one week a second examination of the surface which had now become oxidized permitted very faint tinted $(1\bar{1}0)$ traces to be observed in face A under strong oblique illumination.

These traces were paired with traces in the other face, permitting a two-surface analysis of the $(1\bar{1}0)$ as the operative plane.

This determination of the $\{001\}$ slip direction leads to a consideration of the mechanisms involved. It is apparent that the closest packed direction is the $\{112\}$ with a spacing of approximately 3.0 \AA , and the second closest packing is in the $\{110\}$, where the spacing is about 3.3 \AA . The distance between atoms "in line" in the $[001]$ is 5.0 \AA ; yet this is the observed direction. In view of the complexity of the binding in this structure, it is difficult to predict the easiest path for movement of a dislocation, or dislocations consistent with experimental results.

Laue back reflection photographs of the slipped region of crystal IV give some indication of the mechanisms involved. Rotations about *two* axes were noted in some photographs. Although the axes of rotation could not be determined conclusively, they appeared to be consistent with the $[112]$ in a number of photographs. This was not surprising, since a duplex $[\bar{1}12]$ plus $[1\bar{1}2]$ vector is parallel to the $[001]$.

2.4. $\{172\}$ TWINS

A few traces of twinning on the $\{172\}$ plane were observed in crystals VII, X and XI

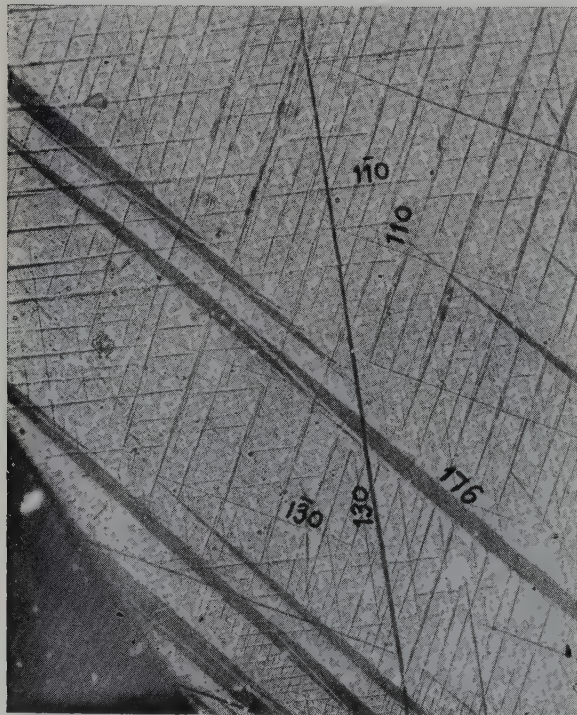


Fig. 6. Sharply defined (110) slip traces in face B of crystal VII. Pol. Lt.

before compression. A few traces were produced during low temperature deformation. A two-surface analysis was possible only on crystal V, which exhibited substantial twinning of this type which appeared to form as a result of complex stresses produced during the kinking process.

Deformation by $\{172\}$ twinning was infrequent at low temperature and entirely absent in all crystals deformed at elevated temperature indicating a relatively high "critical stress" for the formation of such twins relative to other possible modes.

2.5. $\{176\}$ TWINNING

Twinning on the $\{176\}$ was observed at both -196°C and 350°C . Twin traces, particularly at low temperature, tended to be very thick, and to have "feathered" or split ends. Both these characteristics are shown in fig. 6 in which the thick $\{176\}$ twins are readily distinguishable from the $\{110\}$ slip traces and the thin $\{130\}$ twin traces.

Twins of the $\{176\}$ type were found in crystal VIII, near the (001) and in crystals deformed at low temperature near the (100). The latter invariably appeared to originate in kink bands, having maximum thickness near the kink band and becoming thinner away from the bands. Such fluctuations in thickness and tendency to "feather" were noted generally at -196°C and also at 350°C in crystal VIII. There are three points with regard to $\{176\}$ twins which should be noted:

1. The great width of the $\{176\}$ twins (10 to 50 microns) compared with $\{172\}$ or $\{130\}$ twins (about 2 microns) was not unexpected in view of the magnitudes of shear (0.216, 0.228 and 0.299 respectively). Considerably wider twin bands in other metals, such as zirconium⁴) are generally associated with smaller shears, as in this case.

2. It was noted that the poles of $\{176\}$ twins obtained by the two-surface analyses tended to congregate some 2° to 4° away from the $\{176\}$ toward the (100) zone.

3. The area in which $\{176\}$ twins were

observed as an independent mechanism, was quite small in comparison with the predictions of Frank and Thompson⁵) but still consistent with their theory. It would appear that the "critical stress" for formation of such twins is relatively high and that they can form only near the $\{001\}$ when other twinning mechanisms are effectively suppressed.

2.6. $\{130\}$ TWINS

By far the most frequent twinning plane observed was that of the $\{130\}$. All crystals contained a few $\{130\}$ twins after preparation and indeed such twins were found to be highly desirable, since they permitted the orientation of the crystal to be established with greater accuracy than is possible by Laue methods.

Although $\{130\}$ twins were observed in every crystal tested, and at all temperatures, the orientations for which substantial twinning occurred were in good agreement with the predictions of Frank and Thompson⁵), as shown in fig. 7.

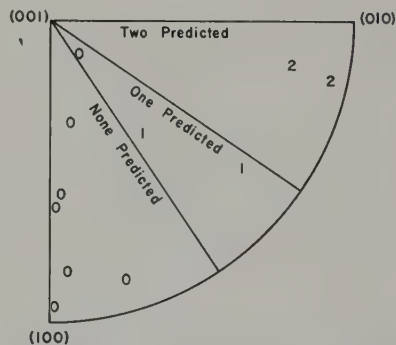


Fig. 7. Operability of $\{130\}$ twins compared with predicted regions.

The appearance of such twins varied substantially with temperature. This was particularly noticeable in crystals I and II which evidenced very thin traces at -196°C , but a thick, lenticular, basket weave pattern of traces after a 350°C compression.

3. Other Modes

One of the reasons for deformation at -196°C was the possibility that new twinning

mechanisms might be observed or that other tentatively identified or predicted twinning modes might be operative. This was found not to be the case. The stresses required for {130} twinning, {176} twins and (100) kinking appear to be sufficiently small at all orientations tested to exclude other mechanisms at -196°C .

The only trace which was not consistent with known modes was in crystal VIII after a heavy compression at 350°C . The trace was that of slip and it appeared to be consistent with the (001) plane. This would not be unexpected at elevated temperatures in view of the number of

slip planes already established which belong to the (100) zone.

References

- ¹⁾ R. W. Cahn, AERE (Harwell) Report, M/R 740 (1951)
- ²⁾ L. T. Lloyd and H. H. Chiswik, Argonne National Laboratory (USA) Report, ANL-5367 (1954)
- ³⁾ E. S. Fisher, Argonne National Laboratory (USA) Report, ANL-5021 (1954)
- ⁴⁾ E. J. Rapperport, Deformation of Zirconium, Sc.D. Thesis (Massachusetts Institute of Technology, 1955)
- ⁵⁾ F. C. Frank and N. Thompson, *Acta Met.* 3 (1955) 30

GRAPHITE-METAL COMPATIBILITY AT ELEVATED TEMPERATURES†

J. C. BOKROS

John Jay Hopkins Laboratory for Pure and Applied Science, General Atomic Division of General Dynamics Corporation, San Diego, California, USA

Received 11 May 1960

Numerous metals and alloys were screened for application as a cladding material on graphite to operate in helium at temperatures up to 1010° C. It was found that the heat-resistant nickel-base alloys, the stainless steels, and molybdenum all carburized rapidly above 816° C. In the case of niobium, a reactive metal, the results emphasize the importance of maintaining high purity helium to prevent embrittlement. Of the alloys tested, nickel-copper alloys appeared to be the most promising for use as a high-temperature graphite cladding. Aging data indicated that Monel is more resistant to graphitization than nickel.

De nombreux métaux et alliages ont été étudiés en vue de leur application comme matériaux de placage sur graphite, en atmosphère d'hélium jusqu'à la température de 1010° C. On a trouvé que les alliages réfractaires à base de nickel, les aciers inoxydables et le molybdène se carburaient tous rapidement au-dessus de 816° C. Dans le cas du niobium, métal très réactif, les résultats soulignent l'importance d'avoir de l'hélium de très haute pureté pour empêcher la fragilisation du métal.

1. Introduction

Power-reactor designs which utilize graphite as a moderator often require that structural and cladding alloys operate in contact with graphite for long periods of time at high temperature. For this type of application, it is essential that alloys resist carburization and retain their mechanical properties.

The semihomogeneous fuel element designed for the Maritime Gas-cooled Reactor (MGCR) ††

De tous les alliages essayés, les alliages Ni-Cu semblent être les plus intéressants pour le placage sur graphite à température élevée. D'après d'anciennes publications, le monel est plus résistant à la graphitisation que le nickel.

Es wurden zahlreiche Metalle und Legierungen für die Umhüllung von Graphit ausgetestet. Die Umhüllung sollte bei Temperaturen bis 1010° C in Heliumatmosphäre brauchbar sein. Die Untersuchung ergab, dass hochwarmfeste Legierungen auf Nickelbasis, rostfreie Stähle und Molybdän oberhalb 816° C unter Karbidbildung mit Kohlenstoff heftig reagieren. Bei Niob weisen die Ergebnisse sehr deutlich auf die Notwendigkeit hin, zur Vermeidung einer Versprödung nur hochreines Helium anzuwenden. Von allen geprüften Legierungen scheinen Nickel-Kupfer-Legierungen als Hüllenwerkstoff für Graphit bei hohen Temperaturen die besten Aussichten zu haben. Ergebnisse über die Alterung liessen erkennen, dass Monel gegen Karbidbildung einen höheren Widerstand aufweist als Nickel.

requires that a metallic fuel cladding operate in contact with graphite in a temperature range of 480° C to 930° C. The cladding must retain the fission fragments and prevent their escape into the high-pressure (1000 psi) helium coolant. The metal does not require structural strength since it is supported by the fuel pellets on the inside and by the graphite moderator on the outside, but it must be ductile so that thermal stresses induced during thermal cycling

† This work was performed for the Atomic Energy Commission—Maritime Administration under Contract AT(04-3)-187.

†† Designed for the U.S. Atomic Energy Commission by General Atomic Division of General Dynamics Corporation.

can be relieved by plastic flow. Obviously, the closer the coefficient of expansion of the cladding is to that of the fuel, the lower the thermally induced stresses. The material selected for this application must necessarily possess the following characteristics:

1. It must resist embrittlement by carburization in the range 480° C to 930° C.
2. It must possess a low thermal coefficient of expansion, similar to that of graphite.
3. It must have a low thermal-neutron capture cross section.
4. It must have a high melting point.
5. It must resist attack by impurities in the helium coolant stream.
6. It must be available and fabricable into the desired cladding configuration.

Metals which do not react with graphite to form carbides are among the choices for this application. The investigations of Hägg¹⁾ have shown that simple geometric concepts can account for the normal interstitial carbide structures and that carbides of the transition elements form simple structures only if the ratio of the radius of the carbon atom to the radius of the metal atom is between 0.41 and 0.59. For example, the elements from scandium through manganese in the periodic table have favorable ratios and form the normal carbide structures in which the carbon atom is octahedrally coordinated. Iron has a borderline ratio of 0.60 and forms a complex carbide structure. The octahedral holes in the two elements following iron, cobalt and nickel, cannot accommodate the carbon atom and simple carbides are not stable. This simple geometric picture, however, is not complete and in many instances it is necessary to take into account bonding in the chemical sense^{2,3)}. The electronic configuration in metals such as copper, silver, and gold with their complete electronic cores cannot accommodate the carbon atom, and as a result carbides are not stable even though favorable radius ratios may exist. Of the metals which do not form carbides,

nickel and copper are readily available, have fairly low capture cross sections for thermal neutrons, and have reasonably high melting points. The maximum solubility of carbon in nickel is reported to be 0.65 wt % at 1318° C, the eutectic temperature. The solubility of carbon in copper, on the other hand, is immeasurably small at temperatures up to the melting point; in fact, this solubility is so low that carbon will not diffuse through copper. The nickel-copper alloy system consists of an isomorphous series of solid solutions⁴⁾, which suggests that the undesirably low melting point of copper and the high solubility of carbon in nickel may be compromised by alloying copper and nickel.

Other metals which could be expected to resist carburization in the range 480° C to 930° C are those refractory metals that form stable refractory carbides but have very high melting points. The temperature range of interest for these metals and their carbides is the low-temperature region ($T < \frac{1}{2}T_{\text{melting}}$) where carbide penetration rates are expected to be low. Readily available metals which have low neutron-capture cross sections and which fall in this group are molybdenum and niobium.

The common heat-resistant nickel-base and iron-base alloys that contain a high percentage of carbide-forming elements are known to carburize at elevated temperatures^{5,6)}. It is necessary to determine for each of these alloys the temperature range in which the carburization rate becomes intolerably high.

2. Materials

The materials selected for evaluation are listed in table 1. These materials include representative austenitic and ferritic stainless steels-nickel, nickel-copper alloys, nickel-iron-chromium-molybdenum alloys, molybdenum, and niobium-base alloys. The important properties of each group of materials are shown in table 2. In addition, coatings of chromium, copper, and diffused aluminum were selected for evaluation.

TABLE 2
Physical properties of selected materials

Metal or alloy	Melting temperature (° C)	Thermal neutron-capture cross section (barns)	Thermal coefficient of expansion (/° C × 10 ⁶)
Graphite	3700 (sublimes)	0.0045	0.5 to 4.3
Molybdenum	2625	2.5	4.9
Niobium	2415	1.1	7.1
Ferritic steels	1120 to 1540	≈ 3.5	11.1 to 11.9
Nickel	1455	4.5	13.3
Nickel-base alloys	1300 to 1425	≈ 4	11.5 to 17.5
Copper	1083	3.5	16.5
Austenitic stainless steels .	1370 to 1450	≈ 3.5	19.2 to 19.8

3. Experimental Procedure

The reaction between metals and graphite in helium was determined by holding small metal disks (4.8 mm diameter and 0.8 mm thick) in contact with graphite disks at temperatures in the range 704° C to 1010° C. Contact between the graphite and metal was achieved by stacking the disks alternately in a graphite die and applying a load of 2000 psi. Samples of each material were removed periodically for evaluation. The exposed samples were sectioned along a diameter perpendicular to the plane of the disk, mounted, polished, and etched for metallographic examination. Hardness impressions were made in the center of the specimens to a depth of 0.025 to 0.050 mm from the surface exposed to graphite. The microstructures and hardness values obtained were compared with those of the control samples.

The purity of the helium atmosphere used in these experiments depended on the temperature at which the graphite was outgassed. The graphite used at 704° C, 816° C, and 927° C was outgassed in vacuum (10 μ) at 496° C prior to loading and at 316° C after loading; the level of the impurities in the helium which evolved from the graphite rose to as high as 4 mole % †. The graphite used at 871° C and 1010° C was

outgassed at 816° C prior to loading and at 649° C after loading. One-half of the experiments conducted at 871° C and 1010° C contained a zirconium getter to remove impurities.

The effect of carburization on the room-temperature tensile properties was determined for a few promising alloys. Sheet-type tensile specimens were pack-carburized in a mixture of 5 % BaCO₃ and 95 % graphite for 500 h in the temperature range 871° C to 927° C. Carbon analysis of the tensile specimens was made before and after carburization. Control specimens having the same thermal history were prepared. The specimens were tensile tested at room temperature in an Instron testing machine using a strain rate of 1.27 mm/min.

4. Results

4.1. MOLYBDENUM

Because molybdenum has a low coefficient of expansion ($4.9 \times 10^{-6}/^{\circ}\text{C}$), which falls just above that reported for graphite (0.5 to $4.3 \times 10^{-6}/^{\circ}\text{C}$), and a very high melting point (2625° C), it is expected to be an excellent cladding material for graphite. It does, however, react with graphite below 1204° C to form a single carbide, Mo₂C. Above 1204° C, MoC is formed in addition to Mo₂C.

A uniform single-phase carbide layer, Mo₂C, was formed at all test temperatures. The values for the maximum layer thickness ob-

† Typical analysis after 1000 h at 704° C were:

- (1) Gettered: Total impurities < 0.005 mole %.
- (2) Not gettered: 0.54 % N₂, 0.81 % CO, 0.11 % H₂, balance He.

served on the specimens tested in the temperature range 704° C to 1010° C are listed in table 3. It will be noted that a definite effect of atmosphere was observed, e.g. carburization was most severe in specimens exposed in impure helium. Hardness values obtained in the center of the molybdenum specimens after exposure revealed little change (< 30 DPH).

TABLE 3

Thickness of Mo₂C layers formed on molybdenum held in contact with graphite at various temperatures in helium (at 2000-psi bearing pressure for 2000 h)

Temperature (° C)	Carbide layer thickness (mm)	
	Zirconium-gettered helium	Ungettered helium
704		0.005
816		0.02 to 0.03
927	0.025 to 0.03	0.04 to 0.06
1010	0.012 to 0.025	0.09 to 0.13

Tensile data for the carburized and control molybdenum specimens showed an increase of 20 % in the tensile strength and a decrease of more than 50 % in elongation due to carburization. Microstructures of the carburized specimen indicated that the reduced ductility and increased strength was probably due to the hard, brittle carbide surface layer.

4.2. NIOBIUM

Niobium has a higher coefficient of expansion ($7.2 \times 10^{-6}/^{\circ}\text{C}$) than molybdenum and a somewhat lower melting point (2415° C). Two niobium carbides have been reported¹⁾, Nb₂C and NbC, which are expected to form on niobium exposed to graphite at elevated temperatures. Because of the high melting temperature of niobium and its carbides, the rate of growth of the surface carbide into the metal in the range 482° C to 927° C is expected to be relatively low. In addition to its strong carbide-forming tendencies, the potential of niobium and its alloys suffers from a tendency to getter oxygen and nitrogen which increases the hardness, decreases the ductility, and leads ultimately to embrittlement.

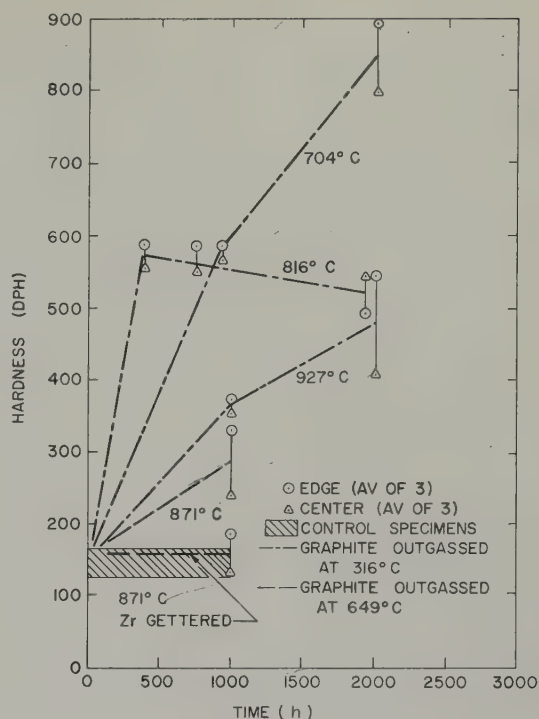


Fig. 1. Room-temperature hardness versus time for niobium + 1 % zirconium held in contact with graphite in helium. Hardnesses take 0.05 mm from surface exposed to graphite.

The exposure of the three niobium alloys to graphite in impure helium (99.9 %) resulted in large hardness increases at all test temperatures (fig. 1). Metallographic examination of the niobium specimens revealed that at 704° C and 816° C an extensive carbide-oxide layer developed and penetrated deeply into the metal. The niobium + 1 % Zr alloy specimens exposed at the same temperature did not show this type of attack. At 871° C and above, both of these materials reacted with graphite to form a duplex carbide layer consisting of NbC and Nb₂C, which diffused very slowly into the metal (refer to table 4).

A limited amount of testing was done on niobium + 10 % Mo + 10 % Ti alloy. Exposure at 704° C and 816° C resulted in a pronounced increase in hardness (500 to 900 DPH) and the formation of a contaminated solid solution layer on the surface. The penetration of the hardening contaminant (probably oxygen) ho-

TABLE 4

Metallographic results of graphite-niobium reactions at various temperatures in helium
(2000-psi bearing pressure)

Material	Maximum penetration (mm)				
	Time (h)	Temp. (° C)	Ungettered helium	Zr-gettered helium	Remarks
Niobium	2000	704	0.27	}	Carbide-oxide layer
	2000	816	0.05		
	1000	871	0.11	0.043 }	Carbide layer
	2000	927	0.08		
	2000	1010	0.08	0.037 }	
Nb + 1 % Zr	2000	704	< 0.025	}	Carbide layer
	2000	816	0.012		
	1000	871	0.037	0.008 }	
	2000	927	0.025		
	2000	1010	0.05	0.037 }	
Nb + 10 Mo + 10 Ti	2000	704	0.23	}	White solid solution surface layer
	2000	816	0.23		
	2000	927	0.13		

mogenized much slower than it did in niobium and the niobium-zirconium alloy. In the latter two materials, the contaminant dissolved and required less than 350 h at 816° C to homogenize. The hardness of the edge and the center of the niobium + 10 % Mo + 10 % Ti alloy specimens exposed for 2000 h at 704°, 816°, and 927° C indicates that homogenization was not complete in 2000 h at 816° C.

4.3. IRON-CHROMIUM ALLOYS

The ferritic steels have moderately low thermal coefficients of expansion, which fall in the range 9.2 to $11.9 \times 10^{-6}/^{\circ}\text{C}$. Equilibrium data ⁷⁾ for the Fe-Cr-C system indicate that at 700° C carburization can result in the formation of one or more of three carbides, depending on the composition. The alloys which contain less than 4 % Cr form only (Fe, Cr)₃C. Compositions in the range 4 % to 10 % Cr can be expected to form (Fe, Cr)₃C, plus the chromium carbide (Cr, Fe)₇C₃. Above 10 % Cr, (Cr, Fe)₂₃C₆, (Cr, Fe)₇C₃, and (Fe, Cr)₃C can exist in equilibrium with ferrite. However, only (Cr, Fe)₂₃C₆ and (Cr, Fe)₇C₃ will form at low carbon content.

At 850° C, the alloys which contain less than

14 % Cr will contain varying amounts of austenite in their microstructures. Because of the high solubility of carbon in austenite, these compositions should carburize readily. In the range 14 % to 20 % Cr, a small amount of absorbed carbon will result in the formation of austenite in the microstructure. Alloys containing more than approximately 20 % Cr can absorb a considerable amount of carbon before austenite forms; these alloys will consist principally of ferrite and (Cr, Fe)₂₃C₆.

Fig. 2 shows the hardness increases observed in specimens carburized for 2000 h at 704° and 816° C. At 816° C, only those alloys which contain austenite in their microstructures, i.e., alloys containing less than 17 % Cr showed evidence of carburization. Alloys having compositions that fall in the alpha or alpha plus (Cr, Fe)₂₃C₆ region did not carburize. At 704° C, alloys having microstructures consisting of alpha or alpha plus (Cr, Fe)₂₃C₆ at the test temperature showed no evidence of carburization. Only the alloys having compositions in the alpha plus (Fe, Cr)₃C or in the alpha plus (Fe, Cr)₇C₃ regions, i.e., alloys containing less than 12 % Cr showed evidence of carburization.

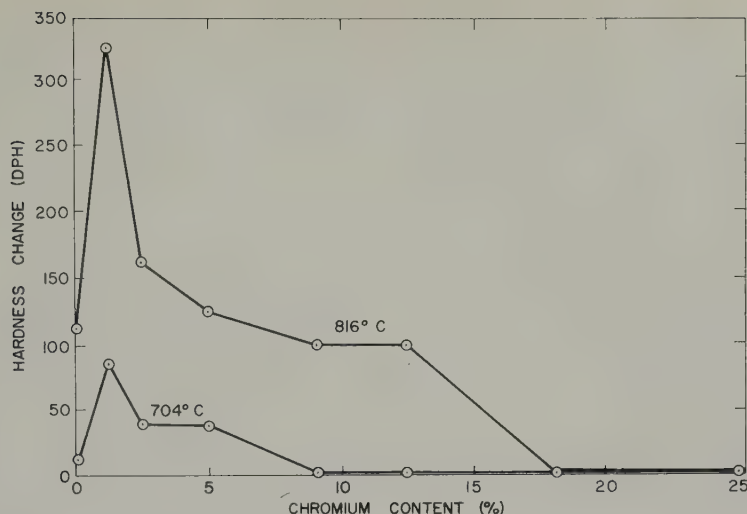


Fig. 2. Room-temperature hardness change versus chromium content for iron-chromium alloys after 2000 h in contact with graphite in helium. Hardnesses taken 0.05 mm from exposed surface.

The two alloys that resisted carburization at 816° C (17 % Cr and 25 % Cr) were tested at higher temperatures and were found to carburize rapidly at 871° C above.

4.4. IRON-CHROMIUM-ALUMINUM ALLOYS

The ferritic alloys in this group exhibit thermal expansion coefficients similar to those of the ferritic steels and differ only in that they have been modified by an aluminum addition to improve their oxidation resistance. The DB-2 alloy resisted carburization at 704° C and 816° C in 2000 h, but at 927° C there was extensive internal oxidation of aluminum and complete carburization. The 25 % Cr + 5 % Al alloy showed a behavior similar to that of the DB-2 alloy. At 816° C some carburization and surface oxidation occurred; at 927° C the reactions were extensive. The hardness data indicated that some carburization may have occurred at 816° C in 200 h.

4.5. NICKEL AND NICKEL-COPPER ALLOYS

Nickel and Monel proved to be very compatible with graphite at temperatures up to and including 1010° C. Effects due to the solution and reprecipitation of graphite, however, were especially notable in nickel, whereas Monel showed little evidence for "graphitization." The

term graphitization implies the precipitation of graphite from solid solution and should not be confused with carburization that implies the absorption of carbon as a carbide or in solid solution. Specimens of "A" nickel exposed at 927° C and above exhibited a random graphite precipitate which grew to a particle size of about 0.03 mm in 2100 h at 1010° C. Graphitization in Monel was much less severe, i.e., the graphite particles that were observed were very much smaller and more widely dispersed.

Carburization and graphitization had very little, if any, effect on the hardness of "A" nickel and Monel. The largest changes in hardness due to dissolved carbon occurred in Monel and amounted to a maximum change of only about 50 DPH numbers.

The formation of graphite in the microstructure of nickel in contact with graphite during annealing immediately suggested that deterioration of nickel might occur by a graphitization mechanism during thermal cycling. It is well known that nickel saturated with carbon at high temperatures graphitizes during aging at about 540° C. To ascertain the effect of graphitization on the tensile properties of nickel and the effect of a copper-alloying addition on the graphitization mechanism, tensile specimens of "A" nickel and Monel were

saturated with carbon at 927° C. Subsequently, some of these specimens were aged for 1000 h at 316°, 427°, 538°, and 649° C. Fig. 3 shows the results of the carburizing and the combination carburizing-aging treatments on the tensile properties of these two alloys. Values for the tensile properties of control specimens, which were subjected to the same thermal treatment used during the carburization, are also included in fig. 3 for comparison. The carburizing and the carburizing-aging treatments did not decrease the room-temperature ductility of either material. Carburization resulted in an increase in strength of both "A" nickel and Monel. Subsequent aging of "A" nickel above 427° C caused a decrease in the room-temperature strength and hardness, whereas the strength and hardness of Monel were increased slightly by the aging treatments. A metallographic examination revealed that graphitization of carburized "A" nickel had occurred during

aging above 427° C, but graphitization of Monel did not occur even after 1000 h at 649° C. The addition of copper to nickel was beneficial because it reduced the solubility of carbon and decreased the graphitization rate.

4.6. NICKEL ALLOYS WITH CHROMIUM, MOLYBDENUM, AND IRON

All tests made on alloys of this type showed carburization at 704° C. The alloy most resistant to carburization, Inconel X, formed a network of carbide at the grain boundaries which penetrated more than 0.25 mm in 2000 h at 704° C. The alloys Inconel, Inconel 702, and Nichrome V carburized rapidly at 704° C and, in addition, were found to be oxidized internally by impurities (CO) in the helium. Inconel 702 was especially vulnerable to internal oxidation, probably because of the 3.3 % Al addition. Metallographic examination of this alloy exposed at 704° C and 816° C revealed considerable

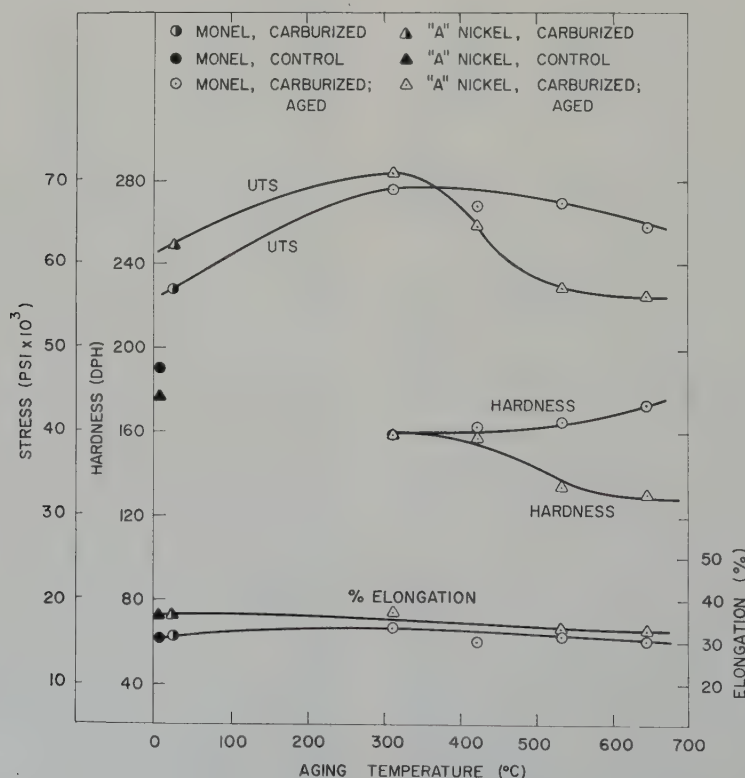


Fig. 3. Ultimate tensile strength and hardness versus aging temperature for carburized "A" nickel and Monel (aging time 1000 h).

internal oxidation and carburization; the internal oxidation was most extensive at 704° C. Incoloy and Hastelloy B resisted internal oxidation, but carburized rapidly at 816° C.

4.7. AUSTENITIC STEEL

As might be expected from the high solubility of carbon in austenite, this group of alloys exhibits relatively low resistance to carburization. In most cases carburization occurred at 704° C, and all alloys except the silicon-modified 25-20 alloy, Type 314 stainless steel, were observed to carburize at 816° C. The results were quite erratic, sometimes showing no carburization for the same alloy exposed at the same temperature. This behavior was evidently caused by a surface effect, since the carburization was observed to be sensitive to helium purity. For example, Type 314 stainless steel carburized rapidly at 871° C in zirconium-gettered helium but carburized very little, if at all, at 927° C in impure helium. Also, Type 310 stainless steel carburized at 704° C in areas where it had welded to a specimen of "A" nickel which was saturated with carbon, but it did not carburize across the steel-graphite interface. Type 304 stainless steel was particularly susceptible to carburization whereas stainless steels with higher chromium content were somewhat more carburization resistant. The alloys 17-14 Cu-Mo and 15-15 N showed no carburization after 2000 h at 704° C, but showed considerable carburization at 816° and 927° C.

The most carburization-resistant austenitic alloy tested was the high silicon 25-20, Type 314 stainless steel. Little, if any, carburization was observed in a 2000 h, 927° C, exposure to graphite in impure helium, but specimens exposed for 1000 h at 871° C in zirconium-gettered helium showed considerable carburization accompanied by large increases in hardness. Again the effect of helium purity was apparent, which suggested that carburization is retarded by films of chromium oxide or spinel which form in impure helium.

4.8. PROTECTIVE COATINGS

Four types of coatings were evaluated as protection against carburization: (1) chromium and copper plating on Types 304 and 430 stainless steel, (2) diffused aluminium on Type 304 stainless steel and Inconel, (3) diffused chromium on Type 316 stainless steel and Inconel, and (4) molybdenum bonded to Type 316 stainless steel.

Copper, in all cases disintegrated at 704° C and 816° C; it was therefore eliminated early in the investigation.

Chromium plate (0.025 mm thick) on Type 304 stainless steel was effective in protecting against carburization at 816° C. This is illustrated by the hardness versus exposure-time curve shown in fig. 4 for plated and unplated Type 304 stainless steel exposed at 704° C, 816° C, and 927° C. The plating was effective to 1746 h at 816° C, but diffused excessively into Types 304 and 430 stainless steel in 1000 h at 927° C.

The diffused aluminum coatings, 0.05 to 0.08 mm, on Type 304 stainless steel and Inconel protected against carburization, but diffused rapidly at 816° C and 871° C. At 816° C

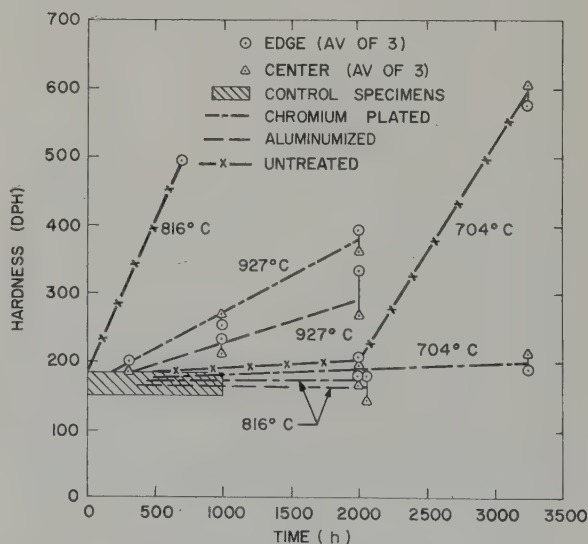


Fig. 4. Room-temperature hardness versus time for Type 304 stainless steel held in contact with graphite in helium. Hardness taken 0.05 mm from edge exposed to graphite.

the coating diffused more than 0.05 mm in 350 h and 0.11 mm in 2000 h. At 927° C the coating diffused more than 0.25 mm in 2000 h.

The aluminized coating on Inconel diffused much slower than it did on Type 304 stainless steel. The coating on a specimen exposed at 871° C for 2700 h diffused about 0.09 mm, making it unsatisfactory for use as a protective coating on thin-walled Inconel tubing for long periods of time (greater than 10000 h) at this temperature. The results, however, indicated that this coating may be useful on heavier sections.

The diffused chromium coatings on Inconel and Type 316 stainless steel did not prevent carburization at 871° C.

A 0.12 mm molybdenum foil placed between Type 316 stainless steel and graphite afforded some protection against carburization at 871° C. However, carburization from the unprotected edges of the specimens made it impossible to determine if the protection was complete.

5. Discussion and Conclusion

Many of the alloys investigated not only carburized but also reacted with impurities present in the helium atmosphere. In particular, all of the alloys which contained appreciable amounts of aluminum as an alloying element and the nickel-base alloys which contained chromium were internally oxidized by an impurity in the helium. At temperatures above 704° C and at low partial pressure (< 0.01 atm), nearly all of the oxygen present in the helium-graphite system, as would be expected, was present as CO (see fig. 5). The free energies of formation (ΔF) of CO at various partial pressures and the carbides and oxides of the important alloying constituents in the alloys tested have been plotted in fig. 6 as a function of temperature in the range 649° C to 982° C^{8,9}). The reaction of a metal oxide with carbon,



proceeds appreciably to the right when the sum of the free energies of formation of CO at the corresponding partial pressure and the metal

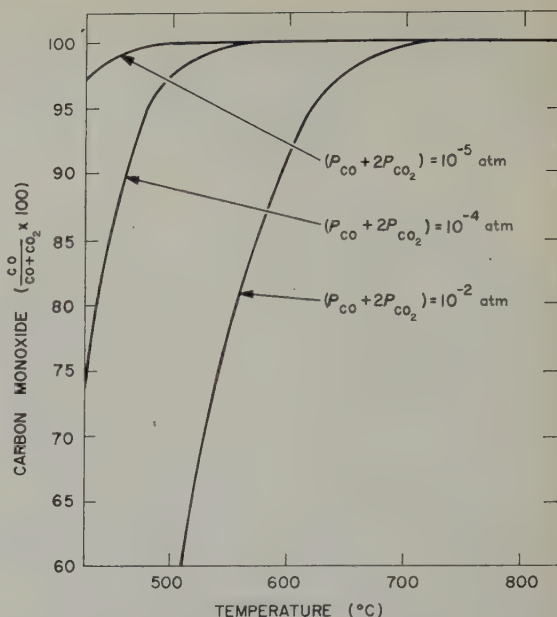


Fig. 5. Carbon monoxide-carbon dioxide in equilibrium with graphite.

carbide becomes more negative than the free energy of formation of the oxide. From the data in fig. 6, it is clear that aluminum in the alloys DB-2 (7 % Al), Fe/Cr/Al (5 % Al), Duranickel (4.5 % Al), and Inconel 702 (3.3 % Al) will tend to be preferentially oxidized. Similarly, the internal oxidation observed in many of the Ni-Cr alloys at low temperatures was undoubtedly due to the preferential oxidation of chromium by CO.

In addition, the tendency for niobium and its alloys to be oxidized at low temperatures and carburized at high temperatures is shown by the slopes of the free energy curves (fig. 6) of the oxides and carbides of niobium and CO. The behavior predicted by these data, however, was observed to be qualitative, since the solubility of oxygen in niobium at these temperatures is appreciable.

Because of the reactivity of niobium and its ability to dissolve embrittling quantities of oxygen in a relatively short time at temperatures as low as 704° C, it can be used only in very pure helium. Data obtained in this laboratory (to be published) indicate that partial pressures as low as 10^{-4} atm CO_2 will embrittle niobium

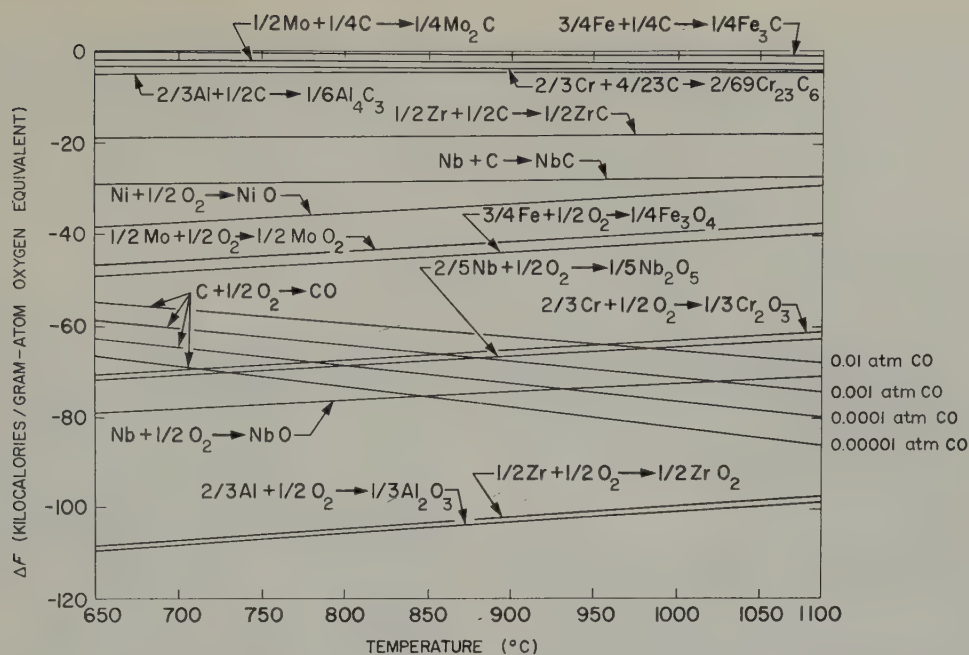


Fig. 6. Free energies of formation of the oxides and carbides of metals and carbon monoxide at various partial pressures.

and niobium + 1 % Zr in less than 500 h at 816° C. It is highly unlikely that a niobium alloy which will resist embrittlement by impurities expected in the helium coolant will be available for use as the fuel cladding in the MGCR fuel element.

The results obtained for molybdenum indicate that the rate of carbide penetration was too high for it to be considered as a thin-walled graphite cladding for long periods of time (10^4 h) at 927° C. At this temperature, the carbide layer grew to a thickness of 0.043 mm in 2000 h. A parabolic (diffusion controlled) rate of growth would predict a thickness of 0.1 mm in a year; the brittle nature of the cladding would then exert a strong influence on the properties of the cladding. At 704° C, the penetration appeared to be sufficiently low for molybdenum to be considered for some applications for as long as 10^4 h.

Because of the low thermal coefficient of expansion of the ferritic stainless steels, their advanced technological development, and their resistance to carburization up to 816° C, these alloys are promising as graphite-cladding ma-

terials at moderate temperatures where high mechanical strength is not required. Type 430 stainless steel (17 % Cr) is probably the best compromise as a cladding material, since alloys which contain more chromium have a higher propensity for sigma formation and alloys which contain less chromium do not have the necessary carburization resistance.

Nickel and nickel-copper alloys appear to be the most satisfactory cladding material for graphite at temperatures as high as 982° C. Preliminary testing of the mechanical properties of carburized nickel and Monel indicates that the room-temperature ductility does not suffer from carburization or graphitization and that copper as an alloying addition to nickel reduces the graphitization rate markedly. Considerably more experimental work is necessary to determine the effects of dissolved and precipitated carbon on the properties of these alloys at elevated temperatures.

Alloys of nickel with molybdenum, chromium, and iron lose the high-temperature strength conferred by these alloying elements when they are carburized and suffer from an appreciable

loss of ductility. The loss in ductility, however, is not as severe as that observed when the austenitic stainless steels are carburized. If the high strength of nickel-base alloys is needed in thin sections at temperatures up to 816° C, they must be protected by a suitable cladding or coating to prevent carburization.

The high thermal coefficient of expansion and the low carburization resistance of the austenitic stainless steels make them a poor choice for a cladding material for graphite. Only Type 314 stainless steel was observed to resist carburization at 816° C, but its applications are limited by the formation of the embrittling sigma phase at this temperature.

All of the coatings evaluated proved to be inadequate at 927° C. Chromium plating diffused into stainless steel and was lost rapidly at 927° C. The aluminized coating diffused excessively in stainless steel at 816° C. The same coating on Inconel diffused much slower at 816° C, but diffusion was still excessive. Copper plating on stainless steel disintegrated at 704° C.

The author is indebted to M. T. Simnad and W. P. Wallace for their helpful discussions, to G. Schmitt for metallography, and to J. Barry, W. Ellis, D. Guggisberg, and C. Mungle for carrying out many of the tests.

References

- ¹⁾ G. Hägg, *Z. physik. Chem.* 12 B (1931) 33
- ²⁾ R. E. Rundle, *Acta Cryst.* 1 (1948) 180
- ³⁾ W. Hume-Rothery and G. V. Raynor, *The Structures of Metals and Alloys* (The Institute of Metals, London, 1954) pp. 217-219
- ⁴⁾ Max Hansen and Kurt Anderko, *Constitution of Binary Alloys* (McGraw-Hill Book Co., Inc., 1958)
- ⁵⁾ A. F. Gerds and M. W. Mallett, Battelle Memorial Institute (USA) Report BMI-1261 (April 14, 1959)
- ⁶⁾ J. B. Giacobbe, *Trans. Amer. Soc. Metals* 45 (1953) 134
- ⁷⁾ *Metals Handbook* (American Society for Metals, 1948)
- ⁸⁾ Alvin Glassner, Argonne National Laboratory (USA) Report ANL-5750 (1957)
- ⁹⁾ L. S. Darken and R. W. Gurry, *Physical Chemistry of Metals* (McGraw-Hill Book Co., Inc., 1953)

PLASTIC ANISOTROPY AND FRACTURE IN BERYLLIUM

A. P. GREEN and J. SAWKILL

Tube Investments Research Laboratory, Hinxton Hall, Cambridge, UK

Received 6 July 1960

The relationship between plastic anisotropy and ductility in beryllium between 20° C and 400° C is explored. Features of the plastic deformation and fracture of single crystals are discussed. They include basal slip, bend plane formation and splitting, crack initiation and propagation. Comparison is made with basal fracture observed in zinc, and Stroh's theory for this type of fracture is applied to beryllium. The deformation and fracture of a polycrystalline aggregate is also discussed, and a qualitative explanation is proposed for the increase in ductility with temperature. Possible means of improving ductility are briefly suggested.

On a étudié la relation entre l'anisotropie de déformation plastique et la ductilité du béryllium entre 20° C et 400° C. Les caractéristiques de la déformation plastique et de la rupture sont discutées dans le cas de monocristaux. Celles-ci concernent le glissement basal, la formation de plan de pliage et de la fissuration, l'initiation et la propagation de la rupture. On compare avec la rupture basale observée dans le zinc, et l'on applique au béryllium, pour ce genre de rupture, la théorie de Stroh. On discute également la

déformation et la rupture d'un aggrégat polycristallin et l'on propose une explication qualitative pour l'accroissement de la ductilité en fonction de la température. Des moyens possibles d'améliorer la ductilité sont brièvement suggérés.

Es wurde der Zusammenhang zwischen der Anisotropie der Plastizität und der Duktilität von Beryllium zwischen 20° C und 400° C untersucht. Die Merkmale der plastischen Verformung und des Bruches werden erörtert. Es handelt sich dabei um Gleiten in der Basisebene, um die Bildung gebogener Ebenen und das Spalten, sowie um Anfang und Fortschreiten von Brüchen. Es werden Vergleiche mit den entlang von Basisebenen verlaufenden Brüchen bei Zink angestellt. Die für diesen Fall von Stroh entwickelte Theorie wird auf Beryllium angewendet. Verformung und Bruchverhalten polykristallinen Materials werden ebenfalls besprochen. Zudem wird eine qualitativ richtige Erklärung für das Anwachsen der Duktilität mit steigender Temperatur vorgeschlagen. Auf einige Möglichkeiten zur Verbesserung der Duktilität wird kurz hingewiesen.

1. Introduction

The aim of this paper is to show the relationship between plastic anisotropy and ductility, or lack of it, in beryllium between 20° C and 400° C. In this temperature range fracture is predominantly transcrystalline, whereas above about 400° C it generally becomes intercrystalline in the polycrystalline metal.

The main relevant experimental observations, taken mainly from Tuer and Kaufmann¹⁾, are as follows:

1.1. SINGLE CRYSTAL DEFORMATION (see table 1)

All the slip directions for both slip systems lie in the basal plane. The critical resolved shear

stress for basal slip is about $\frac{1}{5}$ th of that for prismatic slip at room temperature; but with increasing temperature the shear stress for prismatic slip decreases while that for basal slip increases slightly, and the two become equal between 500° C and 600° C. Twinning involves extension in the *c* direction, and requires much greater shear stress than basal slip.

At room temperature there is no mode for compression perpendicular to the basal plane, but above 700° C it is believed that pyramidal $\{10\bar{1}x\}$ slip can take place. Garber *et al.*²⁾ claim to have observed this down to 200° C, but between 20° C and 400° C it is clear that the shear stress required is very high.

TABLE I

Slip and twinning systems between 20° C and 400° C (from Tuer and Kaufmann¹⁾)

Type	Plane(s)	Directions	Critical resolved shear stress (g/mm ²)	
			20° C	400° C
Basal slip	{0001}	$\langle 11\bar{2}0 \rangle$	1400	1650
Prismatic slip	{10 $\bar{1}$ 0}	$\langle 11\bar{2}0 \rangle$	6650	2700
Twinning	{10 $\bar{1}$ 2}	$\langle 10\bar{1}1 \rangle$	5600 (minimum)	7700 (minimum)

1.2. BEND PLANES AND BENT LATTICES

A consequence of basal slip in both single crystals and polycrystalline metal is the formation of {11 $\bar{2}$ 0} bend planes, and kink bands, perpendicular to the slip direction. (A narrow region bounded by bend planes of opposite sign is referred to as a kink band.)

After tensile testing polycrystalline metal, Kaufmann, Gordon and Lillie³⁾ have observed that some grains exhibit bend planes under polarized light, whereas in others the basal planes are continuously curved. The higher the testing temperature, the greater the continuous curvature of the lattice.

1.3. FRACTURE

Cleavage on the basal plane is the dominant mode of fracture, and the source of room temperature brittleness. It is invariably associated with bend planes.

1.3.1. Single crystals (see table 2)

In room temperature tensile or compression tests, basal slip occurs in most orientations, kink bands and bend planes are formed, and cracking is initiated on the basal plane across "split" bend planes. In tension this leads to complete fracture after 2–3 % plastic strain. In compression, many micro-cracks can be seen before fracture (fig. 1), and *at each crack the bend plane is split*.

Basal cleavage may also occur as a result of twinning, as detailed in column 3 of table 2.

Only if basal slip or twinning does not occur is considerable ductility achieved in tension. Prismatic slip then leads to fracture on {11 $\bar{2}$ 0} planes.

In compression along the *c* axis at room temperature, elastic deformation up to stresses of about 200 000 g/mm² is followed by explosive disintegration.

1.3.2. Polycrystals

There is a wide variation of behaviour with different types of metal and different grain size, texture, direction of testing, or temperature at which the metal was worked (see Williams⁴⁾). Nevertheless, the following broad generalisations are possible in the testing temperature range 20–400° C:

a) Random texture (e.g. hot-pressed powder).

The room temperature elongation is less than about 2 %, but increases rapidly with temperature to 30–40 % at 400° C

b) Pronounced basal texture (e.g. rolled, extruded, or upset 200 mesh powder).

The metal behaves in a similar manner to a single crystal, i.e. 20–40 % elongation if the direction of testing favours prismatic and not basal slip but less than about 2 % in other directions. If the texture is less pronounced, the room temperature ductility is slightly increased in the latter directions, but only at the expense of a decrease in the former directions. The effect of temperature is generally small.

Little work appears to have been done on the metallography of deformation and fracture, but the few observations of Kaufmann *et al.*³⁾, show the presence of many bend planes after tensile testing, and in their fig. 32(d), the cracks appear to be associated with split bend planes.

TABLE 2

Fracture in tensile tests at room temperature (from Tuer and Kaufmann¹)

Range of inclination of c axis to tensile axis (approx.)	Type of deformation preceding fracture	Sequence of events leading to fracture	Strain before fracture (approx.)	Planes of fracture
0°–10°	Twinning	(a) Twinning on one set of planes (b) Twinning on second set of planes (c) Basal slip and formation of $\{11\bar{2}0\}$ bend planes to take up opposing shears.	Very small	(0001) followed by $\{10\bar{1}2\}$
10°–80°	Basal slip	Formation of kink bands (i.e. pairs of $\{11\bar{2}0\}$ bend planes)	Less than 2–3 %	(0001)
80°–90°	Prismatic slip	Single	10 %	$\{11\bar{2}0\}$
		Duplex	60 % at root of neck	$\{11\bar{2}0\}$

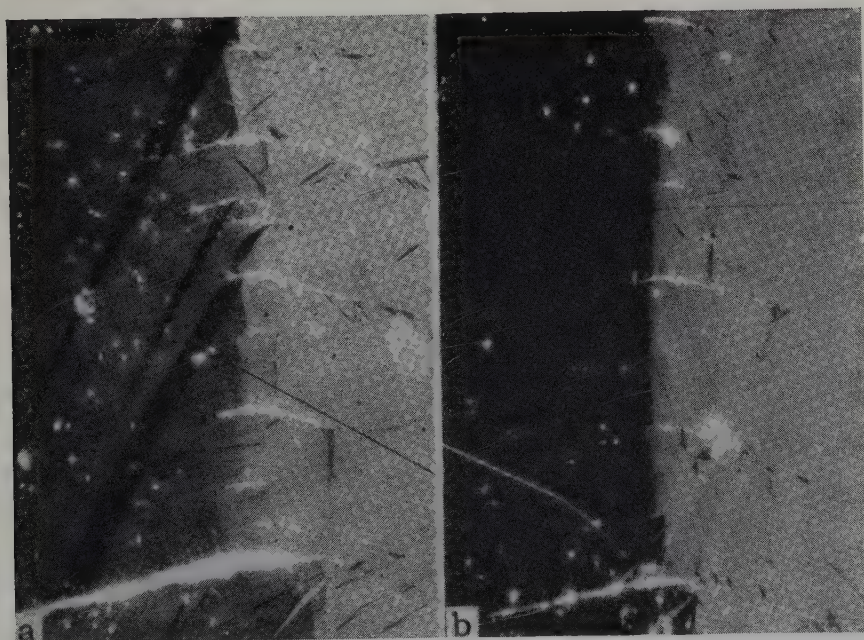


Fig. 1. Cracks in compressed single crystal of beryllium at room temperature. Polarized light. (After Tuer and Kaufmann¹.) $\times 165$.

c) Grain size

The smaller the grain size, the greater the ductility and strength.

2. The Nature of Basal Cleavage in Single Crystals

The observations of basal cracks at split bend planes suggest that the fracture model proposed in part by Orowan⁵⁾ and Friedel⁶⁾, and recently elaborated by Stroh⁷⁾, is applicable to basal cleavage in beryllium single crystals. According to Stroh, the sequence of events leading to fracture is: (a) basal slip, (b) formation of bend planes and/or kink bands, (c) bend plane splitting leading to the formation of micro-cracks, (d) crack propagation.

A bend plane is a wall of edge dislocations, and when it becomes split a crack is initiated because of the very high tensile stress perpendicular to the basal plane at the end of the terminating wall. Friedel⁶⁾ estimated that about 5° misorientation across the wall would produce sufficient stress concentration. Stroh⁷⁾ suggests that bend plane splitting could be produced by the holding up of part of the wall by a weak but extended barrier (such as, for example, a low angle twist boundary formed by dislocations intersecting the slip plane), the remainder being pulled on by the applied stress.

Split bend planes and associated micro-cracks similar to those observed by Tuer and Kaufmann¹⁾ in beryllium have been reported by Gilman⁸⁾ in zinc compressed at -196°C (fig. 2).

Bend planes are the result of non-uniform slip on one set of planes only. Constraints, such as the grips in a tensile test, or inhomogeneities in the crystal⁹⁾, can produce bend planes. The boundary between a constrained non-deforming region and a deforming region is most likely to be a bend plane, since dislocations of one sign will accumulate there. Gilman and Read¹⁰⁾ in tensile tests on zinc single crystals produced kink bands in the neighbourhood of surface scratches, whereas unscratched crystals exhibited no kink bands. They also observed kink bands at non-metallic inclusions and included crystals. Nye¹¹⁾ and Bilby *et al.*¹²⁾ have concluded that in order to avoid far reaching elastic stresses, the lattice distortion (i.e. the final distribution of dislocations) resulting from slip on one set of planes only must be such that the slip surfaces are developable. A simple model of this suggested by Bilby *et al.*¹²⁾ is provided by the behaviour of a pile of inextensible sheets of paper, in which the sheets (i.e. the basal planes in beryllium) undergo any bending deformation without tearing, and slide over one another in any direction but always remain in

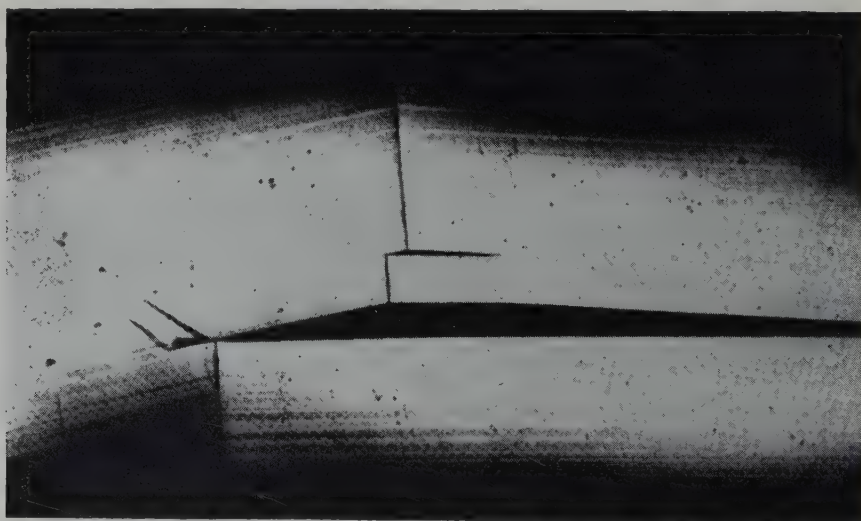


Fig. 2. Cracks in zinc compressed at -196°C . (After Gilman⁸⁾.) $\times 145$.

contact. A bend plane is a degenerate form of such distortion. Thus, in general, the basal planes in beryllium will be continuously bent as a result of plastic deformation, but severe local constraints will lead instead to sharply defined bend planes.

A bend plane may move as a whole, as demonstrated by Washburn and Parker⁹⁾, but the precise cause of bend plane splitting needs closer investigation. Low-angle boundaries certainly occur in beryllium; for example, Sawkill¹³⁾ has revealed sub-grains in cast metal by etching, and Bassett, Menter, and Pashley¹⁴⁾ have observed low-angle twist boundaries in electron microscopic examination of thin films. It may also be that some of the impurities dispersed as particles in commercial metal affect splitting.

Basal crack propagation is made easy in beryllium by the fact that there is no slip direction inclined to the basal plane to relieve the stresses at the tip of the crack, though twinning can occur at a high stress level. Stroh⁷⁾ obtained the following criterion for basal crack propagation in hexagonal single crystals, propagation being regarded as the determining stage of fracture:

$$\tau_s - \tau_0 = k \cos \chi / \sigma_n, \quad (1)$$

where

$$k = \frac{\gamma}{D} \left[\frac{1}{\pi B} \ln \left(\frac{\theta}{B\tau_s} \right) \right] = \frac{\gamma}{D} A, \quad (2)$$

and

τ_s = resolved shear stress on the basal plane at fracture.

τ_0 = resolved shear stress on the basal planes for initial yielding.

σ_n = normal stress component perpendicular to the basal plane.

D = crystal diameter.

χ = angle between tensile axis and slip direction.

γ = energy absorbed in creating unit area of new surface.

B = a complex function of the elastic constants ($2/B$ is roughly equal to a mean elastic extensional modulus).

θ = misorientation across the bend plane.

Eq. (1) gives the variation of strength with orientation, k being practically independent of orientation. The results of Deruyttère and Greenough¹⁵⁾ on zinc at -196°C , and of Vickers¹⁶⁾ on bismuth, agree well with this expression. There should also be a variation of ductility with orientation, since τ_s is related to the strain at fracture, γ_s , through the shear stress-strain curve. Deruyttère and Greenough¹⁵⁾ had in fact shown, before Stroh's theory was published, that for zinc at -196°C the curve of shear stress plotted against shear strain at fracture coincided with the shear stress/strain curve for basal slip. Unfortunately, no data on variations of strength and ductility with orientation are available for single crystals of beryllium, nor have stress-strain curves been published. The only comment by Tuer and Kaufmann¹⁾ is that there is "relatively little strain-hardening" for basal slip.

If linear hardening is assumed,

$$\tau_s = \tau_0 (1 + h \gamma_s), \quad (3)$$

where h is a non-dimensional hardening parameter. The reason for defining the hardening rate in this manner is that if the hardening mechanism is the same in two different metals it is to be expected that they would have geometrically similar stress-strain curves, the stress for a given strain being proportional to the initial yield stress. Then from eqs. (1), (2) and (3), since $\tau_s/\sigma_n = \cot \chi$, the fracture strain is

$$\gamma_s = \left(\frac{\cos \chi \cot \chi}{D} \right) \frac{\gamma A}{h\tau_s\tau_0}. \quad (4)$$

Hence the ductility of different hexagonal crystals is roughly proportional to $\gamma A/h\tau_0^2$. Unfortunately, γ and h are not known for beryllium. If, however, it is assumed that h is the same for beryllium at room temperature as for zinc at -196°C , and that the respective values of γ are in the same ratio, 8.4, as their extensional moduli E in the c direction[†], then

[†] This is justified by arguments similar to those employed by Orowan²³⁾ in estimating theoretical cohesive strength. It is assumed that the surface energy; γ , is proportional to the energy stored between

equation (4) gives γ_s for beryllium as roughly $\frac{1}{10}$ th that for zinc at -196°C . This is about right, and suggests that the relative brittleness of beryllium may well be due to τ_0 being high in comparison with the elastic moduli. Physically this amounts to more stored elastic energy being available, relative to that required for crack propagation, soon after yielding occurs.

It is of interest to compare the analysis by Stroh⁷⁾ with the conclusions of Pugh¹⁷⁾ on the plastic properties of beryllium. Pugh considered the relationship between the elastic and plastic properties of polycrystalline aggregates and in particular used the ratio K/G , where K is the bulk modulus and G the rigidity modulus, as the criterion for malleability. A low value of K/G would indicate brittleness. Beryllium has a low value and so Pugh concluded that the metal was inherently brittle. It is suggested that Stroh's mechanism, based on the analysis of an observed fracture mode, provides a much more rigorous treatment and takes into account in more detail the elastic and plastic properties of the metal.

As outlined in table 2, bend plane splitting and basal cracking also result from twinning. It also appears from the photographs of Tuer and Kaufmann¹⁾, that split bend planes are associated with many of the cracks formed near twins. On examining the displacement boundary conditions imposed by two opposing lenticular shaped twinned regions on the triangular region of untwinned matrix between them, it appears that it is probably impossible to construct a distorted lattice satisfying the geometrical conditions derived by Nye¹¹⁾ and Bilby *et al.*¹²⁾. This implies that this region is suddenly subjected to very high stresses which could be the driving force behind the operation of the Stroh type mechanism, though the exact

two adjacent atomic planes separated by an amount such that the stress between them is a maximum. This energy is roughly proportional to $cE\varepsilon^2$, where c is the atomic spacing in the c direction, and ε is the strain corresponding to the maximum stress. It is further assumed that $c\varepsilon^2$ is roughly the same for beryllium and zinc.

sequence of events is not clear. The pattern of fracture is different from that observed by Bell and Cahn¹⁸⁾ as a result of twinning due to tension parallel to the basal planes in zinc. There, fracture occurred at the actual intersection of twins, rather than in the region between them, either on the twinned basal planes (these planes being nearly perpendicular to the applied stress) or on the basal planes of the matrix (i.e. approximately parallel to the applied stress). The former occurred if the two intersecting twins were both situated on the same side of a plane through their line of intersection and parallel to the applied stress, the latter if they were on opposite sides of such a plane. In beryllium only the latter configuration produces fracture. These differences in fracture behaviour are doubtless due to the fact that zinc contracts, whereas beryllium expands, parallel to the c axis as a result of twinning. Nevertheless, the basic cause of fracture is the same, in that it is due to there being no slip systems to readily accommodate and relieve stress concentrations set up by adjacent pairs of opposing twins.

3. Fracture of Polycrystalline Metal

3.1. FRACTURE AT ROOM TEMPERATURE

A polycrystalline aggregate with a pronounced basal texture can be expected to behave very much like a single crystal, the stress and strain throughout the aggregate being roughly uniform in a tensile test.

In general, however, the plastic deformation of an aggregate results in non-uniform stress and strain, due to the plastic anisotropy of the grains and their differing orientations. This non-uniformity is especially marked in beryllium due to its severe plastic anisotropy. In a single beryllium grain at room temperature it is not even possible to produce an arbitrary plastic strain. An obvious example is that compression is not possible parallel to the c axis. Even when the macroscopic strain can be imposed on a grain, the stress required varies widely with orientation. Hence, in an aggregate with random

texture, some grains are effectively much "harder" than others, and in extreme cases act like rigid inclusions. The strain tends to be concentrated in the "softer" grains at an overall stress level greater than if they had been able to deform freely, owing to the constraints exerted by adjacent "harder" grains.

It is not surprising therefore that such an aggregate of beryllium should exhibit so little ductility at room temperature. The Stroh fracture mechanism may be expected to operate at a very low *overall* strain because (a) the "softest" grains are those deforming by basal slip, with χ around 45° , (b) strain tends to be concentrated in these grains, and bend planes tend to form because of severe constraint by surrounding "harder" grains, and (c) the stress σ_n normal to the basal plane in the "softest" grains when *overall* yielding of the aggregate occurs is higher than it would be in similarly oriented single crystals. In a single crystal with $\chi = 45^\circ$ the applied tensile yield stress $\sigma_0 = 2 \tau_0 / \sin 2 \chi = 2 \tau_0$, and $\sigma_n = \tau_0 \tan \chi = \tau_0$. The average applied tensile stress at which an aggregate yields is considerably higher than σ_0 . Hence in the "softest" grains the local tensile stress σ_1 parallel to the tensile axis must also be greater than σ_0 , otherwise it would be impossible to satisfy force continuity conditions at grain boundaries. These grains must therefore be subject also to a lateral constraining tensile stress σ_2 such that the yield condition, $\sigma_1 = \sigma_2 + \sigma_0$ is satisfied †. It follows that σ_n is increased by an amount σ_2 above $\tau_0 \tan \chi$, its value in a single crystal.

Stroh⁷⁾ questions whether the split bend plane mechanism will operate in a polycrystal and suggests that the constraints of surrounding grains will oppose the motion of bend planes. He further suggests that the presence of grain boundaries provides obstacles which make a piled-up group of dislocations mechanism possible. He deduces that on the split bend plane

† This yield condition is only strictly correct if σ_1 and σ_2 are *principal* stresses. In general this will not be so but qualitatively the argument is not seriously affected.

model the relationship between fracture stress σ in tension and grain diameter d , will be of the form

$$\sigma(\sigma - \sigma_0) = K/d, \quad (5)$$

where σ_0 is the yield stress in tension, and K is a constant. The model based on piled-up groups of dislocations gives

$$(\sigma - \sigma_0)^2 = k/d. \quad (6)$$

For small σ_0 these equations agree, as occurs with zinc¹⁹⁾. For magnesium the experimental values are a better fit with eq. (6). There does not appear to be the necessary information available to test these equations for beryllium, though the metallographic observations of Kaufmann *et al.* mentioned in Section 1.3.1. (b) support the split bend plane model. Certainly, finer grain size gives better mechanical properties, which agrees with both equations.

3.2. EFFECT OF TEMPERATURE

The rapid increase of ductility of a randomly orientated aggregate with temperature may be explained mainly by the decreasing ratio of the critical resolved shear stress for prismatic slip to that for basal slip. This will lead to more prismatic slip, less inhomogeneous deformation, and less severe constraint on those grains which still deform by basal slip alone. Hence, there is more likelihood of the basal planes of the latter grains bending continuously than of forming bend planes, as found by Kaufmann *et al.*³⁾. Moreover, dislocation pile-ups, if they occur, will become less severe, since deformation rather than fracture will be more readily initiated in the neighbouring grains.

Considering crack propagation in a single grain, and applying eq. (4) qualitatively: A remains roughly constant; h may not be much affected in the range 20°C – 400°C but if anything will decrease; γ is unlikely to be effected much until the temperature is well above 400°C and a pyramidal slip system becomes reasonably easy to operate; the main effect will be a decrease in σ_n due to a decrease in the overall yield strength of the aggregate.

However, more important than crack propagation in one grain is transmission of cracks across grain boundaries. The chance of a crack being stopped due to prismatic slip in the neighbouring grain clearly increases as prismatic slip becomes easier, and this means that γ for the aggregate is effectively increased above that for a single crystal.

A similar viewpoint has been adopted by Hauser, Landon and Dorn ²⁰) to account for the increased ductility at low temperatures brought about by alloying magnesium with lithium. The proportion of prismatic to basal slip was observed to increase from negligible to substantial amounts with increasing alloying, and the stress-strain curve for the aggregate was lowered. They also ascribe the transition from brittle to ductile fracture of coarse grained high-purity magnesium, on lowering the temperature from 78° K to 4° K to the introduction of prismatic slip in addition to basal slip. They suggested that the increased ductility is bound up with high energy absorption associated with crack propagation in the presence of easier prismatic slip. This was supported by observations of stopped cracks in the vicinity of the major fracture which were not more than one or two grain diameters in length at 78° K, but were 8–10 grain diameters long following ductile fracture at 4° K.

4. Summary and Conclusions

4.1. SUMMARY OF CAUSES OF BRITTLINESS

It is suggested that severe plastic anisotropy is the main cause of the room temperature brittleness of beryllium. Also, increasing temperature improves ductility, so long as trans-crystalline fracture remains the dominant fracture mode, mainly by decreasing plastic anisotropy, the increase of ductility between 20° C and 400° C being due to lowering of the critical shear stress for prismatic slip.

It is plastic anisotropy which:

(i) leads to the Stroh split bend plane fracture mechanism, because slip on the basal planes alone is the predominant deformation mode.

(ii) makes basal crack propagation relatively easy (i.e. the effective surface energy γ low), because except for twinning at high tensile stress there is no way of plastically relieving the stress at the tip of a basal crack in a single crystal or grain.

(iii) after twinning in tension makes it impossible to relieve by plastic deformation the stresses set up between adjacent pairs of twins without immediately operating the split bend plane fracture mechanism in the presence of a high tensile stress normal to the basal planes.

(iv) (polycrystal only) causes great variation in effective hardness of grains of different orientation in an aggregate. This in turn, leads to the constraints which encourage bend plane formation, concentrates strain in those grains deforming most easily by basal slip, and raises the stress normal to the basal plane in these grains. Furthermore, the "hard" grains provide the barriers which make possible another fracture mechanism, i.e. fracture in a "hard" grain due to a pile-up at its boundary of dislocations generated on the basal plane in a neighbouring "soft" grain.

(v) (polycrystal only) lessens the probability of stopping a basal crack at a grain boundary due to the operation of prismatic slip in the neighbouring grain.

It should be noted that the effects of (iv) and (v) will be less, the greater the degree of preferred orientation, which explains why increasing temperature has much more effect on a randomly oriented aggregate than on one with a pronounced basal plane texture.

It appears, on examining Stroh's criterion for basal cleavage (eq. (4)), that beryllium is more brittle than other hexagonal metals (e.g. zinc, at -196° C), because its critical resolved shear stress for basal slip is high relative to its elastic extensional moduli.

The explanation advanced here for the brittleness of polycrystalline beryllium at room temperature differs greatly from that of Bishop ²¹). He ascribed it mainly to the inability of a single crystal to compress plastically parallel to its *c* axis, whereas we regard this as

only one factor and certainly not the most important. In many cases of brittleness there may be few or no grains so oriented relative to the stress field that they are required to compress in the c direction and thus act like rigid inclusions. In any case, although rigid inclusions can lower ductility, they do not in themselves generally lead to pronounced brittleness unless present in very large quantities.

4.2. IMPROVING DUCTILITY

When ductility is required in only one or two dimensions, it has been found possible to produce suitable textures by appropriate hot or warm working, in which all or most of the basal planes become so oriented that little or no basal slip is required of the material. It is therefore reasonably ductile because only prismatic slip is involved. In general, however, the stress and strain conditions are more complex, and it is impossible to avoid the necessity for reasonable ductility in all directions (see for example, Bishop's ²¹) remarks on the bending of wide flat strips).

There appear to be three basic ways in which overall ductility might be radically improved:

- (a) A decrease in the plastic anisotropy by decreasing the ratio of the critical resolved shear stresses for prismatic and basal slip, preferably by decreasing the former.
- (b) An overall decrease in critical shear stresses.
- (c) Smaller grain size.

The basic reasons for the present plastic anisotropy are not clear. Ellis ²²) has compared beryllium with other close packed hexagonal metals, and it appears that beryllium is out of step with the general trend for prismatic slip to become the primary slip system as c/a decreases. He has also pointed out that interstitial oxygen in titanium and zirconium in amounts well below the solubility limit is known to embrittle these metals, and suggests that something similar is happening in beryllium. The only experimental support for this argument appears to be a few results of Churchman²¹)

on the shear stresses of single crystals of titanium. He measured the critical resolved shear stresses for prismatic and basal slip in titanium of two purities as shown in table 3.

TABLE 3

Critical resolved shear stresses for slip in titanium single crystals (from Churchman ²¹))

Impurity content (combined oxygen and nitrogen) (wt %)	Slip plane	CRSS (kg/mm ²)
0.01	{10 $\bar{1}$ 0}	1.40
	(0001)	6.30
0.10	{10 $\bar{1}$ 0}	9.19
	(0001)	10.90

This shows that with increasing impurity, prismatic slip becomes less favourable, and he explains this in terms of the positions that the oxygen interstitial atoms are likely to assume. It might be conjectured, therefore, that beryllium would be rendered less anisotropic by purification, though whether oxygen is sth principal or the only impurity involved is uncertain. It is important therefore, that the critical resolved shear stresses for basal and prismatic slip be measured for highly purified beryllium. Until this is done, it is impossible to say whether the anisotropy is due to impurities, or is inherent in the lattice. Purification might also result in an overall lowering of yield stresses.

The results of Hauser, Landon and Dorn ²⁰), mentioned in section 3.2, on increasing the ductility of magnesium by alloying it with lithium are also of interest since the improvement was apparently linked with the easing of prismatic slip. However, the difficulty with alloying beryllium is the very low solid solubility in it of many elements.

Failing a decrease in anisotropy or in yield stresses, it is just possible that extreme brittleness might be avoided if bend plane splitting could be delayed to permit higher strains before crack initiation, so that initiation instead of propagation became the determining stage of fracture.

Acknowledgement

We thank the Chairman of Tube Investments Ltd. for permission to publish this paper.

References

- 1) G. L. Tuer and A. R. Kaufmann, *The Metal Beryllium*, Eds. D. W. White and J. E. Burke (Cleveland, ASM, 1955) 372
- 2) R. E. Garber, E. A. Gindin, V. S. Kogan and B. G. Lazarev, *Fiz. Metall. i Metallovedenie* 1 (1955) 529
- 3) A. R. Kaufmann, P. Gordon and D. W. Lillie, *Trans. ASM* 42 (1950) 785
- 4) J. Williams, *Met. Reviews* 3 (1958) 1
- 5) E. Orowan, *Dislocations in Metals*, Ed. M. Cohen (New York, AIME, 1954) 69
- 6) J. Friedel, *Les dislocations*. (Gauthier Villars, Paris, 1956)
- 7) A. N. Stroh, *Phil. Mag.* 3 (1958) 597
- 8) J. J. Gilman, *Trans. AIME* 200 (1954) 621
- 9) J. Washburn, and E. R. Parker, *Trans. AIME* 194 (1952) 1076
- 10) J. J. Gilman and T. A. Read, *Trans. AIME* 197 (1953) 49
- 11) J. F. Nye, *Acta Metallurgica* 1 (1953) 153
- 12) B. A. Bilby, R. Bullough, L. R. T. Gardner and E. Smith, *Proc. Roy. Soc. A* 244 (1958) 538
- 13) J. Sawkill, Unpublished work
- 14) G. A. Bassett, J. W. Menter and D. W. Pashley, *Proc. 4th International Conference on Electron Microscopy* (Berlin, 1958) 353
- 15) A. Deruyttère and G. B. Greenough, *J. Inst. Metals* 84 (1956) 337
- 16) W. Vickers, (1958) unpublished
- 17) S. F. Pugh, *Phil. Mag.* 45 (1954) 823
- 18) R. L. Bell and R. W. Cahn, *J. Inst. Metals* 86 (1958) 433
- 19) G. W. Greenwood, and A. G. Quarrell, *J. Inst. Metals* 82 (1954) 551
- 20) F. E. Hauser, P. R. Landon and J. E. Dorn, *Trans. ASM* 50 (1958) 856
- 21) J. F. W. Bishop, UKAEA Industrial Group Report, IGR-TN/S-791 (1958)
- 22) G. C. Ellis, *Metallurgia* 58 (1958) 243, 265
- 23) E. Orowan, *Rep. Prog. Physics* 12 (1949) 185

LETTERS TO THE EDITORS — LETTRES AUX REDACTEURS

IRRADIATION GROWTH OF ZIRCONIUM — PLUTONIUM ALLOYS

J. A. HORAK and H. V. RHUDE

Metallurgy Division, Argonne National Laboratory, Argonne, Illinois, USA

Received 6 September 1960

In the fuel alloy development program at Argonne National Laboratory concerned with fast breeder reactors, considerable emphasis has been concentrated on the dimensional stability of plutonium alloys under irradiation. Included in these irradiation studies were four cold worked zirconium-plutonium alloy fuel specimens.

Three of the specimens were Zr-5 wt % Pu and the fourth was Zr-7 wt % Pu. Based on the plutonium-zirconium equilibrium diagram¹), the structure of the alloys consisted of plutonium dissolved in alpha zirconium. The specimens were prepared by forging and rolling arc-melted buttons at room temperature into rods 0.40 cm (0.160 in) in diameter. The total reduction in area was approximately 90 %.

The specimens were irradiated in NaK-filled capsules in the MTR to total atom burnups ranging from 0.8 to 1.8 %. The maximum fission density was $2.5 \times 10^{21}/\text{cm}^3$. Initial irradiation temperatures were calculated to be near 500° C.

Fig. 1 shows the preirradiation appearance of the specimens, fig. 2 shows a Zr-5 wt % Pu specimen after irradiation, and fig. 3 shows the postirradiation appearance of the Zr-7 wt % Pu specimens. As shown in the photographs, the specimens grew during irradiation to approximately 2 to 4 times their original lengths with an accompanying decrease in cross section; the cross section became trapezoidal with longitudinal striations that ran the entire length of the specimens. The folded appearance of the specimens is due to the fact that they elongated to the sides of the irradiation capsule and then



Fig. 1. Typical preirradiation appearance of Zr-Pu alloy specimens. 2 ×.



Fig. 2. Typical postirradiation appearance of Zr-5 wt % Pu fuel specimens. 2 ×.

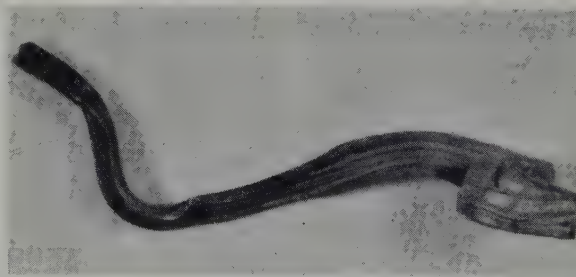


Fig. 3. Postirradiation appearance of Zr-7 wt % Pu fuel specimens. 2 ×.

in directions that offered paths of least resistance. Density decreases were approximately 3 %.

The anisotropic growth of the specimens during irradiation indicates that the cold forging and rolling used to prepare the specimens had produced a high degree of preferred orientation. The trapezoidal cross sections which developed indicate that the thickness reductions were not uniform in all diametral directions. The reactor was shut down 73 times during the period that these specimens were in the reactor. The thermal cycling produced by these shut-

downs and subsequent startups also may have contributed to the growth of these specimens.

The extreme degree of dimensional instability observed in these hexagonal close packed alpha zirconium alloys is similar to that previously observed in highly textured orthorhombic alpha uranium ²⁾.

References

- ¹⁾ M. B. Waldron *et al.*, Second Geneva Conf. (1958) P/71
- ²⁾ J. H. Kittel and S. H. Paine, Nuclear Science and Engineering 3 (1958) 250

IMPROVED MECHANICAL PROPERTIES AND ASSOCIATED CONSTITUTIONAL CHANGES IN COMMERCIALLY PURE INGOT BERYLLIUM AS AFFECTED BY HEAT TREATMENT ABOVE 700° C

A. MOORE

Metals Division, Atomic Weapons Research Establishment, Aldermaston, Berks., UK

Received 30 August 1960

Beryllium is commonly regarded as an unusual and brittle metal. Recent work in the Metals Division at AWRE, however, has shown that the metal is not unusual. It behaves according to established principles for metals and alloys, and in particular its low ductility and ready cleavage at 20°C are associated with a classical ductile/brittle transition at $> 20^\circ\text{C}$, and the minimum at 600°C in the ductility versus temperature relationship is due to a precipitation ageing process. It appears that the latter process can affect the character of the ductile/brittle transition in metal heat treated at higher temperatures but in general the transition occurs well below the ductility minimum at $\approx 600^\circ\text{C}$. In consequence, a high temperature evaluation of mechanical properties and ageing is not influenced by the brittle/ductile transition.

It is not difficult to accept the possibility that a precipitation ageing process could occur in commercial beryllium. The metal is relatively impure (99.7 wt %) and binary equilibrium studies have shown many of the impurity elements to be virtually insoluble in beryllium at 20°C but that the solvent properties of beryllium increase significantly with increasing temperature to $\approx 1000^\circ\text{C}$. The difficulty has been to show a systematic variation in mechanical properties with composition and annealing schedules and to relate such changes in mechanical properties with constitutional changes as detected in metallographic and X-ray diffraction studies. Such an approach has now

been made successfully on beryllium in the range 99.7 wt % to 99.3 wt % pure and in particular containing 0.04 wt % to 0.4 wt % iron. Four of the five alloys used were made from electrolytic flake metal and the remainder from pebble metal of the batch used by Brown, Morrow and Martin¹⁾ in which it was observed that the ductility at 600°C could be increased from 15 % to 70 % by heat treatment at 800°C for 120 hours.

From the present study it has been possible to define on a diagram of temperature (as ordinate) versus composition a boundary above which alloys may be solution treated and below which alloys may be aged. It is only after overageing that maximum ductilities (up to 60 % at 600°C) are obtained. In general an aged condition is produced by air cooling from a hot working temperature of 1050°C and subsequent reheating to the test temperature and it is the properties of such a condition that had led to the belief that beryllium is brittle at $\approx 600^\circ\text{C}$. Observations to date imply that greater ductilities and low yield stresses are obtained in dilute alloys containing relatively low concentrations of precipitating phase and where the matrix has a low solute concentration.

The constitutional diagram is such that the composition range of the zone for solution treatment increases with increasing temperature. It follows, therefore, that with a high impurity content an overaged condition can be obtained by annealing at a higher temperature than for a

lower impurity content alloy. Because of this relative temperature factor, alloys containing ≈ 0.4 wt % can be overaged in ≈ 1 hour at 950°C whereas dilute alloys containing ≈ 0.08 wt % iron require ≈ 100 hours at 700°C . Further it may be that for alloys containing ≤ 0.1 wt % iron the times to produce the ductile state will be prohibitively long unless the degree of purity is such that no solid solution boundary is crossed during cooling to 20°C . Excess additions of impurity should be avoided as even 0.4 wt % iron severely embrittles beryllium at 600°C in the aged condition (< 1 % elongation at 600°C).

A striking feature of the improved ductility at 600°C after overageing is that the fracture mode in such material is fibrous as compared with the aged state where, in general, the fracture is brittle and intergranular. This brittle and intergranular failure not only occurs in the fracture zone but at discontinuous centres throughout the gauge length of the specimen. The intergranular failure of the solution treated state itself undergoes a marked transition with high (0.4 wt % iron) impurity content and becomes transgranular. These changes in fracture mode can be associated with the dissemination of the precipitating impurity phases: where the fracture is intergranular precipitation is concentrated in zones $\approx 2\mu$ thick adjacent to grain boundaries and occurs to a lesser extent at random throughout the matrix, but is generally absent from the actual grain boundary. Where the fracture is transgranular precipitation is found preferentially upon (0001) cleavage planes. In the overaged and ductile state, precipitation is concentrated on grain boundaries and is accompanied by a denudation of precipitation in the $\approx 2\mu$ zones adjacent to grain boundaries. Generally the precipitation is on a fine scale prior to overageing and is in the form of particles $\approx 0.1\mu$ in diameter.

Micro-probe analysis has clearly shown that iron segregates to grain boundaries during ageing in all the alloys and that there is some evidence for the simultaneous migration of chromium and manganese.

Lattice parameter measurements of the beryllium-rich phase have shown that the solution treated state is metastable between 20°C and 900°C and equilibrium is approached only after heating at $> 900^\circ\text{C}$ and cooling slowly. Phases other than beryllium (cph) and beryllium oxide have been identified in the X-ray diffraction patterns; phases A and B (f.c.c., $a = 4.04\text{ \AA}$ and simple cubic, $a = 4.33\text{ \AA}$ respectively) are present in the solution treated state but are dissolved and replaced by phase C (f.c.c., $a = 6.07\text{ \AA}$) during ageing.

Even from this brief survey of some recent observations, it is clear that the brittleness of commercial beryllium at 600°C can be related to a precipitation ageing process. If this conclusion is acknowledged, it follows that effort should be directed to obtaining pure metal which should not show, under any conditions of heat treatment, a ductility minimum at 600°C and that wider use should be made of the present commercial grade after conditioning by heat treatment. It is hoped to publish a full account of the experimental work shortly which should foster a profitable interchange of information with other workers in the field.

At present it is thought that it is the initial segregation of solute, and associated precipitation ageing (hardening) either near grain boundaries or on cleavage planes that causes premature failure in the corresponding regions. Further it is believed that in the overaged state it is not the segregation and coalescence of precipitate in grain boundaries that increases their cohesive strength and which itself could lead to increased ductilities, but rather that the matrix in the immediate neighbourhood is softened.

These present conclusions have been drawn from experimental work carried out by Dr. V. D. Scott, Miss H. M. Lindsay and Messrs. B. Allen, F. Morrow and D. A. Cheer.

Reference

- 1) A. B. Brown, F. Morrow and A. J. Martin, *Nature* 187 (1960) 494

THE RECRYSTALLIZATION OF URANIUM DURING COLD OR HOT FORGING

J. A. SABATO

Division de Metalurgia, Comision Nacional de Energia Atomica, Buenos Aires, Argentina

and R. W. CAHN

Department of Physical Metallurgy, University of Birmingham, UK

Received 28 September 1960

These experiments were originally undertaken to attempt a comparison of the recrystallization kinetics of hot and cold forged samples of uranium metal. This letter describes some surprising initial observations, which indicate that even cold forged metal is partially recrystallised *before* it is annealed at all.

The metal used was uncast billet uranium with low inclusion content, obtained from the UKAEA. Samples were lightly rolled, cut into small pieces 3 mm thick, and annealed at

550° C before use. Samples were deformed hot or cold by controlled impact, to give a reduction in thickness of 50-70 % in one blow. After hot forging, the sample could be quenched *in situ*, either instantaneously or after any desired interval.

The forged samples were electropolished and examined micrographically by polarized light. Measurements of macro- and microhardness (Reichert system) were also made, and in addition back-reflexion X-ray photographs were

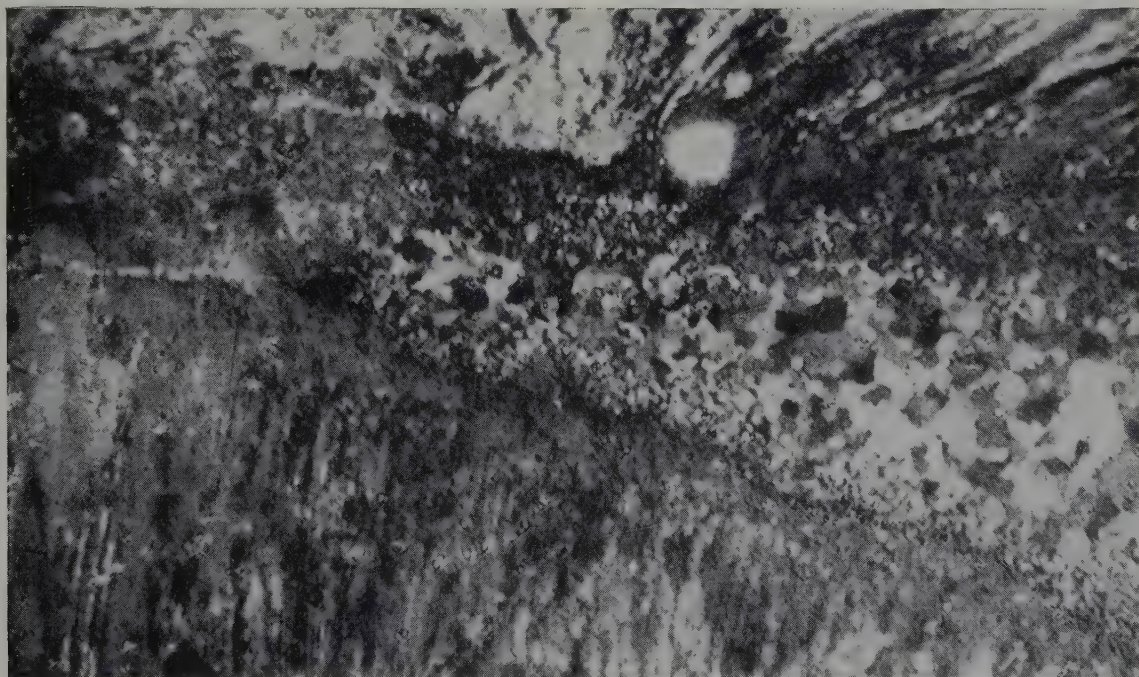


Fig. 1. Uranium, cold-forged to 70 % reduction. Band structure, showing partial recrystallization. $\times 850$.



Fig. 2. Uranium, cold forged to 50 % reduction. Band structure. $\times 450$.

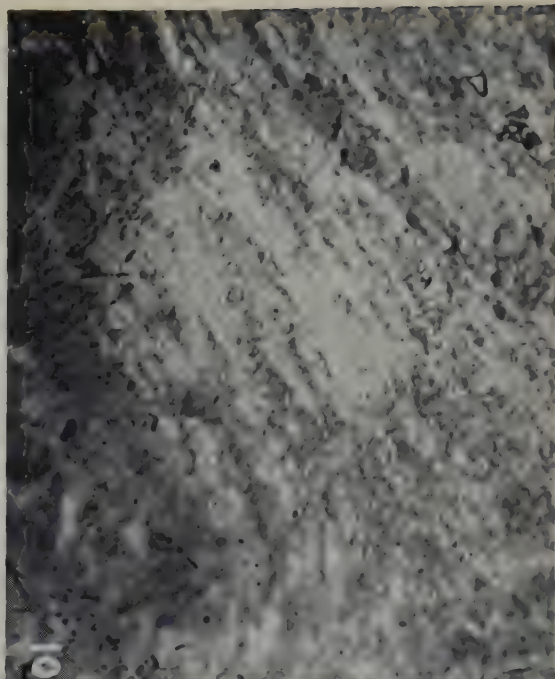


Fig. 4. Uranium, hot forged at 550°C to 50 % reduction, instantaneously quenched. Fine recrystallization. $\times 450$.

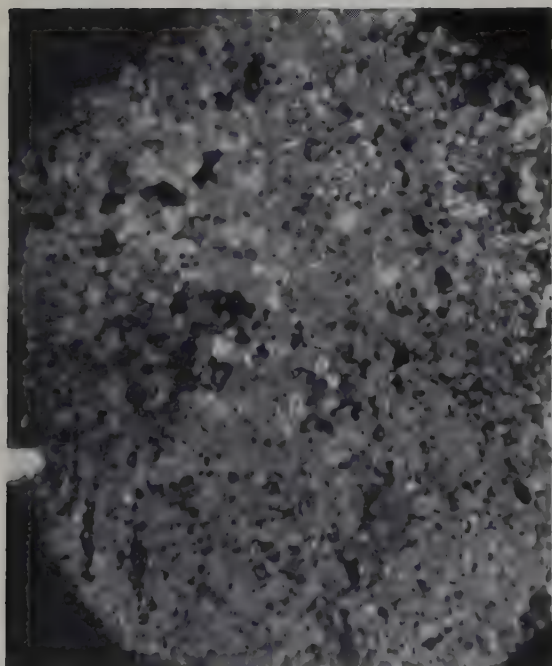


Fig. 3. Uranium, cold forged to 50 % reduction and annealed 1 minute at 550°C . $\times 450$.

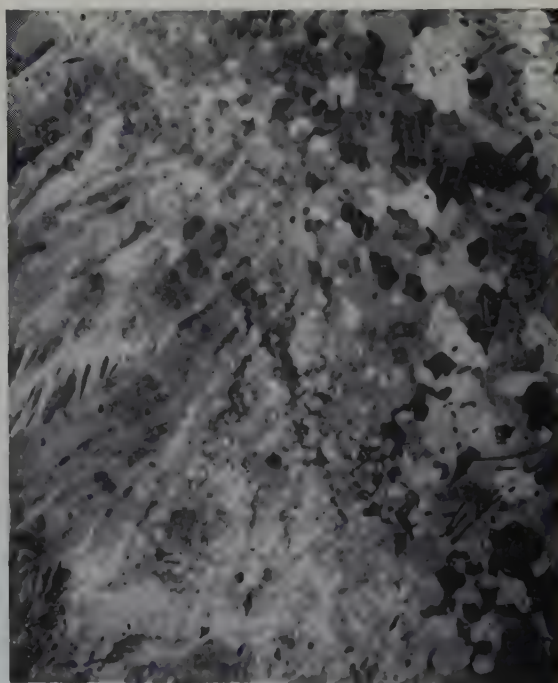


Fig. 5. As fig. 4. Bands of fine and of coarse recrystallization. $\times 450$.

made by unfiltered Cu K radiation, either in a standard camera or by means of a microbeam device which allowed an X-ray beam of 50 μ diameter to be precisely located¹).

Fig. 1 shows a part of a specimen *cold* forged to 70 % reduction. In the centre there appears a band, clearly consisting of recrystallized grains the diameter of which diminishes towards the edges of the band. The rest of the structure is deformed. Fig. 2 shows a similar band in another sample, reduced 50 % by cold forging.

A microbeam diffraction photograph of the band of fig. 2 (which was of approximately the same width as the cross-section of the X-ray beam), gave a coarsely spotty pattern, while another such photograph from the edge of the band showed a speckled pattern superimposed upon continuous diffraction rings. (This kind of pattern is attributed to a polygonised structure.) A third photograph, from a region well away from the band, gave continuous rings only. Normal X-rays photographs (using a 1 mm beam) always gave continuous rings; the resolution did not suffice to reveal the minute recrystallized grains.

Microhardness measurements were made in the same areas as had been selected for the X-ray microbeam photographs. In the region which had given the spotty diffraction pattern, the microhardness was only about half as great as in the neighbouring unrecrystallized region.

All these results, taken together, leave no room for doubt that the bands consist of very small recrystallized grains, even though the sample had not been annealed at all. The fact that the edge of the band appears to be in a polygonised state suggests that this is a transition stage and that under these conditions subgrains may act as nuclei for subsequent recrystallization.

It is noteworthy that the 1:2 ratio of *micro*-hardness values, as between the recrystallized band and the deformed structure nearby, was higher than the ratio of the *macro*hardness values of the original (annealed) and the as forged samples (273 VPN and 367 VPN, respectively). The fact that the ratio of these

numbers is only 1:1.35 suggests that the neighbourhood in which the recrystallized bands were formed had been more heavily distorted than the sample taken as a whole. From the known kinetic energy of the hammer, and mass and specific heat of the specimen, a *mean* temperature rise of 60° C or 100° C was estimated for forging reductions of 50 % and 70 % respectively, assuming all the kinetic energy to have been converted into heat.

A temperature rise of the order of 100° C is inadequate to produce recrystallization in the metal in the second or two during which it is maintained. However, the deformation of cylinders or blocks under impact is far from homogeneous, as recent studies with forged copper cylinders have shown (Kirk²). The central band on the uranium specimens must have been heavily deformed, to judge by analogy with the behaviour of copper specimens, and in accordance with the above argument based on hardness numbers. Such locally enhanced strain must (i) lower the local temperature *needed* for recrystallization, and (ii) increase the local



Fig. 6. Uranium, hot forged at 550° C to 50 % reduction and annealed 1 minute at 550° C. $\times 450$.

adiabatic heat generation per unit volume, and therefore increase the temperature rise. A combination of such factors has presumably been responsible for the genesis of the sharply circumscribed, exceedingly fine-grained recrystallized structure of figs. 1 and 2. The time at temperature must be exceedingly brief, and it is most probable that recrystallization is much more rapid when a deformed specimen is heated rapidly and immediately after deformation, than when the heating is done slowly and at an interval of time after deformation. This would not be surprising, since under the former set of conditions, a plentiful supply of vacancies would be available to accelerate recrystallization.

When a cold-forged sample was briefly annealed, an equi-axed, rather fine recrystallized structure resulted (fig. 3). There were no longer any distinct bands; the fine grains, originally arranged in bands, must have grown to equal the dimension of the grains newly formed during the anneal.

Samples of uranium were also hot forged at 550°C , to 50°C reduction. Here again, there was partial recrystallization even when the sample had been quenched instantaneously after forging. Fig. 4 shows a region of localized, very fine recrystallization, while fig. 5 shows both fine and coarse recrystallized areas, as well as an uncrystallized portion. Fig. 6 shows the effect on the structure of holding the sample for one minute at 550°C before it was quenched.

In these samples, the adiabatic temperature rise (smaller than in the case of cold forging) superheats parts of the sample considerably above 550°C and apparently leads to exceedingly copious nucleation. In instantaneously quenched samples few of these fine grains have any chance to grow, but even a few seconds' holding at 550°C greatly coarsens the structure. Thus figs. 7 and 8 show, for comparison, *macrobeam* X-ray photographs taken after respectively 0 and 20 seconds' holding at 550°C , subsequent to quenching. In fig. 7, the individual spots are too small to resolve.

To summarize, these experiments show that a very fine but inhomogeneous recrystallized

structure can be produced by forging, even at room temperature. It is to be supposed that by careful control of the forging geometry, temperature, and delay time before quenching, the recrystallization could be made more homogeneous without much coarsening the very fine recrystallized grains.

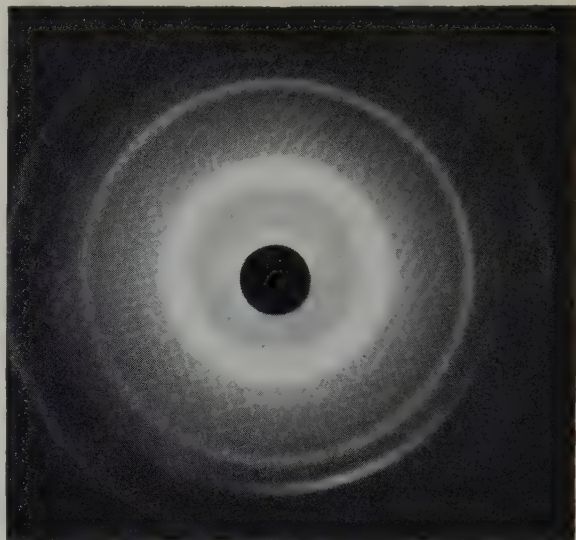


Fig. 7. Back-reflexion *macrobeam* X-ray photograph of uranium, hot forged at 550°C and instantaneously quenched.

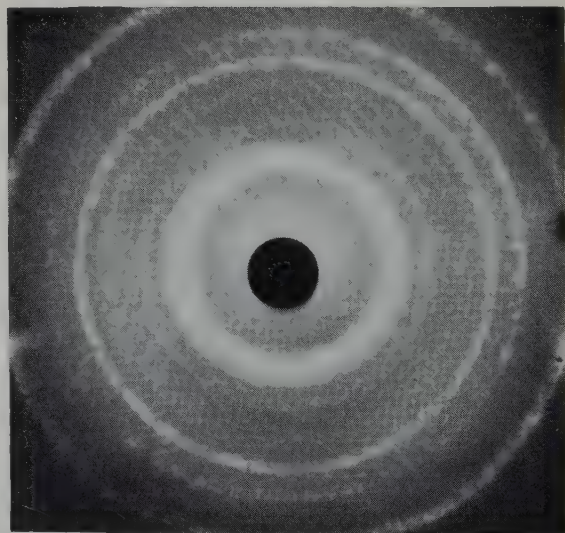


Fig. 8. Back-reflexion *macrobeam* X-ray photograph of uranium, hot forged at 550°C and quenched after 20 seconds' delay.

This work was carried out at Birmingham with financial support from the UK Atomic Energy Authority, to whom we express our thanks. We are obliged to Dr. M. G. Cockcroft for the loan of his special forging equipment. Further experiments on the subject are in progress at Buenos Aires; in the first instance,

aluminium is being used as experimental material.

References

- 1) H. M. Otte and R. W. Cahn, J. Sci. Instr. 36 (1959) 463
- 2) D. Kirk, Ph. D. Thesis (University of Birmingham, 1958)

VERHALTEN VERSCHIEDENER ALUMINIUM-SINTERWERKSTOFFE GEGEN WASSER HOHER TEMPERATUR UND GEGEN SPALTSTOFFE

(VORLÄUFIGE MITTEILUNG)

H. SPINDLER, J. UHLMANN, H. E. RÖLLIG, A. MERZ und F. THÜMLER

*Zentralinstitut für Kernphysik, Bereich Werkstoffe und Festkörper, Rossendorf bei Dresden, und
Forschungsinstitut für metallische Spezialwerkstoffe, Dresden, Deutsche Demokratische Republik*

Eingegangen am 17. Oktober 1960

Als Hüllenwerkstoff der Brennelemente sowie als Kassettenwerkstoff in mit Wasser hoher Temperatur gekühlten Leistungsreaktoren finden gegenwärtig bestimmte Zirkoniumlegierungen technische Verwendung. Neben guter Korrosionsbeständigkeit unter den in Betracht kommenden Betriebsbedingungen weisen diese Werkstoffe auch ausreichende Warmfestigkeitseigenschaften auf. Als Nachteil ist ihre schwierige Herstellungs- und Bearbeitungstechnologie zu nennen, die sich in dem hohen Preis der fertigen Umhüllung widerspiegelt. Neben Bemühungen, den Preis für Zirkonium herabzusetzen, steht die Frage nach geeigneten Austauschwerkstoffen. Hierfür bietet sich aus nuklearen Gründen und wegen der ausgereiften Herstellungstechnologie vor allem das Aluminium an. Trotz der bisherigen umfangreichen Entwicklungen konnte noch kein konkurrenzfähiges Austauschmaterial gefunden werden, und die obere Einsatztemperatur der bestgeeigneten Aluminiumlegierungen liegt mit etwa 230° C sehr wesentlich niedriger als die der Zirkoniumlegierungen. Ausserdem ist das Warmfestigkeitsverhalten der klassischen Aluminiumwerkstoffe bei den erforderlichen Temperaturen unbefriedigend.

Den letztgenannten Nachteil haben die seit einiger Zeit bekannten Aluminiumsinterwerkstoffe nicht. Sie besitzen bei etwa 8-15 % Aluminiumoxyd-Anteil ausgezeichnete Warmfestigkeitseigenschaften sowie gute Kriechfestigkeit, auch bei Temperaturen noch oberhalb

300° C. Es ist deshalb naheliegend, Aluminiumsinterwerkstoffe auf ihre Eignung als Hüllen- und Kassettenwerkstoff in Leistungsreaktoren hin zu untersuchen. Dabei ist nicht nur das bekannte unlegierte Sinteraluminium (SAP) zu beachten, sondern auch geeignet erscheinende legierte Sorten. Bevorzugt sollten zunächst solche Legierungen geprüft werden, die sich bereits als schmelzmetallurgisch hergestellte Werkstoffe relativ gut erwiesen haben. Im Schrifttum finden sich bisher nur wenige Angaben (z.B. ⁵) oder summarische Andeutungen über das Verhalten solcher Sinterwerkstoffe in reinem Wasser hoher Temperatur, über das Verhalten in Wasserdampf hoher Temperatur scheint etwas mehr bekannt zu sein ^{1,2}). Weiter wird von verschiedenen Seiten die Möglichkeit des Einsatzes von unlegiertem SAP in organisch-moderierten und gekühlten Reaktoren geprüft ^{3,4}). Teilweise dürften diese Sinterwerkstoffe wegen ihrer Herstellung aus Al-Al₂O₃-Mischungen ⁵) auch nicht ohne weiteres mit konventionellen Aluminiumsinterwerkstoffen vergleichbar sein †.

Während die Wechselwirkungen zwischen schmelzmetallurgisch gewonnenem Aluminium und Spaltstoffen schon öfters Gegenstand von Untersuchungen waren, (z.B. ^{6,7})) findet man

† Nach Einreichung dieser Arbeit wurde uns noch ein Bericht bekannt ¹⁰) in dem Ergebnisse über das Korrosionsverhalten einiger nickelhaltiger Aluminiumsinterwerkstoffe in Wasser hoher Temperatur mitgeteilt werden (H. W. Schleicher).

im Schrifttum über die Verträglichkeit von SAP mit Spaltstoffen nur wenige kurze Angaben^{4,8)}.

Um ein Urteil über die Leistungsfähigkeit solcher Materialien als möglichen Hüllenwerkstoff geben zu können, sind ausführlichere Untersuchungen notwendig. Über einige vorläufige Ergebnisse zum Korrosionsverhalten und zur Wechselwirkung mit Spaltstoff soll an dieser Stelle kurz berichtet werden.

KORROSIONSV ERHALTEN

Es wurden die folgenden Aluminiumsinterwerkstoffe (ASW) † untersucht, und zwar im Vergleich zu Schmelzlegierungen †† gleicher (metallischer) Zusammensetzung:

ASW aus Reinstaluminium % Al, 99,99
(DIN 1712, Blatt 4)

ASW aus Reinaluminium, % Al, 99,5
(DIN 1712, Blatt 1)

ASW aus Reinstaluminium mit 0,5 Gew. % Fe

ASW aus Reinstaluminium mit 0,5 Gew. % Ni, 0,5 Gew. % Fe und 0,2 Gew. % Si

ASW aus Reinstaluminium mit 9 Gew. % Si, 1 Gew. % Ni

ASW aus Reinstaluminium mit 9 Gew. % Si, 1 Gew. % Ni und 1 Gew. % Ti.

Die Prüfung erfolgte in Autoklaven aus rostfreiem Stahl in Wasser mit einer elektrischen Leitfähigkeit von maximal 5×10^{-6} Siemens/cm⁻¹ (mho/cm), meist bei 300° C. Die Versuchsdauer lag bisher teilweise bis 768 Stunden (= 32 Tage). Das Material wurde im geglühten Zustand eingesetzt, hierbei wurde bei Schmelzlegierungen ein etwas besseres Verhalten als im walzharten Zustand gefunden. Ob dies auch für die Aluminiumsinterwerkstoffe gilt, wurde noch nicht untersucht. Im allgemeinen wurde die nach der Warmverformung erhaltene Oberfläche nicht weiter bearbeitet. Die Versuche ergaben

† Hergestellt im Forschungsinstitut für metallische Spezialwerkstoffe, Dresden.

†† Hergestellt im VEB Leichtmetallwerk, Rackwitz.

das folgende allgemeine Bild. In Wasser von 300° C verhalten sich Sinterwerkstoffe aus unlegiertem Reinst- und Reinaluminium schlecht. Es kommt schon nach kurzer Zeit zur völligen Zerstörung. Bemerkenswert ist jedoch, dass der Angriff beim Sinterwerkstoff gegenüber dem schmelzmetallurgischen Material etwas weniger stark ist bzw. langsamer erfolgt. Weiter wird der Sinterwerkstoff aus Reinaluminium deutlich weniger angegriffen als der aus Reinstaluminium. Dies stimmt mit Beobachtungen anderer Autoren über das Verhalten der Schmelzlegierungen überein. Versagt hat auch der Sinterwerkstoff mit 0,5 Gew. % Eisen. Der entsprechende Schmelzwerkstoff war ebenfalls stark korrodiert.

Die weiteren legierten ASW-Sorten zeigten alle ein wesentlich besseres Verhalten als die bisher besprochenen. Eine Gegenüberstellung der erhaltenen Korrosionswerte mit denen der Schmelzwerkstoffe findet sich in Tafel 1. Beim ASW mit 0,5 Gew. % Ni, 0,5 Gew. % Fe und 0,2 Gew. % Si wurde festgestellt, dass eine nicht einwandfreie Herstellungstechnologie zu schwerem Versagen führen kann. Solche Materialien wurden nicht mit aufgeführt, da sie sich mit an Sicherheit grenzender Wahrscheinlichkeit vermeiden liessen. Die normalen Chargen erwiesen sich als recht gut.

Besonders bemerkenswert ist jedoch das Verhalten der bisher noch nicht beschriebenen Sinterwerkstoffe mit hohem Siliziumgehalt. Zeigen bereits die Schmelzlegierungen ein sehr gutes Verhalten, so wurde beim Sinterwerkstoff eine beträchtliche weitere Erniedrigung der Korrosionsgeschwindigkeit gefunden. Diese Materialien zeigen die günstigsten Werte überhaupt.

Mit unlegiertem Sinteraluminium wurden einige Versuche in Wasser von 150 bis 250° C durchgeführt. Dabei zeigte sich bis 200° C günstiges Verhalten, während oberhalb 200° C ein rascher Angriff unter Aufblähung und Zersetzung des Metalles eintritt. Dies ist ebenfalls eine Parallele zum Verhalten der schmelzmetallurgischen Werkstoffe. Legierte ASW-Sorten wurden bisher in diesem Temperaturbereich noch nicht untersucht.

TAFEL I

Vergleich des Korrosionsverhaltens von Schmelz- und Sinterwerkstoffen aus Aluminium in Wasser von 300° C in Abhängigkeit von der Prüfdauer

Werkstoff		Gewichtszunahme in g/m ² nach				
		48	96	192	384	768 Std.
Reinstaluminium	Sch ^a	←——— völlig zerfallen ———→				
	ASW ^c	←——— völlig zerfallen ———→				
Reinaluminium	Sch ^a	←——— völlig zerfallen ———→				
	ASW ^c	←——— völlig zerfallen ———→				
Al/Fe 0,5 Gew. %	Sch ^a	←——— nicht geprüft ———→				
	ASW ^c	←—— nach 10 Stunden ca 350 ———→				
Al/Ni 0,5, Fe 0,5, Si 0,2 Gew. %	Sch ^a	18,5	21	29	38	51
	Sch ^b	—	16	26	35	47
	ASW ^c	—	22	18	35	49
Al/Si 9, Ni 1 Gew. %	Sch ^a	12	12	18	22	20
	ASW ^c	—	5	7	10	14
Al/Si 9, Ni 1, Ti 1 Gew. %	Sch ^a	12	18	22	17	20
	ASW ^c	—	9	12,5	—	—

^a Schmelzlegierung.

^b Schmelzlegierung, aus dem Schrifttum entnommene Werte nach F. H. Krenz, G. J. Biefer und N. A. Graham ⁹⁾. (Werte graphisch aus Kurve entnommen.)

^c Sinterwerkstoff.

WECHSELWIRKUNG MIT DEM SPALTSTOFF (VERTRÄGLICHKEIT)

Es kamen verschiedene Versuchsreihen zur Untersuchung der Wechselwirkung von unlegiertem Sinteraluminium mit Uran und Urandioxyd zur Durchführung. Hierfür wurden geeignete Probekörper-Paare in besonderen Vorrichtungen mit etwa 1 t/cm² zusammengepresst und im Hochvakuum bis 1200 Std auf Temperaturen bis zu 600° C erhitzt.

Im Falle von Uran und Sinteraluminium zeigten sich ähnlich wie bei Uran und Schmelzaluminium Diffusionserscheinungen. Al diffundierte in Uran, eine Diffusion von U in Al konnte dagegen nicht nachgewiesen werden. In den Diffusionszonen, die metallographisch und röntgenographisch untersucht wurden, liessen sich mehrere intermetallische U-Al-Phasen nachweisen. Die Wachstumsgeschwindigkeit dieser

Schichten scheint geringer zu sein als im Falle des gegossenen Aluminiums. Endgültige Aussagen hierüber können erst aufgrund weiterer Versuche gemacht werden.

Urandoxyd erwies sich bei den bisherigen Versuchen mit Sinteraluminium bis zu den angegebenen höchsten Temperaturen und Glühzeiten als verträglich. Ein sehr geringes Eindringen in das Al an der Berührungsfläche UO₂/ASW, das auf eventuelle Wechselwirkungen hindeuten könnte, überschritt in keinem Falle eine Tiefe von 2 μ . Die Auswertung erfolgte auch hier in der Hauptsache metallographisch und röntgenographisch sowie mit Hilfe von Impulsmessungen.

Wir glauben, aus den bisherigen Ergebnissen, die ohne Einwirkung von Strahlung erhalten worden sind, folgende vorläufige Schlussfolgerungen ziehen zu können:

1. Die Anwesenheit der Oxydphase in Aluminiumsinterwerkstoffen scheint in Wasser hoher Temperatur das Korrosionsverhalten nicht verschlechternd, sondern eher verbessernd zu beeinflussen.

2. Unlegierte Aluminiumsinterwerkstoffe besitzen in Wasser über 200° C keine hinreichende Korrosionsbeständigkeit. Dagegen ist die Beständigkeit von ASW-Sorten, die in ihrer Legierungszusammensetzung den bisher entwickelten besten Aluminium-Schmelzlegierungen entsprechen, diesen Schmelzlegierungen gleichwertig oder sogar überlegen.

3. Als günstigste Legierungen erwiesen sich in dieser Hinsicht bisher Aluminiumsinterwerkstoffe aus Reinstaluminium mit 9 Gew. % Si und 1 Gew. % Ni sowie 9 Gew. % Si, 1 Gew. % Ni und 1 Gew. % Ti.

4. Mit Uranmetall reagiert ASW (unlegiert) ähnlich schmelzmetallurgisch gewonnenem Aluminium, wobei nach den bisherigen Messungen eher eine etwas geringere Reaktionsgeschwindigkeit vorliegt.

Mit Urandioxyd reagiert kompaktes Sinteraluminium auch bei höheren Temperaturen (600° C) nicht oder nur ausserordentlich langsam.

5. Die bisherigen vorläufigen Ergebnisse ermutigen zu Versuchen über längere Zeiträume und unter Strahleneinwirkung. Hierfür verdienen besonders einige legierte Sinteraluminiumsorten wegen der Kombination guter

Warmfestigkeitseigenschaften und guter Korrosionsbeständigkeit in Wasser bei sehr geringer Wechselwirkung mit Urandioxyd grössere Beachtung.

Die Verfasser sind dem VEB Leichtmetallwerk, Rackwitz b. Leipzig, sowie Herrn Dr. Ing. E. Strobel und Herrn Ing. R. Schmidt vom Forschungsinstitut für metallische Spezialwerkstoffe, Dresden, für die Herstellung der Legierungen zu Dank verpflichtet.

Literatur

- ¹⁾ N. J. M. Wilkins und J. N. Wanklyn, *J. Inst. Metals* **88** (1959/60) 134
- ²⁾ C. F. Britton und N. J. M. Wilkins, *J. Nucl. Mat.* **1** (1959) 374
- ³⁾ W. Evans, Atomic Energy of Canada Ltd., Report AECL-573 (1958)
- ⁴⁾ N. Hansen, E. Adolph und J. Christensen, Risø (Dänemark) Report Nr. 13 (Mai 1960)
- ⁵⁾ J. E. Draley und W. E. Ruther, Argonne (USA) Report ANL-5917 (1959)
- ⁶⁾ L. S. de Luca und H. T. Sumsion, Knolls Atomic Power Laboratory (USA) Report KAPL-1747 (1957)
- ⁷⁾ T. K. Bierlein und D. R. Green, Hanford (USA) Report HW-38982 (1955)
- ⁸⁾ M. Boudouresque und K. E. Mann, International Atomic Energy Agency, Report FE/21/I.7 (1960)
- ⁹⁾ F. H. Krenz, G. J. Biefer und N. A. Graham, Atomic Energy of Canada Ltd., Report AECL-604 (1958)
- ¹⁰⁾ R. Weber und U. Zwickler, International Atomic Energy Agency, Report FE/11 Roem 44 (1960)

DISCUSSION

 α - β THERMAL CYCLING OF URANIUM†

A. H. WILLIS

Centre d'Études de l'Energie Nucléaire, Mol-Donk, Belgium

Close inspection will show that the criteria of restricted deformation of the uranium tubes described in the above reference results from the definition of strain used rather than from some physical characteristic of the system. Strain has been defined as the change in length divided by original length, $\Delta x/x_0$, and the circumferential and axial strains were assumed equal and positive. Accordingly, the stated conclusion that the circumferential strain should be less than or equal to $\frac{1}{2}$ (i.e. $r^3 \leq 2c$) indicates only that the specimen thickness cannot be negative, or that the decrease $-\Delta x \leq x_0$.

AUTHOR'S REPLY:

I am very grateful to Mr. Willis for his detailed attention to and comments on my letter. My equations apply for small strains when all definitions are equivalent but are without physical significance for large strains, which occur when the deformation is comparable with the inner radius.

† Discussion of a Letter to the Editors, by W. S. Blackburn, published in J. Nucl. Mat. 2 (1960) 191.

ERRATA

ROGER CHANG: Phase transformation, twinning and anelastic phenomenon associated with zirconium dihydride, J. Nucl. Mat. 2 (1959) 335-340.

1. The symbols "a" and "c" should be interchanged in fig. 1 and also for the lattice parameters given by Softina and co-workers shortly following eq. (2), i.e., $c = 4.44 \text{ \AA}$, $a = 4.97 \text{ \AA}$.

2. In eq. (1), a " $-\eta_1^2$ " term should be included in the numerator (right hand side, first term within the square root sign) of the first two equations involving h and k , i.e.,

$$h = \frac{1}{2\eta_1} \left\{ \sqrt{\frac{2\eta_1^2\eta_2^2 - \eta_1^2 - \eta_2^2}{\eta_2^2 - 1}} - \sqrt{\frac{\eta_1^2 + \eta_2^2 - 2}{\eta_2^2 - 1}} \right\}$$

$$k = \frac{1}{2\eta_1} \left\{ \sqrt{\frac{2\eta_1^2\eta_2^2 - \eta_1^2 - \eta_2^2}{\eta_2^2 - 1}} + \sqrt{\frac{\eta_1^2 + \eta_2^2 - 2}{\eta_2^2 - 1}} \right\}.$$